



UNIVERSITAT POLITÈCNICA DE CATALUNYA  
BARCELONATECH

Escola d'Enginyeria de Barcelona Est

# APPLICATION OF ULTRASOUND IN TWIN- SCREW EXTRUSION AND MICROINJECTION MOLDING: IMPROVEMENTS OF PROPERTIES OF PROCESSED MATERIALS AND NANOCOMPOSITES

Polymers and Biopolymers

**Germán A. Perez Llanos**

Industrial Doctorate Supervised by:

Dr. Jordi Puiggali

Dr. Luis J. del Valle

Barcelona, 2021

**eurecat**

Germán A. Perez Llanos

**APPLICATION OF ULTRASOUND IN TWIN-  
SCREW EXTRUSION AND MICROINJECTION  
MOLDING: IMPROVEMENTS OF PROPERTIES  
OF PROCESSED MATERIALS AND  
NANOCOMPOSITES**

Polymers and Biopolymers

Industrial Doctorate:

Supervised by Dr. Jordi Puiggali and Dr. Luis J. del Valle

Supervised in Eurecat by Maria Eugenia Rodriguez



UNIVERSITAT POLITÈCNICA DE CATALUNYA  
BARCELONATECH  
Escola d'Enginyeria de Barcelona Est



Department of Chemical Engineering  
Barcelona, 2021

Polymeric Materials & Processes Unit  
Cerdanyola del Vallès, 2021



*A mi Familia. En especial a aquellos que ya no están.  
Clara y Francisco siempre en mis pensamientos.  
Gracias.*

# Acknowledgments

I would like to express my sincere gratitude to my two advisors, Dr. Jordi Puiggalí and Dr. Luis Javier del Valle for their patience and immense knowledge, for their continuous support of my PhD study and related research, for being an inspiration to me. I express my thanks for giving me the opportunity to work with them, it was a pleasure and honor.

I would like to extend my gratitude to Dr. M<sup>a</sup> Lourdes Franco and to all the colleagues of PSEP group, specially to Omid, Ina and Matteo, for their support, for being there.

I would also like to thank my advisor M<sup>a</sup> Eugenia Rodriguez, head of “Composites Unit”, and Xavi Plantà, Manager Industrial Technologies Area of Eurecat, for giving me the opportunity to start and be part of this project. I would like to express my sincere gratitude to my colleagues at Eurecat, Marcel, Toni, Carles and to all the “Polymeric Materials & Processes Unit”, with especial mention to Enric Fontdecaba.

I also like to express my thanks to Generalitat de Catalunya and their industrial doctorate plan that allows to develop research studies such this work.

I would like to express my enormous gratitude to who has been a fundamental part in the development of this Thesis, to my family. I owe my deepest gratitude to my parents; I have been extremely fortunate to count on you. I also like to express my heartfelt thanks to my wife Mariela, and my two daughters, Luanna and Laia, for your patience, for your unconditional support.

Last but not the least, I would like to express my gratitude to my nieces and nephews, Andrea, Georgina, you are on a good path, I am proud of you.

# Abstract

The plastics industry is in constant evolution looking to improve the properties of new materials and performance in different applications. Currently, the environmental impact associated with the use of plastics is one of the main concerns for the society. It was reflected in regulations at European level such as *SUP Directive*, *Green Deal* or studies such as *Patents for tomorrow's plastics* by European Patent Office on the trends reflected in research on alternative materials to conventional plastic. In order to transfer these new and more sustainable alternatives to an industrial and realistic environment, first applied research has to be carried out on both the development and processes of the materials to optimize their performance.

In this thesis study, applied research was carried out using ultrasound technology on different nanocomposites and their transformation processes. Advances in the application of ultrasound for different transformation processes have been studied previously to ensure the approach of the practical study. This study focuses on the application of ultrasound in the process of obtaining new formulations by compounding extrusion and in injection molding, specifically in microinjection. The application of nanotechnology in the development of new materials will allow an improvement in performance and will open a range of new possibilities and applications.

To explore the potential of ultrasonic molding (USM) technology, a preliminary process stability study was performed with polypropylene. The evaluation was carried out from a mechanical point of view, in which it was shown that, with an optimization of the process parameters and a correct design approach of the components with the nodal point allow a stability close to production was allowed.

To deepen into the potential of USM technology in synergy with new nanocomposite formulations, a comparative study with the conventional microinjection process was performed. Two different nanocomposites based on a biopolymer matrix of poly 3-hydroxybutyrate with Cloisite 20 (organic modification), and with Cloisite 116 (unmodified) were studied. This research reveals that the USM technology, is stable obtaining micro-pieces, maintaining the chemical structure of the initial biocomposite without degrading and homogeneously achieving an exfoliation of both nanoclays. Conventional microinjection did show slight changes in the level of degradation and chemical structure,

highlighting that it was not possible to micro-mold samples of the material with the unmodified nanoclay.

The stabilization of the compounding extrusion assisted by an ultrasound system has been studied, with a design of a single component that allows the new approach to work in continuous condition and on pre-industrial equipment. Due to the success of the new component, it was possible to carry out the study of new formulations of polypropylene loaded with two different nanoclays (Cloisite 20 and Garamite 1958) and glass bubbles. The new nanocomposites reached the mechanical properties of a conventional material used for door panels in the automotive sector, but with a reduced density. The aim was to demonstrate that it is possible to reduce the weight of plastic components used in the automotive industry and reduce CO<sub>2</sub> emissions for a standard vehicle.

The research carried out in this thesis work has opened a new field of application to nanocomposites for weight reduction with improved mechanical properties when high level of dispersion is reached. In addition, the potential of USM technology for micro-molding applications has been demonstrated, showing high stability without material degradation during the process, and good dispersion of nano-reinforcements.

# Table of Contents

<b>Acknowledgments</b> .....	v
<b>Abstract</b> .....	vi
<b>Glossary of acronyms</b> .....	xii
<b>Listing of Figures</b> .....	xv
<b>Listing of Tables</b> .....	xxv
<b>Structure of the thesis</b> .....	xxvii
<b>1. INTRODUCTION</b> .....	3
1.1 Nanocomposites obtaintion .....	3
1.1.1 Introduction to the process .....	4
1.1.2 Nanocompounds .....	5
1.1.3 Dispersion of additives and fillers .....	6
1.2 Injection Molding .....	8
1.2.1 Introduction to the process .....	8
1.2.2 Microinjection molding.....	10
1.3 Evolution of the ultrasound on polymeric transformation process.....	11
1.3.1 Introduction of ultrasounds components.....	11
1.3.2 Ultrasonic micromolding technology .....	12
1.4 Objectives.....	13
1.5 References.....	15
<b>2. ADVANCES ON THE APPLICATION OF ULTRASONIC TECHNOLOGIES FOR THE MELT PROCESSING OF POLYMERS</b> .....	19
2.1 Introduction.....	19
2.2 Injection molding assisted by an ultrasound system .....	21
2.3 Microinjection molding based in ultrasounds .....	27
2.4 Extrusion assisted by an ultrasound system.....	38
2.4.1 Approach to the ultrasound system.....	38
2.4.2 Effect of the ultrasonic energy during the extrusion process.....	41
2.4.3 Application of ultrasounds under static conditions .....	46
2.4.4 Effect of ultrasonic energy on decrosslink processes .....	47
2.4.5 Effect of ultrasonic energy during the extrusion process on polymer blend processes .....	50
2.4.5.1 Blends with a thermoplastic majority phase from ultrasound assisted extrusion .....	50
2.4.5.2 Elastomeric polymer blends from ultrasound assisted extrusion.....	54
2.4.6 Nanocomposites from ultrasound assisted extrusion.....	55



2.4.6.1	Composites incorporating nanoclays .....	55
2.4.6.2	Nanocomposites incorporating carbon-based fillers.....	61
2.4.6.3	Incorporation of other compounds in ultrasound assisted extrusion processes.....	68
2.5	Conclusions.....	69
2.6	References .....	70
<b>3.</b>	<b>ULTRASONIC DEVICE FOR A POLYMER EXTRUDER MACHINE .....</b>	<b>83</b>
3.1	Introduction.....	83
3.2	Field and state of the Art.....	83
3.3	Brief Description of the Invention.....	84
3.4	Detailed description of an exemplary embodiment.....	92
3.5	Innovation of the invention .....	95
<b>4.</b>	<b>POINT NODAL ULTRASONIC MOLDING OF POLYPROPYLENE: A TECHNOLOGY ABLE TO PREPARE MICROPIECES WITH HIGHLY REPETITIVE PROPERTIES AND GOOD MECHANICAL PERFORMANCE .....</b>	<b>101</b>
4.1	Introduction.....	101
4.2	Experimental section .....	103
4.2.1	Materials .....	103
4.2.2	Ultrasonic micro-molding.....	103
4.2.3	Optimization of the processing parameters.....	108
4.2.4	Measurements .....	109
4.3	Results and discussion.....	109
4.3.1	Rheology.....	109
4.3.2	Mechanical properties .....	109
4.4	Conclusions.....	111
4.5	References.....	111
<b>5.</b>	<b>ULTRASONIC MOLDING OF POLY(3-HYDROXYBUTYRATE): A HIGH- RESOLUTION PROCESS TO GET MICROPIECES WITH MINIMUM MATERIAL LOSS AND DEGRADATION .....</b>	<b>115</b>
5.1	Introduction.....	115
5.2	Experimental section .....	117
5.2.1	Materials .....	117
5.2.2	Nanocomposite preparation: compounding extrusion of P3HB .....	118
5.2.3	Conventional injection and micro-injection molding.....	119
5.2.4	Ultrasonic micro-molding.....	119
5.2.5	Ultrasonic micro-molding equipment.....	120
5.2.6	Measurements .....	122
5.3	Results and discussion.....	124
5.3.1	Optimization of processing parameters .....	124

5.3.2	Molecular weight .....	125
5.3.3	Chemical characterization.....	126
5.3.4	Geometry and morphology of processed specimens .....	127
5.3.5	X-ray diffraction patterns of P3HB processed samples.....	129
5.3.6	Thermal properties and crystallinity of micro-molded specimens.....	130
5.3.7	USM processing of C20/P3HB and C116/P3HB nanocomposites. Molecular weight distribution .....	133
5.3.8	Morphology of C20/P3HB and C116/P3HB nanocomposites .....	134
5.3.9	X-ray diffraction of C20 and C116 nanocomposites .....	136
5.3.10	Thermal stability of P3HB clay nanocomposites .....	138
5.3.11	Calorimetric properties and crystallinity of C20/P3HB and C116/P3HB nanocomposites .....	139
5.3.12	Isothermal crystallization of C20/P3HB nanocomposites: Lamellar thickening and equilibrium melting temperature.....	144
5.3.13	Influence of processing on the mechanical properties of neat P3HB and nanocomposites loaded with the C20 and C116 clays. ....	146
5.4	Conclusions.....	150
5.5	References.....	151
<b>6.</b>	<b>PROCESSING AND PROPERTIES OF POLYMER NANOCOMPOSITES AND NANOCOATINGS AND THEIR APPLICATIONS IN THE PACKAGING, AUTOMOTIVE AND SOLAR ENERGY FIELDS .....</b>	<b>157</b>
6.1	Introduction.....	157
6.2	Processing.....	161
6.2.1	Nanocomposites.....	161
6.2.1.1	Wet Chemical Processing.....	164
6.2.1.2	Thermoplastic Processing.....	165
6.2.2	Nanodeposits .....	167
6.2.2.1	Common Processing .....	168
6.2.2.2	Electrospraying.....	170
6.2.3	Limitations and Process Improvements.....	171
6.2.3.1	Dispersion Quality and Reaggregation .....	171
6.3	Material Properties.....	173
6.3.1	Nanocomposites.....	173
6.3.1.1	Barrier Properties .....	174
6.3.1.2	Mechanical Properties: Reinforcement and Light Weighting vs. Conventional Composites .....	178
6.3.1.3	Viscosity = Processability vs. Mechanical Properties.....	182
6.3.1.4	Polymer Blend Compatibilization .....	183
6.3.1.5	Flammability Resistance .....	183

6.3.1.6	Electrical Properties—Electronics .....	184
6.3.1.7	Microwave Absorbing Property .....	185
6.3.2	Nanodeposits .....	185
6.3.2.1	Repellence to Selected Liquids.....	185
6.3.2.2	Self-Cleaning through Photocatalysis .....	189
6.4	Applications of Polymer Nanocomposites .....	190
6.4.1	Packaging.....	190
6.4.1.1	Barrier Materials .....	190
6.4.1.2	Easy-to-Empty Features .....	194
6.4.2	Solar Panels.....	195
6.4.3	Automotive Parts .....	198
6.5	Nanosafety .....	199
6.6	Conclusions.....	206
6.7	References.....	206
<b>7.</b>	<b>ULTRASOUND ASSISTED EXTRUSION TO PREPARE LIGHT AND REINFORCED POLYPROPYLENE NANOCOMPOSITES FOR AUTOMOTIVE APPLICATIONS....</b>	<b>233</b>
7.1	Introduction.....	233
7.2	Experimental section .....	235
7.2.1	Materials .....	235
7.2.2	Compounding extrusion .....	236
7.2.3	Preparation of nanocomposites from the BF970MO heterophasic copolymer.....	236
7.2.4	Preparation of nanocomposites from the ISPLEN PP080G2M polypropylene homopolymer .....	237
7.2.5	Preparation of injected samples.....	238
7.2.6	Measurements .....	238
7.3	Results and discussion.....	240
7.3.1	Extrusion parameters.....	240
7.3.2	Rheological measurements .....	241
7.3.3	Dispersion of nanoclays .....	243
7.3.4	Thermal properties of nanocomposites .....	245
7.3.5	Mechanical properties of nanocomposites.....	248
7.3.6	Influence of the incorporation of hollow glass spheres .....	257
7.4	Conclusions.....	259
7.5	References.....	260
	<b>CONCLUSIONS .....</b>	<b>265</b>

## Glossary of acronyms

XRD	X-Ray Diffraction
WAXD	Wide Angle X-Ray Diffraction
SAXS	Small Angle X-ray Scattering
SEM	Scanning Electron Microscope
TEM	Transmission Electron Microscopy
FTIR	Fourier-Transform Infrared spectroscopy
AFM	Atomic Force Microscopy
FEM	Finite Element Method
MFI	Melt Flow Index
GPC	Gel Permeation Chromatography
DSC	Differential Scanning calorimetry
TGA	Thermogravimetric analysis
DTGA	Differential Thermogravimetric Analysis
OP	Oxygen Permeability
WVTR	Water Vapor Transmission Rate
OPV	Organic Photovoltaic
BIPV	Building-Integrated Photovoltaics
tfPV	Thin-Film Photovoltaics
Tuft	Tubes by Fiber Templating
Pvd	Physical Vapor Deposition
Cvd	Chemical Vapor Deposition
Ald	Atomic Layer Deposition
OLED	Organic Light Emitting Diodes
EHDP	Electro-Hydrodynamic Processing
ESD	Electrospray Deposition
TSDC	Thermally Stimulated Depolarization Currents
LBL	Layer by Layer
PFCS	Paraffin Wax-Fixed Candle Soot
ESD	Electrostatic Dissipative Coating
NIOSH	Institute for Occupational Safety and Health
UV	Ultraviolet
Mw	Molecular Weight
Eb	Elongation At Break

TS	Tensile Strength
YM	Young Modulus
SME	Specific Mechanical Energy
$T_g$	Glass Transition Temperature
% wt	Weight Percentage
TSE	Twin Screw Extrusión
SSE	Single Screw Extrusion
USM	Ultrasonic Molding
P3HB	Poly(3-Hydroxybutyrate)
PLA	Poly lactide
PBS	Polybutylene Succinate
PCL	Polycaprolactone
PBT	Polybutylenterephthalat
PMMA	Poly (Methyl Methacrylate)
PC	Polycarbonate
COC	Cyclic Olefin Copolymer
POM	Polyoxymethylene
PVC	Polyvinyl Chloride
PTFE	Polytetrafluoroethylene
PPS	Polyphenylene Sulfide
PP	Polypropylene
HDPE	High Density Polyethylene
UHMWPE	Ultra-High Molecular Weight Polyethylene
XHDPE	Crosslinked High Density Polyethylene
LDPE	Low Density Polyethylene
mLLDPE	Metallocene-Catalyzed Linear-Low Density Polyethylene
PA6	Polyamide 6
PS	Polystyrene
PET	Polyethylene Terephthalate
PEN	Polyethylene Naphthalate
PEI	Polyetherimide
POE	Polyolefin Elastomer
NR	Natural Rubber
EPDM	Ethylene Propylene Diene Rubber
SBR	Styrene-Butadiene Rubber

EVA	Ethylene Vinyl Acetate
LCP	Liquid Crystalline Polymer
EVOH	Ethylene Vinyl Alcohol
CFRP	Carbon Fiber Reinforced Plastic
C20	Cloisite 20
C116	Cloisite 116
BEN	Sodium Bentonite Clay
OMMT	Organomodified Montmorillonite
MMT	Montmorillonite
IA	Itaconic Acid
CHX	Chlorhexidine
TCS	Triclosan
FAFP	Flash Aluminum Flake Pigments
CB	Carbon Black
CNT	Carbon Nanotubes
CNF	Carbon Nanofibers
MWCNT	multiwalled carbon nanotubes
SWCNT	Single-Walled Carbon Nanotubes
Gr	Graphene
GO	Graphene Oxide
rGO	Reduced Graphene Oxide
GNP	Graphene Nanoplatelets
ATH	Aluminum Trioxide
ZB	Zinc Borate

# Listing of Figures

<b>Figure 1.1.</b> Compounding extrusion equipment with detail of twin-screw and their different elements: transport (A), mixing (B) and kneading (C). .....	p.5
<b>Figure 1.2.</b> Carbon allotropes: Graphite (3D), Graphene (2D), Carbon nanotubes (1D), Fullerene (0D) and Diamond (3D). .....	p.6
<b>Figure 1.3.</b> A) TEM images B) XRD C) Scheme of dispersion of a nanoclay within a polymer matrix.....	p.7
<b>Figure 1.4.</b> Tortuous path for molecules in a matrix containing platelets in a parallel array (with finite width, L, and thickness, W).....	p.8
<b>Figure 1.5.</b> Scheme of injection molding machine.....	p.9
<b>Figure 1.6.</b> Filling time during the simulated injection process (a) for a 4 cavities mold (b).....	p.10
<b>Figure 1.7.</b> Babyplast, microinjection molding machine.....	p.11
<b>Figure 1.8.</b> Components of an ultrasonic system: 1) Ultrasonic power supply (Branson) 2) Converter 3) Booster 4) Horn 5) Acoustic stack.....	p.12
<b>Figure 1.9.</b> Ultrasonic molding equipment, Sonorus 1G. Inset of processing method with the vibrating sonotrode and plunger pressure.....	p.13
<b>Figure 2.1.</b> Schematic diagram of injection molding assisted by an ultrasound system.....	p.22
<b>Figure 2.2.</b> a) Images of flow length and shape for 1 mm (left) and 3 mm (right) thick specimens that were achieved at 0%, 50%, 70% and 100% of ultrasonic oscillation power and the indicated packing pressures. b) Stress fringe patterns of 1 mm thick specimens achieved for 0% and 100% of ultrasonic oscillation power during 4 s. ....	p.24
<b>Figure 2.3.</b> Scheme showing the mechanism for improvement of surface replication of optical lenses (a) and polarizer images showing the residual strain (b). ....	p.25
<b>Figure 2.4.</b> Schematic illustration of mold surface (left) and SEM micrograph of the surface microstructure of PC microlenses. ....	p.26

**Figure 2.5.** a) Scheme showing the main components of a basic micromolding equipment. Different distinctive steps of the ultrasound micromolding process (inset show details of the interphase between partially molten PLA pellets. b) Examples of PLA specimens obtained under processing conditions of 10 pellets (loaded material), 10 s (processing time), 28.4  $\mu\text{m}$  (amplitude), 3 bars (pressure).....p.28

**Figure 2.6.** Scheme summarizing the influence of amplitude and pressure on PLA processed specimens obtained using a 3 s molding cycle. Mw refers to the molecular weight.....p.29

**Figure 2.7.** a) Supplied ultrasonic generator energy in function of the applied pressure and the oscillation time. b) Comparison between supplied generator, dissipated and melting powers in function of the applied pressure and the oscillation time. ....p.31

**Figure 2.8.** Scheme showing the ultrasonic plasticization of polymer pellets in the feeding camera.....p.32

**Figure 2.9.** a) Scheme of the physical model applied to evaluate the heating effect of friction between polymeric interfaces. b) Finite element model to evaluate local heating at the polymer contact interphase. c) Plot of the temperature dependence with ultrasonic amplitude (frequency 20 kHz and force 300 N). d) Plot of the temperature dependence with ultrasonic frequency (amplitude 30  $\mu\text{m}$  and force 300 N). ....p.33

**Figure 2.10.** a) Model of the microneedle array specimen. b) The filling process and volume fraction of melt in the microneedle array cavity with and without the effect of ultrasonic vibration. c) Melt viscosity distribution in the corner region with and without the effect of ultrasonic vibration. ....p.36

**Figure 2.11.** a) Initial shapes of UHMWPE specimens: Untreated polymer powder, circular and irregular pieces cut off from melt pressed films. b) Molecular weight of three differentiated zones of specimens fabricated by applying 90% and 100% of the ultrasonic amplitude (i.e., 50.6  $\mu\text{m}$  and 56.2  $\mu\text{m}$ ). ....p.37

**Figure 2.12.** Schematic diagrams of extrusion equipment assisted with ultrasound with vertical (left) and horizontal axis (right) dispositions.....p.39

**Figure 2.13.** Ultrasound systems dotted with more than one sonotrode (e.g., two (a) or up to six (b)). ....p.40

**Figure 2.14.** Die modification: new chamber placed in the die (left) or in a previous step (right).....p.40



<b>Figure 2.15.</b> Ultrasound system placed along the extruder barrel. ....	p.42
<b>Figure 2.16.</b> Evolution of die pressure with the ultrasound intensity for extrusion of PS at different screw velocities and temperatures of 210 °C (left) and 220 °C (right).....	p.42
<b>Figure 2.17.</b> Surface morphology images taken at different magnification of m LLDPE extrudates obtained without (a, b) and with (c, d) ultrasonic treatment. ....	p.43
<b>Figure 2.18.</b> Dependence of the apparent viscosity drop for different LLDPE/LDPE mixtures with ultrasonic irradiation time. ....	p.44
<b>Figure 2.19.</b> Schematic invention based on the incorporation of two horns in the extrusion barrel.....	p.45
<b>Figure 2.20.</b> Schematic drawing showing an online casting film equipment assisted by ultrasounds.....	p.46
<b>Figure 2.21.</b> Schematic description of the recombination reaction induced by ultrasounds between crosslinked and linear PP radicals. ....	p.46
<b>Figure 2.22.</b> Schematics configuration of screws for: compounding (a) and decrosslinking (b). The flow direction is from the right to the left.....	p.49
<b>Figure 2.23.</b> SEM images of the lamellar structure of etched cryofractured surfaces of HDPE (a), XHDPE (b), and decrosslinked XHDPE at ultrasonic amplitudes of 7.5 $\mu\text{m}$ (c) and 13 $\mu\text{m}$ (d). An ultrasound assisted twin-screw extruder with the decrosslinking configuration was employed. ....	p.49
<b>Figure 2.24.</b> SEM micrographs of POE extrudates processed without (a) and with (b) ultrasounds; and POE/PS (80/20) blends processed without (c) and with (d) ultrasounds. ....	p.52
<b>Figure 2.25.</b> SEM micrographs of LCP1/LCP2 extruded blends without (a-c) and with (d-i) ultrasound treatment. Blends had compositions of 75/25 (a, d, g), 50/50 (b, e, h) and 25/75 (c, f, i) and the amplitudes of ultrasounds were 7,5 mm (d-f) and 10 mm (g-i)). Arrows indicate the machine extrusion direction. ....	p.54
<b>Figure 2.26.</b> Reactive extrusion system assisted by ultrasounds in presence of supercritical nitrogen. ....	p.57

- Figure 2.27.** TEM micrographs of HDPE incorporating 5 wt.% of clay processed without (a) and with (b) ultrasonic treatment at an amplitude of 5  $\mu\text{m}$ . Models of tortuous diffusion paths for conventional composites (c) and clay nanocomposites (d). .....p.58
- Figure 2.28.** Scheme of the functionalization reaction of LDPE induced by ultrasounds to get the grafted IA derivative.....p.59
- Figure 2.29.** Schematic of coaxial (a) and barrel (b) ultrasonic system. The second case is dotted with two horns that vibrate longitudinally. ....p.60
- Figure 2.30.** Volume resistivity (a) and thermal conductivity (b) of nanocompounds versus CNF concentration. ....p.62
- Figure 2.31.** Optical micrographs of PP nanocomposites incorporating 1 wt.% of CNTs (left) and the corresponding analyzed images (right). Samples were obtained using the DC (left) and MD methods (right) and corresponded to untreated (a, d), and ultrasound treated (b-f) samples. Ultrasound amplitudes were 10  $\mu\text{m}$  (b, e) and 13  $\mu\text{m}$  (c, f).....p.63
- Figure 2.32.** Schematic illustrations of phase transition and structure development pathways. The corresponding SAXS/WAXS patterns during deformation of PP/MWCNTs nanocompounds with MWCNT concentrations lower than 2 wt.% are shown. The formation of cavities in the plastic zone is also illustrated. ....p.64
- Figure 2.33.** Inside cavitation mechanism in the PP/MWCNT nanocompound when ultrasounds were applied in two different places. a) Ultrasonic treatment was applied in the masterbatch dilution step. b) Ultrasonic treatment was applied in the masterbatch preparation step. ....p.65
- Figure 2.34.** Outside (a) and inside (b) cavitation mechanism in nanocomposites obtained with ultrasound assisted processes. SEM images of PP nanocomposites incorporating CNT (c), GNP (d) and CB (e) at low (left) and high (right) magnifications. ....p. 66
- Figure 2.35.** Schematic of the exfoliation and dispersion mechanism of GNPs in a PP matrix with different ultrasound power treatments.....p.68
- Figure 3.1.** Ultrasonic system (a) and their exploded view (b). The components described: (10) Chamber, (11) Inlet bore, (12) Outlet bore, (13) Sonotrode housing bore, (20) Ultrasonic head, (21) Distal portion, (22) Proximal portion, (23) Sonotrode, (24) Ultrasonic amplifier, (25) Ultrasonic transducer, (30) Ring seal, (40) Anchoring device,

(41) Pressure device, (42) Tightening device, (PN1) Nodal plane 1, (PN2) Nodal plane 2, (S1) Surface 1, (S2) Surface 2, (S3) Surface 3.....p.91

**Figure 4.1.** Scheme illustrating the main components of first USM prototypes. ....p.104

**Figure 4.2.** Scheme showing the main steps of a USM process. ....p.105

**Figure 4.3.** Ultrasound micro-molded polypropylene specimen where the high resolution of the processing technology is highlighted by the capacity to distinguish guitar strings with a thickness of only 70  $\mu$ m.....p.106

**Figure 4.4.** a) Scheme showing the main parts of a micro-molding equipment dotted with the point nodal configuration. b) Main processing steps required for ultrasound micromolding using the nodal point approach.....p.107

**Figure 4.5.** Tensile test curves a) Sonorus 1G b) Sonorus 2G with nodal point approach. ....p.110

**Figure 5.1.** Schematic diagram of Twin-Screw Extruder for compounding. ....p.118

**Figure 5.2.** Schematic diagram of injection molding with their 4 steps during the process. ....p.119

**Figure 5.3.** Representative scheme of an ultrasonic molding process (USM). ....p.120

**Figure 5.4.** a) Sonorus 2G<sup>®</sup> prototype including the clamping unit at the bottom (left) and detail showing the main USM components (right). The inset shows the mold and the cavity for the designed specimen geometry. Courtesy of the firm ULTRASON S.L. b) Nodal point ultrasonic configuration (feeding, melting/injection, cooling and ejection steps). ....p.121

**Figure 5.5.** GPC curves corresponding to the initial P3HB pellets (blue), P3HB sample processed under optimal conditions (i.e., amplitude of 36 % of amplitude, a velocity of plunger of 2.5 mm/s) (red), and sample processed under non optimal conditions (i.e., amplitude of 80 % of amplitude, a velocity of plunger of 4 mm/s) (orange). ....p.126

**Figure 5.6.** FTIR spectra of raw P3HB (black lines), for molded P3HB specimens obtained by the USM technology (blue lines) and by conventional micro-injection (green lines), and sample micro-injected under non optimal conditions (red lines).....p.127

- Figure 5.7.** SEM micrograph showing different low magnification images of micro-injected (a) and USM (b) P3HB specimens. Outer (top) and cross-section) bottom images are provided.....p.128
- Figure 5.8.** SEM micrograph showing a cross-section of an USM micro-molded P3HB specimen where spherulitic aggregates with radial lamellae can be envisaged (orange dashed ellipsoid). .....p.128
- Figure 5.9.** a) X-ray diffraction profile of an USM processed specimen of P3HB. b) X-ray diffraction profiles showing the region between 13 and 18 which is highly susceptible to the aging process. Melt extruded sample (blue), USM processed sample (black) and USM processed sample after an aging process (orange). .....p.130
- Figure 5.10.** DSC first heating (a), cooling (b) and second heating (c) runs for injected P3HB specimens (red lines) and micro-molded P3HB specimens obtained by conventional micro-injection (blue lines) and by the USM technology (green lines). .....p.132
- Figure 5.11.** GPC curves corresponding to the initial P3HB pellet (blue), C20/P3HB nanocomposite containing 3 wt.% (garnet) and 8 wt.% (orange) of C20 clay and 3 wt.% (green) of C166. All samples were processed under optimal conditions (i.e., amplitude of 36 % of amplitude and a velocity of plunger of 2,5 mm/s). Values of the weight average molecular weight are indicated in all cases.....p.134
- Figure 5.12.** TEM micrographs at increasing magnification from top to the bottom of C20/P3HB (left) and C116 (right) compounded nanocomposites with clay content of 5 wt.%. .....p.135
- Figure 5.13.** High (right) and low (left) magnification SEM micrographs of cross-sections C20/P3HB (a) and C116/P3HB (b) nanocomposite specimens with a clay content from 5 wt.% and processed by the USM technology. Dashed ellipsoids point out the presence of exfoliated clays.....p.136
- Figure 5.14.** a) X-ray diffraction profile of an USM processed specimen of P3HB (blue) with 5 wt.% of C20 (orange) and C116 (gray) nanoclays. b) X-ray diffraction profiles of C116/P3HB nanocomposites with a clay content of 5 wt.% showing the region between 13 and 18, which is highly susceptible to the aging process. Melt extruded sample (blue), USM processed sample (black) and USM processed sample after an aging process (orange). .....p.137

**Figure 5.15.** TGA (a) and DTGA (b) curves of different USM processed samples: neat P3HB (green), distal (black) and proximal (pink) parts of nanocomposites with 5 wt.% of Cloisite 116, proximal part of the nanocomposite with 5 wt.% of Cloisite C20 (blue) and proximal part of 8 wt.% (lilac) of Cloisite 116. .... p.139

**Figure 5.16.** DSC first heating (a), cooling (b) and second heating (c) runs for micro-molded C20/P3HB specimens obtained by conventional micro-injection. The nanocomposite wt.% increase from the top to the bottom profile: 3 wt.% (black), 5 wt.% (red) and 8 wt.% (blue). ....p.141

**Figure 5.17.** DSC first heating (a), cooling (b) and second heating (c) runs for micro-molded C20/P3HB specimens obtained by USM technology. The nanocomposite wt.% increase from the top to the bottom profile: 3 wt.% (black), 5 wt.% (red) and 8 wt.% (blue). ....p.142

**Figure 5.18.** DSC first heating (a), cooling (b) and second heating (c) runs for micro-molded C116/P3HB specimens obtained by USM technology. The nanocomposite wt.% increase from the top to the bottom profile: 3 wt.% (black), 5 wt.% (red) and 8 wt.% (blue). ....p.143

**Figure 5.19.** a) Isothermal crystallization DSC curves for C20/P3HB nanocomposite containing 5 wt.% of the clay. b) DSC heating curves of the above melt crystallized samples. ....p.145

**Figure 5.20.** Hoffman-Week plot for the C20/P3HB nanocomposite containing 5 wt.% of clay. ....p.146

**Figure 5.21.** Stress-strain curves for neat P3HB specimens processed by USM with the nodal point configuration. Samples differ in the storage time: 1 day (blue), 1 month (red), 1 year (black). ....p.147

**Figure 5.22.** a) Stress-strain curves for neat P3HB specimens processed by USM with (a) and without (b) the nodal point configuration. ....p.148

**Figure 5.23.** a) Stress-strain curves for neat P3HB (blue), PHB5C20 (red) and PHB5C166 (black) specimens processed by USM and using the nodal point configuration. b) Comparison of stress-strain curves for PHB5C20 specimens processed by USM with (blue) and without (red) the nodal point configuration and by conventional micro-injection (black). ....p.150

<b>Figure 6.1.</b> Different types of composites arising from the interaction of layered silicates and polymer. (I) Phase separated microcomposite, (II) intercalated nanocomposites and (III) exfoliated nanocomposites. ....	p.162
<b>Figure 6.2.</b> Melt intercalation synthesis of polymer/clay nanocomposite. ....	p.162
<b>Figure 6.3.</b> Mechanism of clay dispersion and exfoliation during melt processing.....	p. 165
<b>Figure 6.4.</b> Surface of a polyethylene terephthalate film with particle, partially covered by a SiO <sub>x</sub> layer.....	p.169
<b>Figure 6.5.</b> Comparison of oxygen permeability (OP) and water vapor transmission rate (WVTR) properties for different polymers normalized to 100 μm thickness.....	p.175
<b>Figure 6.6.</b> “Tortuous pathway” created by incorporation of exfoliated clay nanoplatelets into a polymer matrix film. In a film composed only of polymer (I), diffusing gas molecules on average migrate via a pathway that is perpendicular to the film orientation in a nanocomposite (II), diffusing molecules must navigate around impenetrable particles/platelets and through interfacial zones which have different permeability characteristics than those of the virgin polymer. ....	p.177
<b>Figure 6.7.</b> Comparison of modulus reinforcement (relative to matrix polymer) for nanocomposites based on montmorillonite (MMT) versus glass fiber for a PA 6 matrix .....	p.179
<b>Figure 6.8.</b> Structure of montmorillonite (phyllosilicate clay).....	p.191
<b>Figure 7. 1.</b> Scheme of the ultrasound assisted co-rotating twin-screw extruder.....	p.237
<b>Figure 7.2.</b> SEM images of Cloisite 20 (left), Garamite 1958 (center) and hollow glass spheres (right). ....	p.241
<b>Figure 7.3.</b> Melt Flow Index (g/10") of nanocomposites obtained by extrusion without (blue bars) and with the assistance of ultrasounds (gray bars): a) PP1/Cloisite 20, b) PP1/Garamite 1958, c) PP2/Cloisite 20 and d) PP2/Garamite 1958.....	p.242
<b>Figure 7.4.</b> TEM micrographs of PP1/Cloisite 20 (a, c) and PP1/Garamite 1958 (b, d) nanocomposites incorporating 5 w.% of nanoparticles without (a, b) and with assistance of ultrasounds (c, d). Inset of (c) points out the presence of intercalated structures. Red arrows indicate the flow direction.....	p.244

**Figure 7.5.** X-ray diffraction profiles of PP1/Cloisite 20 with a 8 wt.% content of nanoclay. All profiles have been normalized to get a similar intensity for the PP peak at  $2\theta = 14.18^\circ$ . The different profiles correspond to: Cloisite 20 (yellow), neat PP1 (black), nanocomposites obtained without (red) and with assistance of ultrasounds (blue).....p.245

**Figure 7.6.** Second heat run of PP2 (black), PP2/Cloisite 20 nanocomposites loaded with 5 wt.% of clay and processed without (blue) and with (red ultrasounds) (a), and PP2/Garamite 1958 nanocomposites loaded with 8 wt.% of nanoparticles and processed without (blue) and with (red) ultrasounds. ....p.247

**Figure 7.7.** Comparison of elastic modulus between different nanocompounds extruded with (gray bars) and without (blue bars) ultrasounds: a) PP1/Cloisite 20, b) PP1/Garamite 1958, c) P2/Cloisite 20, d) PP2/Garamite 1958. Dashed lines indicate the values of the corresponding neat polymers. ....p.249

**Figure 7.8.** Young's modulus of PP1/Cloisite 20 (a) and PP2/Cloisite 20 (b) nanocomposites according to the Reuss (green), Voigt (blue), and Halpin–Tsai (for intercalated and exfoliated structures with oriented and random clay dispositions in yellow and red respectively) models. Experimental modulus are indicated in each case by the square symbols (black) into the inset. ....p.252

**Figure 7.9.** Stress-strain curves for representative nanocomposites loaded with Cloisite 20 (a) and Garamite 1958 (b), at 3 wt.% in green, 5 wt.% with and without ultrasounds, red and blue respectively, and 8 wt.% in black. ....p.253

**Figure 7.10.** Comparison of tensile strength between different nanocompounds extruded with gray bars) and without (blue bars) ultrasounds: a) PP1/Cloisite 20, b) PP1/Garamite 1958, c) P2/Cloisite 20, d) PP2/Garamite 1958. Dashed lines indicate the values of the corresponding neat polymers. ....p.255

**Figure 7.11.** Comparison of tensile flexural modulus between different nanocompounds extruded with gray bars) and without (blue bars) ultrasounds: a) PP1/Cloisite 20, b) PP1/Garamite 1958, c) P2/Cloisite 20, d) PP2/Garamite 1958. Dashed lines indicate the values of the corresponding neat polymers. ....p.256

**Figure 7.12.** Comparison of flexural strength between different nanocompounds extruded with gray bars) and without (blue bars) ultrasounds: a) PP1/Cloisite 20, b) PP1/Garamite 1958, c) PP2/Cloisite 20, d) PP2/Garamite 1958. Dashed lines indicate the values of the corresponding neat polymers. ....p.257

**Figure 7.13.** SEM micrographs of the fracture surface of PP2/Cloisite 20 nanocomposite incorporating 10 wt.% of hollow glass spheres. .... p.258

**Figure 7.14.** Variation of density with the percentage of added nanoparticles, blue for Cloisite 20 and red for Garamite 1958. Six different point with different amounts of glass spheres added to the nanocomposites. ....p.259



## Listing of Tables

- Table 4.1.** Mechanical properties of samples obtained by Sonorus 1G and Sonorus 2G with nodal point approach.....p.110
- Table 5.1.** Properties of the selected nanoclays.....p.118
- Table 5.2.** Processing windows for P3HB (A, B, C and D) and for P3HB with 5 % of Cloisite 20 (E, F, G, and H) and mechanical properties related to the measured temperature and pressure. ....p.125
- Table 5.3.** Average molecular weights and polydispersity index of representative USM processed samples of P3HB and the initial pellet as a control. For the sake of completeness data for a micro-injected P3HB sample is also provided. ....p.126
- Table 5.4.** Average molecular weights and polydispersity index of representative USM processed samples of P3HB and the initial pellet as a control. For the sake of completeness data corresponding to micro-injected pieces containing 5 wt.% of C20 and C166 are also given. ....p.134
- Table 5.5.** Young modulus, maximum strength, and break elongation for processed specimens of P3HB and its nanocomposites with C20 and C116 clays. Standard deviations are indicated.....p.149
- Table 6.1.** Models for predicting barrier properties of platelet filled nanocomposites.....p.177
- Table 6.2.** Glass transition changes with nano-filler incorporation. SWCNT = single-walled carbon nanotubes; MMT = montmorillonite; MWCNT = multi-walled carbon nanotubes. ....p.182
- Table 6.3.** Examples of polymer-clay nanocomposites and their barrier improvements. Permeabilities are expressed as improvement ratios: the ratio of the gas permeability or transmission rate of the virgin polymer to the gas permeability or transmission rate of the polymer-clay composite, measured at the same conditions.....p.192
- Table 6.4.** Representative examples of graphene-based nanocomposites targeting to improve gas barrier properties.....p.193

<b>Table 7.1.</b> Extrusion parameters for processing PP1/Cloisite 20 nanocomposites. ....	p.237
<b>Table 7.2.</b> Extrusion parameters for processing PP1/Garamite 1958 nanocomposites. ....	p.237
<b>Table 7.3.</b> Extrusion parameters for processing PP2/Cloisite 20 nanocomposites. ....	p.238
<b>Table 7.4.</b> Extrusion parameters for processing PP2/Garamite nanocomposites. ....	p.238
<b>Table 7.5.</b> X-ray diffraction data for reference samples and representative nanocomposites studied in this work. ....	p.245
<b>Table 7.6.</b> Thermal properties of processed nanocomposites. ....	p.247
<b>Table 7.7.</b> Mechanical properties of PP1/Cloisite 20 nanocomposites. ....	p.253
<b>Table 7.8.</b> Mechanical properties of PP2/Cloisite 20 nanocomposites. ....	p.254
<b>Table 7.9.</b> Mechanical properties of PP1/Garamite 1958 nanocomposites. ....	p.254
<b>Table 7.10.</b> Mechanical properties of PP2/Garamite 1958 nanocomposites. ....	p.254

# Structure of the thesis

This Thesis consists of seven chapters followed by final conclusions drawn from the whole work.

**Chapter 1.** A general introduction of transformations processes for thermoplastic materials used during the Thesis. This chapter includes a brief description of the compounding extrusion process that was used to obtain new nanocomposites; a brief description of conventional injection molding and micromolding and a brief description of the ultrasonic molding technology. All of them were studied in the following chapters.

## Part I

**Chapter 2.** Includes the state of the art for the ultrasonic technologies applied to the melt processing. A special focus was done for compounding extrusion and microinjection molding, all of them assisted or based on ultrasounds. The benefits to apply ultrasonic energy was described for different application such as blending, decrosslink, improve the productivity due to the reduction of viscosity, higher replication or to improve the dispersion of nanofillers. A potential use of ultrasonic systems was revealed.

**Chapter 3.** Describes the design of a new component that allow enhance the stability of the ultrasonic system for extruder machines. The implementation of this new approach in a pilot extruder equipment proves that the ultrasound system can be coupled to the industrial machine to work in continuous conditions. The stability of the process ensures the homogeneity of the material obtained by compounding extrusion process.

**Chapter 4.** Presents an evaluation of the ultrasonic molding process to obtain micropieces of polypropylene from a mechanical point of view. The study compares the behavior of microsamples obtained with and without nodal point approach during the tensile tests. The nodal point approach has been proved to be suitable to the production of microsized pieces with highly repetitive results.

**Chapter 5.** Describes an evaluation of a nanocomposite microsamples obtained by different molding technologies. A comparison between the conventional micromolding and ultrasonic molding was performed. In contrast to the conventional process, the ultrasonic technology shown no change for the chemical structure of the poly-3-

hydroxybutyrate based nanocomposites. The most important difference between both technologies have seen for nanocomposites with non-modified nanoclays at 8 wt.%, while the conventional injection molding failed to obtain samples, the ultrasonic technology could obtain them.

## **Part II**

**Chapter 6.** Presents an overview of the applications of nanocomposites and nanocoating in different sectors, automotive, packaging and solar energy fields. Several technologies were described to improve the dispersion of nanoparticles, giving the basics in terms of composition and of processing aspect to reach the optimal properties. As an outlook, up to date nanosafety issues were discussed in this chapter.

**Chapter 7.** Describes the study performed to obtain nanocomposites of polypropylene with two different nanoclays (Cloisite 20 and Garamite 1958) and glass bubbles by compounding extrusion assisted with ultrasound system. The aim of this study was to reach similar mechanical properties to the commercial material used for door panels, but with a lower density to prove that the plastic components in automotive sector can be substituted for lightweight materials to reduce the CO<sub>2</sub> emission. The results showed that a 11 % of the total weight can be reduced for door panels increasing the dispersion of nanoclays by the application of ultrasounds during the extrusion process.

# 1.

## INTRODUCTION



# 1. INTRODUCTION

## 1.1 Nanocomposites obtaintion

One of the most employed process in the industry to modify the performance of a neat polymer is the *compounding extrusion*. The process mixes a polymer base with an additive and/or filler to obtain new materials with different properties named compounds (or composites). It is the main process used to obtain masterbatches, materials with high content of additive or filler, such colors or calcium carbonate. Materials with electrical conductivity, improved mechanical properties or resistance to UV (ultraviolet) radiation when the neat polymer have not these properties, are only an example of compounds that can be obtained with the compounding extrusion.

For the last decades, composites and nanocomposites materials have been widely reported in the scientific literature to provide substantial enhancement of properties even at a low nanoparticle content. In nanotechnology, polymer nanocomposites are defined as solids consisting of a mixture of two or more phase separated materials. One or more dispersed phases are in nanoscale where the major phases correspond to a polymeric matrix. Materials can be referred to as nanoscaled when their size, meaning at least one of the three external dimensions range from approximately 1 nm to 100 nm. Nanocomposites can be processed by conventional wet and dry processing techniques, yet in adjusted conditions compared to their neat counterparts.

The nanocomposite performance depends on different nanoparticle features such as the size, aspect ratio, specific surface area, volume fraction, compatibility with the matrix and degree of dispersion. The suitable dispersion of nanoparticles remains the key in order to obtain the full nanocomposites potential in terms of e.g., mechanical and barrier properties. In fact, although a long time has gone in the nanocomposites' era, the dispersion state of nanoparticles remains the key challenge in order to obtain the full potential of enhancement of at low filler loading. Indeed, the extremely high surface area leads to change in the macromolecular state around the nanoparticles (e.g., composition gradient, crystallinity, changed mobility, etc.) that modifies the overall material behavior.

The nanoparticles dispersion can be characterized by different states at nano-, micro- and macroscopic scales. For example, nanoclay based composites can show three

different types of morphology: immiscible (e.g., microscale dispersion, tactoid), intercalated and exfoliated (miscible) composites [1]. The affinity between matrix and filler increases from tactoid over intercalated to exfoliated clays [2]. Several strategies have been used to improve the dispersion quality, including either chemical or physical approaches. Surface modification to enhance the compatibility of the matrix and fillers is often used, for example through the grafting of organosilanes, or using long chains alkyl ammonium clay platelets intercalating ions [3,4]. Alternatively, when applicable, in situ polymerization may be preferred to reach a good dispersion [5].

At present, several compounder companies should solve the problematic of the particles (micro or nano) agglomeration in different polymeric matrices. In order to avoid the agglomeration of the nanoparticles during the twin screw extrusion (TSE) process to obtain the nanocomposite, an ultrasound system was developed to be coupled at the die of the extruder. With an enhancement on the dispersion degree of the nanoparticles the performance of the nanocomposite developed will be the optimal, opening the possibilities of the nanocomposites to new applications.

### **1.1.1 Introduction to the process**

Extrusion allows melting a polymer with a high energy input during a short time. Due to the supply of heat and energy input caused by friction between the screws, the mass melts, becomes formable and is pressed through the extruder die. The exfoliation is favored at high shear rates with a correct choice of the location to introduce the nanoparticles, while longer residence time favors a better dispersion [6].

The development of a nanocomposite with a high degree of dispersion should be accompanied by the best molding process for each application. The injection molding was the selected process for the present work. The literature reveals how the different parameters of the injection molding process might affect directly in the quality of the injected part and their properties. The formulation is important, but the process parameters also show a relevant importance.



Compounding extrusion is a process where a neat polymer can be mixed with additives and/or fillers to obtain new properties. The equipment (**Figure 1.1**) is composed mainly by six parts: Motor, screw, heating barrel, die, feeders and Control system. The feeders will introduce the materials into the extruder, the neat polymer at the beginning and the additives/fillers later in a second step. The heating barrel allows the necessary temperature to melt the processed polymer aided with the shear applied by the screw (usually twin-screw) with a rotational movement. The die is the final component that the material passes through before being pelleted. The control system will give the inputs to the equipment: flow of each feeder (g/min), speed of screws (rpm) given by the motor, temperature profile of the heating barrel.

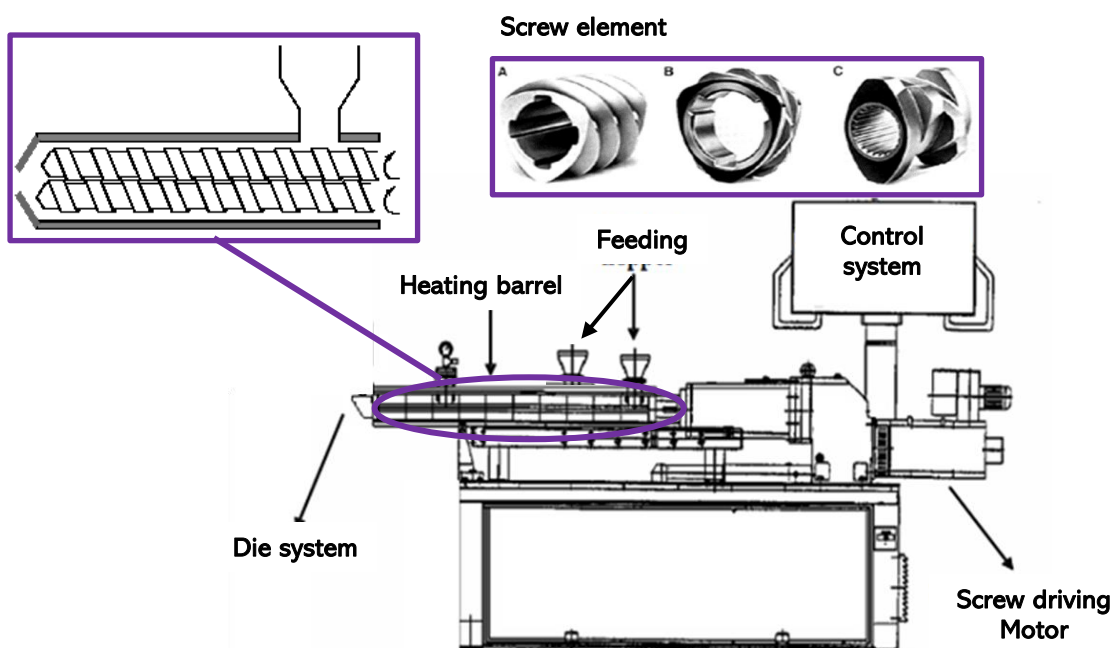


**Figure 1.1.** Compounding extrusion equipment with detail of twin-screw and their different elements: transport (A), mixing (B) and kneading (C).

For the process of compounding extrusion, the design of the screw will be critical to control de

### 1.1.2 Nanocompounds

The need to obtain new materials that meet the demands of industries such as automotive, aeronautics or medical, is clear. the requirements to be met by new materials are very demanding. The polymer composites materials are defined as a combination of two more phase separated materials, materials that in the appropriate cases have a synergistic effect to improve their performance (i.e., carbon fiber reinforced plastic (CFRP)). When the minor amount of one of the components is nanoscale sized (range

from approximately 1 nm to 100 nm), the materials are referred as nanocomposites or nanocompounds. The last decades, nanocomposites materials have been widely studied by the scientific community due to the potential applications in different sectors. Each advanced step in the development of new nanoparticles (**Figure 1.2**) is a great advance in the investigation of new nanocomposite materials with improved properties.

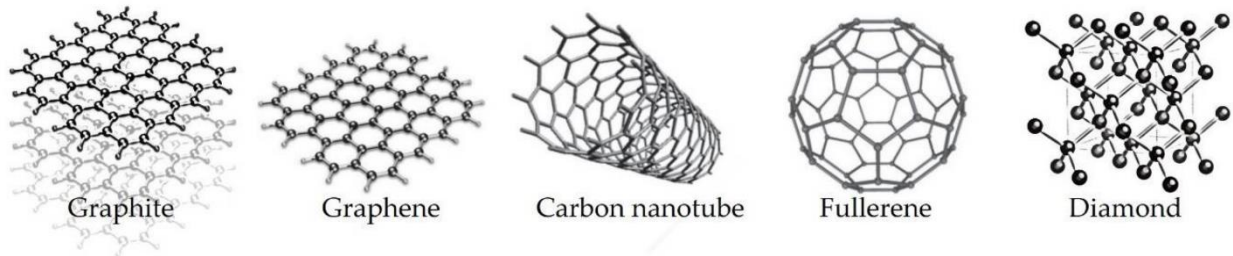


**Figure 1.2.** Carbon allotropes: Graphite (3D), Graphene (2D), Carbon nanotubes (1D), Fullerene (0D) and Diamond (3D). Reproduced from [7]

The nanocomposite performance depends on different nanoparticle features such as the size, aspect ratio, specific surface area, volume fraction, compatibility with the matrix and degree of dispersion. The suitable dispersion of nanoparticles remains the key in order to obtain the full nanocomposites potential, such as improved mechanical and barrier properties.

### 1.1.3 Dispersion of additives and fillers

The aggregation of nanoparticles is followed by an insufficient dispersion in the desired formulations. To characterize the dispersion quality, there are different techniques used for structure characterization of nanocomposites: X-ray diffraction (XRD), Scanning Electron Microscope (SEM), Transmission Electron Microscopy (TEM), infrared spectroscopy (IR) and atomic force microscopy (AFM) [8]. **Figure 1.3** shows typical samples of composites prepared with clays particles and polymers and the correspondent TEM and XRD analyses corresponding with three different situations represented with a scheme.

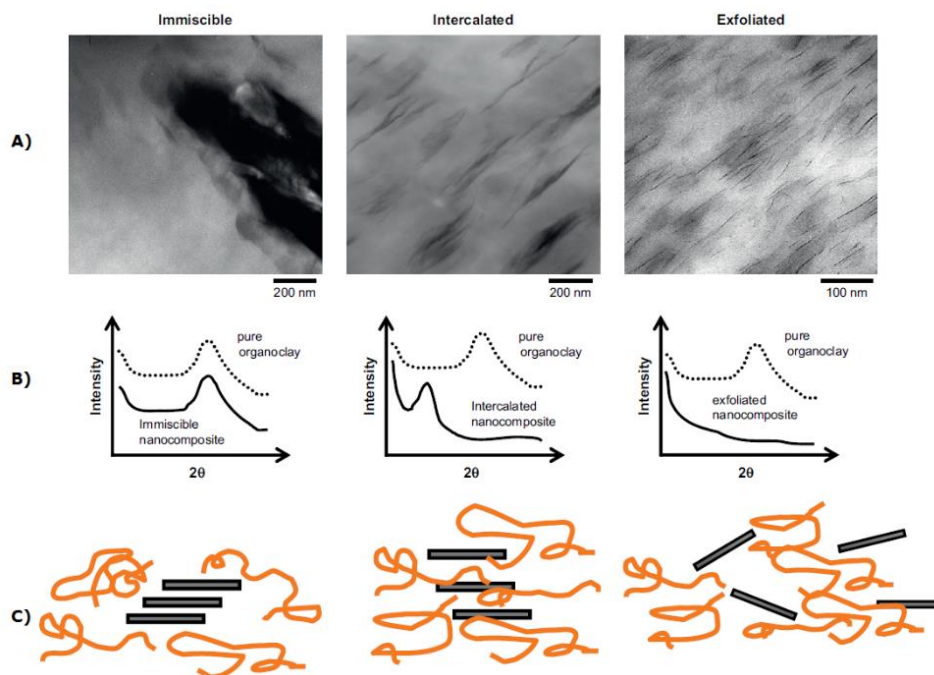


**Figure 1.3.** A) TEM images B) XRD C) Scheme of dispersion of a nanoclay within a polymer matrix. Adapted from [9]

The most important requirements for a polymer-based compound reinforced by nanoparticles are the combination of an optimum surface tension with a maximum dispersion of the separated/exfoliated particles. The physical requirements to achieve it are similar to equal surface energy of polymer and particle surface, low agglomerate energy, low polymer viscosity and high mixing efficiency in the process.

### Particle Surface modification

Most of the inorganic minerals have hydrophilic surfaces and are therefore not compatible with hydrophobic polymer matrices. The aim of filler surface modification is consequently a hydrophobilization to enhance compatibility and enhance the intercalation or exfoliation. Resulting organophilic and hydrophobic clays with lower surface energy of the layers contribute to the polymer diffusion between the layers and finally to a clay platelet delamination.

### Ultrasonic oscillations

In terms of physical methods, besides the use of mechanical mixing methods (high speed mixer, extruder, etc.), the application of ultrasonic vibrations has been reported to be effective in enhancing the dispersion state of nanoparticles both in solvent casting and melt mixing processes [10]. Ultrasonic cavitation transfers high amounts of energy, being

able to disrupt physical and chemical interactions. Additionally, ultrasound energy can break C-C bonds, leading to a formation of long-chain radicals. Those radicals might build chemical bonds on the clay surface in nanocomposite systems [11], and therewith enhance the compatibility of polymer and filler and also between immiscible polymers [12].

The final aim of the transformation processes that uses nanocompounds as a raw material is to optimize the parameters to reach a high level of nanofiller dispersion that ensures the major improvement on the target property. The improvement of barrier properties can exemplify how important is the dispersion and the alignment of the nanofillers. This property is usually improved by adding platelets nanosized into the polymer matrix to create a tortuosity that difficult the diffusion of the gas (typically oxygen or water) as shown in **Figure 1.4**. The alignment of the platelets can be achieved in the injection molding process following the flux direction of the material.

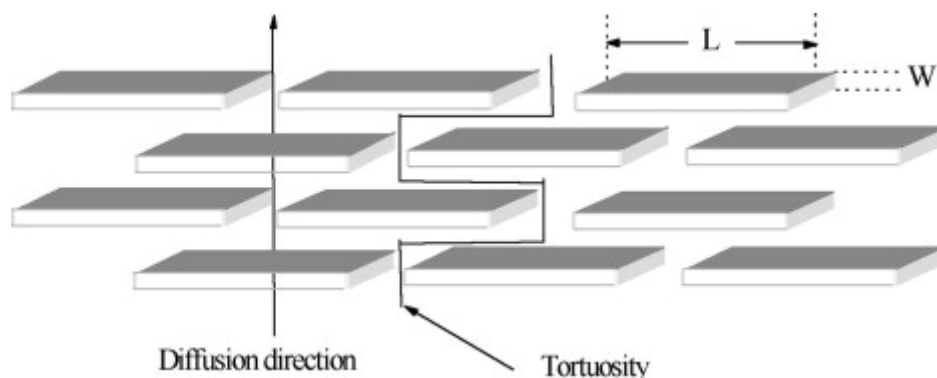


**Figure 1.4.** Tortuous path for molecules in a matrix containing platelets in a parallel array (with finite width,  $L$ , and thickness,  $W$ ). Reproduced from [13].

## 1.2 Injection Molding

### 1.2.1 Introduction to the process

The injection molding is the industrial process employed to obtain items that are used on a daily basis. It is a transformation process that is cyclical, starting with the melting of the thermoplastic material in the form of pellets. Once the material is melted in the injection cylinder, the material is pushed into a mold whose cavity has the shape of the part to be molded. During the cooling and consolidation of the material within the mold, the injection cylinder reloads molten material, preparing for the next injection cycle (**Figure 1.5**).

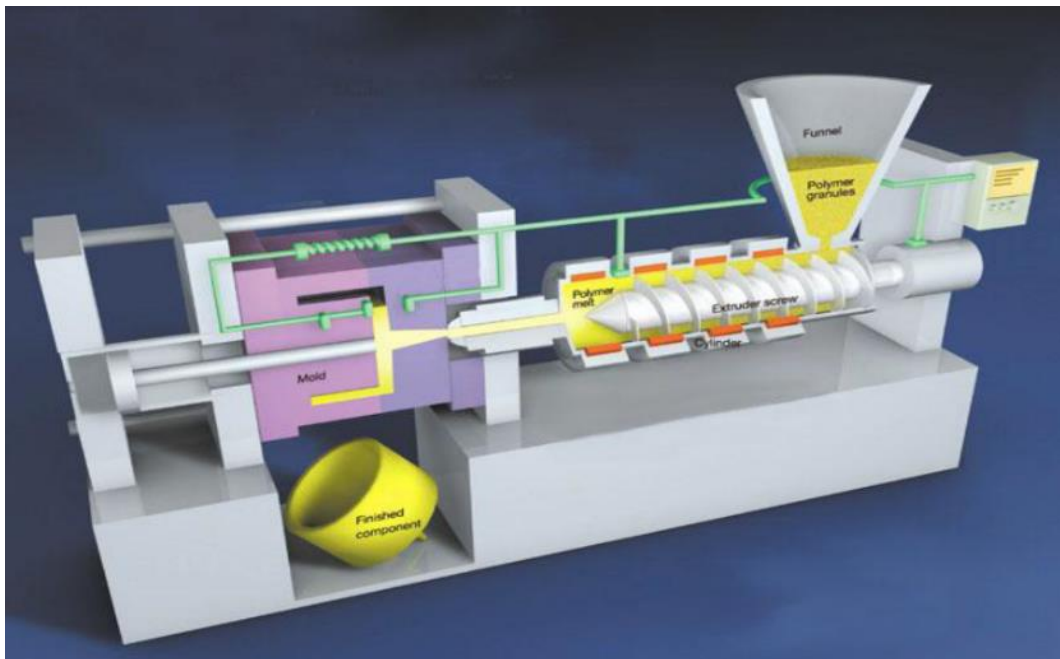


**Figure 1.5.** Scheme of injection molding machine.

Over the last decades the injection molding process was supported by other technologies that allowed an evolution of the equipment and the transformation process itself. It is the case of the control of the parameters, where the manufacturers of the injection machines have incorporated the improvements for each component of the equipment, such as can be the screw design, heating barrel, clamping system or the data recording. It is important to emphasize that mold makers also incorporate new technological advances, such as surface treatments, heating/cooling systems, monitoring or injection simulation processes. The trend in the field of transformation process is go towards a digitalization of the process, industry 4.0, where the sensors, the data information and the simulations are crucial.

Software's for simulations of the process modifying parameters of a specific injection machine, material and mold are usually used in order to ensure the correct process windows and to verify the optimal mold function. This simulation gives outputs as can be the cooling time, maximal pressure of injection or the packing pressure needed for the piece taking into account the polymer properties, process conditions and geometry of the injected specimen.

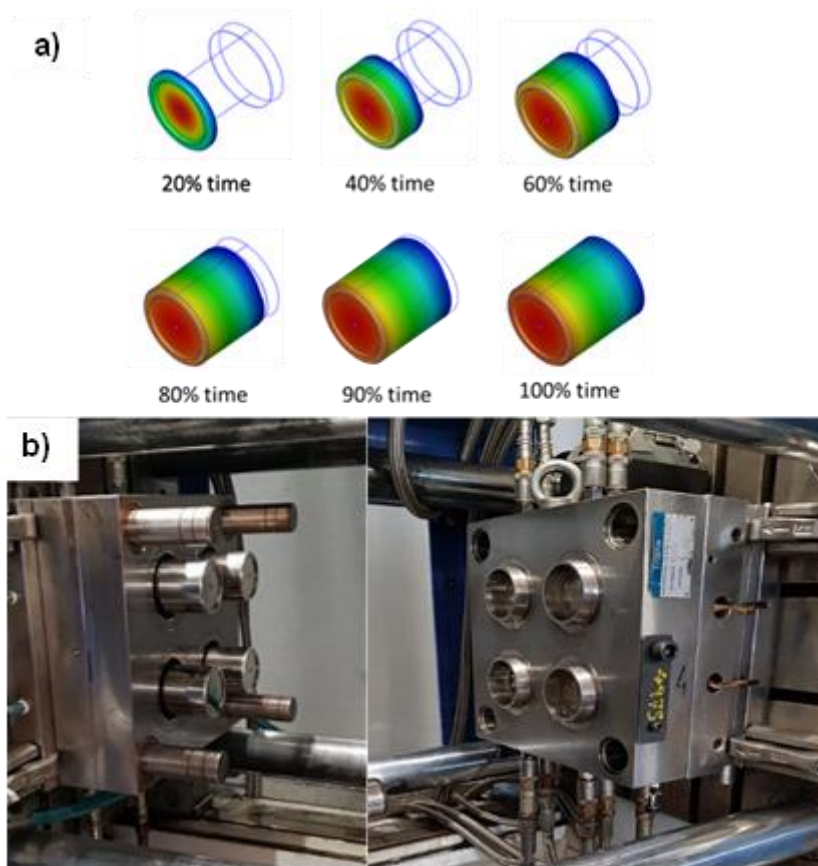


**Figure 1.6.** Filling time during the simulated injection process (a) for a 4 cavities mold (b).

## 1.2.2 Microinjection molding

The evolution of injection molding has allowed it to be a process used for applications in highly demanding sectors such as the medical or aeronautical, and even opening up new fields of application such as plastronics. One of the pathways of evolution of this transformation process has led to injection by micromolding, pushed by sectors where the miniaturization of components is a principal technological driver.

The conventional injection molding equipment were downscaled with different and new challenges for the process. The Babyplast appears in 1995 (**Figure 1.7**), a micromolding machine, is a great example of this evolution, being an equipment that produces microsized pieces in large quantities.

The microinjection molding preferred to the conventional injection molding for low mass injected parts (feed less than 90%), lower process time and not enough mass production to justify the investment of a conventional machine with the cost related to the molds.



**Figure 1.7.** Babyplast, microinjection molding machine.

Other technologies were appearing later. It is the case of the ultrasonic molding (USM), based on the application of high-power ultrasound in the material to bring it to a molten state instead of a heated injection cylinder with a screw.

## 1.3 Evolution of the ultrasound on polymeric transformation process

### 1.3.1 Introduction of ultrasounds components

Currently, ultrasonic energy is used in different application:

- Homogenization, dispersion or deagglomeration of a component in a solvent
- Sonochemistry (reactions, encapsulation, emulsifying, etc.)
- Cell extraction (i.e., for extraction of P3HB produced by fermentation)
- Welding plastics
- Cleaning systems
- Measures and detection of imperfection in a sample (i.e., gas traps in composites)
- Others

The main ultrasonic components (**Figure 1.8**) are the power supply that transfer the electric energy to the converter, a piezoelectric component that converts this energy into kinetic energy to create oscillatory movements; this oscillatory energy will be transferred

to the horn or sonotrode, the final component that it is in contact with the medium to apply the longitudinal vibration. Between the converter and the sonotrode can be located a booster, component that can increase or decrease the oscillatory movement, depending on their design and the final application.

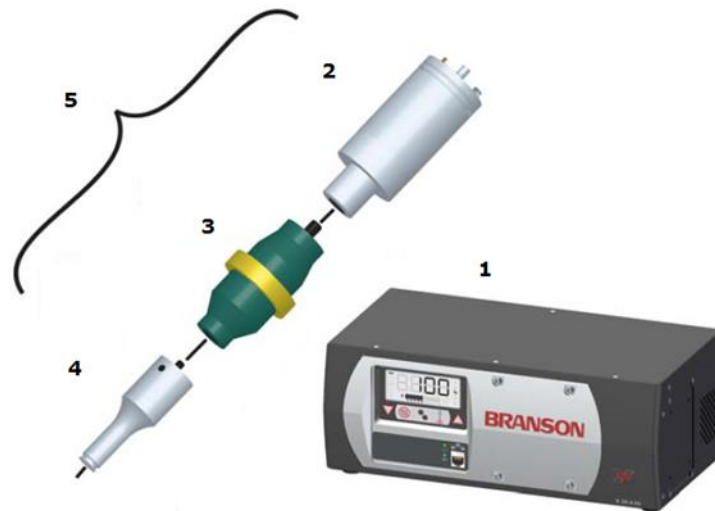


**Figure 1.8.** Components of an ultrasonic system: 1) Ultrasonic power supply (Branson) 2) Converter 3) Booster 4) Horn 5) Acoustic stack.

Related to the polymer application, the ultrasonic energy is mainly used in industrial fields to clean of metal components such as mold or screw, detection of gap traps and welding two different components (i.e., coffee cups paper-polymer weld).

### 1.3.2 Ultrasonic micromolding technology

By investigation carried out in the field of polymer processing, the technological center ASCAMM (now Fundació EURECAT) has developed a new injection machine based on ultrasonic energy. As a result of this growing technology, Ultrason, a spin-off of EURECAT is created in 2010 and develops their first prototype in 2011, named Sonorus 1G (**Figure 1.9**). The technology requires a low mass of material to produce micropieces, a requirement for sectors such as medical or pharmaceutical where the material cost is critical. The process will apply the ultrasonic energy by the sonotrode pushing the fed material by a plunger. When the material is in contact with the sonotrode in vibration it will be molten and pushed to the cavity of the mold.



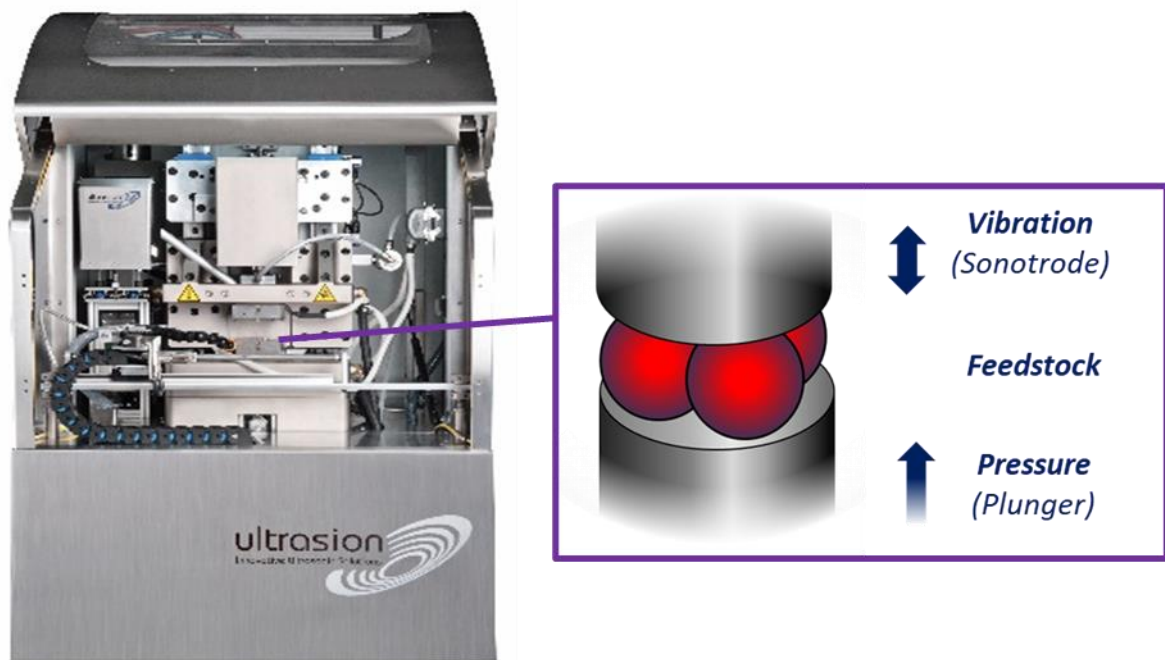


**Figure 1.9.** Ultrasonic molding equipment, Sonorus 1G. Inset of processing method with the vibrating sonotrode and plunger pressure.

The described technology is in continuous evolution, with improvements in monitorization of the process, component designs, mechanical function of the equipment and software. Currently, there are different aspects to improve, being the main focus understand the influence of the ultrasounds on the polymeric material and their fillers/additives, but it was already demonstrated the potential of the technology: improve the dispersion of fillers/additives, lower mass to produce micropieces, lower time of the process, better replication on the surfaces, less tension of pieces, etc.

## 1.4 Objectives

The present Thesis study was performed under the Industrial Doctorate plan of Generalitat de Catalunya in collaboration with PSEP (Synthetic polymers: Structure and Properties. Biodegradable polymers) group of Polytechnic University of Catalonia (UPC) and EURECAT, the technology center of Catalonia.

The main aim of this PhD work corresponds to the evaluation of the ultrasonic energy effect during the melting transformation process of thermoplastics polymers and nanocomposites. To reach this goal, the Thesis work is divided in two different blocks with the specific objectives listed below:

## Part I:

- ! To explore the potential of the ultrasound systems employed in literature for melt processing different polymeric families and develop a new approach to be evaluated.
- ! To analyze the compounding extrusion assisted by an ultrasound system in order to improve the stabilization of the transformation process at pilot scale level. To develop new design of components were envisaged.
- ! To evaluate the new approach of ultrasonic molding considering the nodal point for a neat polymeric material.
- ! To evaluate the effect of ultrasonic molding considering the nodal point for a neat biopolymer poly(3-hydroxybutyrate) (P3HB) and their nanocomposites and nanoclays Cloisite 20 (C20) and Cloisite C116 (C116): P3HB/C20 and P3HB/C116.
- ! To compare the conventional micromolding process and the ultrasonic molding for the nanocomposites P3HB/C20 and P3HB/C116.

## Part II

- ! To explore the nanotechnology in the development of new materials and their potential applications in different sectors such as automotive or packaging.
- ! To study the twin-screw compounding extrusion assisted with an ultrasound system optimized with the new approach for the development new nanocomposites of PP/C20 and PP/Garamite1958 with glass bubbles.
- ! To improve the dispersion of nanoclays by application of ultrasonic energy during the compounding extrusion and to evaluate their influence on mechanical properties.
- ! To study new nanocomposites formulations that replace the conventional plastic components used in automotive sector to reduce their associated weight and, therefore, reduce the CO<sub>2</sub> emissions.

## 1.5 References

1. Paul, D.R.; Robeson, L.M. *Polymer*, 49, 15, 3187–3204, 2008.
2. McAdam, C.P.; Hudson, N.E.; Liggat, J.J.; Pethrick, R.A. *J. Appl. Polym. Sci.*, 108, 4, 2242-2251, 2008.
3. P.T. Bertuoli, D. Piazza, L.C. Scienza and A. J. Zattera, "Preparation and characterization of montmorillonite modified with 3-aminopropyltriethoxysilane," *Applied Clay Science*, no. 87, p. 46–51, 2014.
4. Huskić, M.; Žigon, M.; Ivanković, M. *Appl. Clay Sci.*, 85, 109-115, 2013.
5. Usuki, A.; Kojima, Y.; Kawasumi, M.; Okada, A.; Fukushima, Y.; Kurauchi, T.; Kamigaito, O. *J. Mater. Res.*, 8, 1179–1184, 1993.
6. Dennis, H.R.; Hunter, D.L.; Chang, D.; Kim, S.; White, J.L.; Cho, J.W.; Paul, D.R. *Polymer*, 42, 23, 9513- 9522, 2001.
7. Giubileo, F.; Di-Bartolomeo, A.; Lemmo, L.; Luongo, G.; Urban, F. *Appl. Sci.*, 8, 4, 526-547, 2018.
8. Sinha Ray, S.; Okamoto, M. *Prog. Polym. Sci.*, 28, 1539–1641, 2003.
9. Galimberti, M. Rubber Clay Nanocomposites. In *Advanced Elastomers-Technology, Properties, and Applications*, 91, IntechOpen Limited, London 2012.
10. Xia, H.; Wang, Q.; *J. Appl. Polym. Sci.*, 87, 11, 1811-1817, 2003.
11. Lapshin, S.; Swain, S. K.; Isayev, A.I. *Polym. Eng. Sci.*, 48, 8, 1584-1591, 2008.
12. Lin, H.; Isayev, A.I. *J. Appl. Polym. Sci.*, 102, 3, 2643–2653, 2006.
13. Choudalakis, G.; Gotsis, A.D. *Europ. Polym. J.*, 45, 4, 967-984, 2009

# ———— Part I ————

# 2.

## ADVANCES ON THE APPLICATION OF ULTRASONIC TECHNOLOGIES FOR THE MELT PROCESSING OF POLYMERS



## 2. ADVANCES ON THE APPLICATION OF ULTRASONIC TECHNOLOGIES FOR THE MELT PROCESSING OF POLYMERS

### 2.1 Introduction

Ultrasonic waves are highly attractive for researchers and industries due to their increasing applications in melt processing of thermoplastic polymers, the development of medical and cleaning products and the efficient dispersion of nanoparticles in polymer composites. Accurate and homogeneous products with improved physical and mechanical properties can be achieved through ultrasound-assisted processes, which can also offer cost effective benefits. Ultrasonic waves are currently being employed in different processes including extrusion, compounding, blending, devulcanization, decrosslinking, injection and microinjection molding [1-3].

Extrusion and injection molding are both the most important production processes of plastics. A potential use of ultrasonic energy to assist the mentioned processes of transformation has been evidenced with different experimental investigations. It is fundamental the comprehension of the effect of ultrasounds in polymer melts in order to optimize the ultrasonic system and adapt it to the different kinds of polymers for future applications [4].

The absorption of the ultrasonic energy generates an increase of temperature in the material and an oscillatory movement of constitutive molecules. The application of pressure should made feasible a directed flow of the material towards the nozzle or the mold.

The application of an ultrasonic oscillation in a material can generate a local heating and consequently an increase of temperature ( $\Delta T$ ) that is defined by equation 1:

$$\Delta T = I \cdot t \cdot \frac{(1 - e^{-2 \cdot \varepsilon \cdot x})}{x \cdot \rho \cdot H} \quad (1)$$

where  $I$  denote the sound intensity,  $t$  is the oscillation time,  $\varepsilon$  is the coefficient of ultrasonic energy absorption,  $x$  is the distance,  $\rho$  is the density of the material, and  $H$  is the heat capacity.

The sound intensity can be calculated by equation 2:

$$I = \frac{1}{2} \cdot \rho \cdot c \cdot (\omega \cdot A_x)^2 \quad (2)$$

where  $c$  is the sound velocity,  $\omega$  is the angular frequency ( $2\pi f$ , where  $f$  is the frequency) and  $A_x$  represents the amplitude at distance  $x$ .

This amplitude is defined by equation 3:

$$A_x = A_0 \cdot (e)^{-\alpha \cdot x} \quad (3)$$

where  $A_0$  is the original amplitude, and  $\alpha$  is the attenuation coefficient.

Extrusion is a continuous process of plastic transformation that is mainly employed to produce profiles, films, filaments, or new composites and blends. In the last decades, the ultrasonic energy was demonstrated to be effective to reach a high degree of dispersion of nanofillers within a polymeric matrix during the extrusion process as well as to improve the compatibility between immiscible polymers [5-8]. XRD, TEM, SEM or AFM analyses are frequently employed to verify the dispersion of the filler that explains the physicochemical changes on the material induced by the ultrasonic treatment [9].

Production of pieces with complex geometries and complicated design is mainly performed by injection molding due to its intrinsic advantages over other processing technologies. Research has also been focused to improve production by means of the application of ultrasounds. It has been demonstrated that the ultrasonic energy is effective to melt the polymer, extend the flow length and enhance the filling efficiency. The extra vibrations provided by ultrasounds can be beneficial during heating since melt viscosity can be decreased and a homogenous flow can be obtained despite the lack of a suitable heat conduction of polymers. Furthermore, the applied injection pressure can be decreased with the consequent energy savings.

Micro-injection molding has also been developed for the production of small pieces which cannot be obtained by conventional molding. Nevertheless, there are several challenges like filling efficiency, skin layer and accuracy of microparts, which can only be satisfactorily overcome by means of new ultrasonic micromolding technologies. As then will be explained in detail, cycle time in micromolding can be significantly shortened since ultrasonic energy dissipates energy rapidly compared to the heat conduction attained in



the barrel of a conventional micro-injection equipment. In addition, other advantages are offered by this technique: low polymer content in each cycle (around 200 mg), reduced amount of rejected material due to high dosage precision, potentially low degradation due to short exposure time to the energy source, low investment costs and low energy consumption. Different studies are nowadays focused on the development of ultrasonic micromolding and specifically on its application for different types of materials and the comprehension of the influence of processing parameters on the final properties.

The present review is organized in three sections that deals about injection molding assisted by ultrasounds, ultrasonic micromolding and extrusion assisted by ultrasounds. Additionally, other specific sections are focused on specific applications such as decrosslinking, devulcanization, and preparation of blends, composites and nanocomposites.

## **2.2 Injection molding assisted by an ultrasound system**

Ultrasonic injection molding has recently been developed for the manufacture of polymer devices with suitable surface roughness and size, while an easy and cost-effective processing is achieved. In this technique, energy transformation is facilitated by the interfacial friction and viscoelastic heating induced by the application of ultrasonic waves. Several researchers and industrial partners are currently focusing their efforts to develop the molding assisted by ultrasounds for high quality and large-scale production of thermoplastic polymers.

For plastics components with microstructures having a high aspect ratio, it is usual the presence of defects created during molding due to a poor filling quality. Pieces with this high aspect ratio are susceptible to a rapid decrease of the melt temperature. Therefore, high viscosity and low flow velocity are expected and consequently a worsening of the mold filling quality [10-13]. The ultrasonic energy is helpful since it can maintain the melt temperature and enhance the filling process even for microstructures [14,15]. The effect of ultrasounds during the mold filling was supported by numerical analysis [16-21]. Other positive effects of the ultrasonic energy to assist the injection molding process are the improvement of the weld line strength [22,23], the flow of the melt polymer [24], [25] and a reduction of the interface friction during the ejection of the plastic part [26].

**Figure 2.1** shows a representative scheme of the injection molding assisted by an ultrasound, where the ultrasonic system was located within the moving mold part. The ultrasound system includes an external generator that send the voltage signal to the transducer (i.e., the element that transforms the electrical waves in mechanical oscillations) and a horn or sonotrode that transfers the ultrasonic energy to the polymer. Different variations have been proposed, being the most noticeable the location of the horn in the mold.

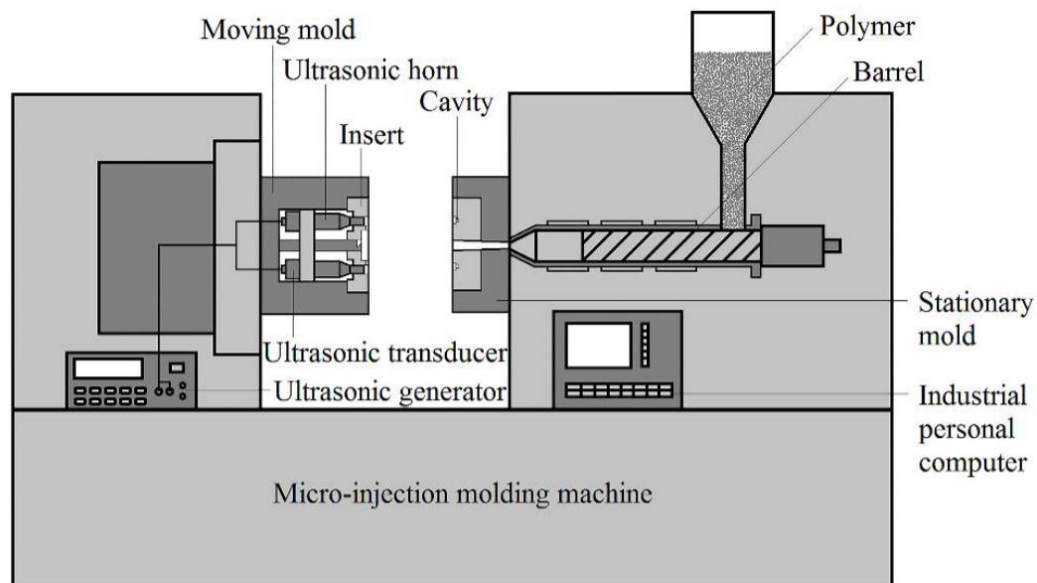


**Figure 2.1.** Schematic diagram of injection molding assisted by an ultrasound system. Reproduced from [19].

Yang *et al.* carried out several studies using ultrasonic-assisted injection molding to provide general information about the advantages of this technique compared to traditional injection molding. Specifically, they used a mold containing an ultrasonic oscillator with a close-type horn to distribute the vibration direction from parallel to vertical in relation to the flow of the selected polymer (i.e., polycarbonate (PC) [3] and composites of polycarbonate with 30 wt.% of glass fibers [10]). Interestingly the flow length and shape were correctly modified using the ultrasonic oscillation after selection of a convenient packing pressure (**Figure 2.2a**). According to the images, the melt absorbed energy and vibrated perpendicular to the direction of flow. This feature allows engineers to design parts without the typical thick frozen layer and diminish residual stress in the final products. It was also demonstrated that the decrease of flow resistance and melt viscosity allowed that the injection pressure was reached at the end of the mold cavity, and the

pressure loss between the near and far ends of the gate was significantly decreased. In fact, pressure loss decreased when the ultrasonic power increased.

The non-uniform temperature distribution in the mold, which is typically achieved during a relatively rapid cooling, caused a non-uniform solidification of the material in the different regions of the mold. In this way, induced stresses and differential shrinkages are highly probable when conventional injection molding is used. These features influenced on the properties of processed specimens (e.g., mechanical and optical). By contrast, the simultaneous application of ultrasonic waves favored a uniform distribution of stress in the mold cavity. The polymer melt is vibrated and compressed at high frequency resulting in a uniform distribution of stress in the cavity as shown in **Figure 2.2b**. The increase on the oscillation time allowed the melt to cool and froze. Therefore, the ultrasonic oscillation was not useful to decrease the pressure loss. The application of ultrasounds prevented a complete fitting of the melt on the mold surface and gave rise to a lower surface quality when the oscillation time was relatively high (e.g., greater than 1.5 s). For the composites with glass fibers, the absorption of ultrasonic energy in the system provided the local heat and then improved the melt flow behavior. This change in the melt flow reduced the capacity of molecular orientation and the shear effect. In addition, for the thick parts, the freezing rate was reduced/modified and therefore it was easier to eliminate glass fiber streaks, floating fibers, and fiber orientation.

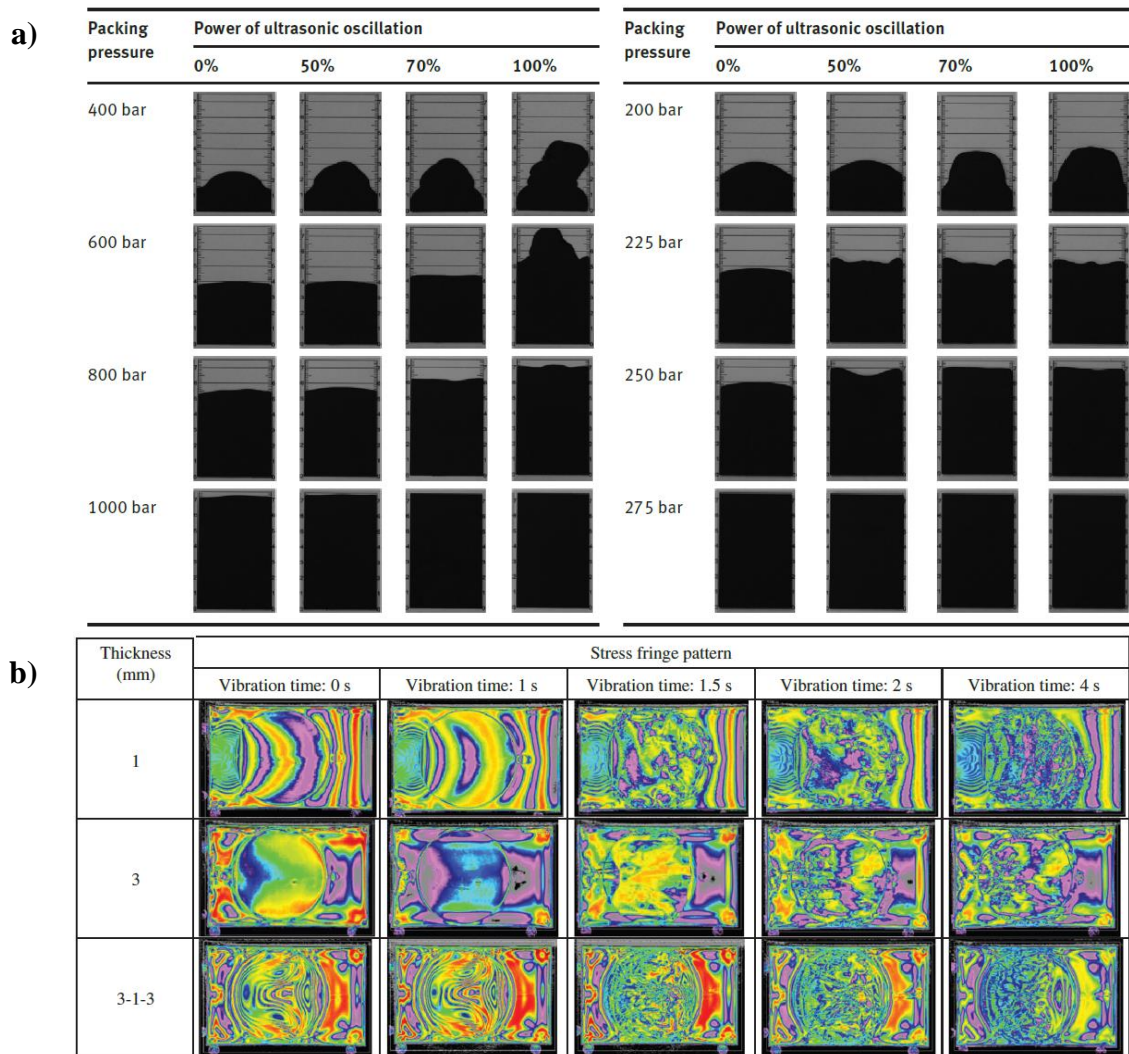


**Figure 2.2.** a) Images of flow length and shape for 1 mm (left) and 3 mm (right) thick specimens that were achieved at 0%, 50%, 70% and 100% of ultrasonic oscillation power and the indicated packing pressures. b) Stress fringe patterns of 1 mm thick specimens achieved for 0% and 100% of ultrasonic oscillation power during 4 s. Adapted from [10].

Injection molding assisted by ultrasounds was also applied to produce poly (methyl methacrylate) (PMMA) thick pieces with favorable flow, less pressure loss (even with a lower mold temperature) and lower residual stress compared to those produced using conventional injection molding [11]. Molecular weight measurements showed a decrease of the average molecular weight,  $M_w$ , which was more pronounced when mold temperature decreased (i.e., from 70 °C to 30 °C). Thus, the generated shear force was higher at the lower mold temperature and resulted in uncoiling and chain scissioning when sensitive polymers like PMMA were employed. Processing parameters such as vibration amplitude, applied power and vibration time were crucial to provide the proper amount of ultrasonic energy to get PMMA specimens of high quality.

The flow behavior during the ultrasonic assisted injection molding of polypropylene (PP) was investigated by Jiang *et al.* [12]. Similarly, to the above studies, the filling front velocity of the PP melt was improved by ultrasonic vibration and the velocity gradient of the melt in the cavity decreased. In other words, the velocity distribution became more uniform thanks to the application of ultrasonic vibration. This improvement was more obvious near both sides of the mold cavity than in its center.

Sato *et al.* [13] designed an ultrasonic injection molding system for fabrication of polycarbonate (PC) optical lenses. They verified that the final product had a smoother surface than that obtained by conventional injection molding. The skin layer was modified as shown in **Figure 2.3a** as consequence of the reduction of deformation resistance. The local heating between the molten and skin layer reduced the deformation resistance and eliminated shrinkage problems. Due to local heat generation, the concave lenses showed much less residual optical strain than lens obtained from conventional injection molding, more specifically the decrease was evident near to the lens center as shown in the polarized images of **Figure 2.3b**.

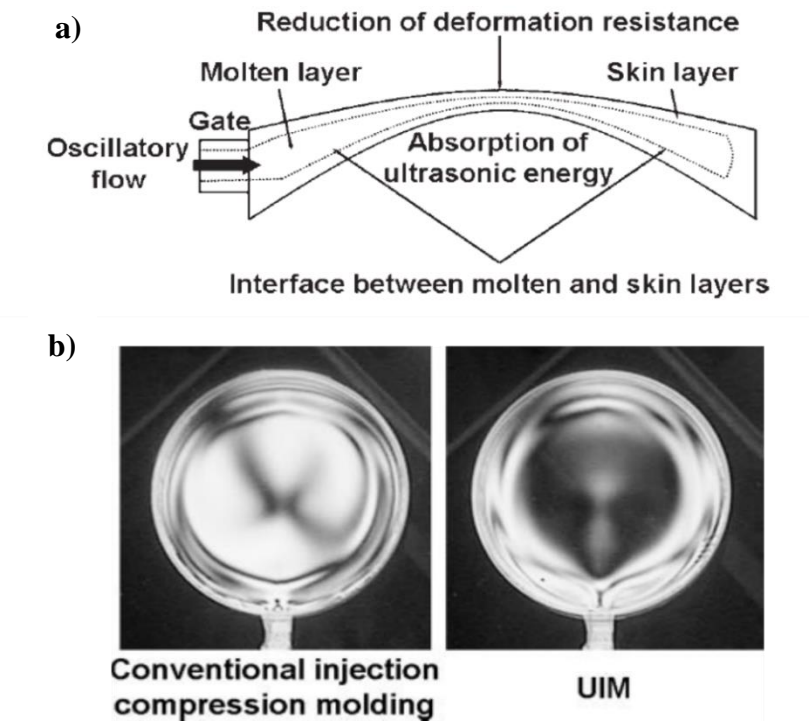


**Figure 2.3.** Scheme showing the mechanism for improvement of surface replication of optical lenses (a) and polarizer images showing the residual strain (b). Reproduced from [13].

Sato *et al.* [27] focused another study on microlenses constituted by PC. The aim of the work was the evaluation of the capacity for the replication of microstructures on their

surface for diffractive applications (**Figure 2.4**). It was demonstrated that the replication accuracy obtained with injection molding assisted with ultrasounds was higher compared to that obtained from conventional processes.

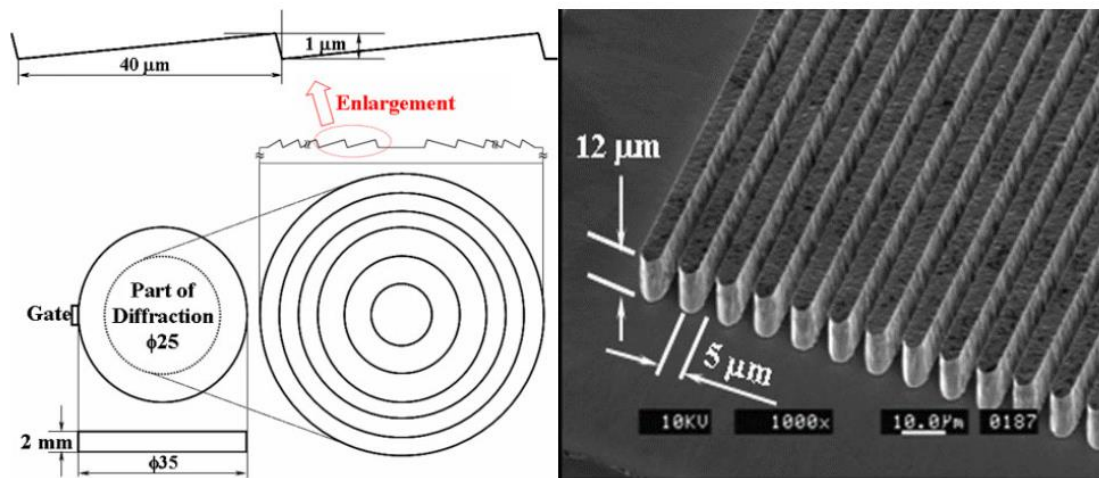


**Figure 2.4.** Schematic illustration of mold surface (left) and SEM micrograph of the surface microstructure of PC microlenses. Reproduced from [27].

Ultra-high molecular weight polyethylene (UHMWPE) is one of the promising polymers in several applications due to outstanding physico-mechanical properties: such as high impact strength, chemical stability, low friction coefficient and good abrasion resistance. Besides the advantages of this polymer compared to other polyolefins, it has drawbacks in tensile modulus, hardness, and easily creeping tendency. Thereby, incorporation of additives (e.g., graphite) would be an appropriate way to improve its performance. However, processing of this polymer and mixing with rigid particles face several challenges because of the high melt viscosity and difficulties in molding. Sánchez-Sánchez *et al.* [14] studied the fabrication of small pieces based on the UHMWPE/graphite system using the ultrasound assisted injection to overcome some of the indicated challenges. Even the most problematic thin samples were prepared with higher mechanical performances than showed by samples coming from conventional injection. Graphite content and mold temperatures had a significant influence on final properties.

Complex injection processes usually generate defects named weld lines. These are the consequence of joining two separated polymer melt streams in multigated molds or a flow of the polymer melt around obstacles (e.g., cores and pins). It is known that final mechanical properties worsened when multiple welds are present in the final piece. The

weakness of the weld lines is derived from three main factors: the poor bonding at the interface, a molecular orientation parallel to the interface and finally the production of V-notches around the weld line surfaces. The presence of these lines was more dramatic during the processing of blends owing to the more complicated morphology in the weld line region. Lu *et al.* [15] studied the influence of melt temperature and ultrasonic oscillation on the weld line strength of polystyrene (PS) and a blend of PS with high density polyethylene (HDPE). It was found that the weld line strength of both systems could be enhanced by increasing the temperature of the melt. However, the application of ultrasonic oscillation improved the weld strength of samples at all temperatures. In addition, different modes were considered for ultrasonic assisted injection molding: a) Application of ultrasonic oscillations into the mold during the whole injection process and b) Application of waves after filling the mold. The latter is more effective to improve the weld line strength of PS and PS/HDPE blends. Liu *et al.* [16] also studied the effect of the melt temperature and oscillation time on the weld line strength of PS molded samples. They verified that the enhancement of the weld line strength was consequence of molecular entanglement across the weld line interface. Basically, an increase of the melt temperature may cause at first an enhanced of the weld line strength, but cautions should be taken into account since then derives in an increased weakness. The use of low melting temperatures and high oscillation times can improve significantly the strength.

## **2.3 Microinjection molding based in ultrasounds**

Several applications of polymeric materials such as microelectronics, micromechanics, microoptics and microbiomedical devices require new techniques for fabrication of small parts. Among the different techniques, ultrasound microinjection molding appears an ideal system in terms of benefits like minimum material lost, minimum processing time, minimum cost, high resolution, high mold filling, good repeatability and even maintenance of properties. The potential of ultrasonic micromolding is enormous and continues to grow through the positive results reported in several research works as those described in the present review.

Comparison of mechanical properties of manufactured samples by conventional and ultrasonic micromolding indicated not a clear privilege of this technique, however it seems that in some cases polymer degradation could be decreased as consequence of the lower residence time [23]. Thus, Gaxiola-Cockburn *et al.* [24] verified the improvement of physical and mechanical properties of recycled PP specimens when they were prepared by ultrasound micromolding. Several studies have been focused on the processing of polylactide (PLA) due to its great potential for biomedical applications. **Figure 2.5** shows a scheme of the simple equipment employed for the fabrication of PLA micropieces (basic components are the controller, the piezoelectric transducer, the pneumatic pressure system, the thermally controlled mold and the acoustic unit composed of booster and sonotrode), the main processing steps and some details of representative processed specimens [25]. It should be pointed out the ability of this fabrication process to get a high resolution (e.g., note the capacity to reproduce the strings at the front of the guitar), which is hardly possible in conventional injection molding. However, micrographs show also in some cases the presence of inhomogeneities and non-uniform opacity in the final samples. **Figure 2.6** summarizes the effects caused by the applied pressure and amplitude on degradation and quality of final products, and the filling of the mold.

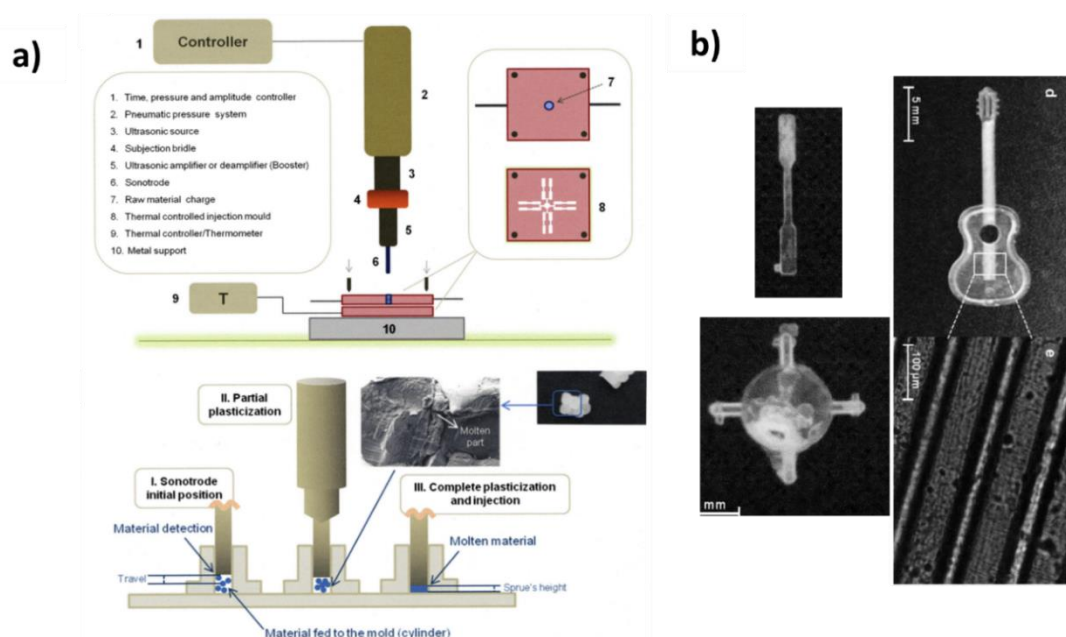


**Figure 2.5.** a) Scheme showing the main components of a basic micromolding equipment. Different distinctive steps of the ultrasound micromolding process (inset show details of the interphase between partially molten PLA pellets). b) Examples of PLA specimens obtained under processing conditions of 10 pellets (loaded material), 10 s (processing time), 28.4  $\mu\text{m}$  (amplitude), 3 bars (pressure). Reproduced from [25].



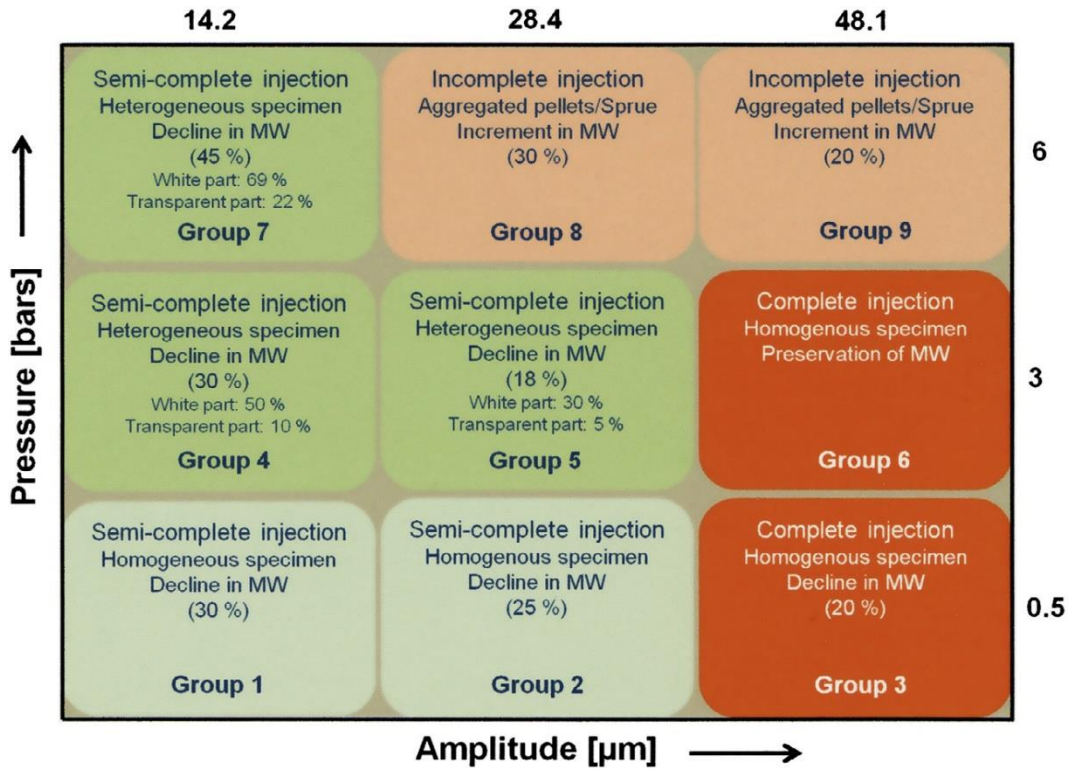


**Figure 2.6.** Scheme summarizing the influence of amplitude and pressure on PLA processed specimens obtained using a 3 s molding cycle. Mw refers to the molecular weight. Reproduced from [25].

Besides the experimental analysis to find the optimized parameters in ultrasonic micromolding, several modeling and numerical methods were developed to evaluate the energy flow involved in the process [17,18].

Dissipated energy (oscillation and sonotrode movements) together with the energy required to melt the material were considered in the corresponding energy balance. The fundamentals of acoustic/ultrasound energy [28] were applied for the modeling of dissipated energy per cycle. In fact, the energy applied by the sonotrode is responsible of an increase of the temperature that melts the material and makes feasible that this material fills the corresponding mold cavity. It was proposed the equation 4 to evaluate the dissipated heat flux ( $\dot{q}_{avg}$ ) during the injection process:

$$\dot{q}_{avg} = \frac{P}{A} = 4 \cdot p \cdot a \cdot \omega \quad (4)$$

where  $P$  is the generated power given by the product of the applied sonotrode force,  $F$ , and the acoustic vibration velocity,  $v_{avr}$  (i.e.,  $P = F \cdot v_{avr}$ ) [29],  $A$  is the sonotrode area,  $a$  is

the oscillatory amplitude of the sonotrode tip,  $\omega$  is the angular frequency of the ultrasonic vibration, and  $p$  is the applied pressure.

On the other hand, the basic thermodynamic equation 5 can be applied to determine the energy required ( $Q_m$ ) to melt the material:

$$Q_m = m \cdot C_p \cdot \Delta T + m \cdot \Delta H_m \quad (5)$$

where  $C_p$  is a heat constant,  $\Delta T$  is the temperature increase need to reach the temperature of fusion,  $\Delta H_m$  is the melting enthalpy, and  $m$  is the amount of material that is melted in each cycle.

The indicated modeling approach was useful to assess the energy flow involved in the ultrasound micromolding process [18], being derived an interesting comparison between generator, dissipated and required average power. Specifically, the processing of polyamide 12 pellets (Rilsamid™ PA 12 G AMNO TLD) was evaluated using an adapted ultrasonic welding pneumatic press dotted with a 1500 W power generator and an acoustic unit able to provide 35  $\mu\text{m}$  of vibration amplitude at a frequency of 30,000 Hz at the tip of the sonotrode. **Figure 2.7a** displays the energy supplied after each cycle by the generator to process 300 mg of polyamide with different processing parameters. The supplied energy was significantly reduced by increasing both the applied pressure and the ultrasonic time. It is clear that more energy is required to perform the melting cycle when the pressure is low. In addition, the increase of the length of vibration time results in a higher amount of supplied energy, a longer time of the polymer in its melt state and a good filling of the mold cavity.

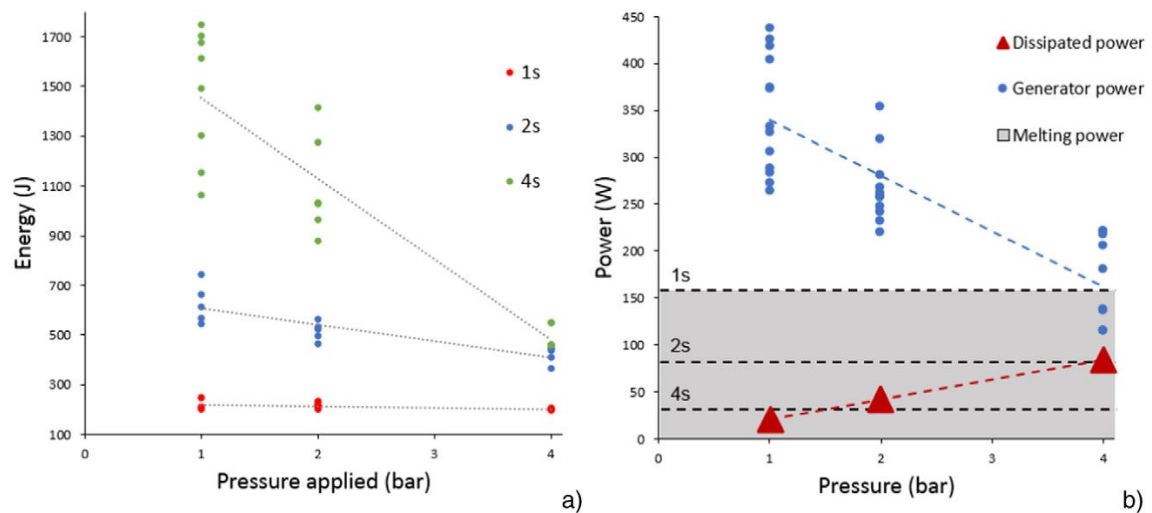


**Figure 2.7.** a) Supplied ultrasonic generator energy in function of the applied pressure and the oscillation time. b) Comparison between supplied generator, dissipated and melting powers in function of the applied pressure and the oscillation time. Reproduced from [18].

**Figure 2.7b** shows that in the region of lower energy dissipated by the sonotrode (as given by equation 5), more energy from the generator is required to complete the process. A higher pressure would be more efficient to increase the process efficiency (i.e., it can increase from 10% to 50 %). In addition, the power supplied by the sonotrode is less than that required for melting the polymer when the oscillation time is 1 s. Therefore, complete specimens (i.e., without defects) can be obtained with reduced average supplied power, if a high cycle time is selected. Experimental results were in good agreement with the hypothesis derived from the theoretical evaluation.

It is known that about 20% of the total energy required in a conventional injection molding process is involved in the heating of the polymer in the plasticizing unit [19] and consequently the optimization of this step appears fundamental. The type and quantity of material, the processing time, and the type of generator (i.e., electric, hydraulic or hybrid) determine the energy efficiency of the injection processes. Ultrasonic injection molding can decrease the energy consumption with reducing the scrap to less than 10 %. Comprehension of the heat generation in the plasticizing camera is fundamental for saving energy and even to improve the quality of processed specimens. **Figure 2.8** shows a scheme of the ultrasonic plasticization process based on the friction heating model. Temperature is raised under the action of the ultrasonic vibration as consequence of the friction produced by polymer particles in their contact interface.

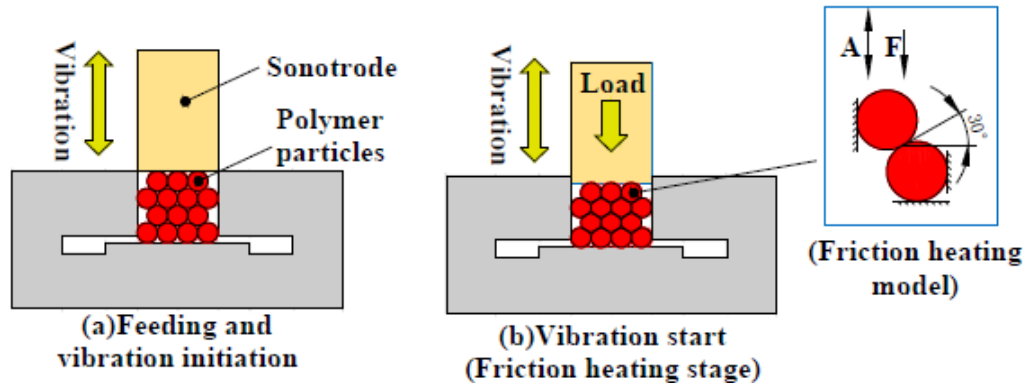


**Figure 2.8.** Scheme showing the ultrasonic plasticization of polymer pellets in the feeding camera. Reproduced from [20].

A finite element method (FEM) for simulation of the heat produced by interfacial friction was considered and the results were compared with the experimental data attained with amorphous polymethyl methacrylate (**Figure 2.9**). The geometry consisted of two rods with a diameter of 10 mm and a contact surface inclination of 30°. The transient heat conduction process was modeled by means of equation 6 [30]:

$$\rho \cdot c \cdot \frac{\partial T}{\partial t}(x, y, z, t) = k^2 \cdot \nabla T(x, y, z, t) + Q(x, y, z, t) \quad (6)$$

where  $Q$  is the internal heat generation rate;  $x, y, z$  and  $t$  indicate point coordinates and time,  $T$  the temperature;  $\nabla$  is the spatial gradient operator;  $\rho, c$  and  $q$  are the density of the materials, specific heat capacity and the heat flux vector, respectively.

Results plotted in **Figures 2.9c** and **9d** clearly show the effect of ultrasonic amplitude and frequency to reach the melting state of PMMA. At high amplitude, temperature increases rapidly and reaches the melting point at a shorter vibration time. A similar trend was also observed when the frequency was increased. The finite element analysis also verified that the roughness of the contact surface significantly influenced the heat generated by friction as well as the compaction state of the friction surface and the moisture content.

Lee and Kim [21] performed an interesting flow analysis for ultrasonic processing and evaluated the effect of different parameters on the filling of the mold cavity. The ultrasonic vibration can facilitate the cooling of polymer melt since the filling process can be completed in a short period of time.

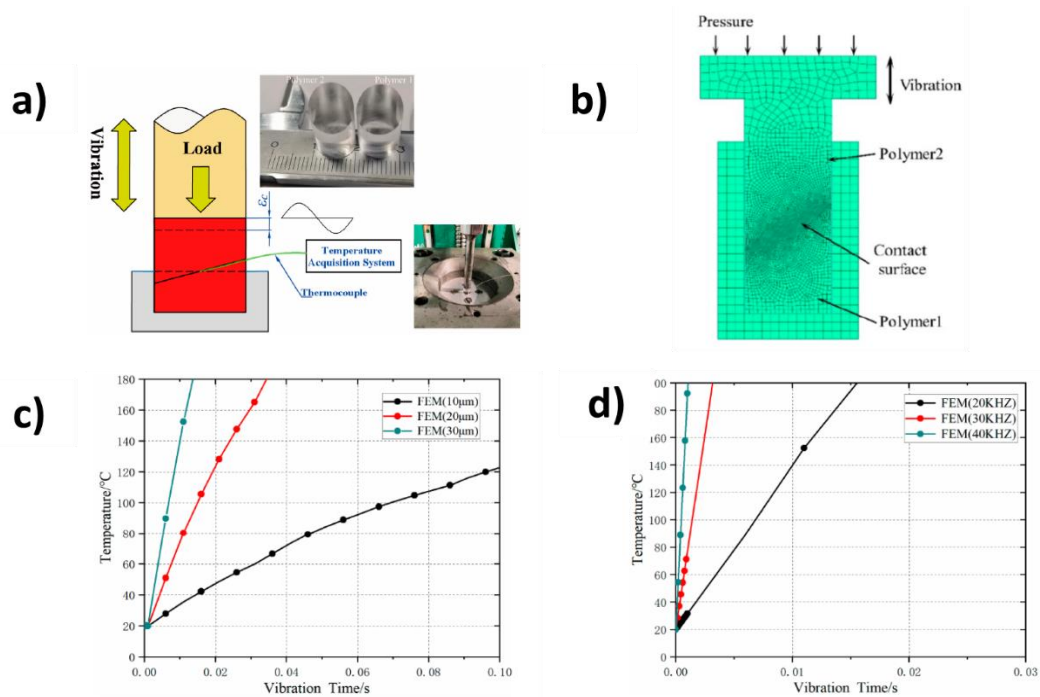


**Figure 2.9.** a) Scheme of the physical model applied to evaluate the heating effect of friction between polymeric interfaces. b) Finite element model to evaluate local heating at the polymer contact interphase. c) Plot of the temperature dependence with ultrasonic amplitude (frequency 20 kHz and force 300 N). d) Plot of the temperature dependence with ultrasonic frequency (amplitude 30  $\mu\text{m}$  and force 300 N). Adapted from [20].

Different numerical techniques, including computational fluid dynamics, fluid-structure interaction and coupled Lagrangian-Eulerian methods were also considered to evaluate the effect of ultrasonic vibration on the polymer flow. Temperature of the die and the applied pressure were specifically optimized for the injection molding of PP and low density polyethylene (LDPE), being viscosity predicted using the Cross-Williams-Landel-Ferry model [2], [22].

Ultrasonic micromolding has also been found effective to render a good dispersion of nanoparticles when added to different biodegradable polymers [26]. Different nanoclays (e.g., N757, C20A, C25A, and N848) were assayed to prepare nanocomposites up to a 6 wt.% content using PLA and a poly (alkylene dicarboxylate) as polymeric matrices. TEM micrographs showed a homogeneous dispersion of exfoliated layers and XRD data showed the disappearance of reflections associated to the corresponding interlayer clay spacing. It is meaningful that the exfoliated structure was even observed when the neat N757 clay was incorporated, a feature that highlighted the advantages provided by ultrasounds since no organic compatibilizer was necessary.

Incorporation of clays into PLA and polybutylene succinate (PBS) matrices was also compared [31]. The presence of clays enhanced PBS degradation under the ultrasound power, but as previously indicated had no effect on PLA. PBS degradation was more dramatic when organomodified clays were added, being therefore relevant the capacity of achieving exfoliated structures when the pristine clays were employed. It was also shown that the clay particles were oriented parallel to the flow direction and had different effects on crystallization kinetics (nucleation and crystal growth rate) and the crystal structure of the two studied polymers.

Improvement of the dispersion degree for micro- and nanosized silica particles were also investigated for the ultrasonic microinjection molding of poly (nonamethylene azelate) as example of a biodegradable polymer [32]. It was shown that there was no degradation of polymer during the processing with ultrasonic vibration using different functionalized silica particles. Molecular weight remains constant whereas the crystallization kinetics and spherulite growth varied with addition of the different particles [32]. It was also shown that this technique provided a suitable process for dispersion of carbon nanotubes (CNTs) in a polycaprolactone (PCL) matrix and rendered products without any defect due to enhanced capacity to fill the mold [33]. Nanocomposites with high CNT loading (i.e., 5 wt.%) showed a good dispersion after ultrasonic micromolding. which facilitates PLA crystallization.

Recently, medicated PLA micropieces were fabricated by incorporation of triclosan (TCS) and chlorhexidine (CHX) as drugs with antibacterial activities [34]. Contrary to conventional injection molding, ultrasonic injection molding brought no significant degradation during melt processing, especially in the case of TCS. Drug release was also found to be slow in the final products and depended on hydrophilic character of the molded samples. Evaluation of mechanical and physical properties indicated that this technique was a suitable new processing technology for producing medicated micropieces from biodegradable and biocompatible polymers such as PLA loaded with pharmacological drugs. It has also demonstrated the capacity to prepare PLA/hydroxyapatite hybrid scaffolds that increased biocompatibility [34 and even the capacity to get scaffolds with a controlled porosity has been evaluated [35].

One example of a microspecimen especially useful is medicine, biology and micro-electromechanical systems are the polymeric microneedle arrays. These show excellent material properties, chemical stability, and good biological compatibility. Like for other

microparts, ultrasonic injection molding can provide a good opportunity to fabricate these accurate devices with low manufacturing cost, short production cycle, mass-production, good repeatability and following a simple process. The improvement of the mold filling quality and the enhancement of material properties by using the ultrasonic vibration was investigated by Gao *et al.* for microneedle array specimens [36]. These authors generated a specimen model (**Figure 2.10a**) to investigate the effect of ultrasonic vibration on the melt flow field inside the microneedle cavity and the mold filling quality. The filling process and volume fraction of the melt in the microneedle array is shown in **Figure 2.10b**. This reveals that the starting time for filling the microneedle regions are the same without and with ultrasonic vibration, but the time required to fill the microneedle regions was reduced by 27.78% (from 0.18 s to 0.13 s) and the time required to fill the whole cavity was reduced by 31.25% (from 0.32 s to 0.22 s). This faster filling process may reduce the heat dissipation of the melt, allowing to achieve a higher melt filling capability and produce less molding defects. The melt viscosity and the melting temperature played the main roles during processing and filling the mold cavities. Comparison of melt viscosity distribution with and without ultrasonic vibration (**Figure 2.10c**) revealed that viscosity decreased significantly using the ultrasonic energy, specially at the position further away from the corner (i.e., from 0.1 to 0.2 mm). The melt viscosity in the corner region had no obvious changes. The high viscosity gradient showed in these graphs demonstrated that the melt could fill the cavity easier in the corner region and that the final products could have much fewer molding defects and higher molding quality.

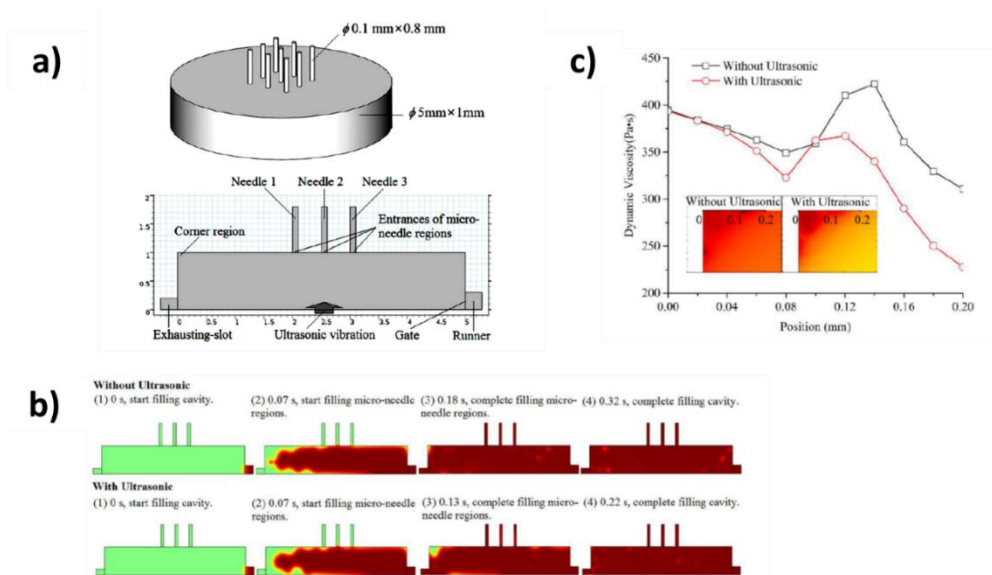


**Figure 2.10.** a) Model of the microneedle array specimen. b) The filling process and volume fraction of melt in the microneedle array cavity with and without the effect of ultrasonic vibration. c) Melt viscosity distribution in the corner region with and without the effect of ultrasonic vibration. Adapted from [36].

Chemical degradation of polymers is mainly a consequence of cavitation (i.e., nucleation, grown and collapse of microbubbles), which induces a high shear force on polymer chains that ultimately led to a chain scission. This problem was enhanced for high molecular weight polymers since chain scission progresses up to reach a limit in molecular weight. This limit depends also on experimental conditions like the intensity and frequency of applied ultrasounds. Samples with a molecular weight lower than its limiting value remain unaffected by the applied ultrasounds [37-39]. Basically, molecular chains have in this case enough mobility and a relatively low tensile strength that can be quickly recovered [40]. The study of the capacity of ultrasounds to process UHMWPE has been performed [14] and a factorial design has been applied to determine the effect of the most relevant process parameters on the filling quality and the polymer degradation. The effect caused by the different geometry of the raw polymer (i.e., commercial powder, and circular and irregular pieces cut off from melt pressed films) was also evaluated. The factorial design indicated that the best processing conditions corresponded to an amplitude of  $56.2\ \mu\text{m}$ , a mold temperature of  $100\ ^\circ\text{C}$  and the use of irregular shaped pieces as raw material. Molecular degradation was evidenced, being increased with the ultrasound amplitude. Furthermore, degradation was enhanced in the distal part (i.e., the furthest one from the feeding point to the mold) since the polymer received high ultrasonic energy for a larger exposure time (**Figure 2.11**). Degraded samples revealed an oxidation process that led



to the appearance of carbonyl bands in the FTIR spectra and an increase of terminal vinyl groups (FTIR signal at  $910\text{ cm}^{-1}$ ). The degree of crystallinity increased when degradation was higher, a feature that led to the improvement of some mechanical properties (e.g., the Young modulus increased from 241 to 395 MPa), but was problematic for the elongation at break since it was reduced from 3.6% to 0.2%.

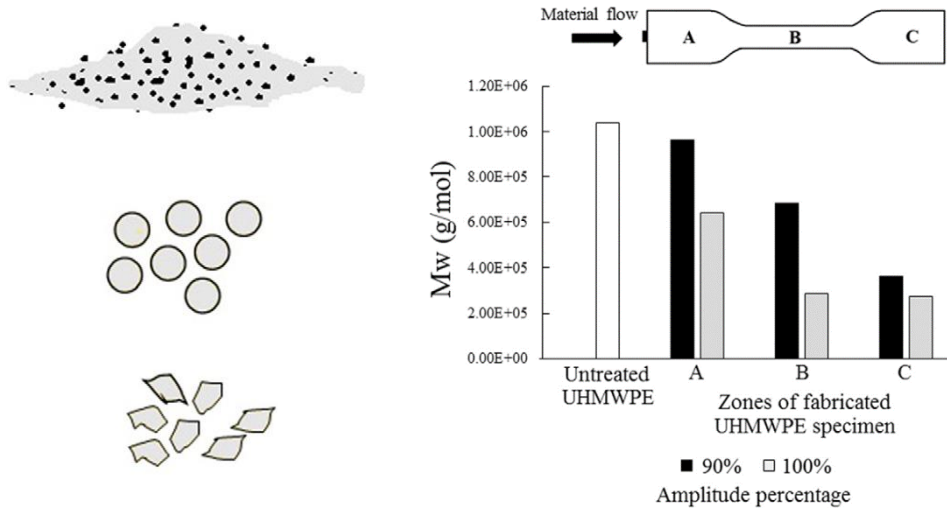


**Figure 2.11.** a) Initial shapes of UHMWPE specimens: Untreated polymer powder, circular and irregular pieces cut off from melt pressed films. b) Molecular weight of three differentiated zones of specimens fabricated by applying 90% and 100% of the ultrasonic amplitude (i.e.,  $50.6\ \mu\text{m}$  and  $56.2\ \mu\text{m}$ ). Adapted from [14].

Marson *et al.* [41] found that the inaccuracies of micromolded products were in part caused by the ejection friction. It is well reported the breakage inside the mold of microinjected parts upon ejection [42]. Unfortunately, demolding is still performed using conventional ejection pins which offer poor mechanical stability [43]. The polymer melt is capable to replicate the mold topography in such a way that a “mechanical interlocking” is derived in the interphase [44]. A proper separation of the molded specimen from the tool requires a good deformation capacity for the polymer. Demolding force can be decreased by the reduction of the surface roughness [45] but new alternatives are continuously being proposed. Thus, the dissimilar propagation and dissipation of electronic waves through the polymer part and the mold steel appear as an interesting concept [46]. Specifically, the ejection force can be decreased as consequence of the different oscillation of the interphase materials that led to a reduction of adherence and friction. Masato *et al.* [46] designed a new ultrasonic assisted demolding system to study the effect of mold roughness for different polymers (polystyrene (PS), cyclic olefin

copolymer (COC) and polyoxymethylene (POM)). A linear correlation was found between the demolding force peak and the surface roughness. Furthermore, the experimental results showed that the ultrasound vibration had a positive effect on the friction force values acquired during ejection, with a maximum reduction of 16% for PS.

## **2.4 Extrusion assisted by an ultrasound system**

Extrusion allows melting a polymer with a high-energy input during a relatively short time. Due to the supply of heat and the energy input caused by friction between the screws and the polymer, the molten material becomes formable and can be pressed through the nozzle to be converted in a continuous polymer product. The extrusion technology has been developed for the last decades, and still now there are research on the design of each component of the extrusion equipment such the screw, the barrel, or the die. The main objective is to optimize the productivity and/or to improve the material properties. Related to this point, the application of ultrasonic energy during the extrusion process has demonstrated to be highly effective.

A general description of the current state of the extrusion process assisted by ultrasounds encompasses research work on compound extrusion, on the mixing between polymers and/or fillers and on the relevant physicochemical changes that occurred as consequence of the ultrasound energy.

### **2.4.1 Approach to the ultrasound system**

The study of new compounds prepared by extrusion mainly consists of the evaluation of the effect caused by the addition of fillers or additives to a polymeric matrix in order to improve its specific properties. The equipment for the extrusion is in continuous evolution to enhance the productivity, the dispersion of additive/fillers, the compatibility between components, the energetic efficiency, etc. The extrusion for compounding assisted by an ultrasound system was designed at first time to improve the dispersion of nanofillers, but different approaches were developed during the last years to reach a chemical or physical effect on the polymer, to improve the compatibility between two or more polymers (blending) or by contrast, to decrosslink a polymer network. The ultrasonic energy has a different effect dependently on the polymer, amplitude or energy of the ultrasound wave, the orientation of the ultrasonic waves or the situation of the ultrasound system in the extruder.

Different equipment has been proposed to assist the extrusion process with ultrasound waves. Some possibilities are shown in **Figures 2.12-15** and can be summarized as follows:

- a) The ultrasonic wave direction that affects the molten polymer can be varied. For example, the ultrasound system can be coupled to the die of the extruder according to vertical or horizontal axes (**Figure 2.12**). The main difference between both approaches is focused on the surface with ultrasonic energy that is in direct contact with the material. On one side, if the sonotrode is placed in vertical axis, the material pushed by the screw extruder will not make pressure to the mentioned surface of the sonotrode. On the other side, if the sonotrode is placed in the horizontal axis, the material will be pushed to be direct contacted with the vibrating surface of the sonotrode, reducing the contact time between the material and the sonotrode, but with more pressure at the contact surface.

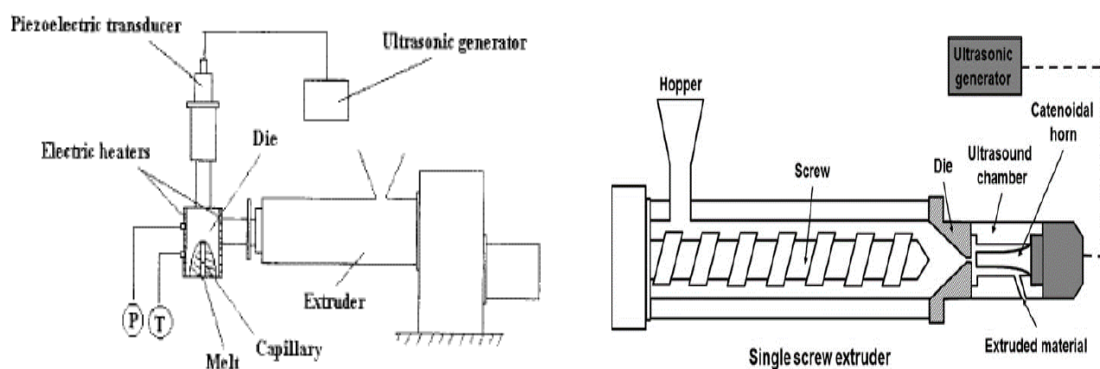


**Figure 2.12.** Schematic diagrams of extrusion equipment assisted with ultrasound with vertical (left) and horizontal axis (right) dispositions. Adapted from [47] and [48].

- b) The ultrasound system has a high flexibility that allows changing easily parameters such amplitude, frequency, or even the number of sonotrodes that are coupled to the extruder (**Figure 2.13**). During the process, the contact of the material with the ultrasonic energy has a low time. Increase the number of sonotrodes is an approach

to ensure the application of ultrasounds to all processed material, and allow to decrease the power supplied by each sonotrode.

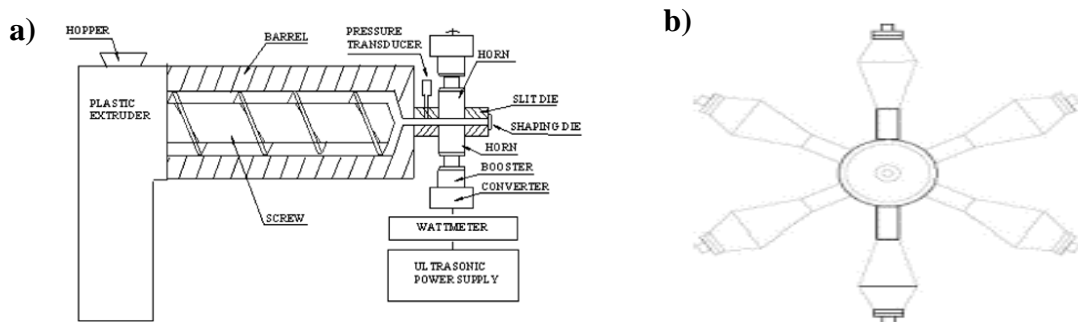


**Figure 2.13.** Ultrasound systems dotted with more than one sonotrode (e.g., two (a) or up to six (b)). Adapted from [49] and [50].

c) Coupling element requires an accurate design of the ultrasound system. For example, the die extrusion element can be modified to optimize the specific site at which the ultrasonic energy is applied to the molten polymer.

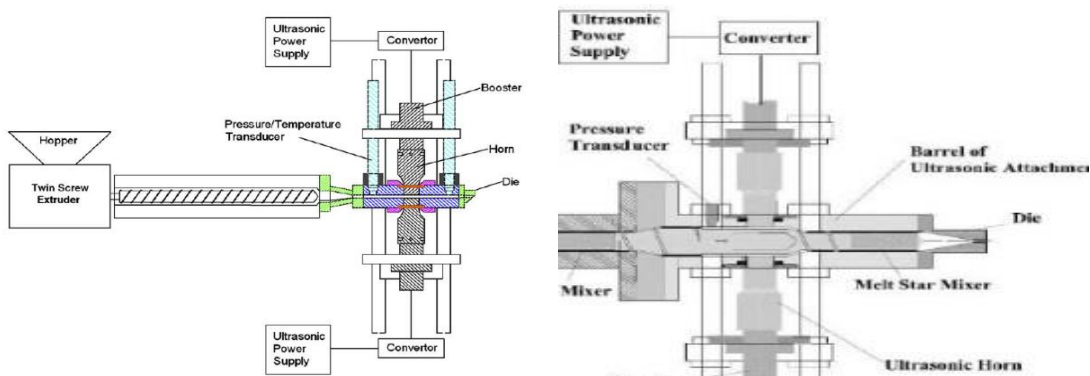


**Figure 2.14.** Die modification: new chamber placed in the die (left) or in a previous step (right). Adapted from [51] and [52].

d) Application of ultrasounds in an early step of the extrusion process. For example, in intermediate positions of the barrel where the polymer is still in the molten state. The approach allows study the effect of ultrasounds during the molten and extrusion steps at less pressure compared to the die extrusion. A new design of screws could be needed [53,54].

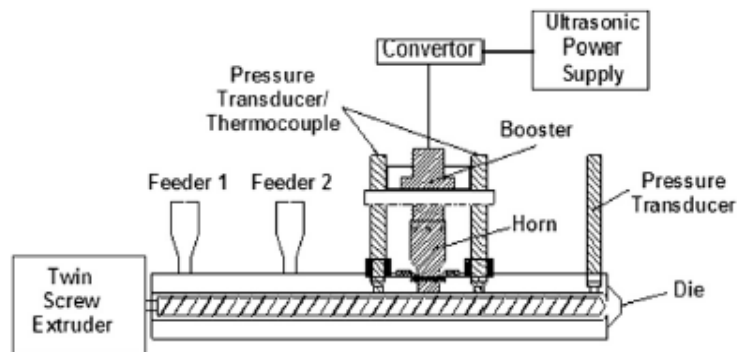


**Figure 2.15.** Ultrasound system placed along the extruder barrel. Reproduced from [54].

### 2.4.2 Effect of the ultrasonic energy during the extrusion process

The rheological behavior of a specific polymer in a single screw extruder and irradiated with ultrasonic waves has been studied. Works show how the die pressure and the viscosity of the processed polymer decrease with the ultrasonic energy, while the mass production could be increased. Basic principles about the effect of ultrasonic treatment on polymer melts were established by Bernhardt in 1954 [55]. Bernhardt has evaluated different polymer melts (e.g., PS, PE and PVC (polyvinyl chloride) with 50% of dioctyl phthalate) under static conditions. The results demonstrated that all these materials showed a reduction of viscosity. It was concluded that the ultrasonic energy could be used during a continuous process to enhance the homogenization and dispersion of colorants and fillers in plastic melts [55].

Several years later, Isayev *et al.* progressed in the study of the continuous extrusion process assessed by ultrasounds. In particular, it was demonstrated that ultrasounds could improve the processability of PP, PS, LDPE and a PP/CaCO<sub>3</sub> composite without deterioration of the mechanical properties (e.g., tensile properties and impact strength) [56]. It was fundamental the reduction of the die pressure and die swell. Chen *et al.* showed a similar effect with PS, focusing the study on the improved rheological behavior with an ultrasonic treatment. An increase of productivity of PS with the ultrasound system was accompanied again with a decrease of die pressure at different temperatures (**Figure 2. 16**), melt viscosity and flow activation energy [57].

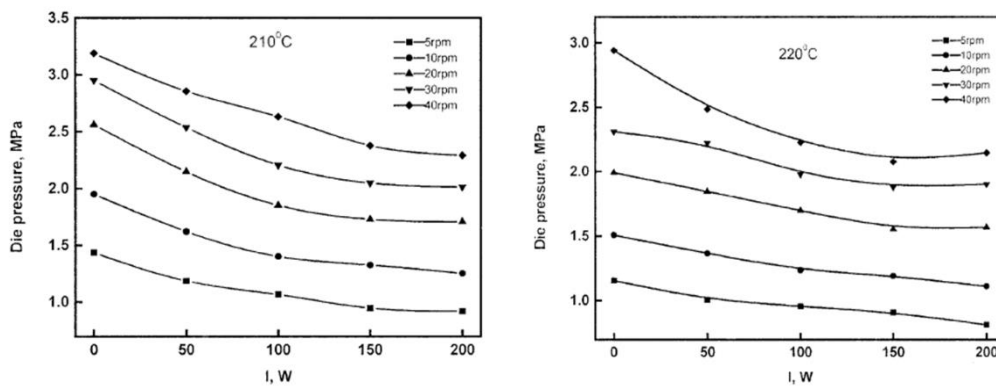


**Figure 2.16.** Evolution of die pressure with the ultrasound intensity for extrusion of PS at different screw velocities and temperatures of 210 °C (left) and 220 °C (right). Reproduced from [57].

The effect of the ultrasonic energy during the extrusion process of PS has been evaluated from a rheological and molecular mechanism point of view [58]. It was argued that the molten polymer absorbed the ultrasonic energy, being increased the activity and freedom mobility of molecular chains or segments. At the same time, the ultrasonic energy had a chemical effect on the polymer, changing the original molecular structure (i.e., decreasing the molecular weight). In the nozzle, elastic tensile strains were reduced due to the disturbed flow of polymer in the entry zone that was able to change the stream patterns [58]. Other studies were done with PP, being confirmed the reduction of the die pressure and the polymer viscosity in the ultrasound assisted single screw extrusion. It has also been indicated that the extrudate swell (*Barus* effect) was reduced, and interestingly the crystalline structure of the polymer changed since the content of the beta crystalline form was increased (i.e., the alpha form was converted to the beta form) [59]. J. Chen *et al.* discussed about the relevance of the physical or chemical effects when ultrasonic energy was applied during the extrusion of PP. It was concluded that the physical effect played a more important role. Thus, ultrasounds increased the motion of molecular chains or segments while molecular entanglements and interactions were decreased. Molecular configuration changed also to a less ordered disposition. Furthermore, the reduction of the non-Newtonian flow characteristics of the melt was responsible of a high viscosity drop. Nevertheless, chemical effects have mainly be associated to irreversible and permanent changes of the molecular weight and its distribution [60].

Wu *et al.* have studied the ultrasound assisted extrusion processing of metallocene-catalyzed linear-low density polyethylene (mLLDPE), with special remark on the material of the nozzle since a synergic with ultrasounds can be derived. Thus, an increased

productivity and a reduction of dye pressure and melt viscosity could be attained when the nozzle was made of PTFE (Polytetrafluoroethylene) [61]. Basically, PTFE had higher sensitivity to ultrasounds than a typical steel material. An enhancement on the orientation of the entangled segments, which reduced viscosity and flow activation energy was demonstrated. Ultrasonic energy has also provided positive effects on the processing of thermoplastic blends and specifically a better homogeneous dispersion has been found for mixtures of a polyolefin elastomer (POE) and mLLDPE [62]. Guo et al. studied the surface morphology of LLDPE extrudate when the ultrasonic energy was applied. **Figure 2.17** shows the phenomenon of shark-skin for the material under conventional conditions (a and b). This phenomenon disappears when the ultrasonic energy was applied during the extrusion for the same material (c and d) [63].

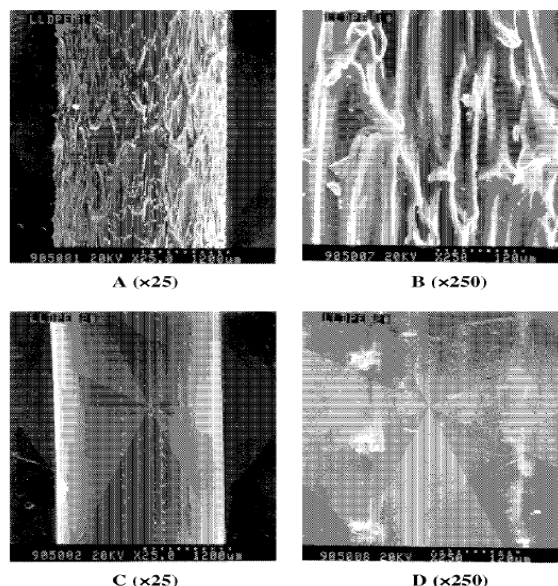


**Figure 2.17.** Surface morphology images taken at different magnification of m LLDPE extrudates obtained without (a, b) and with (c, d) ultrasonic treatment. Reproduced from [53].

The effect of ultrasonic irradiation on mLLDPE/LDPE blends have also been evaluated [64]. A reduction of pressure and apparent viscosity (**Figure 2.18**) of the material has been revealed as well as an increase of productivity under the presence of ultrasonic oscillation. The positive effect has been clearly observed for the neat LLDPE sample and blends with high content of LDPE. For samples with a 10 wt.% of LDP the results were less clear since the addition of a small amount of LDPE may enhance the molecular entanglement between LDPE and mLLDPE.

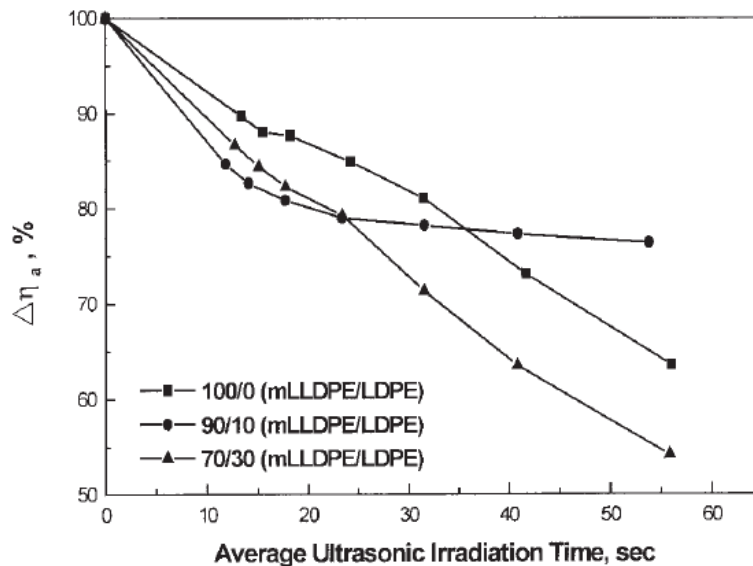


**Figure 2.18.** Dependence of the apparent viscosity drop for different LLDPE/LDPE mixtures with ultrasonic irradiation time. Reproduced from [64].

Guo *et al.* insisted on the ultrasound assisted processing of LLDPE and observed an inhibition or even disappearance of the melt fracture/surface distortion in the extrudate [47]. The extrusion of HDPE was carefully studied by Muniesa *et al.* [65], being observed an increase of the flow rate by 10% and a reduction of the die pressure by 16% that caused a reduction in the apparent viscosity and a higher productivity or extrudate output. The apparent viscosity was reduced due to thixotropic effects of temporal molecular movements. The pressure loss was explained by the reduction of elongational flow due to the HDPE vibrations when ultrasounds were applied. Possibilities of the use of ultrasound assisted systems to improve miscibility and the dispersion of micro/nano reinforcements were also discussed [65].

The ultrasonic energy applied during the extrusion process was demonstrated to be an useful method to increase the crystallinity of a slow crystallizable polymer as Rieckert and Isayev demonstrated [66]. In their patent, it was shown how the application of ultrasound by two horns located in the extrusion barrel (**Figure 2.19**) increased for example the crystallinity of bottle grade polyethylene terephthalate (PET) in such a way that characteristic cold crystallization was not detected in a subsequent heating.



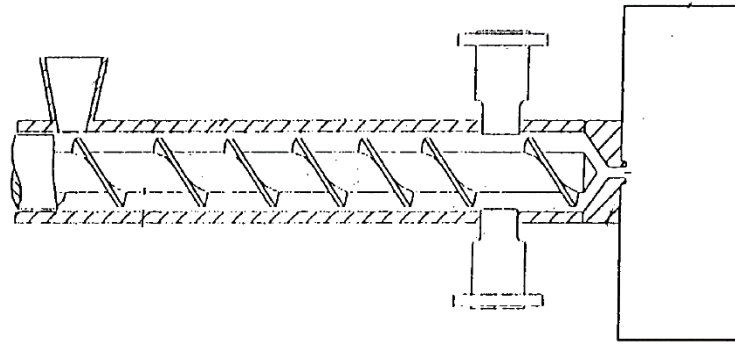


**Figure 2.19.** Schematic invention based on the incorporation of two horns in the extrusion barrel. Adapted from [66].

On the other hand, Isayev *et al.* have studied the effect of ultrasonic waves in the foam sector. The work showed a decrease of pressure on the nozzle when the amplitude of ultrasound increased, resulting in a reduced cell size and more uniform cells, and at the same time, an improvement of mechanical properties such the Young modulus and tensile strength [67].

Niknezhad *et al.* have studied the use of an ultrasonic system to obtain in a single step casting films from both LLDPE and its nanocomposite with the organomodified Cloisite 20A clay (**Figure 2.20**) [68]. An increase in the complex viscosity and the storage modulus was observed as well as a reduction in the tangent loss of the nanocomposite. Basically, the rheological data suggested an improvement of compatibility between the clay and the polymer matrix when ultrasounds were applied. The work clearly revealed the benefits of the use of ultrasound to disperse the nanoclay, to improve the mechanical properties of the nanocomposite (in both machine and transversal directions) and to render a material with lower oxygen permeability. Nevertheless, NMR studies demonstrated an increase in branching of LLDPE when ultrasounds were applied.

Quiñones *et al.* have studied the preparation of transparent films based on the nanocomposite of PP with carbon nanotubes (PP/CNT). The extrusion assisted by ultrasounds improved the dispersion of the CNT nanofiller, enhancing brightness, and both electrical and thermal conductivities. An increase of complex viscosity, Young and storage modulus was also revealed [69].

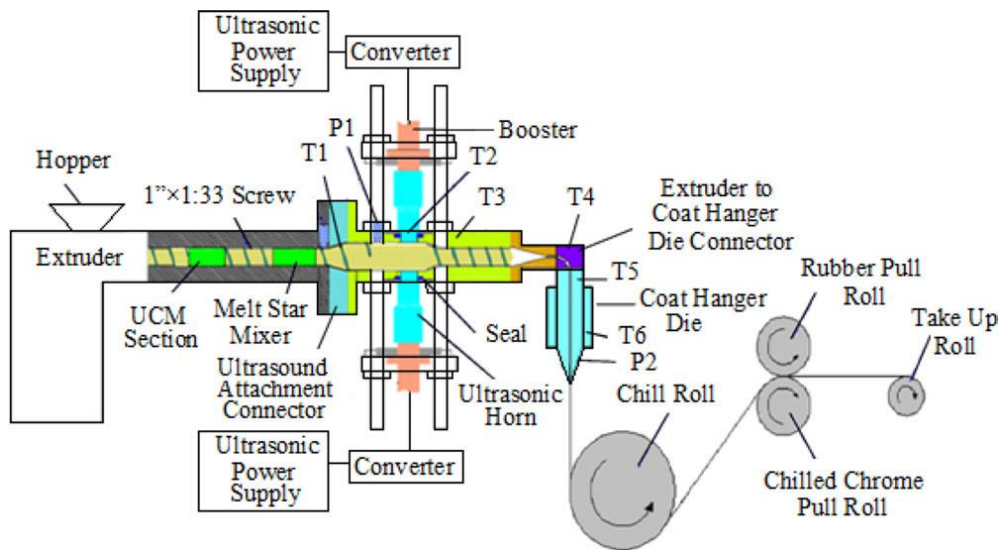


**Figure 2.20.** Schematic drawing showing an online casting film equipment assisted by ultrasonics. Reproduced from [68].

Recently, Yang *et al.* have applied the ultrasonic energy to prepare a crosslinked PP. The ultrasound energy could induce a chain scission and a recombination reaction of molten PP flowing through the exit die assembled with the ultrasonic system (**Figure 2.21**). The additional energy given by the ultrasonic waves could cause the formation of a new crosslinked system with higher molecular weight [5].

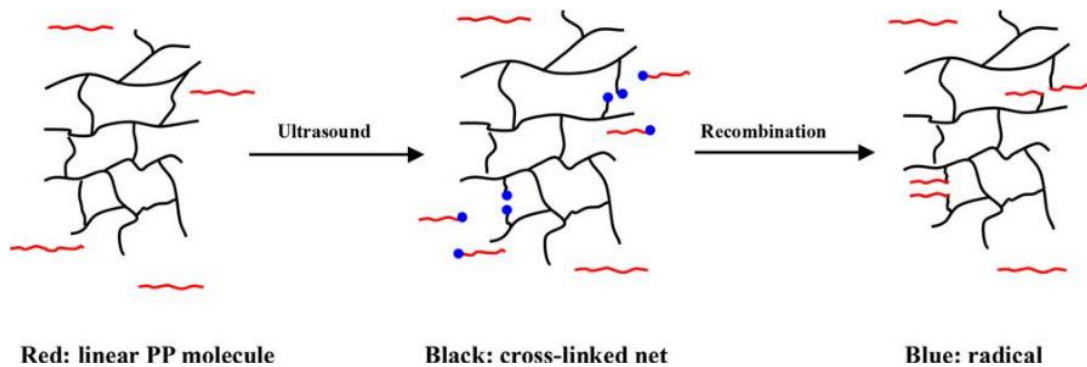


**Figure 2.21.** Schematic description of the recombination reaction induced by ultrasonics between crosslinked and linear PP radicals. Reproduced from [5].

### 2.4.3 Application of ultrasonics under static conditions

Ultrasonics have a clear effect in continuous processes, but different applications have also been considered to modify the material under static conditions. Thus, Hong *et al.* evaluated the effect of ultrasonics in a HDPE incorporating flash aluminum flake pigments (FAFP). The finality was to avoid a post-processing such as spray coating, painting or metallization. The apparent viscosity decreased for the neat polymer and the

HDPE/FAFP composite. A model for the polymer melt was proposed to clarify the relationship between the ultrasonic intensity and the viscosity [70]. The application of the ultrasounds on static conditions was also done to breakdown filler agglomerates in different nanocomposites such as PS/Ni [7], PANI/nano-SiO<sub>2</sub> [8], PMMA/clay [71] or iPP/SiO<sub>2</sub> [72]. Tan *et al.* employed also maleic anhydride to react with the hydroxyl groups present in the SiO<sub>2</sub> nanoparticle surface. An enhancement on the mechanical properties was also observed as consequence of the reduction of silica agglomerates and the improved interface compatibility.

#### **2.4.4 Effect of ultrasonic energy on decrosslink processes**

Different approaches have been done to decrosslink PE networks by extrusion assisted by ultrasounds. The main interest corresponds to the similar chemical structure of this material with rubber vulcanizates and the potential interest in terms of material recyclability.

PE has been crosslinked with organic peroxide and subsequently different levels of ultrasonic energy have been applied under both static and continuous conditions [73]. Crosslink density of treated materials were evaluated through gel fraction and swell ratio measurements. The crosslinked network was found that only supported a certain amount of the applied amplitude strain, becoming the most strained links broken when the applied energy exceeded a limiting value. The effect of decrosslinking decreased with the thickness of the sample, probably as a consequence of the reduction of the material ability to transmit energy after its surface was decrosslinked.

The presence of a three-dimensional network makes difficult the recycling of crosslinked materials. Several works have been focused, for example, on decrosslinking networks of different types of PE. Thus, mechanochemical milling [74,75] and co-rotating intermeshing twin-screw extrusion [76] were effective for LDPE. The ultrasonic-assisted extrusion technology has also been found as a good procedure to devulcanize various rubbers [77-80]. Applications of ultrasonic-assisted extrusion using a single screw has been explored in detail for crosslinked HDPE (XHDPE) [81]. Preliminary works showed that a severe thermal degradation could occur as consequence of a relevant overheating from the dissipation of ultrasonic energy [82]. Obviously, in this case inferior properties were attained for XHDPE after the decrosslinking process. Nevertheless, new design developments and optimization of the processing parameters led to decrosslinked

materials with similar properties than virgin XHDPE. Processing-structure-property relationship had not a clear trend, a feature that was justified according to the fact that mechanical properties (i.e., Young modulus, yield stress and yield strain depended on crystallinity but also on the crosslink density in the gel, and in the molecular and branched architecture in the sol. In fact, SEM images showed that the decrosslinked XHDPE can be considered as a composite constituted by sub-micron gel particles embedded on a matrix of its sol fraction. The study also revealed that ultrasonic waves clearly enhanced the decrosslinking process and provoked a more selective chain scission than observed with a mechanically induced decrosslinking. In fact, the rupture of the crosslinked structure was most effective for XHDPE with a higher crosslinking degree [83]. In summary, breakages not only depend on the bond energy but the structure of the network plays also a relevant role. The highly preferential breakage of crosslinks led to a high improvement of processability, and even mechanical properties of peroxide cured XHDPE after performing the ultrasonic decrosslinking. Furthermore, FTIR analyses could not show any evidence of thermooxidative degradation, probably as a consequence of the insignificant oxygen concentration in the fully filled region of the extruder where ultrasound waves were applied.

Comparison between decrosslinking of HDPE and LDPE by ultrasonic energy during extrusion gave interesting results [84,85]. Gel fraction and crosslinking density were decreased for both samples, but the change of mechanical properties was highly different. Thus, worse properties with respect to the initial sample were found for decrosslinked XLDPE since a significant degradation of main chains was produced. By contrast, the preferential breakage of crosslinks for XHDPE led to an improvement of properties.

Huang *et al.* studied the effect of the screw design for the decrosslinking of XHDPE by ultrasonic treatment during a twin-screw extrusion. It was found that the screw configuration with conveying and reverse conveying elements was an effective screw configuration [86]. This configuration could reduce the mechanical degradation of XHDPE during the extrusion process (**Figure 2.22**). Moreover, processability was significantly improved due to the effective reduction of the gel fraction and the crosslink density. Measurements of the activation energy for flow allowed revealing the presence of highly branched sol in the treated sample.

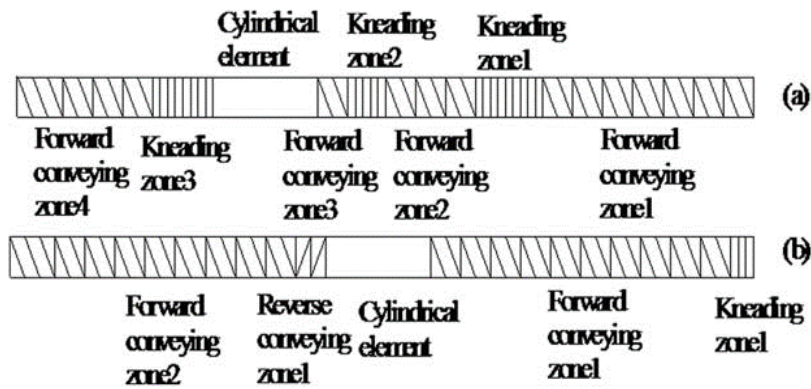


**Figure 2.22.** Schematics configuration of screws for: compounding (a) and decrosslinking (b). The flow direction is from the right to the left. Reproduced from [86].

SEM analyses revealed that the gel fraction influenced the lamellar morphology of samples (**Figure 2.23**). Thus, well-developed lamellae (similar to those observed for HDPE samples) could be detected in the decrosslinked XHDPE with a gel fraction of 0.15. The observed change on the lamellar morphology indicated an increase on crystallinity and justified the observed increase of the Young modulus. Basically, the presence of crosslinks inhibited molecular chain folding and hindered the lamellar growth.

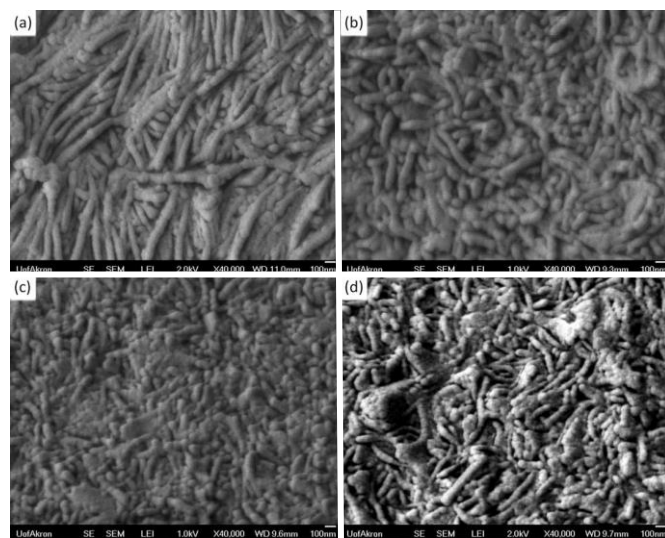


**Figure 2.23.** SEM images of the lamellar structure of etched cryofractured surfaces of HDPE (a), XHDPE (b), and decrosslinked XHDPE at ultrasonic amplitudes of 7.5 μm (c) and 13 μm (d). An ultrasound assisted twin-screw extruder with the decrosslinking configuration was employed. Reproduced from [86].

In 2019, Isayev published a patent where the focus was the decrosslinking and devulcanization using both single and twin-screw extrusion assisted by ultrasounds. A LDPE film and dicumyl peroxide crosslinked HDPE were used in the demonstrative case

studies. Designs were based on special arcuate (single screw) or double - arcuate flow paths that confine the material to flow under the horn in order to be exposed to the ultrasonic waves. Processing of selected samples was carried out using ultrasound characteristics of 20 kHz and 10  $\mu\text{m}$  for the LDPE processed in the single extruder and 40 kHz and 10  $\mu\text{m}$  for the XHDPE processed in the twin-screw extruder [54].

A theoretical modelling of the ultrasonic decrosslinking of XDPE using a twin-screw extruder has recently been formulated [87,88]. This study followed previous simulation works concerning rubber devulcanization under continuous conditions [89-92]. Simulation tried to take into account different factors: a) Cavitation phenomenon, b) Propagation of the ultrasonic energy, c) Rupture of the crosslinked network, and d) The shear viscosity, which is affected by both gel fraction and crosslink density. Despite the great advances on the theoretical simulation, there are still some challenges to be solved such as the deficient estimation of bubble nucleation and the overprediction of the effect caused by the flow rate.

#### **2.4.5 Effect of ultrasonic energy during the extrusion process on polymer blend processes**

Ultrasonic treatment during extrusion can increase the miscibility or the compatibilization of two different polymers. Studies have mainly been focused to thermoplastic and elastomeric materials. Isayev and Hong patented the technology of extrusion (twin or single screw) assisted by an ultrasound system with different configurations and applied them to improve blend compatibilization and induce copolymerization. The induced chemical interaction between two or more components during the ultrasonic assisted process suggest an improvement of miscibility and open potential applications in the recycling of immiscible plastics, or even in the production of materials with good chemical and physical properties [93].

##### **2.4.5.1 Blends with a thermoplastic majority phase from ultrasound assisted extrusion**

Ultrasonic treatment can improve the flow behavior of a thermoplastic polymer due to the capacity of ultrasonic waves to enhance orientation of the entangled segments. Apparent viscosity can consequently be decreased as well as the viscous flow activation energy. Wu *et al.* demonstrated the increase of temperature die and the slip velocity of a mLLDPE

melt at the capillary wall of the extruder die. The homogeneity of mLLDPE/ Polyolefin elastomer (POE) blends can be clearly improved due to the break of the minority phase into small pieces [62]. Extrusion blending of LLDPE and LDPE has been found, as previously indicated, highly effective when the process was assisted with an ultrasound system [64].

Oh *et al.* studied the compatibility of polypropylene and natural rubber (PP/NR) via the extrusion assisted by ultrasounds using an equipment dotted with two horns coupled on the extrusion die (**Figure 2.13a**) [49]. Mechanical properties of immiscible PP/NR blends of various concentrations were found clearly improved with respect to those determined for the corresponding ultrasound untreated samples. Nevertheless, no significant differences between viscosities of ultrasound treated and untreated blends were detected. Analyses of SEM micrographs were highly interesting since revealed a smaller size of domains in the treated blends. Furthermore, AFM observations indicated the development of interfacial roughening and a better interfacial adhesion, which were probably the cause of the improved mechanical properties.

Compatibilization between immiscible blends has been attempted by ultrasonic treatments during prolonged batch mixing (e.g., PE/PS [94], PP/PS [95] and PMMA/PS [96]) or extrusion at short residence times. In general, interfacial adhesion and compatibilization between phases can take place as consequence of copolymer formation at the interface. Thus, blends of isotactic PP and ethylene propylene diene rubber (EPDM) have been prepared by the extrusion assisted process [97,98]. Degradation was evidenced during the ultrasonic treatment, being bond breakages dependent on the blend ratio and processing conditions like the number of horns, wave amplitude and flow rate. Nevertheless, mechanical properties of the 50/50 blend were improved for certain conditions. FTIR spectra demonstrated the formation of copolymer at the interface while SEM micrographs showed smaller domains in the ultrasound treated sample.

Jiang *et al.* focused their work on blends of the ethylene- $\alpha$ -olefin copolymer (POE) and polystyrene (PS) that were prepared in a co-rotating twin-screw extruder assisted with ultrasounds. [99]. As expected, reduction of die pressure and an improvement on the mechanical properties (i.e., the stress at break of POE/PS (80/20) compatibilized blend increased from 9.2 to 11.0 MPa). The physical aspect of ultrasound treated, and untreated samples was compared by means of SEM micrographs. A lower size of the dispersed

phase was observed for the treated sample, suggesting an improved compatibility. A smoother surface of the extrudate (i.e., without the characteristic sharkskin of the untreated sample) was observed together with a decrease of the extrudate diameter that when ultrasonic energy was applied (**Figure 2.24**).

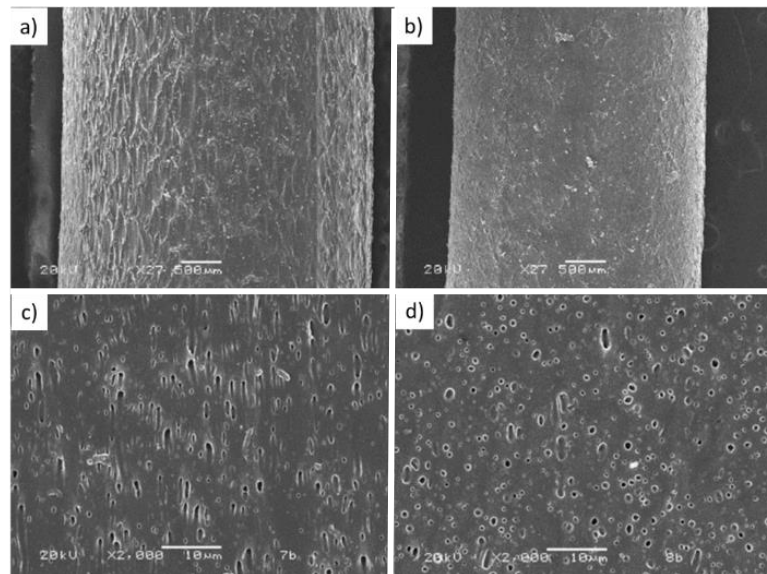


**Figure 2.24.** SEM micrographs of POE extrudates processed without (a) and with (b) ultrasounds; and POE/PS (80/20) blends processed without (c) and with (d) ultrasounds. Adapted from [99].

Ultrasonic treatment was also found effective for blending PP with nylon 6 (PA6) since compatibilization was improved and a 50–100% increase of the tensile toughness was reached in some cases. Ultrasonic energy caused two effects on PA6: ionic condensation reactions and degradation. The improvement of mechanical properties for the treated blends was attributed to condensation reactions which yielded a higher crystallinity, higher molecular weight, and a more uniform crystal size distribution. However, a complete compatibilization of PP and PA6 was not achieved due to the low coupling selectivity of reactive radicals [100].

PET/polyethylene naphthalate (PEN) blends usually have better mechanical, thermal and barrier properties than the single PET component. Main problem concerning the use of the indicated blends is the immiscibility of the two components, which on the other hand can decrease transparency as consequence of the light interaction with phase boundaries. A certain level of copolymerization between the two components may prevent phase separation and therefore *in situ* interchange reactions (e.g., alcoholysis, acidolysis, transesterification) are usually induced. The effect of ultrasonic treatment during extrusion



of PET and PEN homopolymers and the PET/PEN (50/50) blend has been evaluated by Gunes *et al.* [101]. Single polymers easily experimented under the action of ultrasounds a certain degradation that led to reactive hydroxyl and carboxyl terminal groups. In the case of PET, homopolymerization reactions have also been detected. The ultrasonic energy was able to increase transesterification reactions in the PET/PEN mixture by 31% over that observed in the extrusion process without ultrasounds. Therefore, processed blends had a relative high randomization that led to a shift on the glass transition temperature, an increase of the melt viscosity and a lack of crystallinity.

Gunes *et al.* also studied two different blends where at least included a thermotropic liquid crystalline polymer (LCP). On one hand blends of two different LCPs based on 6-oxy-2-naphthoyl and *p*-oxybenzoyl moieties (LCP1), and *p*-oxybenzoyl, terephthaloyl and hydroquinone moieties (LCP2) were extruded under an ultrasonic treatment. Improved mechanical properties were found for LCP1 moldings, while some degradation was characteristic of LCP2. Nevertheless, LCP1/LCP2 blends showed an improvement of resulting properties with a synergistic effect on fibrillation due to an enhancement on the molecular orientation [102]. SEM micrographs showed the presence of intertwined fibrils with diameters around 100 nm. Fibril interconnectivity and size were dependent on the ultrasonic treatment and on the specific blend composition, being the best results attained with the 50/50 blend (**Figure 2.25**).

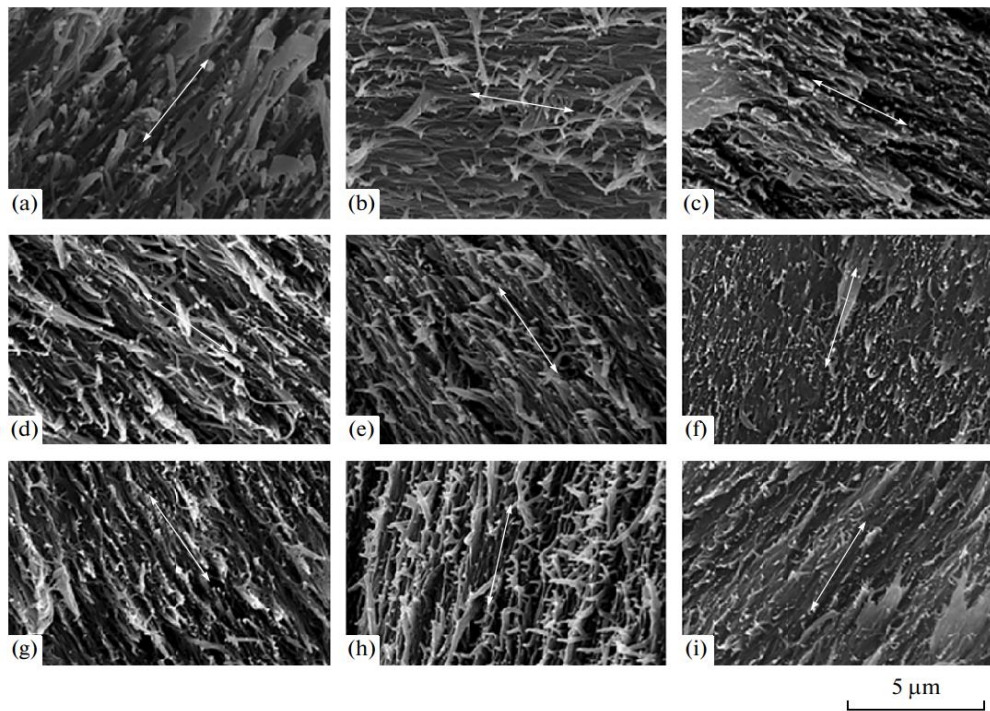


**Figure 2.25.** SEM micrographs of LCP1/LCP2 extruded blends without (a-c) and with (d-i) ultrasound treatment. Blends had compositions of 75/25 (a, d, g), 50/50 (b, e, h) and 25/75 (c, f, i) and the amplitudes of ultrasounds were 7,5 mm (d-f) and 10 mm (g-i). Arrows indicate the machine extrusion direction. Reproduced from [102].

On other hand, a blend of PEN/LCP was also processed [103] with a positive result concerning copolymer formation under the action of ultrasounds. Furthermore, the LCP component promoted higher crystallinity of the blend due to its capability to act as a nucleating agent. Interfacial adhesion in spun fibers at intermediate draw ratios was improved with ultrasounds as well as the ductility of the material.

#### 2.4.5.2 Elastomeric polymer blends from ultrasound assisted extrusion

Ultrasonic treatment has been employed on rubber vulcanizates to conduct a devulcanization during an extrusion process and improve their recyclability [104-108]. The technology was also employed to improve homogeneity between rubber and plastics as discussed in the previous section [109-111].

Liang and Isayev studied the effect of ultrasonic treatment on the molecular structure of NR. A degradation was verified from storage and loss modulus, complex viscosity and loss tangent measurements. The ultrasonic energy created also long chain branched

structures, which led to an increase of the capacity to establish bounds with fillers. During the process, the die pressure decreased because of thixotropic phenomenon, which reduced the friction and the chain scission [112]. Ultrasounds assisted extrusion of BR and their blends was also evaluated [113], being again detected the formation of long chain branches able to increase the interaction with filler added to the elastomer [113] and facilitating the creation of gel. Similar conclusions were derived from the study of SBR rubbers [114,115].

On the other hand, it has been established that the ultrasonic treatment improves the adhesion and the compatibility between blends of two elastomeric materials as reported for SBR/BR [116] and NR/SBR [117] blends. Application of single and twin-screw extruders assisted with ultrasounds to specifically carry out the devulcanization of elastomeric materials has recently been patented [118]

#### **2.4.6 Nanocomposites from ultrasound assisted extrusion**

A good dispersion of nanofillers is probably the most valuable effect of the ultrasonic system coupled to the extrusion compounding equipment, a preparation procedure of nanocomposites that has been patented by Isayev [119]. An improvement in productivity due to a reduction of viscosity is characteristic as previously indicated for other applications. The compounds developed with this technology can be classified following the type of nanofiller added to the polymer matrix.

##### **2.4.6.1 Composites incorporating nanoclays**

Multiple works have been focused on the preparation of nanocomposites from clay nanofillers. Cloisite 15A and 20A have been incorporated to a PP matrix with different approaches and configurations of the ultrasound system (i.e., one step single extruder and a two-step process using firstly a co-rotating twin-screw extruder and then a single-screw extruder equipped with an ultrasonic die attachment). The results showed that the ultrasonic treatment was efficient to render an intercalation of polymer molecules into the clay galleries and a partial exfoliation even for short residence times. Unfortunately, cautions should be taken since polymer degradation (breakage of C-C bonds leading to long chain radicals) was found when ultrasound waves had a high amplitude or intensity. For the optimized conditions, it was seen that the high degree of dispersion of nanoclays led a substantial improvement of mechanical properties such as elongation at break and

toughness. Comparing the nanocomposites obtained with the same configuration but using different clays, it was found a higher degree of intercalation when nanoclays with lower cation exchange capacity were employed [120,121]

Lapshin *et al.* have studied the preparation of nanocomposites from Cloisite C20A and HDPE and PP matrices. Application of ultrasound waves during extrusion provided partially exfoliated structures with a high degree of clay dispersion and improved elongation at break and toughness [122]. An interesting modification of Halpin-Tsai theory [123] for composite materials was employed by the authors in order to predict with more accuracy the incomplete exfoliation of clay platelets and their effect on the Young modulus. Basically, the model considered the decrease of the reinforcement efficiency of high aspect ratio clay platelets as consequence of their incomplete exfoliation and even the loose of a perfect biaxial platelet orientation [124]. Nanocomposites of PP incorporating OMMT nanoclays showed good degree of exfoliation when ultrasound waves were applied as well as a reduction of the size of PP spherulites that justified the observed increase of mechanical properties [125].

Martínez-Colunga *et al.* studied the effect of ultrasounds during the extrusion compounding of Cloisite C20A with isotactic PP and maleic anhydride as a coupling agent. It was found that ultrasounds favored simultaneous polymer functionalization and clay dispersion [126-128]. Previous works demonstrated the benefits of using maleic anhydride-grafted polypropylene as a compatibilizer [129]. Maleic anhydride grafting induced by ultrasounds was also successfully performed with HDPE, LLDPE and EPDM matrices [127,128]. For a high ultrasonic energy, it was observed the formation of PP macroradicals that supported the grafting reaction with MA. The clear increase on the elastic modulus observed for the derived nanocomposites was attributed to the great clay dispersion, which was also verified by XRD diffraction at low angles.

A different approach was studied for the same compound under the effect of ultrasonic energy and the presence of supercritical fluid nitrogen (**Figure 2.26**). It was found that the new approach led to the possibility of forming new chemical bonds which contributed to improve compatibility in a synergistic effect [130].

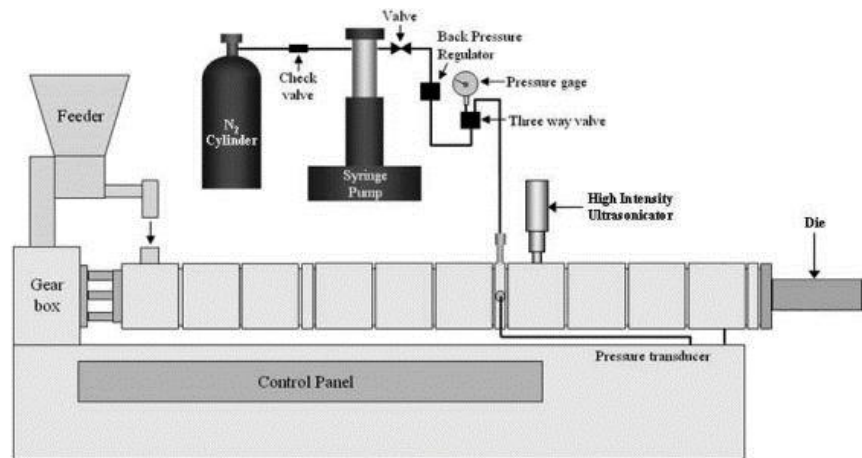


**Figure 2.26.** Reactive extrusion system assisted by ultrasounds in presence of supercritical nitrogen. Reproduced from [130].

An intumescent flame-retardant nanocomposite of PP incorporating the sodium bentonite clay (BEN), pentaerythritol and ammonium polyphosphate was also obtained by extrusion assisted by ultrasounds. Processes using single screw and twin-screw extruders were compared. The flame-retardant intumescent content was diminished from 30 phr to 21 phr using the application of ultrasonic energy during extrusion. Moreover, with the addition of the chemically modified clay it could be obtained a V0 rating (i.e., low volatile organic group) classification. Improvements in the mechanical properties such as impact resistance, strain at break and tenacity have been determined as well as the attainment of a better degree of dispersion. Particles with smaller size were produced with the single screw equipment and therefore the increased surface area allowed to get higher interactions between the polymer matrix and the particles [50].

Single screw extrusion (SSE) assisted with ultrasound was highly effective to get HDPE nanocomposites with the organomodified C20A clay [131]. The spacing indicative of the interlayer separation was increased by 50% and the oxygen permeability was clearly reduced (i.e., from 75.9 to 61.8 cm<sup>3</sup> day m<sup>-2</sup>) as consequence of the tortuous diffusion paths that were created in a matrix having well dispersed clays (**Figure 2.27**). The degree of crystallinity was decreased for a 5 wt.% clay content due to the high interfacial interactions and the consequent decrease of molecular mobility.

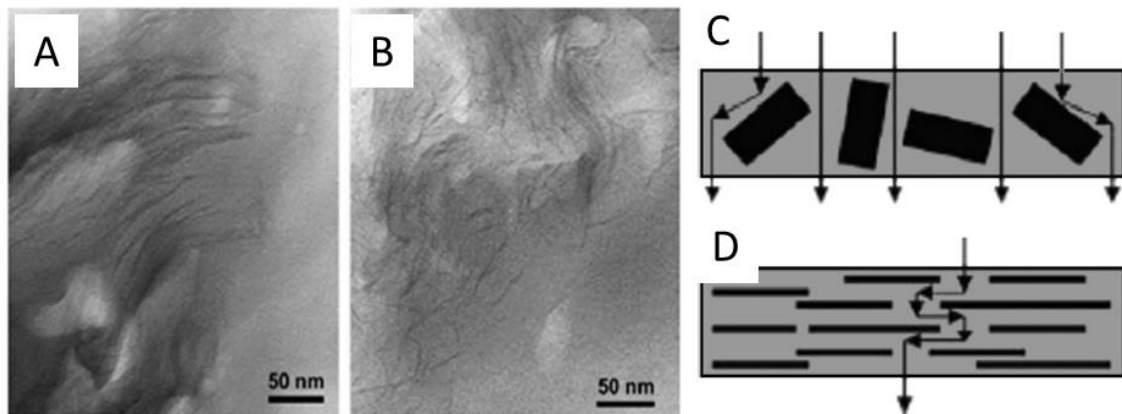


**Figure 2.27.** TEM micrographs of HDPE incorporating 5 wt.% of clay processed without (a) and with (b) ultrasonic treatment at an amplitude of 5  $\mu\text{m}$ . Models of tortuous diffusion paths for conventional composites (c) and clay nanocomposites (d). Reproduced from [131].

HDPE nanocomposites incorporating the organomodified OMMT clay were also prepared by ultrasound assisted extrusion and the influence of nanoparticles in the crystallization behavior of HDPE was investigated [132]. The ultrasonic treatment did not significantly modify the degree of intercalation of the clay but led to the formation of smaller tactoids and even some exfoliated platelets. Therefore, the heterogeneous nucleation mechanism was enhanced in the sonicated samples leading to smaller spherulites and improved mechanical properties.

LDPE has been *in situ* functionalized with itaconic acid (IA) (**Figure 2.28**) under the action of ultrasounds [133] that facilitated the dispersion of the MMT montmorillonite during TSE compounding. The grafting level, clay dispersion, and clay exfoliation was directly influenced by the concentration of the added IA. Samples with 1 wt.% of IA and processed at 186 °C under 460 W of ultrasonic power showed the best performance in mechanical properties.

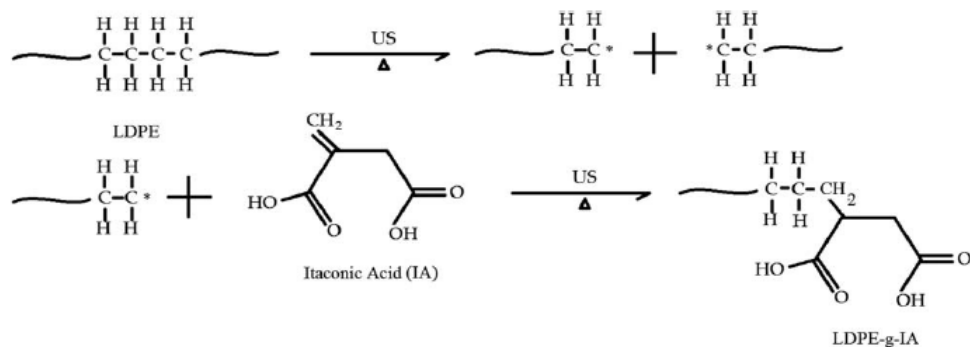


**Figure 2.28.** Scheme of the functionalization reaction of LDPE induced by ultrasounds to get the grafted IA derivative. Reproduced from [133].

Nanocomposites based on LLDPE and Cloisite C20A have been obtained combining ultrasonic treatment and film casting in a single step extrusion. A significant clay dispersion was obtained up to 7.5 wt.% content without requiring the addition of a compatibilizer. Films had a lower oxygen permeability and were transparent even for a clay load of 10 wt.% [68].

Moving away from polyolefins, interesting results have been attained in the study of nanocomposites based on nylon 6 and different organomodified clays (i.e., C30B, C15A and C93A). The difference on the chemical structure of the nanoclays influenced on the dispersion. Thus, an exfoliated system was attained with C30B, while intercalated structures were observed for clays C15A and C93A. The intercalated clays induced the generation of nylon crystals having the characteristic  $\gamma$ -form. The author suggested that this behavior could be caused by two possibilities: a) The  $\gamma$ -form was induced by the clay surface as consequence of kinetic factors; b) The nanoclays changed the thermodynamics of the system destabilizing the typical and more stable  $\alpha$ -form. The ultrasonic treatment had a different effect on the mechanical properties depending on the clay component. Elongation of break was highly dependent on the ultrasound intensity. Barrier properties were improved, even if the addition of nanoclays led to a reduction of crystallinity [134].

Li *et al.* studied also the nanocomposite of PA6 with OMMT. TEM observations clearly indicated an improved dispersion of OMMT that was induced by ultrasonic oscillations. This better dispersion favored the formation of smaller spherulites and consequently the improvement of the elongation at break, yield strength and impact strength. Treatment with 100 W ultrasonic irradiation had a negative effect of thermal stability since

accelerated decomposition reactions of 16-C alkyl quaternary ammonium and ammonium end groups took place. The simple addition of 3 wt.% of MMT favored the  $\gamma$ -form instead to the energetically favored  $\alpha$ -form of pristine polyamide [135].

The effect of ultrasounds under both static and dynamic conditions has been studied for the nanocomposite of PMMA and Cloisite C20A. It was again verified the reduction of the nanoclay size during sonication and the good clay dispersion in the matrix phase. Properties such as mechanical performance, storage modulus and thermal stability were improved with the ultrasonic treatment [71]. Similar studies and conclusions have been obtained from other thermoplastic polymers like PLA/functionalized sepiolite [136], EVA (Ethylene vinyl acetate)/C20A and C6A [137], and PP/polyphenylene sulfide (PPS)/OMMT [138].

The effect of ultrasounds during the extrusion process has also been studied for elastomeric matrices. Thus, EPDM was compounded with nanoclays and also with silica nanoparticles [139]. In both cases, the application of ultrasounds improved the interactions between the nanofiller and the elastomer [139]. Isayev *et al.* also studied this system but differentiating between silica nanoparticles treated with silane and the untreated ones during SSE process with two different configurations of the ultrasound system (**Figure 2.29**). Samples treated with ultrasound showed a good dispersion of silica particles, with lower aggregate size than found in untreated samples. Size was as small as 0.3  $\mu\text{m}$  independently of the silane treatment. In any case, silane improved the compatibilization between silica and the polymer matrix and consequently mechanical properties [109].

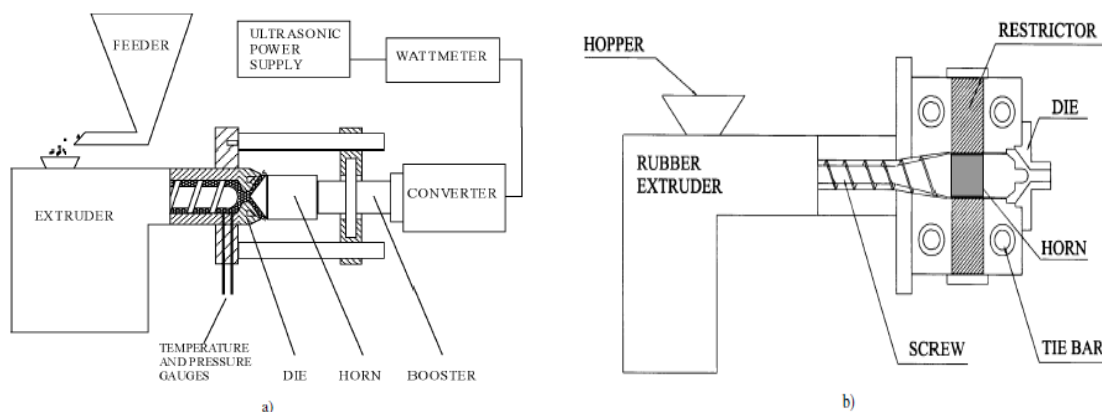


**Figure 2.29.** Schematic of coaxial (a) and barrel (b) ultrasonic system. The second case is dotted with two horns that vibrate longitudinally. Adapted from [109].



Extrusion of star styrene-butadiene rubber (SBR) has been performed without and with ultrasonic treatment at different amplitudes (i.e., 3.5, 5, 7.5, and 10  $\mu\text{m}$ ). Die pressure could be decreased when ultrasounds were applied due to thixotropic and degradation effects [115]. A long chain branching without gel formation was observed when the ultrasonic amplitude was 3.5  $\mu\text{m}$ . A slight formation of gel was detected at 5  $\mu\text{m}$ , but at higher values the gel generation increased in a such way that hindered the mixing of star SBR with silica. Extruded star SBR was compounded with carbon black (CB) and silica with and without silane as a compatibilizer agent. It was found that the long-chain branching induced by the ultrasonic treatment improved the rubber–filler interactions, reduced the filler–filler interactions and caused a clear improvement of mechanical properties.

Nanocomposites of propylene-based plastomers (propylene–ethylene copolymers having rubber-like properties and processability of plastics) with nano  $\text{SiO}_2$  particles (1-4 wt.%) were prepared by an ultrasound-assisted extrusion system. Rheological measurements indicated that ultrasound-induced compatibilization was predominant over degradation effects. Nucleation was clearly improved due to the better dispersion of the nanofiller when ultrasounds were applied [140].

#### **2.4.6.2 Nanocomposites incorporating carbon-based fillers**

Carbon black (CB), carbon nanofibers (CNF), multiwalled carbon nanotubes (MWCNTs), graphene (Gr) and their nanoplatelets (GNP), and graphite are the main studied fillers of different polymer matrices that have been extruded with the help of ultrasonic waves. The incorporation of these fillers should improve general properties and in particular the electrical ones. The biggest challenge, specially, for the incorporation of such kinds of carbon-based fillers is to achieve a good dispersion of the primary agglomerates while a subsequent reaggregation is avoided. Ultrasonically assisted single screw extrusion process was effective to reduce the percolation threshold of PEI (Polyetherimide)/CNF, as consequence of the improved dispersion and the high aspect ratio of the filler. An increase of Young modulus and both electrical and thermal conductivities was observed (**Figure 2.30**) [52]. Nevertheless, the lack of adhesion between CNF and PEI matrix caused a decrease in the tensile strength at high loadings.

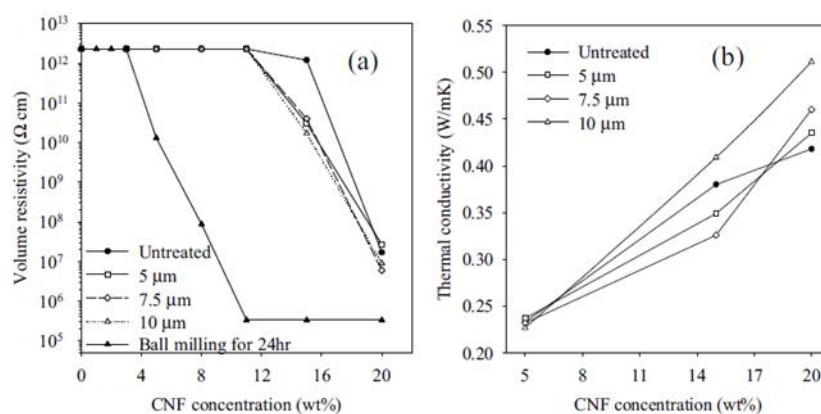


**Figure 2.30.** Volume resistivity (a) and thermal conductivity (b) of nanocompounds versus CNF concentration. Reproduced from [52].

LCPs materials are characterized by their long, rigid and rod-like constitutive molecules that can be easily aligned under flowing conditions. Materials had good mechanical properties but unfortunately very low conductivity. This feature prevents their use in high performance devices and justify compounding with conductive nanofillers like CNFs. Specifically, LCP Vectra 400P and CNFs were extruded using an ultrasound assisted equipment [141]. The ultrasound system consisted of two horns attached to the die zone (gap of 4 mm for the flow of the polymer melt) and oscillating at 40 kHz with variable amplitudes (i.e., from 0 to 3.2  $\mu\text{m}$ ). Dispersion was clearly improved by the application of ultrasounds and the LC rich areas could disappear. Processing conditions could be optimized in order to keep at least the same mechanical properties that the neat polymer, a feature that was not achieved in previous studies. As expected, a significant improvement of conductivity was attained with the nanocomposite.

Choi *et al.* studied the addition of CNFs and MWCNTs within SBR. A highly significant reduction in the electrical percolation threshold was found for the filled vulcanizates. Molecular structure was also changed due to formation branched structures that increase the glass transition temperature. In addition, ultrasound waves had also an effect on curing since allowed decreasing the induction time. Addition of ZnO was found positive since improved dispersion and facilitated gel formation under the applied ultrasonic energy [142].

Nanocomposites of PP incorporating MWCNTs is probably the most studied system concerning the effect of ultrasounds on the extrusion of carbon-based nanocompounds. Thus, Zhong *et al.* compared the dispersion attained with a co-rotating twin-screw micro-extruder (direct compounding, DC) and the masterbatch dilution technique (MD) both with

and without ultrasounds. Results clearly indicated that in both cases ultrasonic energy improved dispersion and processing (**Figure 2.31**). Diluted masterbatches led to a better dispersion level, with higher values of storage modulus, viscosity, electrical conductivity, and mechanical properties [143].

The same type of nanocomposites was also obtained with a SSE assisted by ultrasounds. In this case, the ultrasound treatment had no significant effect on the Young modulus and yield stress, but increased nanofiller dispersion, ductility and toughness. The prepared samples had oriented and aligned particles that acted as nucleation sites for the crystallization. Interestingly SAXS and WAXS patterns suggested the formation of shish kebab superstructures. The work also indicated that the improved dispersion of MWCNTs was due to the acoustic cavitation mechanism (**Figure 2.32**), which caused severe turbulences, broke polymer chains and reduced the large aggregates into smaller particles [48].

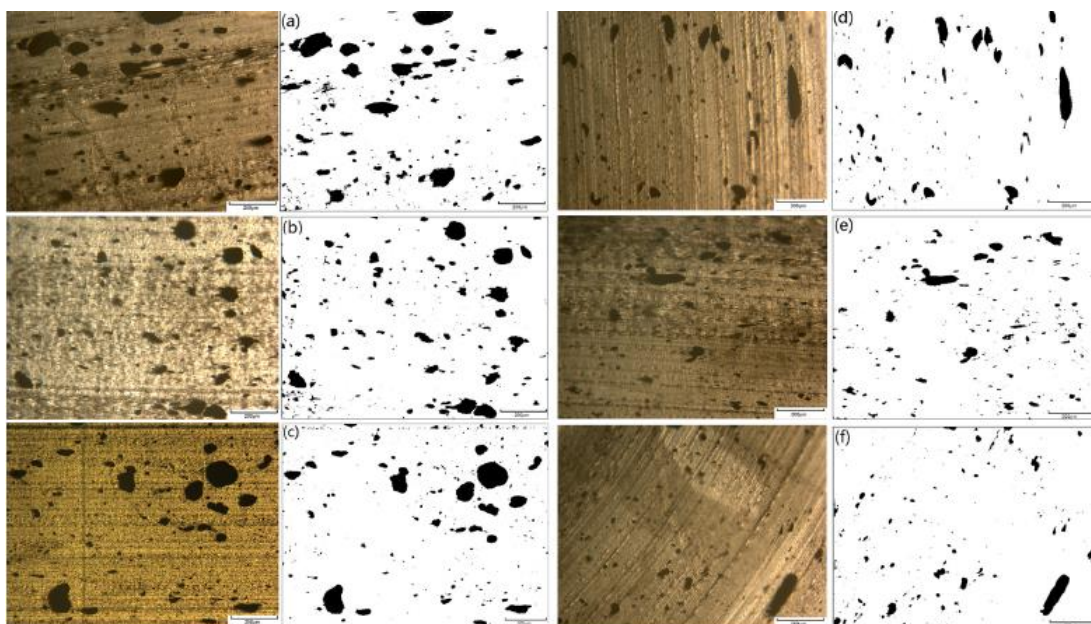


**Figure 2.31.** Optical micrographs of PP nanocomposites incorporating 1 wt.% of CNTs (left) and the corresponding analyzed images (right). Samples were obtained using the DC (left) and MD methods (right) and corresponded to untreated (a, d), and ultrasound treated (b-f) samples. Ultrasound amplitudes were 10  $\mu\text{m}$  (b, e) and 13  $\mu\text{m}$  (c, f). Reproduced from [143].

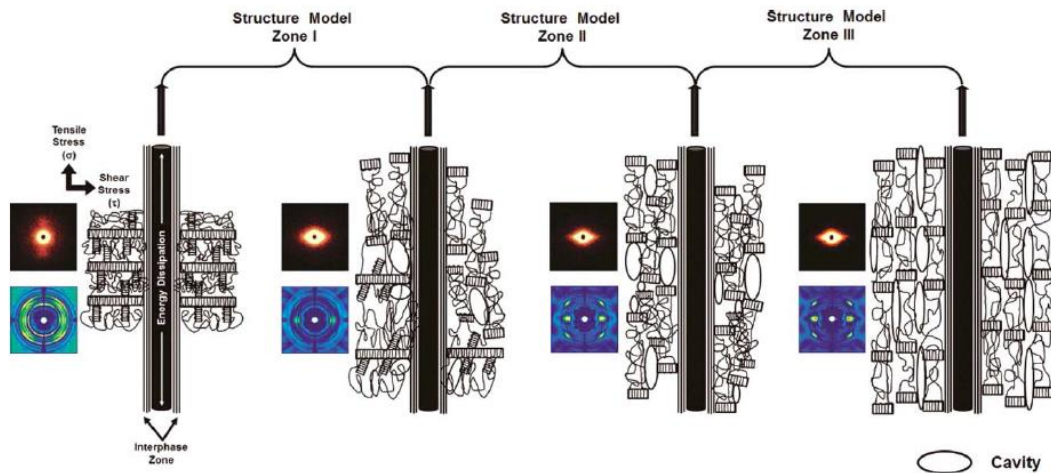


**Figure 2.32.** Schematic illustrations of phase transition and structure development pathways. The corresponding SAXS/WAXS patterns during deformation of PP/MWCNTs nanocomposites with MWCNT concentrations lower than 2 wt.% are shown. The formation of cavities in the plastic zone is also illustrated. Reproduced from [48].

Ávila-Orta *et al.* processed PP/MWCNTs nanocomposites using TSE and PPs with different molecular weights (i.e.,  $M_w$  ranging from 670,000 to 144,000 g/mol)). The best improvement on electrical properties was attained with the highest molecular weight sample. It was also found, that in this case the size of the agglomerates was smaller [144]. Zhong *et al.* performed a similar work evaluating also the influence of the amplitude of applied ultrasounds. Again, the sample with higher molecular weight led to a better dispersion, improved rheological properties and a lower electrical percolation threshold. The dominant mechanism for the breakage of agglomerates during the ultrasonic treatment was consequence of bubble cavitation. The ultrasound system was also located in two different steps of the compounding process to compare the dispersion level (**Figure 2.33**) [145].

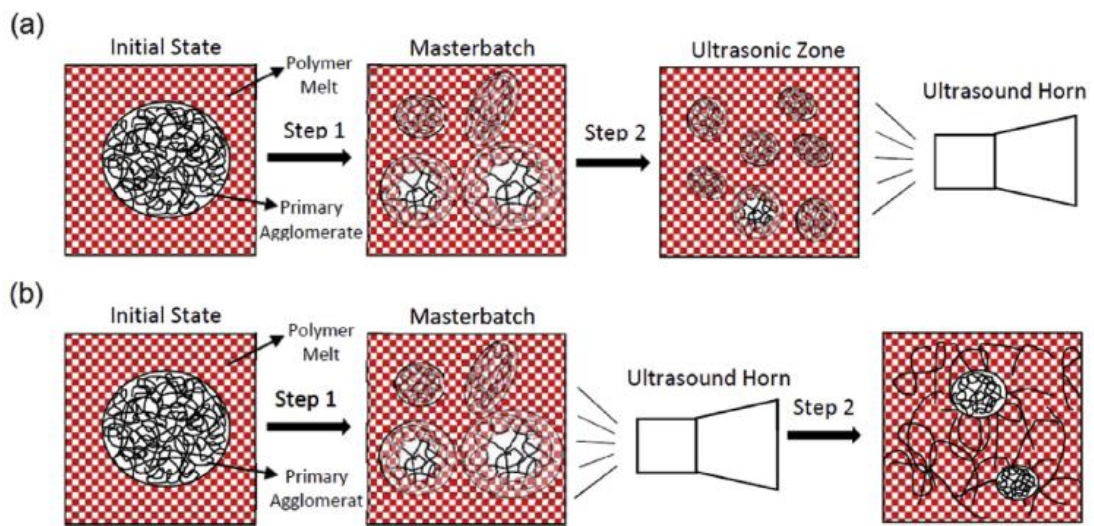


**Figure 2.33.** Inside cavitation mechanism in the PP/MWCNT nanocompound when ultrasounds were applied in two different places. a) Ultrasonic treatment was applied in the masterbatch dilution step. b) Ultrasonic treatment was applied in the masterbatch preparation step. Reproduced from [145].

Yang *et al.* focused their work on the PP/MWCNT system using chlorinated PP. It was seen a remarkable decrease on the volume resistivity with the ultrasonic irradiation as consequence of the improved interfacial adhesion. A MWCNT content higher than 3 wt.% led to a significant increase of crystallinity as well as elastic modulus, viscous modulus, and complex viscosity [146].

An improvement on electrical and thermal conductivities, complex viscosity, storage modulus and Young's modulus were also reported by Quiñones-Jurado *et al.* who were interested on the production of transparent films with low electrostatic charge and high dispersion of carbon nanotubes [69]

Zhong *et al.* compared the effect of ultrasounds in TSE compounding of metallocene PP with three different carbon fillers: CNT, CB and GNP. A good dispersion was verified in the three cases under the action of ultrasounds, but the effect on the final properties was different. The dispersion was associated to the inside and outside cavitation bubble mechanism (**Figure 2.34**), which allowed improving rheological behavior and electrical threshold, and reduced the size of agglomerates and the contact surface ratio for CNT and CB based nanocomposites, but no for those incorporating GNP. For CNT filler, the electrical resistivity dropped significantly when the CNT filler was employed, while the elongation at break was only improved for compounds incorporating CB. The storage modulus and complex viscosity increased for CB and CNT nanocomposites. Interestingly,

the evaluated carbon fillers acted as a nucleation agent that favored the  $\gamma$ -form of PP, being the effect higher for CNT and lower for CB nanocomposites [53].

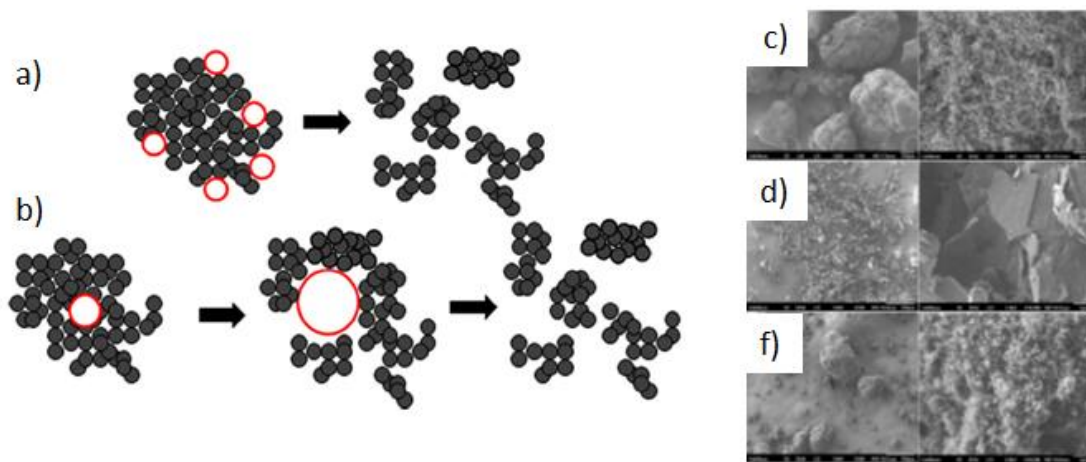


**Figure 2.34.** Outside (a) and inside (b) cavitation mechanism in nanocomposites obtained with ultrasound assisted processes. SEM images of PP nanocomposites incorporating CNT (c), GNP (d) and CB (e) at low (left) and high (right) magnifications. Adapted from [53].

PEI/MWCNT nanocomposites were also evaluated using an ultrasound system with two horns coupled at the die of a TSE and a seal made on Vespel<sup>®</sup> with 40% of graphite [51]. Application of ultrasonic energy produced thixotropic changes in the molten polymer and molecular chain scission. The improvement on the dispersion by ultrasounds had more effect on the rheological properties than in the electrical conductivity. Specifically, the increase in the storage modulus indicated an improvement on the interaction between the MWCNT and the PEI matrix when ultrasounds were applied [51].

Nanocomposites of PA6 with MWCNT were studied by Blanco *et al.* using a twin screw microextruder with one horn [147]. A deagglomeration of carbon nanotubes was observed as well as a drop in the electrical resistivity by three orders of magnitude when the ultrasounds were applied. The influence of ultrasonic energy was higher for lower temperatures and lower rotation speeds due to the longer residence time. It was also observed an acceleration of molecular motion that made long entangled molecular chains unravel without polymer degradation [147]. Espinoza-Gonzalez *et al.* studied the related PA12 nanocomposite. It was indicated that the level of dispersion of nanofillers could be controlled but the polymer matrix was susceptible to branching reactions [147]

PP/MWCNT nanocomposites were evaluated by Gao *et al.* The effects of the polymer molecular weight and ultrasounds were estimated and particularly the best dispersion of nanofillers and electrical and percolation thresholds were found for the lowest molecular weight sample. A larger effect of ultrasonic energy was observed at low MWCNT contents, with improvement in mechanical properties such as Young modulus and elongation at break [149,125].

Elastomeric polymers with carbon black were studied during the extrusion compounding assisted by ultrasounds. For SBR, the most relevant effects of ultrasounds were related to the reduction of the extractable content and the increase of crosslinking density, mechanical properties and glass transition temperature. The electrical percolation threshold of vulcanizates was also decreased for these nanocomposites. It is interesting to note that the generated gel could act as an additional crosslinked structure. Moreover, the long-chain branching induced by the ultrasounds improved the polymer-filler interactions [115,151]. NR/CB nanocomposite showed a decrease of the complex dynamic viscosity, bound rubber, crosslinking density and gel fraction. Thus, NR chain scission was suggested to take place with the application of ultrasounds [152].

PEI/Graphite nanocomposites were also prepared by TSE assisted by ultrasounds. Untreated, modified and expanded graphite were considered, but only the expanded graphite was influenced by the applied ultrasonic energy. In this case, the degree of dispersion that could be attained was so high that a highly significant improvement on the electrical properties was observed and specifically the electrical volume resistivity was reduced by 3 orders of magnitude [153]

He *et al.* performed an exhaustive study of the ultrasound conditions that permit an exfoliation of GNPs in a PP matrix (**Figure 2.35**) [154]. Good results were obtained in terms of electrical and thermal conductivity, decrease of apparent viscosity and decrease of the crystallinity [154]. A similar result of dispersion was reported by Jiang and Drzal using a solid state ball milling and solid state shearing pulverization as a pretreatment to prepare the HDPE/GNP nanocomposite [155].

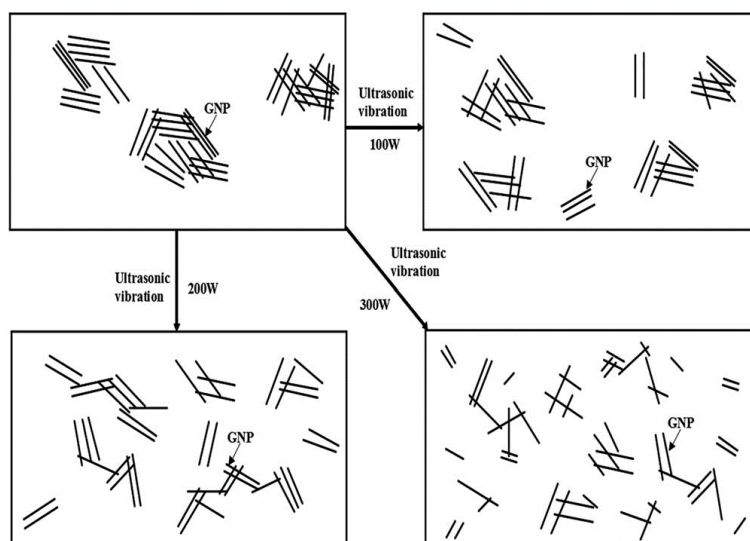


**Figure 2.35.** Schematic of the exfoliation and dispersion mechanism of GNPs in a PP matrix with different ultrasound power treatments. Reproduced from [154].

### 2.4.6.3 Incorporation of other compounds in ultrasound assisted extrusion processes

Metal hydroxides are the most frequent additives for flame retardant polymers. Low cost and toxicity, minimal corrosion and easy of handling are some of the advantages together with reduced smoke emission during combustion. Probably, aluminum trioxide (ATH) is the most employed hydroxide for thermoplastics elastomers and thermosettings (1 de [156]). A great disadvantage of ATH is the fact that it should be incorporated in a large amount (e.g., 40-65 wt.% to render a flame retardant effect. Addition of zinc borate (ZB) can provide a synergic effect that allowed reducing the amount of ATH [157]. Basically, ATH decomposes giving  $\text{Al}_2\text{O}_3$  and the polymer forms a cross-linked network and a carbonaceous char that is enhanced in the presence of ZB. Sanchez-Olivares *et al.* studied the effect caused by on-line ultrasound application during extrusion of HDPE loaded with different amounts of ATH and ZB flame-retardants. Dispersion of additive particles was improved as well as the flame retardant properties in such a way that the additive load could be reduced. Furthermore, the reduced load decreased the negative impact of added particles on the final mechanical properties.

The effect of ultrasounds to prepare PP nanocomposites incorporating glass fibers,  $\text{MgAl}(\text{SiO}_3)_2$  whiskers and mica was studied by Chen *et al.* When ultrasound vibration was applied during the extrusion, cavitation was easily formed near the solid surface of added particles. Shock waves from the bubble implosion helped to improve dispersion



and orientation of fillers. Ultrasound vibration increased the orientation of acicular fillers to the flow direction, while sheet mica flakes were oriented with their surface perpendicular to the direction of the ultrasound vibration. Mechanical properties resulted clearly improved after filler orientation [158].

## 2.5 Conclusions

The ultrasonic system has been an effective technology to be implemented in two of the most important transformation processes, the injection molding (conventional and micro) and the extrusion. Due to the experimental results shown throughout this review, it has been proven as a promising technology to be implemented since the performance of the processed material can be clearly improved.

Several investigations were done to improve the processability of the material looking for the optimal properties during the injection molding assisted by ultrasounds. The focus was put on the rheological behavior, but as some studies shown, the effect of the ultrasonic waves is physical as well as chemical, promoting different changes on the polymeric structure.

The ultrasonic micromolding is based on the cavitation mechanism that enhances the polymer flow through the cavity of the mold. Several parameters have been studied as force, time of ultrasound application, or input velocity of the material. However, the equipment for ultrasound molding is currently in a continuous evolution, being considered different configurations that are mainly focused to attain a high repeatability degree for each injected sample. The optimal configuration of the technology should be determined for each kind of polymer and application. It is also desirable to progress in the theoretical simulation in such a way that a model of the behavior for the processed material under the action of ultrasonic energy could be formulated and adapted according to the selected polymer and its response to the applied energy. The design of the mold and the horn, including the material employed, intensity and amplitude of ultrasonic energy, should be considered in the futures works to find the optimal model of the process that can be supported by a simulation software. At the same time, the conventional simulation software can be adapted to simulate the different effects of the ultrasound on the polymeric material.

On the other hand, the extrusion assisted by an ultrasound system is an interesting process technology that can improve the dispersion of the fillers in different polymer matrices, the adhesion of the fillers with the polymer surfaces and the interfacial interaction between blended polymers. These interactions are usually enhanced by chain breakages induced by a high ultrasonic energy. Ultrasounds had also a positive effect for materials with difficult recyclability such as crosslinked HDPE or elastomeric polymers since their processability can be enhanced through decrosslinking or devulcanization reactions. Several academic studies have been made about extrusion assisted by ultrasounds. Nevertheless, more studies are necessary to optimize this process for a correct application in the industry where the high amounts of processed materials could lead to environmental problems and the stability and repeatability of each component of equipment should be ensured.

In summary, reported data indicated the great potential of processing technologies that make use of ultrasounds. The effect of ultrasounds appears beneficial for a wide range of materials and applications. Nevertheless, we consider that more studies must be done to understand the physical effect of the ultrasounds on the processed material. It appears even necessary to postulate new approaches and improvements of the equipment supported by the simulation of the material behavior during its transformation under the ultrasonic energy.

## 2.6 References

1. Qiu, Z.; Yang, X.; Zheng, H.; Gao, S.; Fang, F. *Appl. Opt.*, 54, 8399-8405, 2015.
2. Moles, M.; Roy, A.; Silberschmidt, V. *Phys. Procedia*, 87, 61–71, 2016.
3. Yang, Y. J.; Huang, C. C.; Lin, S. K.; Tao, J. *J. Polym. Eng.*, 34, 7, 673–681, 2014.
4. Ávila-Orta, C.; Espinoza-González, C.; Martínez-Colunga, G.; Bueno-Baqués, D.; Maffezzoli, A.; Lionetto, F. *Adv. Polym. Technol.*, 32, 1, 2013.
5. Yang, M.; Li, J.; Guo, S. *Polym. Eng. Sci.*, 57, 8, 821–829, 2017.
6. Cabello-Alvarado, C. J.; Quiñones-Jurado, Z. V.; Cruz-Delgado, V. J.; Avila-Orta, C. A. *Materials (Basel)*, 13, 17, 2020.
7. Kumar, R.V.; Koltypin, Y.; Palchik, O.; Gedanken, A. *J. Cell. Mol. Med.*, 86, 1, 160–

- 165, 2002.
8. Xia, H.; Wang, Q. *J. Appl. Polym. Sci.*, 87, 11, 1811–1817, 2003.
  9. Sinha, S.R.; Okamoto, M. *Prog. Polym. Sci.*, 28, 11, 1539–1641, 2003.
  10. Yang, Y. J.; Huang, C.C.; Tao, J. *J. Polym. Eng.*, 36, 2, 119–128, 2016.
  11. Yang, Y. J.; Huang, C.C., *J. Polym. Eng.*, 38, 9, 905–914, 2018.
  12. Jiang, K.Y.; Ji, Z.; Li, H.; Wang, M.J.; Yu, T.M. *Int. Polym. Process.*, 32, 3, 290–297, 2017.
  13. Sato, A.; Ito, H.; Koyama, K. *Polym. Eng. Sci.*, 49, 4, 768–773, 2009.
  14. Sánchez-Sánchez, X.; Hernández-Avila, M.; Elizalde, L.E.; Martínez, O.; Ferrer, I.; Elías-Zuñiga, A. *Mater. Des.*, 132, 1–12, 2017.
  15. Lu, C.; Yu, X.; Guo, S. *Polym. Eng. Sci.*, 45, 12, 1666–1672, 2005.
  16. Liu, S.; Lin, K.; Tsai, S.; Liu, S.; Lin, K.; Tsai, S. *Plast. Rubber Compos*, 37:1, 23–28, 2008.
  17. Negre, P.; Grabalosa, J.; Ferrer, I.; Ciurana, J.; Elías-Zuñiga, A.; Rivillas, F. *Procedia Eng.*, 132, 7–14, 2015.
  18. Grabalosa, J.; Ferrer, I.; Elías-Zuñiga, A.; Ciurana, J. *Mater. Des.*, 98, 20–30, 2016.
  19. Godec, D.; Rujnic-Sokele, M.; Sercer, M. *Polimeri*, 33, 3–4, 112–117, 2012.
  20. Peng, T.; Jiang, B.; Zou, Y. *Polymers (Basel)*, 11, 9, 1407–1419, 2019.
  21. Lee, J.; Kim, N. *J. Mater. Process. Technol.*, 201, 1–3, 710–715, 2008.
  22. Lee, J.; Kim, N.; Lee, J. *Korea Aust. Rheol. J.*, 20, 2, 79–88, 2008.
  23. Masato, D.; Babenko, M.; Shriky, B.; Gough, T.; Lucchetta, G.; Whiteside, B. *Int J. Adv. Manuf. Technol.*, 99, 113–125, 2018.
  24. Gaxiola-cockburn, R.; Mart, O.; El, A.; Olvera-Trejo, D.; Res, E.; Soria-Hern, C.G.

*Polymers (Basel)*., 12, 9, 2033-2055, 2020.

25. Sacristán, M.; Plantá, X.; Morell, M.; Puiggali, J. *Ultrason. Sonochem.*, 21, 1, 376–386, 2014.
26. Díaz, A.; Franco, L.; Casas, M.T.; del Valle, L.J.; Aymamí, J.; Olmo, C.; Puiggali, J. *J. Polym. Res.*, 21, 584-595, 2014.
27. Sato, A.; Sakaguchi, H.; Ito, H.; Koyama, K. *Plastics, Rubber and Composites*, 39, 7, 315-320, 2010.
28. Rienstra, S.W.; Hirschberg, A. *An introduction to Acoustic*, Eindhoven, 2015.
29. Levy, A.; Le Corre, S.; Fernandez-Villegas, I. *J. Mater. Process. Technol.* 214, 1361–1371, 2014.
30. Ye, Y.; Cai, J.; Jiang, X.; Dai, D.; Deng, D. *Adv. Eng. Softw.*, 86, 39-48, 2015.
31. Planellas, M.; Sacristán, M.; Rey, L.; Olmo, C.; Aymamí, J.; Casas, M.T.; del Valle, L.J.; Franco, L.; Puiggali, J. *Ultrason. Sonochem.*, 21, 4, 1557–1569, 2014.
32. Díaz, A.; Casas, M.T.; Puiggali, J. *Appl. Sci.*, 5, 4, 1252–1271, 2015.
33. Olmo, C.; Amestoy, H.; Casas, M.T.; Martínez, J.C.; Franco, L.; Sarasua, J.R.; Puiggali, J. *Polymers (Basel)*., 9, 8, 322-349, 2017.
34. Olmo, C.; Franco, L.; del Valle, L.J.; Puiggali, J. *Appl. Sci.*, 9, 11, 2360-2376, 2019.
35. Olmo, C.; Franco, L.; Vidal, A.; del Valle, L.J.; Puiggali, J. *Express Polym. Lett.*, 15, 389-403, 2021.
36. Gao, S.; Qiu, Z.; Ouyang, J. *Polymers (Basel)*., 11, 1, 151-62, 2019.
37. Suslick, K.S.; Price, G.J. *Annu. Rev. Mater. Sci.* 29, 295–326, 1999.
38. Schaefer, M.; Icli, B.; Weder, C.; Lattuada, M.; Kilbinger, A.F.M.; Simon, Y.C. *Macromol.* 49, 1630–1636, 2016.
39. Caruso, M.M.; Davis, D.A.; Shen, Q.; Odom, S.A.; Sottos, N.R.; White, S.R.; Moore, J.S. *Chem. Rev.*, 109, 11, 5755-5798, 2009.

40. Bhateja, S.K.; Andrews, E.H.; Yarbrough, S.M. *Polym. J.* 21, 739–750, 1989.
41. Marson, S.; Attia, U.; Lucchetta, G.; Wilson, A.; Alcock, J.R.; Allen, D.M. *J. Micromec. Microeng.*, 21, 11, 115024-115032, 2011.
42. Masato, D.; Sorgato, M.; Lucchetta, G. *Microsyst. Technol.*, 23, 8, 3661–3670, 2017.
43. Araújo, B.J., Pouzada, A.S. *O Molde*, 54:36–41, 2002.
44. Masato, D.; Sorgato, M.; Lucchetta, G. *Mater. Des.*, 95, 219–224, 2016.
45. Sasaki, T.; Koga, N.; Shirai, K.; Kobayashi, Y.; Toyoshima, A. *Precis. Eng.*, 24, 3, 270–273, 2000.
46. Masato, D.; Sorgato, M.; Lucchetta, G. *Int. J. Adv. Manuf. Technol.*, 96, 1–4, 345–358, 2018.
47. Guo, S.; Li, Y.; Chen, G.; Li, H. *Polym. Int.*, 52, 1, 68–73, 2003.
48. Mata-Padilla, J.M.; Ávila-Orta, C.A.; Medellín-Rodríguez, F.J.; Hernández-Hernández, E.; Jiménez-Barrera, R.M.; Cruz-Delgado, V.J.; Valdéz-Garza, J.; Solís-Rosales, S.G.; Torres-Martínez, A.; Lozano-Estrada, M.; Díaz-Barriga-Castro, E. *J. Polym. Sci. Part B Polym. Phys.*, 53, 7, 475–491, 2015.
49. Seok, J.; Isayev, A.I.; Rogunova, M.A. *Polymer*, 44, 8, 2337–2349, 2003.
50. Sanchez-Olivares, G.; Sánchez-Solis, A.; Calderas, F.; Medina-Torres, L.; Herrera-Valencia, E.E.; Rivera-Gonzaga, A.; Manero, O. *Polym. Eng. Sci.*, 53, 9, 2018–2026, 2013.
51. Isayev, A.I.; Kumar, R.; Lewis, T.M. *Polymer.*, 50, 1, 250–260, 2009.
52. Isayev, A.I.; Jung, C.; Gunes, K.; Kumar, R. *Int. Polym. Process.*, 23, 4, 395–405, 2008.
53. Zhong, J.; Isayev, A.I.; Zhang, X. *Eur. Polym. J.*, 80, 16–39, 2016.
54. Isayev, A.I. “Single and twin screw extruders with ultrasound horns for decrisslinking and devulcanization, US10465059B2, 2019.

55. Bernhardt, E.C. *Ind. Eng. Chem.*, 46, 4, 742–746, 1954.
56. Isayev, A.I.; Wong, C.M.; Zeng, X. *Adv. Polym. Technol.*, 10, 1, 31–45, 1990.
57. Chen, G.; Guo, S.; Li, H. *J. Appl. Polym. Sci.*, 84, 13, 2451–2460, 2002.
58. Chen, Y. Li, H. *J. Polym. Sci. Part B Polym. Phys.*, 45, 10, 1226–1233, 2007.
59. Cao, Y.; Li, H. *Polym. Eng. Sci.*, 42, 7, 1534–1540, 2002.
60. Chen, J.; Chen, Y.; Li, H.; Lai, S.-Y.; Jow, J. *Ultrason. Sonochem.*, 17, 1, 66–71, 2010.
61. Wu, H.; Guo, S.; Chen, G.; Lin, J.; Chen, W.; Wang, H. *J. Appl. Polym. Sci.*, 90, 7, 1873–1878, 2003.
62. Wu, H.; Bao, W.; Guo, S. *Polym. Eng. Sci.*, 50, 11, 2229–2235, 2010.
63. Guo, S.; Li, Y.; Chen, G.; Li, H. *Polym. Intern.*, 52, 1, 68-73, 2002.
64. Wu, H.; Guo, S.; Chen, G.; Shi, H. *J. Appl. Polym. Sci.*, 94, 6, 2522–2527, 2004.
65. Muniesa, M.; Fernández, Á.; Clavería, I.; Javierre, C.; Sarasua, J.A.; Blanco, M. *Polimery/Polymers*, 60, 3, 209–216, 2015.
66. Rieckert, H.H.; Isayev, A.I. US assisted process for increasing the crystallinity of slow crystallizable polymers, US20040138410A1, 2004.
67. Isayev, A. I.; Mandelbaum, S. *Polym. Eng. Sci.*, 31, 14, 1051–1056, 1991.
68. Niknezhad, S.; Isayev, A.I. *J. Appl. Polym. Sci.*, 129, 1, 263–275, 2013.
69. Quiñones-Jurado, Z.V.; Waldo-Mendoza, M.A.; Mata-Padilla, J.M.; González-Morones, P.; Martínez-Colunga, J.G.; Soriano-Corral, F.; Cruz-Delgado, V.J.; Ziolo, R.F.; Avila-Orta, C.A. *Polymers (Basel)*, 10, 1, 2018.
70. Hong, X.; Xiao, X.; Zhang, Z.; Zhang, J.J. *J. Appl. Polym. Sci.*, 134, 23, 1–8, 2017.
71. Ryu, J.G.; Lee, J.W.; Kim, H. *Macromol. Res.*, 10, 4, 187–193, 2002.
72. Tan, X.; Xu, Y.; Cai, N.; Jia, G. *Polym. Compos.*, 30, 6, 835–840, 2009.

73. Jenkins, J.A. "Ultrasonic decrosslinking of crosslinked Poly(ethylene)," Thesis, 2007.
74. Zhang, X.; Lu, C.; Liang, M. *J. Appl. Polym. Sci.*, 122, 2110-2120, 2011.
75. Wu, H.; Liang, M.; Lu, C. *J. Appl. Polym. Sci.*, 122, 257-264, 2011.
76. Oh, S.S.; Bang, D.S.; Lee, J.K. *Elastomer*, 39, 131-141, 2004.
77. Isayev, A.I.; Ghose, S. Ultrasonic Devulcanization of Used Tires and Waste Rubbers, in *Rubber Recycling*, CRC Press, , Boca Raton, FL, 2005, p. 341.
78. Isayev, A.I. Recycling of Rubber, in *Science and Technology of Rubber*, Eds., Academic Press, New York, 2005, 663–701.
79. Isayev, A.I.; Oh, J.S. Tire Materials: Recovery and Reuse, in *The Pneumatic Tire*, Eds., NHTSA U.S. Department of Transportation, Washington, DC, 2005, 670–691.
80. Sun, X.; Isayev, A.I. *Rubber Chem. Technol.*, 81, 19-46, 2008.
81. Isayev, A.I.; Huang, K. *Polym. Eng. Sci.*, 54, 12, 2715–2730, 2014.
82. Isayev, A.I.; Jenkins, J. *SPE ANTEC Technical Paper*, 53, 109, 2008.
83. Huang, K.; Isayev, A.I. *RSC Adv.*, 4, 73, 38877–38892, 2014.
84. Isayev, A.I.; Huang, K. *AIP Conf. Proc.*, 1713, 0300041-0300045, 2016.
85. Huang, K.; Isayev, A.I. *Polymer.*, 70, 290–306, 2015.
86. Huang, K.; Isayev, A.I.; Zhong, J. *J. Appl. Polym. Sci.*, 131, 17, 8506–8521, 2014.
87. Huang, K.; Isayev, A.I. *Polym. Eng. Sci.*, 57, 10, 1035–1046, 2017.
88. 88. Huang, K.; Isayev, A.I. *Polym. Eng. Sci.*, 57, 10, 1047–1061, 2017.
89. Isayev, A.I.; Yushanov, S.P.; Chen, J. *J. Appl. Polym. Sci.*, 59, 5, 803–813, 1996.
90. Isayev, A.I.; Yushanov, S.P.; Chen, J. *J. Appl. Polym. Sci.*, 59, 5, 815–824, 1996.
91. 91. Isayev, A.I.; Yushanov, S.P.; Kim, S.H.; Levin, V.Y. *Rheol. Acta*, 35, 6, 616–

- 630, 1996.
92. Yushanov, S.P.; Isayev, A.I.; Kim, S.H. *Rubber Chem. Technol.*, 71, 2, 168–190, 1998.
  93. Isayev, A.I.; Hong, C.K. Ultrasound assisted continuous process for making polymer blends and copolymers US6528554, 2003.
  94. Chen, G.; Guo, S.; Li, H.; *J. Appl. Polym. Sci.*; 86, 23–32, 2002.
  95. Kim, H.; Lee, J.W. *Polymer*, 43, 2585–2589, 2002.
  96. Kim, H.; Ryu, J.G.; Lee, J.W. *Korea-Aust Rheol J*, 14, 3, 121–128, 2002.
  97. Feng, W.; Isayev, A.I. *Polymer*, 45, 4, 1207–1216, 2004.
  98. Feng, W.; Isayev, A.I. *Polym. Eng. Sci.*, 44, 11, 2019–2028, 2004.
  99. Jiang, G.; Wu, H.; Xie, T.; Guo, S. *J. Appl. Polym. Sci.*, 112, 4, 2136–2142, 2009.
  100. Lin, H.; Isayev, A.I. *J. Appl. Polym. Sci.*, 102, 3, 2643–2653, 2006.
  101. Gunes, K.; Isayev, A.I.; Li, X.; Wesdemiotis, C. *Polymer*, 51, 5, 1071–1081, 2010.
  102. Gunes, K.; Isayev, A.I. *Polym. Sci. - Ser. A*, 52, 11, 1124–1136, 2010.
  103. Gunes, K.; Isayev, A.I. *J. Appl. Polym. Sci.*, 122, 1, 354–365, 2011.
  104. Isayev, A.I.; Ghose, S. Ultrasonic devulcanization of used tires and waste rubbers. In *Rubber Recycling*, CRC Press, Boca Raton, 2005.
  105. Hong, C.K.; Isayev, A.I. *Rubber Chem. Technol.*, 75, 1, 133–142, 2002.
  106. Isayev, A.I.; Tukachinsky, A. *Rubber Chem. Technol.*, 68, 2, 267–280, 1995.
  107. Isayev, A.I.; Liang, T.; Lewis, T.M. *Rubber Chem. Technol.*, 87, 1, 86–102, 2014.
  108. Kim, J.K.; Lee, S.H.; Hwang, S.H. *J. Appl. Polym. Sci.*, 90, 9, 2503–2507, 2003.
  109. Isayev, A.I.; Hong, C.K.; Kim, K.J. *Rubber Chem. Technol.*, 76, 4, 923–947, 2003.
  110. Chen, G.; Guo, S.; Li, H. *J. Appl. Polym. Sci.*, 86, 1, 23–32, 2002.



111. Chen, Y.; Li, H. *Polym. Eng. Sci.*, 44, 8, 1509–1513, 2004.
112. Liang, T.; Isayev, A.I. *Polym. engineering Sci.*, 60, 5, 925–934, 2020.
113. Liang, T.; Isayev, A.I. *Adv. Ind. Eng. Polym. Res.*, 2, 1, 13–24, 2019.
114. Oh, J. S.; Ghose, S.; Isayev, A.I. *J. Polym. Sci. Part B Polym. Phys.*, 41, 22, 2959–2968, 2003.
115. Liang, T.; Isayev, A.I. *J. Appl. Polym. Sci.*, 136, 18, 1–15, 2019.
116. Liang, T.; Isayev, A.I. *J. Elastomers Plast.*, 51, 7–8, 603–625, 2018.
117. Choi, J.; Isayev, A.I. *J. Elastomers Plast.*, 47, 2, 170–193, 2015.
118. Isayev, A.I. Single and twin screw extruders with ultrasound horns for decrosslinking and devulcanization, US10465059B2, 2019.
119. Isayev, A.I.; Swain, S.K.; Lapshin, S. Process for preparing polymer nanocomposites and nanocomposites prepared therefrom, US20100152325A1, 2010.
120. Lapshin, S.; Isayev, A.I. *J. Vinyl Addit. Technol.*, 13, 1, 40–45, 2007.
121. Isayev, A.I.; Lapshin, S. *J. Vinyl Addit. Technol.*, 12, 2, 78–82, 2006.
122. Lapshin, S.; Swain, S.K.; Isayev, A.I. *Polym. Eng. Sci.*, 1584–1591, 2008.
123. Halpin, J.; Kardos, J. *Polym. Eng. Sci.*, 16, 344–352, 1976.
124. Brune, D.A.; Bicerano, J. *Polymer.*, 43, 2, 369–387, 2002.
125. Zhao, L.; Li, J.; Guo, S.; Du, Q. *Polymer.*, 47, 7, 2460–2469, 2006.
126. Martínez-Colunga, J.G.; Sánchez-Valdés, S.; Ramos-deValle, L.F.; Muñoz-Jiménez, L.; Ramires-Vargas, E.; Ibarra-Alonso, M.C.; Lozano-Ramírez, T.; Lafleur, P.G. *J. Appl. Polym. Sci.*, 131, 16, 1–8, 2014.
127. Peng, B.; Wu, H.; Bao, W.; Guo, S.; Chen, Y.; Huang, H.; Lai, S.-Y.; Jow, J. *Polym. Eng. Sci.*, 52, 3, 518–524, 2012.

128. Ye, Y.; Qian, J.; Xu, Y. *J. Polym. Res.*, 18, 6, 2023–2031, 2011.
129. Lee, E.C.; Mielewski, D.F.; Baird, R.J. *Polym. Eng. Sci.*, 44, 9, 1773–1782, 2004.
130. Sohn, C.H.; Shim, D.C.; Lee, J.W. *Macromol. Symp.*, 249–250, 580–585, 2007.
131. Swain, S.K.; Isayev, A.I. *Polymer*, 48, 1, 281–289, 2007.
132. Li, J.; Jiang, G.J.; Guo, S.Y.; Zhao, L.J. *Plast. Rubber Compos.*, 36, 7–8, 308–313, 2007.
133. Martínez-Colunga, J.G.; Sánchez-Valdes, S.; Blanco-Cardenas, A.; Ramírez-Vargas, E.; Ramos-deValle, L.F.; Benavides-Cantu, Roberto, Espinoza-Martínez, A.B.; Sanchez-Lopez, S.; Lozano-Ramírez, T.; Lafleur, P.G.; Karami, S. *J. Appl. Polym. Sci.*, 135, 20, 1–10, 2018.
134. Isayev, A.I.; Swain, S.K. *J. Appl. Polym. Sci.*, 114, 4, 2378–2387, 2009.
135. Li, J.; Zhao, L.; Guo, S. *J. Macromol. Sci. Part B Phys.*, 46B, 3, 423–439, 2007.
136. García, L.; Castell, P.; Peinado, V.; Muniesa, M.; Fernández, A. *Mater. Res. Innov.*, 18, S285-S289, 2014.
137. Minaei-Zaim, M.; Ghasemi, I.; Karrabi, M.; Azizi, H. *Iran. Polym. J. (English Ed.)*, 21, 8, 537–546, 2012.
138. Kim, K.Y.; Ju, D.U.; Nam, G. J.; Lee, J.W. *Macromol. Symp.*, 249–250, 283–288, 2007.
139. Tan, H.; Isayev, A.I. *Rubber Chem. Technol.*, 81, 1, 138–155, 2008.
140. Peng, B.; Wu, H.; Bao, W.; Guo, S.; Chen, Y.; Huang, H.; Chen, H.; Lai, S.-Y.; Jow, J. *Polym. J.*, 43, 1, 91–96, 2011.
141. Kumar, R.; Isayev, A.I. *Polymer*, 51, 15, 3503–3511, 2010.
142. Choi, J.; Isayev, A.I. *Rubber Chem. Technol.*, 85, 1, 14–37, 2012.
143. Zhong, J.; Isayev, A.I.; Huang, K. *Polym. (U. K.)*, 55, 7, 1745–1755, 2014.
144. Ávila-Orta, C.A.; Quiñones-Jurado, Z.V.; Waldo-Mendoza, M.A.; Rivera-Paz, E.A.;

- Cruz-Delgado, V.J.; Mata-Padilla, J.M.; González-Morones, P.G.; Ziolo, R.E. *Materials.*, 8, 11, 7900–7912, 2015.
145. Zhong, J.; Isayev, A.I. *Polymer.*, 107, 130–146, 2016.
  146. Yang, L.; Zhang, Z.; Wang, X.; Chen, J.; Li, H. *J. Appl. Polym. Sci.*, 128, 3, 1510–1520, 2013.
  147. Blanco, M.; Sarasua, J.A.; Lopez, M.; Gonzalo, O.; Marcaide, A.; Muniesa, M.; Fernández, A. *Macromol. Symp.*, 321–322, 1, 80–83, 2012.
  148. Espinoza-Gonzalez, C.; Avila-Orta, C.; Martinez-Colunga, G.; Lionetto, F.; Maffezzoli, A. *IEEE Trans. Nanotechnol.*, 15, 5, 731–737, 2016.
  149. Gao, X.; Isayev, A.I.; Yi, C. *Polymer*, 84, 209–222, 2016.
  150. Gao, X.; Isayev, A.I.; Zhang, X.; Zhong, J. *Compos. Sci. Technol.*, 144, 125–138, 2017.
  151. Choi, J.; Isayev, A.I. *Rubber Chem. Technol.*, 84, 1, 55–73, 2011.
  152. Choi, J.; Isayev, A.I. *Rubber Chem. Technol.*, 86, 4, 633–652, 2013.
  153. Zhong, J.; Isayev, A.I. *J. Appl. Polym. Sci.*, 132, 5, 2015.
  154. He, S.; Zhang, J.; Xiao, X.; Hong, X. *Polym. Eng. Sci.*, 58, 3, 377–386, 2018.
  155. Jiang, X.; Drzal, L.T. *J. Appl. Polym. Sci.*, 124, 1, 525–535, 2012.
  156. Sanchez-Olivares, G.; Sanchez-Solis, A.; Calderas, F.; Medina-Torres, L.; Herrera-Valencia, E.E.; Castro-Aranda, J.I.; Manero, O.; Di Blasio, A.; Alongi, J. *Polym. Degrad. Stab.*, 98, 11, 2153–2160, 2013.
  157. Shen, K.K.; Kochesfahani, S.; Jouffret, F. *Polym Adv Technol*, 19, 6, 469-474, 2008.
  158. Chen, Y.; Li, H. *J. Appl. Polym. Sci.*, 97, 4, 1553–1560, 2005.



# 3.

## ULTRASONIC DEVICE FOR A POLYMER EXTRUDER MACHINE



# 3. ULTRASONIC DEVICE FOR A POLYMER EXTRUDER MACHINE

## 3.1 Introduction

An ultrasonic device comprising a chamber provided with an inlet bore, which receives a melted pressurized polymer, an outlet bore and a sonotrode housing bore through which a distal portion of an ultrasonic head is inserted into the chamber, wherein the distal portion is separated from the rest of the ultrasonic head by a first nodal plane (PN1) wherein there is a first surface (S1) in contact with a complementary surface of a ring seal that closes the chamber, and wherein the ultrasonic head includes a second nodal plane (PN2) away from and parallel to the first nodal plane (PN1) coinciding with or adjacent to a second surface (S2) wherein an anchoring device presses the ultrasonic head against the ring seal ensuring a tight closure.

## 3.2 Field and state of the Art

The present invention relates to the field of ultrasonic devices for a polymer - thermoplastic, for instance-extruder machine, wherein the ultrasonic device acts on the melted or re-softened polymer (with or without additives) to improve the properties and the quality of the obtained product.

Ultrasonic devices are known in the industry for the melting and fluidification of polymers, typically including an ultrasonic transducer generating ultrasonic vibration and an ultrasonic head that transmits said vibration.

The inclusion of a distal portion of an ultrasonic device is known within a chamber whereby the melted polymer enters in a pressurized condition, allowing the ultrasonic device to be brought into contact therewith. The feeding of the polymer to the chamber is carried out by means of an extruder apparatus provided with one or two helical conveyors that compress and melt said polymer, pushing it within the chamber, from which it is extruded through an outlet opening. For example, document US6528554B1 shows a solution of this type.

In this type of device, a distal portion of the ultrasonic device, distal relative to the ultrasonic transducer, is inserted within the chamber through a sonotrode housing bore.

To keep the melted polymer from being filtered through said sonotrode housing bore, a ring seal is arranged retained around a section of the ultrasonic head. To reduce the interference of the ring seal with the vibration of the ultrasonic head, said ring seal is attached in a proximal position to a nodal plane of the ultrasonic head.

It will be understood that the ring seal may or may not have a circular shape. Frequently, said ring seal keeps the ultrasonic head in a radial direction so that, in order to increase the contact surface between the ring seal and the ultrasonic head, the ring seal will cover adjacent areas of the nodal plane, where the vibration amplitude is not zero, causing the wear of said ring seal. Document EP1536936B1 shows a solution of this type.

In other alternative solutions, the ultrasonic head will be provided, coinciding with said nodal plane, with an annular projection in the shape of a flange surrounding it. The ring seal is attached above and underneath said flange retaining it and achieving a tight sealing. Document US6036467A, for example, shows a solution of this type.

However, said flange has a certain thickness and, therefore, its upper and lower surfaces, where the ring seal is attached, are not coplanar with the nodal plane, but are adjacent thereto; therefore, the vibration amplitude in those two planes will not be zero, but, being reduced, a certain vibration will exist that produces the deterioration of the ring seal over time. Additionally, the manufacturing of the ultrasonic head provided with said flange entails a complication and the increase in cost thereof.

### **3.3 Brief Description of the Invention**

The present invention relates to an ultrasonic device for an extrusion machine of melted or re-softened polymers (with or without additives) by means of an extruder apparatus.

It is understood that an ultrasonic device is a device comprising an ultrasonic transducer, which makes an ultrasonic head vibrate which, placed in contact with the melted polymer by means of the extruder apparatus, modifies its physicochemical properties by the effect of the vibration and of the heat generated by said vibration.

It will be understood that an extruder apparatus of a polymer is an apparatus intended to melt, mix and convey a polymer to the extrusion outlet. The inclusion of an ultrasonic device in contact with the melted polymer is also known in this type of apparatus, typically in a proximal position to the extrusion outlet bore, such that the polymer be treated by the



ultrasonic device before being extruded outside the extrusion machine, although it may also be located in other positions along the extruder apparatus.

In the present invention, the proposed ultrasonic device includes, in a manner known per se in the industry:

A chamber provided with an inlet bore for a melted pressurized polymer, provided with an outlet bore for the melted pressurized polymer, and provided with a sonotrode housing bore, said chamber being connectable or integrable in a polymer extruder apparatus which introduces the melted pressurized polymer through the inlet bore.

An ultrasonic head including at least one sonotrode, the ultrasonic head being provided with a distal portion and with a proximal portion separated by a first nodal plane, wherein the distal portion is totally constituted by said sonotrode and is introduced in the chamber through the sonotrode housing bore projecting in cantilever into the chamber, the distal portion being intended to remain in contact with the melted pressurized polymer contained in the chamber, and wherein the proximal portion, which is at least partially constituted by said sonotrode, remains outside the chamber and in connection with an ultrasonic transducer and includes at least a second nodal plane away from and parallel to the first nodal plane;

A ring seal in contact with the ultrasonic head in coincidence with the first nodal plane and the ring seal being configured to seal the sonotrode housing bore of the chamber containing the melted pressurized polymer.

It will be understood that the ring seal may be circular or have any other closed geometric shape.

The polymer extruder apparatus is a device that melts and pressurizes the resulting melted polymer into the chamber through the inlet bore, thus getting the chamber to be filled with the melted and pressurized polymer, which pushes it to exit through the outlet bore. The chamber may be located after the extruder apparatus or may be integrated in the extruder apparatus, said chamber remaining between two portions of the extruder apparatus or traversed by part of said extruder apparatus.

The ultrasonic device modifies the polymer properties before its extrusion, to ensure, for example, that there is no presence of pellets or non-melted particles and that its texture

is homogeneous before the extrusion, to improve the additive dispersion in the melted polymer, improve the mixing of polymers of different classes, improve productivity, reduce polymer degradation and even reduce the energy consumption of the machine.

The ultrasonic device consists of an ultrasonic transducer generating ultrasonic vibration, in contact with an ultrasonic head that transmits said vibration to the inner portion that is projected within the chamber where it remains in contact with the polymer.

Typically, the polymer extruder apparatus consists of an inlet for material in pellet or powder form on an end of the cylindrical fusion chamber, which contains one or two spindles, although other embodiments are also contemplated. In the apparatuses of this type, the rotation of the spindles compresses the polymer, conveys, kneads and mixes it with additives if there are any, being also liable to include heaters that increase the temperature of the polymer to favor its melting. The flow of melted polymer is introduced into the chamber that contains the distal portion of the ultrasonic head through an inlet bore for its treatment. Said chamber may be located at the end of the cylindrical fusion chamber of the extruder apparatus, or in an intermediate portion thereof, so that the one or more spindles go through said chamber of the ultrasonic device.

The melted polymer goes through the chamber of the ultrasonic device and exits therefrom through the outlet bore driven by the pressure applied thereon by the extruder apparatus, said polymer being then guided to a forming die where the polymer is extruded to the desired shape.

When the chamber of the ultrasonic device is connected to the end of the extruder apparatus, the forming die may be placed in the outlet bore of said chamber. If, on the contrary, the chamber of the ultrasonic device is integrated in an intermediate portion of the extruder apparatus, the polymer will be removed from said chamber by the extruder apparatus itself that will guide it to an outlet of the extruder apparatus connected to said forming die.

The ultrasonic head is provided with a distal portion, contained within the chamber, and with a proximal portion, arranged outside the chamber, the entire ultrasonic head being subjected to an ultrasonic vibration in the shape of a stationary wave.

In any body subjected to a vibration in the shape of a stationary wave, one or several planes are generated wherein the vibration is zero; these planes are known as nodal.

Between the distal portion and the proximal portion there is a first nodal plane, and the proximal portion of the ultrasonic head also includes a second nodal plane parallel to and away from the first nodal plane.

In the present case, the distal portion of the ultrasonic head is within the chamber, in contact with the melted pressurized polymer. To keep said melted polymer from flowing outside the chamber through the sonotrode housing bore of the chamber instead of through the outlet bore, a ring seal is arranged around the ultrasonic head, in coincidence with the first nodal plane where the vibration is zero. This keeps the ring seal from interfering with the vibration of the ultrasonic head, while avoiding the wear of said ring seal due to vibration.

The present invention proposes, in a way unknown to the state of the art, that:

- the first nodal plane be coplanar with a first annular surface of the ultrasonic head on which an annular surface of the ring seal rests parallel to the first surface.
- the second nodal plane be coplanar with or coplanar to a second surface of the ultrasonic head on which an anchoring device, in cooperation with a pressure device, applies pressure that is transmitted to the ring seal through the proximal portion of the ultrasonic head, producing a tight sealing of the chamber.

Thus, it is proposed that the ultrasonic head be provided with a first annular surface coplanar to the first nodal plane where, therefore, the vibration will be zero in all points of its surface, and with a second surface, annular or not, coplanar or adjacent to the second nodal plane. Therefore, said first and second surfaces are parallel to each other.

The second surface may be defined, for example, in an annular bulge in the shape of a flange around the ultrasonic head, or in an annular slot or step created in said ultrasonic head.

A pressure device will apply pressure on the second surface of the ultrasonic head through an anchoring device attached to or resting on said second surface of the

ultrasonic head where, thanks to its correspondence of or proximity to the second nodal plane, the amplitude of the vibration will be zero or reduced.

The pressure applied by the pressure device will be perpendicular to the first and second surfaces of the ultrasonic head and will push the second surface in the direction of the first surface.

The first surface of the ultrasonic head will be in contact with an annular surface of the ring seal and will be pressed against it thanks to the pressure applied by the pressure device, achieving a tight sealing between both surfaces that will not be affected by the vibration of the ultrasonic head, since the first surface coincides with the first nodal point and, therefore, the amplitude of the vibration is zero on all its surface.

According to an embodiment of the invention, the proximal portion of the ultrasonic head may be at least partially constituted, besides the sonotrode, by an ultrasonic amplifier sandwiched between the sonotrode and the ultrasonic transducer. In such a case, it is not recommended that the second nodal plane should coincide with the joint between the ultrasonic amplifier and the sonotrode, since greater stresses exist in this region that could damage the joint between both elements.

Alternatively, it is also contemplated that all of the proximal portion of the ultrasonic head be constituted by the sonotrode, no ultrasonic amplifier existing.

In any case, the distal portion of the ultrasonic head will have a smaller cross section than the proximal portion of the ultrasonic head, and in the transition between the smaller cross section distal portion and the larger cross section proximal portion, the first annular surface of the ultrasonic head, coinciding with the first nodal plane, will be defined.

It is also contemplated that a third annular surface be arranged around the sonotrode housing bore of the chamber in contact with another annular surface of the ring seal and opposite the first annular surface of the ultrasonic head.

In such a case, the ring seal will be a tubular body, not necessarily circular, retained between the first annular surface and the third annular surface thanks to the pressure applied by the pressure device, which will avoid the leakage of melted polymer through both gaskets.

The space contained between the distal portion of the ultrasonic head and the surrounding ring seal, which will be filled with polymer, will be considered to also form part of the chamber.

The third annular surface may define an annular seat configured to provide a precise positioning of the ring seal.

Preferably, the ring seal will be metallic or ceramic, which makes it much more resistant to high temperatures and to the vibration compared with other materials such as the majority of plastics. The use of metal or ceramic to form said ring seal is possible thanks to its contact with the ultrasonic head being produced exactly by the first nodal plane where the amplitude of the vibration is zero. Attaching the ring seal to any other surface of the ultrasonic head, even if it were in a position adjacent to the first nodal plane, would subject said ring to vibrations that require the use of materials with a certain degree of flexibility, such as some types of plastics or rubbers, but which, with vibrations and temperature, suffer from wear and cause leakages of melted polymer.

According to another embodiment, the ring seal defines an inner gap with a larger cross section than the cross section of the distal portion of the sonotrode, said cross section difference between both elements preferably being equal or lower than 2.5 mm.

This size difference allows the vibration of the distal portion in its interior without it interfering with the walls of the ring seal arranged surrounding it. Additionally, this space will form an annular duct in communication with the rest of the chamber, lengthening it, which will be filled with polymer. Within said annular duct, the vibration amplitude of the distal portion will be smaller the closer it is to the first nodal plane, getting to be zero. This means that the polymer contained in said annular duct will solidify in the area coinciding with the first surface of the ultrasonic head, cooperating with the sealing of the gasket, avoiding polymer leaks therethrough.

Said pressure device will include, according to a preferred embodiment, a number of connectors attached by one end to the anchoring device and by another end to a body that contains the chamber. The force applied by the connectors will compress the proximal portion of the ultrasonic head ensuring the correct sealing of the chamber. Preferably, the force produced by the pressure device will be adjustable.

An exemplary embodiment of the pressure device may consist of multiple bars arranged around the ultrasonic head, perpendicular to the first and second nodal planes, that serve as a guide for an axial displacement of the anchoring device, and a number of tightening devices that allow to apply an amount of stress to the ultrasonic head. The anchoring device may be, for example, a flat plate parallel to the first and second nodal planes with a hole to allow the passage of a part of the ultrasonic head therethrough supporting a peripheral part of said hole on the second surface of the ultrasonic head.

If said flat plate constitutive of the anchoring device included a number of through holes in its periphery through which the described bars could be inserted as part of the pressure device, said bars would be able to guide the axial displacement of the anchoring device. If, in addition, the bars were threaded and nuts were included as tightening devices, pressure could be adjusted to that the ultrasonic head adjusting said nuts is subjected to.

Other solutions are also contemplated, such as, for example, the use of pistons or springs.

It is also contemplated that the body that contains the chamber be formed by a single piece or by two or more coupled complementary half bodies. In the case of being formed by two or more half bodies, it is preferable that the inlet bore and the outlet bore be defined in the joining plane between both half bodies, being partially defined in one or the other of the two opposed half bodies, such that by separating said half bodies the interior of said inlet and outlet bores will be easily accessible, allowing the cleaning of any polymer remain that might be left.

Preferably, the sonotrode housing bore will be defined in one of said half bodies and the pressure device will also be attached to this half body, such that this half body, the ring seal, the anchoring device and the ultrasonic head form one joint assembly. This will allow to separate the two half bodies for cleaning or maintenance tasks of the interior of the chamber and of the bores without the need to uncouple the ultrasonic head from the half body to which it is attached.

Other characteristics of the invention will appear in the following detailed description of an exemplary embodiment.

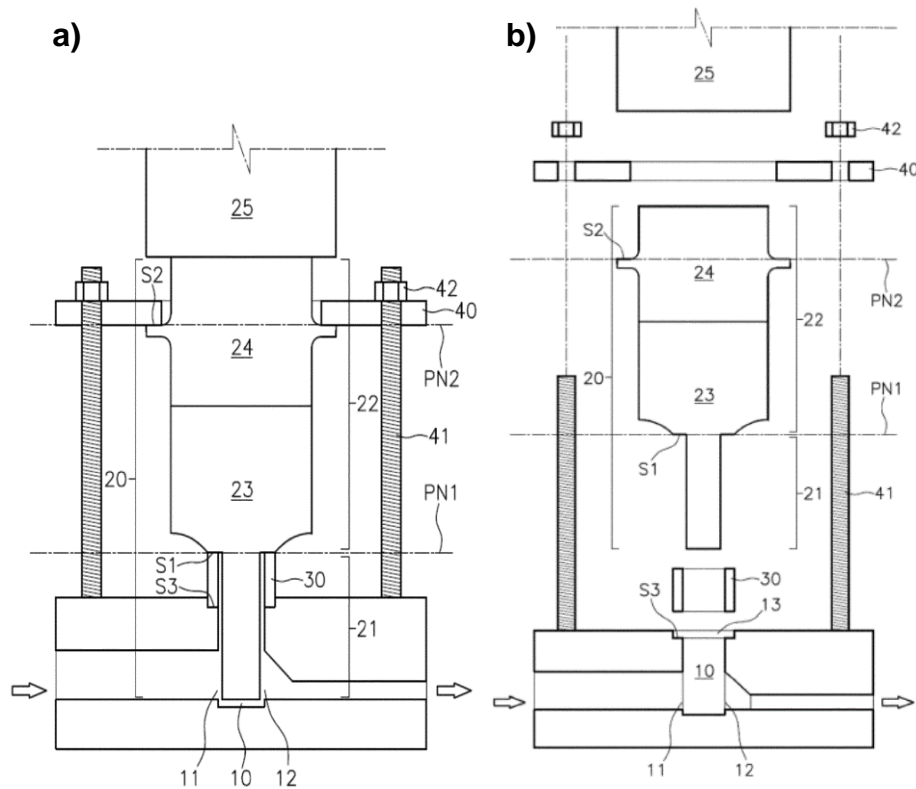


**Figure 3.1.** Ultrasonic system (a) and their exploded view (b). The components described: (10) Chamber, (11) Inlet bore, (12) Outlet bore, (13) Sonotrode housing bore, (20) Ultrasonic head, (21) Distal portion, (22) Proximal portion, (23) Sonotrode, (24) Ultrasonic amplifier, (25) Ultrasonic transducer, (30) Ring seal, (40) Anchoring device, (41) Pressure device, (42) Tightening device, (PN1) Nodal plane 1, (PN2) Nodal plane 2, (S1) Surface 1, (S2) Surface 2, (S3) Surface 3.

The foregoing and other advantages and characteristics will be more completely understood from the following detailed description of an exemplary embodiment with reference to the attached drawings, which must be taken by way of illustration and not limitation, wherein:

- a. shows a schematic cross section of the ultrasonic device wherein the polymer extruder apparatus is not shown but wherein the direction in which the melted polymer is displaced from said extruder apparatus to the outlet bore is indicated, by means of an arrow, shown in a simplified way
- b. shows the same ultrasonic device of but in an exploded view.

### **3.4 Detailed description of an exemplary embodiment**

The attached figures show exemplary embodiments with an illustrative non-limiting character of the present invention.

According to a preferred embodiment, the proposed ultrasonic device will be specially adapted for its use in a polymer extrusion machine (with or without additives).

Said extruder includes a polymer extruder apparatus that pressurizes the melted polymer into the chamber 10 through an inlet bore 11. Said chamber will be provided, in addition to inlet bore 11, with a sonotrode housing bore 13 and with an outlet bore 12 connected to a forming die that determines the geometry of the extruded polymer product produced by said extruder apparatus.

The inlet 11 and outlet 12 bores may be aligned or not aligned.

The polymer extruder apparatus includes, in this example, a cylindrical fusion chamber, which contains one or two spindles and a granular polymer inlet at the beginning of the cylindrical fusion chamber, although other embodiments are also contemplated. In the apparatus of this type, the rotation of the spindles compresses the polymer, conveys, kneads and mixes it with additives, if there are any, being also capable of including heaters that increase the temperature of the polymer to favor its melting. The melted polymer flow is introduced in the chamber that contains the distal portion of the ultrasonic head through an inlet bore 11.

Said chamber containing the distal portion of the ultrasonic head may be connected, through the inlet bore, at the end of the extruder apparatus, or, on the contrary, may be integrated in an intermediate portion of said extruder apparatus, such that the vibration produced by the ultrasonic head will be applied to the polymer contained in the extruder apparatus. In such an embodiment, the spindle, or the spindles, will preferably go through said chamber, although it is also contemplated that one or two spindles may be located before and one or two after said chamber.

The proposed ultrasonic device is formed by a vibration-generating ultrasonic transducer 25 in connection with an ultrasonic head 20 to which it transmits the generated vibration.



Said ultrasonic head 20 will be formed, in turn, by an ultrasonic amplifier 24 in direct contact with the ultrasonic transducer 25, and by a sonotrode 23 connected to said ultrasonic amplifier 24.

A distal portion 21 of the ultrasonic head 20, corresponding to a portion of the sonotrode 23, will be contained within the chamber 10 inserted projecting in cantilever into it through the sonotrode housing bore 13, said distal portion 21 remaining in contact with the pressurized melted polymer to which vibration is applied modifying its properties before exiting through the outlet bore 12 of the chamber.

The rest of the ultrasonic head 20 constitutes a proximal portion 22 that remains outside the chamber 10.

The ultrasonic transducers 25 typically generate a vibration in the shape of a sinusoidal wave that spreads in the ultrasonic head 20 in the shape of a stationary wave. Any body subjected to a stationary wave generates one or several nodal planes wherein the vibration amplitude will be zero at all times.

The proposed ultrasonic head 20 will be configured so that a first nodal plane PN1 is defined between the distal portion 21 and the proximal portion 22. This allows that, in correspondence of said first nodal plane PN1, a ring seal 30 may be arranged around the ultrasonic head 20, and in contact therewith, thus sealing the sonotrode housing bore 13, keeping the melted pressurized polymer contained in the chamber 10 from flowing towards the outside the chamber 10 therethrough.

Said ring seal 30 could affect the vibration of the ultrasonic head 20 or said vibration could affect the sealing produced by the ring seal 30. For this reason, it is proposed that the ring seal 30 consists of a tubular body through which the distal portion 21 of the ultrasonic head 20 is inserted, said tubular body being provided with an annular surface of the ring seal 30 parallel and coplanar to the first nodal plane PN1 of the ultrasonic head 20. The ultrasonic head 20 is also provided with a first annular surface S1 coplanar with the first nodal plane PN1 complementary with the annular surface of the ring seal 30.

In an assembled position, the ultrasonic head 20 is arranged with its first annular surface S1 resting on and in contact with the annular surface of the ring seal 30.

Said surfaces being coplanar with the first nodal plane PN1, the vibration amplitude on all points of said annular surface will be equal to zero, so that the sealing produced between both will not be affected by the vibration of the ultrasonic head 20.

The ultrasonic head 20 will also be configured to generate, in its proximal portion 22, a second nodal plane PN2 parallel to and separated from the first nodal plane PN1. Preferably, said second nodal plane PN2 will be away from the joint between the sonotrode 23 and the ultrasonic amplifier 24, to avoid subjecting said joint to excessive stresses that may damage the joining means, such as, for example, a threaded joint.

The ultrasonic head 20 will also be provided with a second surface S2 parallel to the first surface S1 and coplanar or adjacent to the second nodal plane PN2, such that the vibration amplitude in the second surface S2 will be zero or highly reduced.

The second surface S2 may be formed by multiple second partial surfaces, all of them coplanar to each other, forming an annular discontinuous surface, without this affecting the invention.

An anchoring device 40, which in this embodiment it is proposed to be a flat plate provided with a central through hole through which part of the ultrasonic head 20 goes, is placed resting on and in contact with the second surface S2, the periphery of said central hole remaining in contact with the second surface S2 of the ultrasonic head 20.

A pressure device 41 applies pressure to said anchoring device 40 in a direction perpendicular to the first and second nodal planes PN1 and PN2, which is transmitted to the ultrasonic head 20 through the second surface S2, compressing part of the ultrasonic head 20 against the ring seal 30, thus ensuring that the pressure of the melted polymer contained in the chamber 10 does not causes leaks through the joint of the ring seal 30 with the first surface S1 of the ultrasonic head 20. The pressure applied by the pressure device 41 will be greater than the pressure of the melted polymer of the chamber 10.

The arrangement of the first surface S1 and the geometry of the ring seal 30, together with the compression direction applied on the ultrasonic head 20, produces a sealing between the ultrasonic head 20 and the ring seal 30 in an axial direction of said ultrasonic head 20, instead of in a radial direction, as is common in the art.

In the present embodiment, the pressure device 41 consists of at least two bars parallel to each other and perpendicular to the first and second nodal planes PN1 and PN2 of the ultrasonic head 20 that have an end attached to a body that contains the chamber 10 and an end that traverses through holes of the anchoring device 40, allowing for the guidance of the anchoring device in an axial direction defined by the bars.

Said bars will preferably be threaded bars and will be provided with a number of nuts as a tightening device 42 that will allow to shift the anchoring device 40 towards the body that contains the chamber 10 compressing the sandwiched ultrasonic head 20. Alternatively, it is contemplated that the threaded bars may rotate, driven by a motor, for example, the nuts being attached to or integrated in the anchoring device 40.

It is also proposed that the ring seal 30 be an independent piece of the body that contains the chamber 10, thus facilitating its maintenance and replacement. In such a case, the body that contains the chamber 10 will be provided, around the sonotrode housing bore 13, with a third surface S3 parallel and opposite to the first surface S1 of the ultrasonic head 20, and the ring seal 30 will also have an annular flat surface configured to remain seated on the third surface S3, retaining the ring seal 30 between the ultrasonic head 20 and the body that contains the chamber 10. The pressure applied by the pressure device ensures that both gaskets of the ring seal 30 are sealed, avoiding the ejection of the melted polymer.

It will be understood that the different parts that constitute the invention described in an embodiment may be freely combined with the parts described in other different embodiments even if such a combination has not been explicitly described, provided that no prejudice exists in the combination.

### **3.5 Innovation of the invention**

A. An ultrasonic device for a polymer extruder comprising:

A chamber (10) provided with an inlet bore (11) for melted pressurized polymer, an outlet bore (12) for melted pressurized polymer, and a sonotrode housing bore (13), said chamber being connectable or integrable in a polymer extruder apparatus for the feeding of melted pressurized polymer to the inlet bore;

An ultrasonic head (20) including at least one sonotrode (23), the ultrasonic head (20) being provided with a distal portion (21) and with a proximal portion (22) separated by a first nodal plane (PN1), wherein the distal portion (21) is completely constituted by said sonotrode (23) and it is inserted in the chamber (10) through the sonotrode housing bore (13) projecting in cantilever into the chamber (10), the distal portion (21) being intended to remain in contact with the melted pressurized polymer contained in the chamber (10), and wherein the proximal portion (22), that is at least partially constituted by said sonotrode (23), remains outside the chamber (10) and in connection with an ultrasonic transducer (25) and includes at least one second nodal plane (PN2) away from and parallel to the first nodal plane (PN1);

A ring seal (30) in contact with the ultrasonic head (20) in coincidence with the first nodal plane (PN1) and the ring seal (30) being configured to seal the sonotrode housing bore (13) of the chamber (10) that contains the melted pressurized polymer;

Characterized in that the first nodal plane (PN1) is coplanar with a first annular surface (S1) of the ultrasonic head (20) on which an annular surface of the ring seal (30) rests parallel to the first surface (S1); the second nodal plane (PN2) is coplanar or adjacent to a second surface (S2) of the ultrasonic head (20), parallel to the first surface (S1), on which an anchoring device (40), in cooperation with a pressure device, applies pressure in a direction perpendicular to the first surface (S1) that is transmitted to the ring seal (30) through the proximal portion (22) of the ultrasonic head (20) producing a tight sealing of the chamber (10).

- A. A device according to claim 1, wherein the proximal portion (21) of the ultrasonic head (20) is at least partially constituted by an ultrasonic amplifier (24) sandwiched between the sonotrode (23) and the ultrasonic transducer (25).
- B. A device according to claim 2, wherein the second nodal plane (PN2) is away from the joint between the sonotrode (23) and the ultrasonic amplifier (24).
- C. A device according to claim 1, wherein the entire proximal portion (22) of the ultrasonic head (20) is constituted by the sonotrode (23).
- D. A device according to any of the previous claims, wherein the distal portion (21) of the ultrasonic head (20) has a smaller diameter than the proximal portion (22) of the ultrasonic head (20).

- E. A device according to claim 5, wherein a transition between the distal portion (21) of smaller diameter and the proximal portion (22) of larger diameter defines the first annular surface (S1).
- F. A device according to any of the previous claims, wherein the chamber (10) is provided with a third annular surface (S3) around the sonotrode housing bore (13) opposite the first annular surface (S1) of the ultrasonic head (20), and in contact with another annular surface of the ring seal (30), which a tubular body retained between the first annular surface (S1) and the third annular surface (S3).
- G. A device according to claim 7, wherein the third annular surface (S3) defines an annular seat configured to provide precise positioning of the ring seal (30).
- H. A device according to claim 7 or 8, wherein the ring seal (30) is metallic or ceramic.
- I. A device according to claim 7, 8 or 9, wherein the ring seal (30) defines an inner gap with a larger cross section than the cross section of the distal portion (21) of the sonotrode (20).
- J. A device according to any of the previous claims, wherein the pressure device includes a number of connectors attached by one end to the anchoring device (40) and by another end to a body containing the chamber (10).



# 4.

**POINT NODAL ULTRASONIC  
MOLDING OF POLYPROPYLENE: A  
TECHNOLOGY ABLE TO PREPARE  
MICROPIECES WITH HIGHLY  
REPETITIVE PROPERTIES AND  
GOOD MECHANICAL  
PERFORMANCE**





# **4. POINT NODAL ULTRASONIC MOLDING OF POLYPROPYLENE: A TECHNOLOGY ABLE TO PREPARE MICROPIECES WITH HIGHLY REPETITIVE PROPERTIES AND GOOD MECHANICAL PERFORMANCE**

## **4.1 Introduction**

It is well known that the oscillatory energy of a sonotrode can be transformed into a thermal energy able to heat and melt a polymeric material [1]. Ultrasound waves produce remarkable effects on the media through which they propagate, but there is still lacking a complete understanding of the physical process that occurs in the polymer melt [2]. Main issues correspond to the comprehension of bubble cavitation, the effect of viscous frictional forces on potential molecular chain scissions, and the relation between the polymer chemical structure and the vibrational motion under the applied ultrasonic waves. Despite the limitations caused by these uncertainties, ultrasonic waves have multiple applications that include conventional extrusion and injections processes assisted by ultrasounds [3,4] and the welding of polymers [5].

Ultrasonic energy has more recently been applied to develop a new micro-molding technology, which is still under development but has potential advantages over conventional and well-established processing technologies guided to the production of miniaturized pieces as it is the case of microinjection [6]. This ultrasonic molding technology (USM) has been demonstrated to be able to process with minimum molecular degradation the biodegradable polylactide (PLA) [7,8], which is the bioplastic with the highest volume consumption in the world. Furthermore, other highly consuming thermoplastics have been evaluated (e.g., polyamides [9] and polypropylene [10]) with rather promising results. The USM technology has also been successfully applied to get homogeneous dispersions of drugs like triclosan [11], silica nanospheres [12], exfoliated clay nanoparticles [13,14] and multiwalled carbon nanotubes [15], and more recently to prepare porous scaffolds [10,16].

The chemical structure of the polymer and even of the added compounds had a great influence on the USM processability. Thus, evidence of molecular degradation was observed for poly (butylene succinate) (PBS) [13] or when chlorhexidine was incorporated as a pharmacologic active compound [11]. In these cases, it was necessary a careful selection of the processing parameters, which were only valid within a very narrow window. An additional problem of the first USM prototypes was the lack of a perfect repeatability of the properties of molded specimens. This feature is obviously a limitation for industrial applications and depends on the susceptibility of the polymer to experiment a molecular degradation (e.g., low for PLA and high for PBS).

Application of USM has also great interest to get miniaturized pieces from other commodity polymers like propylene (PP). The technique was found in this case very effective and even gave better results than using the more conventional microinjection technology [10]. However, a small repeatability in the mechanical behavior of the molded specimens was found. Main reasons were attributed to the inhomogeneous thermal and rheological properties of the melt that led to a non-repetitive filling of the mold, the sustainment of the ultrasound vibration during filling and packing phases that led to high temperature, and temperature peaks that were detected close to the injection location [10].

The design of the sonotrode geometry (shape, frequency, resonant length, and gain) is fundamental for the transfer of maximum energy and avoid the occurrence of vibrations with different frequency that could lead to energy loss and even damage of the acoustic unit (sonotrode and booster) at the interface surfaces [17].

Under the resonance undulatory condition the amplitude of the sonotrode vibration has a sinusoidal variation along its length. For molding applications half-wave stepped sonotrodes are usually applied. These have a length that corresponds to the half of the acoustic wavelength ( $\lambda$ ) of the sonotrode when a perfect cylinder geometry is selected (i.e., a more precise calculation by numerical methods is required for other geometries). The gain of the sonotrode corresponds to the ratio between the input and output amplitudes (i.e., the longitudinal vibrations at the beginning and at the end of the sonotrode). It is obvious that there is a plane (i.e., that is located at a distance of  $\lambda/4$  from the sonotrode ending surface for a cylinder geometry) where the longitudinal vibration is equal to zero. This specific position of the sonotrode is named nodal plane or nodal point and it is the basis of a new ultrasound micromolding prototype [18]. Basically, the mold

feed channels are placed to face the sonotrode nodal point (i.e., the zone without longitudinal vibration), a feature that was found highly efficient to get a great repeatability of the properties of polymethylene oxide processed specimens [18].

The present work has a main goal the study of the USM processing of PP using the nodal point technology and its comparison with the results attained with former USM technologies. Special attention will be paid to the stress-strain tests since probably they are those most sensitive to physical and chemical defects of processed specimens. Furthermore, these tests reflect the behavior of the global piece and not of the local fragments used, for example, in the evaluation of thermal properties. It is also clear the interest to develop a micromolding technology able to process PP, which is a polymer that accounts for approximately the 20% world plastic demand.

## 4.2 Experimental section

### 4.2.1 Materials

The Polypropylene (PP) used in this study, is a commercial polymer Hostacom PPU X9067HS from Lyondellbasell (Wilmington, USA). The commercial polymer is characterized by its very high stiffness and toughness that make an ideal material for automotive parts. The PP polymer has a melt flow index of 15 g/10 min (measured at 230°C with 2.16 Kg according to the ISO 1133 standard).

### 4.2.2 Ultrasonic micro-molding

Ultrasound micro-molding equipment is characterized by several basic elements (**Figure 4.1**): a) Electric generator with a controller able to regulate the processing parameters, b) Piezoelectric transducer that converts the electric signal to a mechanical vibration, c) Acoustic unit doted of a booster able to amplify or reduce the wave amplitude and a sonotrode that transfers the mechanical vibration energy to the polymeric material, d) sonotrode e) Dosing unit to introduce the desired number of pellets into the plasticizing camera, and f) Mold with the corresponding feed channels and ejectors.

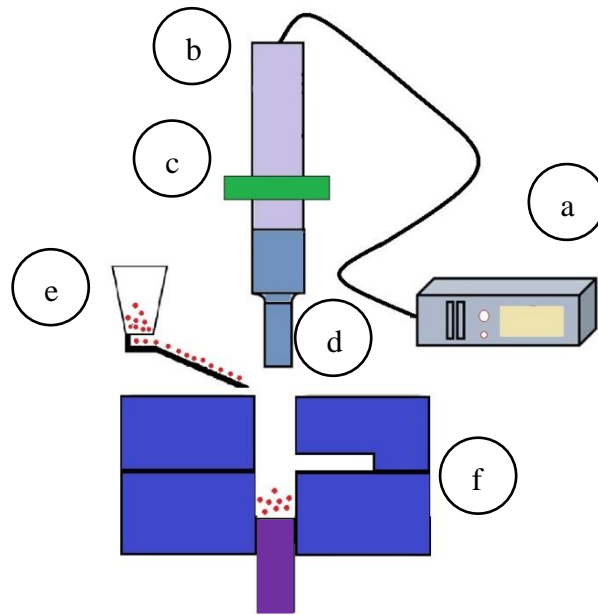


**Figure 4.1.** Scheme illustrating the main components of first USM prototypes.

**Figure 4.2** shows the different processing steps according to the basic scheme of first USM prototypes (e.g., Sonorus 1G):

- 1) Load of the polymer in a pellet form by the dosing system that provides a specified number of pellets. The sonotrode is in an upper position to facilitate the dosage inside the plasticizing camera, and the mold in the close position.
- 2) The sonotrode comes down until it becomes in contact with the introduced pellets. Immediately, it starts to vibrate with the specified amplitude and residence time, while acts as a plunger that applies the specified pressure to the sample. This pressure firstly allows to compact the polymer and then provoke the flow of the polymer, once it has been melted due to the sonotrode vibration energy, towards the mold through the feed channels.
- 3) Cooling of the mold once it has been filled and stopping of the sonotrode vibration.

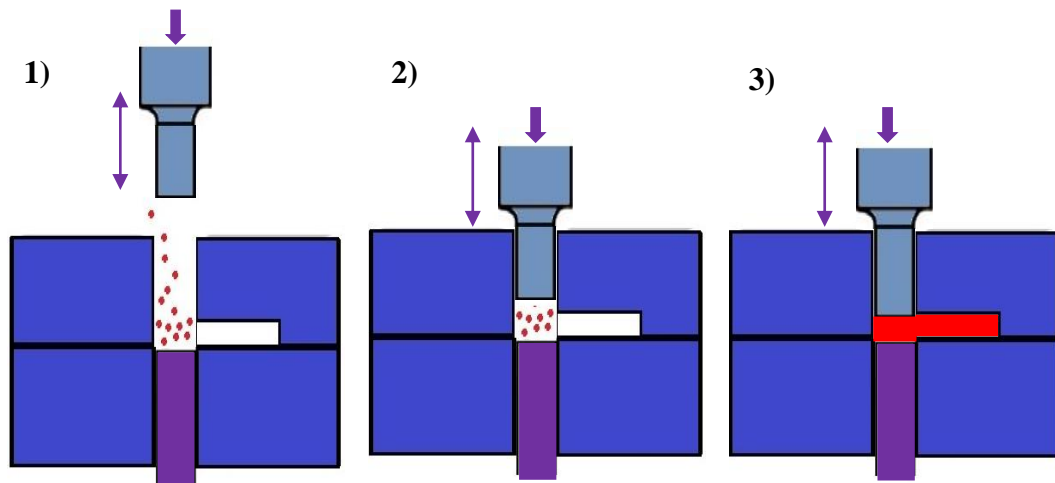


**Figure 4.2.** Scheme showing the main steps of a USM process.

Operational parameters that should carefully selected for a given polymer and molding geometry correspond to the amplitude of the ultrasonic wave (i.e., the applied energy), the applied pressure and the residence time. Advantages of the technology are the low amount of polymer required for molding, the low loss of material in both sprue and running channels, the ability to perform the molding process in a time so short as 0.5 s (i.e., the short residence time to high temperature), the great resolution of the molded specimens (i.e., specimen details of 200 nm can be visualized, **Figure 4.3**), the effect of the ultrasound waves to facilitate the flow of the polymer melt, and finally the capability of incorporation nanoparticles, drugs, plasticizers and other compounds.

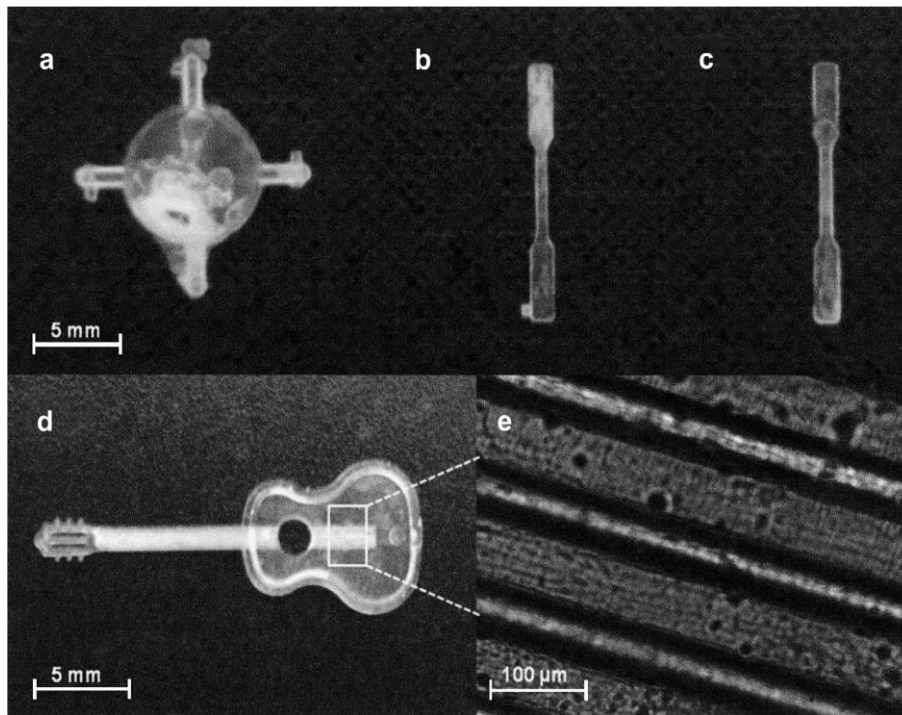


**Figure 4.3.** Ultrasound micro-molded polypropylene specimen where the high resolution of the processing technology is highlighted by the capacity to distinguish guitar strings with a thickness of only 70  $\mu\text{m}$ . Reproduced from [8]

### Point nodal ultrasound USM configuration

- a) The point nodal configuration was applied to the new Sonorus 2G prototype, which also incorporated other modifications that were designed to improve final performance. Basically, the following changes were made.
- b) In order to minimize the formation of burrs in the molding unit, the equipment was provided with a robust clamping unit that was able to deliver a 150 kN.
- c) A perfectly sealed plasticizing camera dotted with bushing gaskets to fix the position of the sonotrode.
- d) An additional plunger, which in this case provided the pressure necessary to compact the polymer and induce the flow of the polymer melt (note that these functions were carried out by the sonotrode in the previous version).
- e) An appropriate design that faces up to nodal plane of the sonotrode with the feeding channel.

**Figure 4.4a** shows the characteristic parts of the Sonorus 2G micromolding machine, while the main processing steps are illustrated in **Figure 4.4b**. Note that after the dosage step, the sonotrode descends from its elevated position (loading position) to that in which its nodal plane faces up the feeding channel. This movement implies a small compaction of the loaded pellet. Nevertheless, the plunger in the element that applies the final pressure while it is moving to its upper position. The compacted pellets become in close contact with the sonotrode ending surface and melts under the energy transmitted by the mechanical vibration. Note that the control parameter to the packing step is not the pressure, but the velocity of the plunger. The control system can detect the change on the pressure due to the velocity of the plunger, and then stars a packing pressure (similarity to the conventional injection molding and the screw of injection).

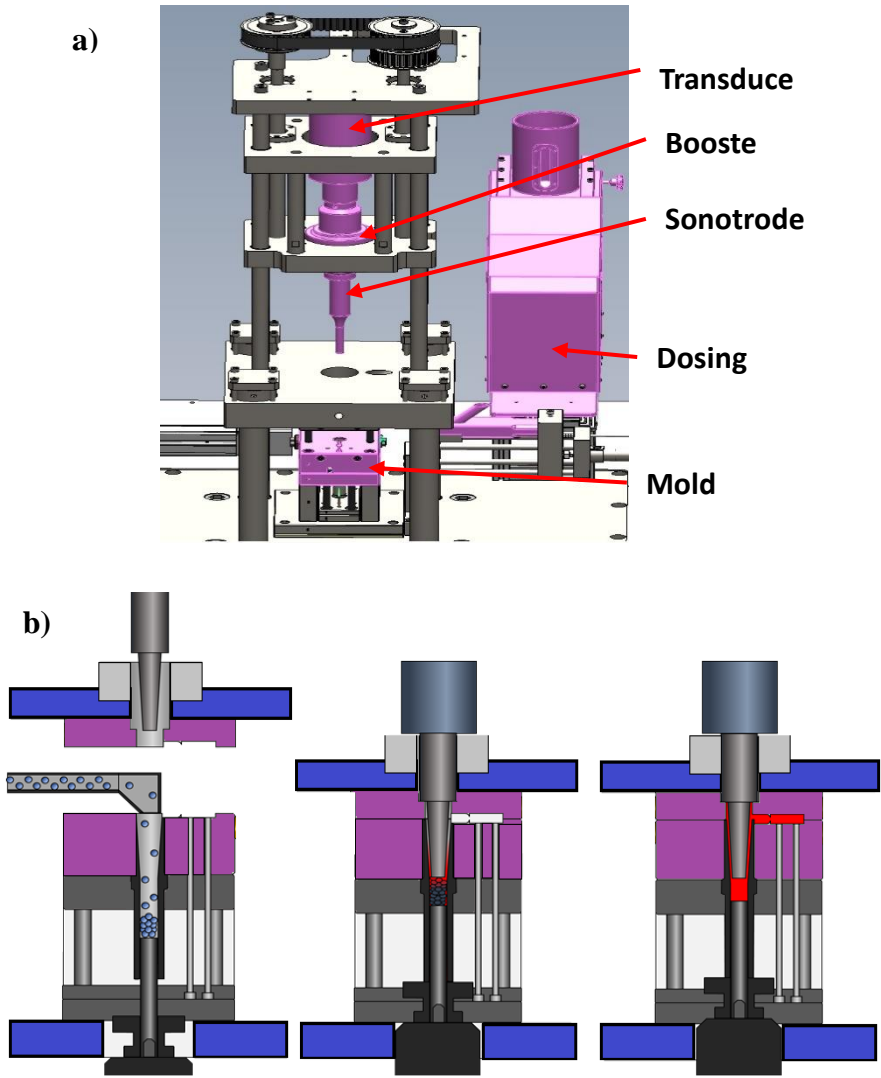


**Figure 4.4.** a) Scheme showing the main parts of a micro-molding equipment dotted with the point nodal configuration. b) Main processing steps required for ultrasound micromolding using the nodal point approach.

## USM equipment

The USM experiments without a nodal point approach were performed with Sonorus 1G (Ultrason S.L., Barcelona, Spain), based on a controller, a transducer, a pneumatic pressure system, a thermally controlled mold and an acoustic unit. The controller (1000W - 30 kHz digital ultrasound generator from Mecasonic fitted with a 3010 DG digital system) regulates the oscillation time, molding pressure and amplitude of the ultrasonic wave. The transducer (Mecasonic) converts electrical energy into kinetic energy and creates undulatory movement. The pneumatic pressure system (Ultrason S.L.) applies a constant molding pressure (0–6 bar) to the material while ultrasound is generated by the sonotrode tip.

USM experiments were also performed with the Sonorus 2G<sup>®</sup> prototype (Ultrason S.L., Barcelona, Spain). The USM apparatus was equipped with a Branson<sup>®</sup> DCX 30 kHz ultrasonic generator (1500 W), a converter from Branson<sup>®</sup> model CR 30 kHz at 1500W max, a focused Langevin piezoelectric transducer that can deliver 15 $\mu$  of peak-to peak amplitude when it is working at 100% of gain, a green booster 1:1 (amplitude ratio) from Branson<sup>®</sup>, a sonotrode operating in longitudinal vibration mode designed by Eurecat, an electric servomotor control (Berneker and Rainer) with software from Ultrason S.L. (Barcelona, Spain) and a thermally controlled mold. This mold was designed to prepare one test specimens of dimensions 3.5 cm  $\times$  0.6 cm  $\times$  0.1 cm (tested zone 1.2 cm  $\times$  0.2 cm  $\times$  0.1 cm) and equipped with and ejection system to easily release the molded sample.

### 4.2.3 Optimization of the processing parameters

To define the optimal process window for each equipment, different parameters were evaluated. Depending on the equipment, a procedure to reach the optimal configuration change. For the Sonorus 2G, the velocity and the ultrasonic amplitude are the main parameters to change in order to achieve the optimal point. The design of experiments was performed with a previous simulation with a specific software to design the “seal” (new component designed for the nodal point approach). On the hand, most extensive empirical study should be done without the nodal point and the Sonorus 1G. It is needed to find an appropriate energy and molding force to fill the mold. In this case, the pressure is a variable parameter. For both approaches, twenty microsamples were obtained to carry out the tensile tests (the first 5 injected specimens are discarded).



#### 4.2.4 Measurements

Tensile deformation tests were performed using the Zwick Roell Z050 Universal Tester (Barcelona, Spain) equipped with a cell charge of 500 N and testXpert 8.1 software (Zwick, Ulm, Germany) under UNE EN 527 at a velocity of 50 mm/min. Ten specimens were tested for each processing condition.

The fluidity of processed specimens was tested with the Modular Flow Index equipment from CEAAT, according to the ISO 1133 standard with the test conditions of a polypropylene, weight 2.160 Kg and temperature of 230 °C.

### 4.3 Results and discussion

#### 4.3.1 Rheology

Measures of viscosity were performed to evaluate a possible degradation of the tested materials. The material before the process of injection molding were measured at at 230°C with 2.16 Kg according to the ISO 1133 standard, with a result of 15 g/10 min. The measures of didn't show a significant difference with the raw material 18 g/10min and 19.5 g/10min, for Sonorus 2G with nodal point and Sonorus 1G respectively.

On the other hand, in order to evaluate the most aggressive condition of the Sonorus 2G, a MFI (melt flow index) measurements were obtained for samples injected in optimal conditions (16 mm/s) and for samples in non-optimal conditions reducing drastically the velocity of the plunger, that difficult the filling step (2 mm/s). For the last case, a degradation level can be observed with a visual inspection, that is confirmed by the rheology measurements 46,981 g/10min versus 18 g/10min.

#### 4.3.2 Mechanical properties

The results of the tensile test shown a similar behavior in the first zone of the curve as shown in **Figure 4.5** (inset). In general terms, the mechanical tests reveal an improved and stabilized behavior for the samples performed with the nodal point approach with the Sonorus 2G equipment. **Table 4.1** summarize the values obtained with each technology, where it can see that the difference of stability during the tensile test. The main difference can be reported on the Elongation at break (Eb) and the tensile strength (TS) that has the 2G with nodal point, 733 vs 307 % and 37.7 vs 28.8 MPa respectively.

The ultrasonic energy has different effect for the same polymer following the approach and the processing conditions. It is needed a deepest research to understand the mechanical test results and this change of the behavior of the material.

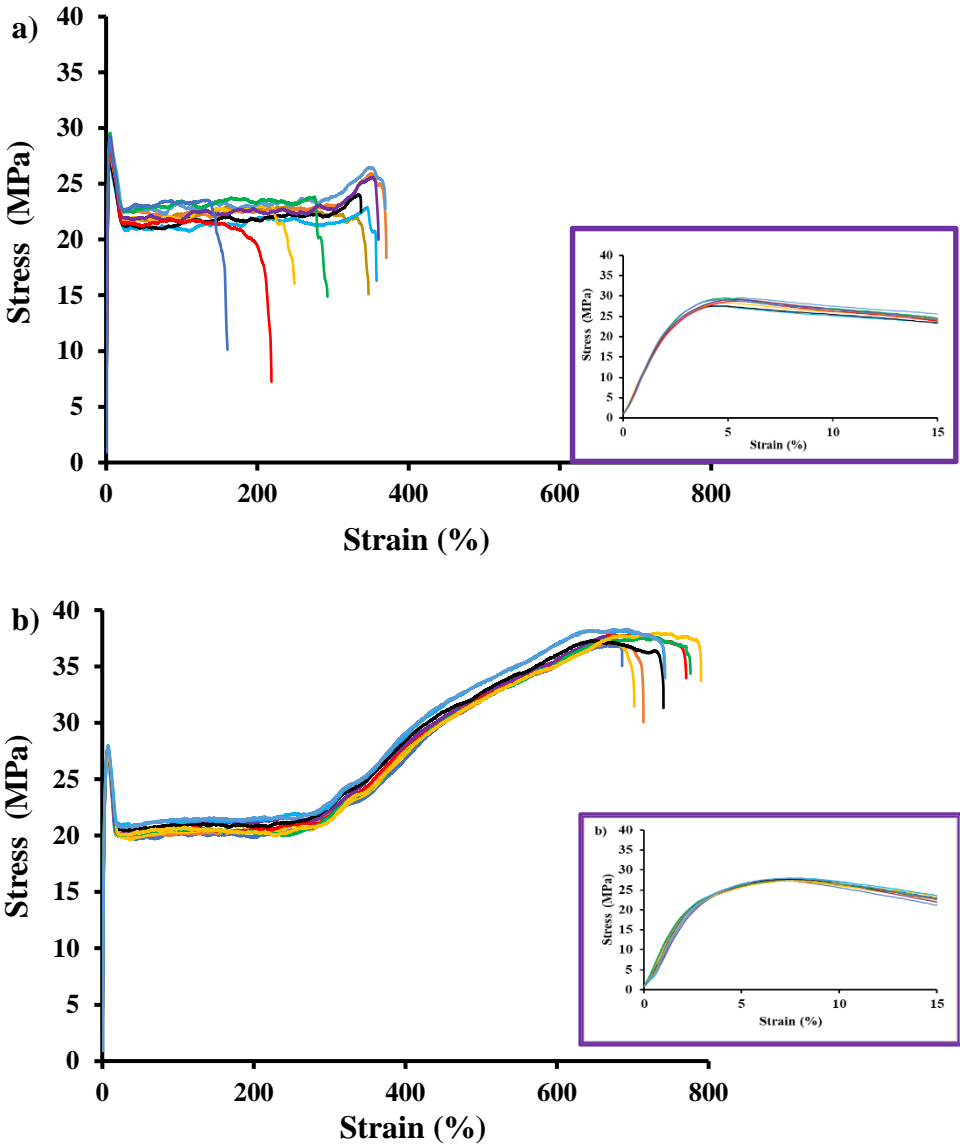


**Figure 4.5.** Tensile test curves a) Sonorus 1G b) Sonorus 2G with nodal point approach.

**Table 4.1.** Mechanical properties of samples obtained by Sonorus 1G and Sonorus 2G with nodal point approach.

Sample	YM (MPa)	TS (MPa)	Eb (%)
Sonorus 1G	1106 ±45	28.8 ± 0.8	307 ± 74
Sonorus 2G	969 ±28	37.7 ± 0.5	733 ± 40

## 4.4 Conclusions

The ultrasonic molding technology have been proved as an optimal technology to obtain microsamples with improved properties. Several studies proven the potential of this technology in different fields an application (medical, pharma, optics, etc.). A preliminary comparison between the USM technology with the USM considering the nodal point was carried out in order to evaluate the possible changes in the material. The tensile test reveals that an increase in the stabilization was reached with an improvement on the tensile strength and the elongation at break. Moreover, the samples performed with USM nodal point technology revealed a new behavior of the material that allows to have a higher value of strength while the sample is stretching.

More tests are needed to understand the new phenomena that improves the properties and the effect on the molecular structure of the polymer.

## 4.5 References

1. D. Ensminger, D.; Stulen, F.B. *Ultrasonics: Data, Equations and Their Practical Uses*, CRC Press, 2008.
2. Ávila-Orta, C; Espinoza-González, C.; Martínez-Colunga, G.; Maffezzoli, A.; Bueno-Baqués, D.; Lionetto, F. *Adv. Polym. Tech.* 32, 1, E582–E602, 2012
3. Isayev, A.I.; Kumar, R.; Lewis, T.M. *Polymer*, 50, 1,250–260, 2009.
4. Yang, Y.J.; Huang, C.C.; Lin, S.K.; Tao, J. *J. Polym. Eng.* 34, 7, 673–681, 2014.
5. Benatar, Ultrasonic welding of advanced thermoplastic composites, Massachusetts Institute of Technology, 1987.
6. Sortino, M.; Totis, G.; Kuljanic, E. *Procedia Eng.* 69, 1296–1305, 2014.
7. Ceresana. Bioplastics - Study: Market, Analysis, Trends - Ceresana. [www.ceresana.com](http://www.ceresana.com). Archived from the original on 4 November 2017. Retrieved 9 May 2018.
8. Sacristán, M.; Plantá, X.; Morell, M.; Puiggali, J. *Ultrason. Sonochem.* 21, 1, 376–386, 2014.

9. Grabalosa, J.; Vazquez, E.; Ferrer, I.; Elias-Zúniga, A.; Rivillas, F. Proceedings of the 2nd International Conference on Design and Processes for Medical Devices 52–56, 2014.
10. Masato, D.; Babenko, M.; Shriky, B.; Gough, T.; Lucchetta, G.; Whiteside, B. *Int. J. Adv. Manuf. Technol.* 99, 1-4, 113–125, 2018.
11. Olmo, C.; Franco, L.; del Valle, L.; Puiggali, J. *Appl. Sci.*, 10, 3106-3127, 2020.
12. Díaz, A.; Casas, M.T.; Puiggali, J. *Appl. Sci.* 5, 4, 1252–1271, 2015.
13. Planellas, M.; Sacristán, M.; Rey, L.; Olmo, C.; Aymamí, J.; Casas, M.T.; del Valle, L.J.; Franco, L.; Puiggali, J. *Ultrason. Sonochem.* 21, 4, 1557–1569, 2014.
14. Díaz, A.; Franco, L.; Casas, M.T.; del Valle, L.J.; Aymamí, J.; Olmo, C.; Puiggali, J. *J. Polym. Res.*, 21, 584, 2014.
15. Olmo, C.; Amestoy, H.; Casas, M.T.; Martínez, J.C.; Franco, L.; Sarasua, J.-R.; Puiggali, J. *Polymers*, 9, 322-339, 2017.
16. Olmo, C.; Franco, L.; del Valle, L.J.; Puiggali, J. *eXPRESS Polym. Let.*, 15, 389-403, 2021.
17. Tadvi, M.; Pandey, A.; Prajapati, J.; Shah, J. Conference Proceedings: International Mechanical Engineering Congress & Exposition. 2016, IMECE 2015-53023.
18. Janer, M.; López, T.; Planta, X.; Riera, D. *Ultrasonics*, 114, 106418, 2021.

# 5.

**ULTRASONIC MOLDING OF  
POLY(3-HYDROXYBUTYRATE): A  
HIGH-RESOLUTION PROCESS TO  
GET MICROPIECES WITH MINIMUM  
MATERIAL LOSS AND  
DEGRADATION**



# 5. ULTRASONIC MOLDING OF POLY(3-HYDROXYBUTYRATE): A HIGH-RESOLUTION PROCESS TO GET MICROPIECES WITH MINIMUM MATERIAL LOSS AND DEGRADATION

## 5.1 Introduction

Poly(3-hydroxybutyrate) (P3HB) is the shortest chain length member of the polyhydroxyalkanoate family and has a great interest due to its high potential for biomedical and packaging applications. P3HB can be considered a bio-based polymer since it is mainly obtained by bacterial fermentation from *Ralstonia eutropha* using a propionate rich medium as a carbon source [1]. Although, the 3-hydroxybutyrate unit has a chiral center, only one optically active form is produced by bacteria and therefore the polymer has a perfect configuration that allows to reach a high degree of crystallinity above 50%) [2]. P3HB has a glass transition temperature close to 10 °C, and similar mechanical properties but higher hydrophilicity than commodity polymers such as polyethylene and even polyethylene terephthalate. The easy production, low cost, promising properties, natural origin, and especially biodegradability and biocompatibility of P3HB are the main reasons to insist on the development of materials based on P3HB including blends and copolymers including 3-hydroxybutyrate units. These derivatives try to avoid the major drawbacks of the neat P3HB (i.e., high stiffness caused by its rigid molecular chain and low degradation rate and slow resorbability caused by its high degree of crystallinity) and render materials able to replace the more conventional fossil-based polymers. An added problem of P3HB is the ageing phenomena that can easily take place at room temperature and causes a remarkable recrystallization with the consequent negative impact in the reduction of the elongation at break [3].

P3HB has a high melting temperature of approximately 170 °C, which unfortunately is were reported at 222.8 °C and after a treatment for 8 h at 160°C, respectively [4-6]. Processing in the molten state of P3HB (e.g., by means of typical twin-screw extruders) led to a significant thermal degradation due to the high temperature, shear stress and pressure at which the polymer is submitted during an appreciable period [7]. Therefore, the polymer is hard to process and only a narrow window for the processing conditions is

available. This feature together with the above indicated issues clearly limited its application and fail to meet most of the industrial demands [8]. Processing difficulties have been tried to solve by adding plasticizers, by modifying the polymer structure and even by blending [9-11].

Properties of materials can be easily improved by adding nanoclays able to render intercalated or exfoliated structures [12]. The use of organomodified nanoclays is recommended to enhance their compatibility with hydrophobic polymers. Usually, quaternary ammonium salts are selected as most efficient surfactants, but their use is problematic in the case of P3HB nanocomposites since thermal degradation is increased under the usual preparation conditions (i.e., molten state, and high temperature) [13]. Different studies reported the effect of nanoclays on P3HB properties. Thus, montmorillonites modified with tributylhexadecylphosphonium bromide rendered intercalated structures from both casting and extrusion that slowed the degradation rate [13]. Nanocomposites of P3HB with Cloisite 30B showed a decrease of both glass transition temperature and melting temperature (i.e., 7 °C and 15 °C, respectively, for a weight clay content of 3%) together with a slight and remarkable increase of crystallinity (i.e., 3%) and degradation temperature (i.e., 11 °C), respectively [13]. Results point out a plasticizer effect of the intercalated clay and an improvement of processability derived from the higher difference between melting and decomposition temperatures [5].

The application of high-power ultrasound waves has recently been demonstrated as an efficient technology to get micro-molded specimens [14]. Application of ultrasound waves has previously been demonstrated to be efficient to facilitate conventional injection and extrusion processes and also as welding process for polymers [15-17]. Ultrasonic micro-molding (USM) is still in a development phase for industrial applications but appears as a promising alternative to conventional micro-injection [18]. Sectors like biomedical, electronic and telecommunications are expected to be benefited with this new molding process that offers clear advantages over conventional processes. It should be mentioned for example an extremely short processing time (note that a reduction of the residence time may minimize thermal degradation effects), capacity of the material to flow at lower temperatures (ultrasound waves decrease the polymer viscosity), high spatial resolution, energy saving and reduced loss of material in the sprues and the plasticizing camera [19]. USM has been demonstrated to be efficient for processing polylactide [14], polypropylene [20] and polyamides [21] with a minimum molecular weight loss, and even



a scarce degradation as it is the case of the biodegradable poly (butylene succinate) [22]. Furthermore, polymer matrices can be homogeneously loaded with pharmacological compounds [23], carbon nanotubes [24] and glass nanoparticles [25]. Cautions should be taken to minimize degradation depending on the polymer matrix and the functional groups of the selected drug. More interestingly, homogeneous dispersions can also be attained when USM is applied to get clay nanocomposites [22,26]. Indeed, exfoliated structures can be obtained in some cases using the pristine clay (i.e., without performing an organic modification) [22,26].

The present work has two main goals that try to give a new solution to process P3HB: a) To explore the applicability of USM to get P3HB molded specimens. It is expected that minimum polymer degradation should be produced due to the short residence time to high temperature, the peculiar heating process (i.e., conversion of a mechanical energy to a thermal energy by dissipation of the sonotrode oscillatory energy through the polymer that is in close contact), and the easy melt flow. b) To study the preparation of P3HB based nanocomposites. The incorporation of clays should facilitate processing, as above indicated, while some material properties are expected to be improved.

## 5.2 Experimental section

### 5.2.1 Materials

The P3HB sample used in this study is a commercial product (P304) supplied by Biomer (Krailling, Germany). It is a high crystalline and linear reference (60-70 % crystallinity), which liquify when heated and freeze when cooled, with a fast crystallization between 80 °C and 100 °C, and slow crystallization speed below 60 °C and above 130 °C. Due to the melting behavior, it is not possible to measure its melt flow index under the established conditions for PHA's.

Two different nanoclays were investigated: Cloisite 116, a natural bentonite, and Cloisite 20, a natural organic montmorillonite modified with dimethyl dihydrogenated tallow quaternary ammonium cations (**Table 5.1**). Both clays were provided by BYK Chemie GmbH (Wesel, Germany) and used as received.

**Table 5.1.** Properties of the selected nanoclays.

Name of clay	Structure of surfactant	Cation Exchange capacity	$d_{001}$ (Å)	Typical Dry Particle Size	Packed Bulk Density	Density
Cloisite 20	$\begin{array}{c} \text{CH}_3 \\   \\ \text{CH}_3 - \text{N}^+ - \text{HT} \\   \\ \text{HT} \end{array}$	95 meq/100g Clay	31.6	<10 $\mu\text{m}$ (d50)	175 g/L	1.77 g/cm <sup>3</sup>
Cloisite 116	---	116 meq/100g Clay	12.5	<15 $\mu\text{m}$ (d50)	340 g/L	2.80 g/cm <sup>3</sup>

Nanocomposites will be named indicating the abbreviations of the polymer, the wt.% of the added nanoclay and the abbreviation of the nanoclay (e.g., P3HB5C20 is the P3HB nanocomposite containing 5 wt.% of the C20 clay).

### 5.2.2 Nanocomposite preparation: compounding extrusion of P3HB

A conventional co-rotating twin screw extruder ZSK 18 MEGAlab from Coperion was used to obtain the nanocomposites. The equipment has an outer diameter ( $D_a$ ) of 18 mm and a  $D_o/D_i$  of 1.55 with a two co-rotating screw designed to improve the filler/additive dispersion, and 7 temperature-controlled zones. The nanocomposites were obtained with a decrease temperature profile 175/175/170/170/165/160/160 °C, a throughput of 7 kg/h and maintaining a Specific Mechanical Energy (SME) applied to the material of 150 kJ/kg.

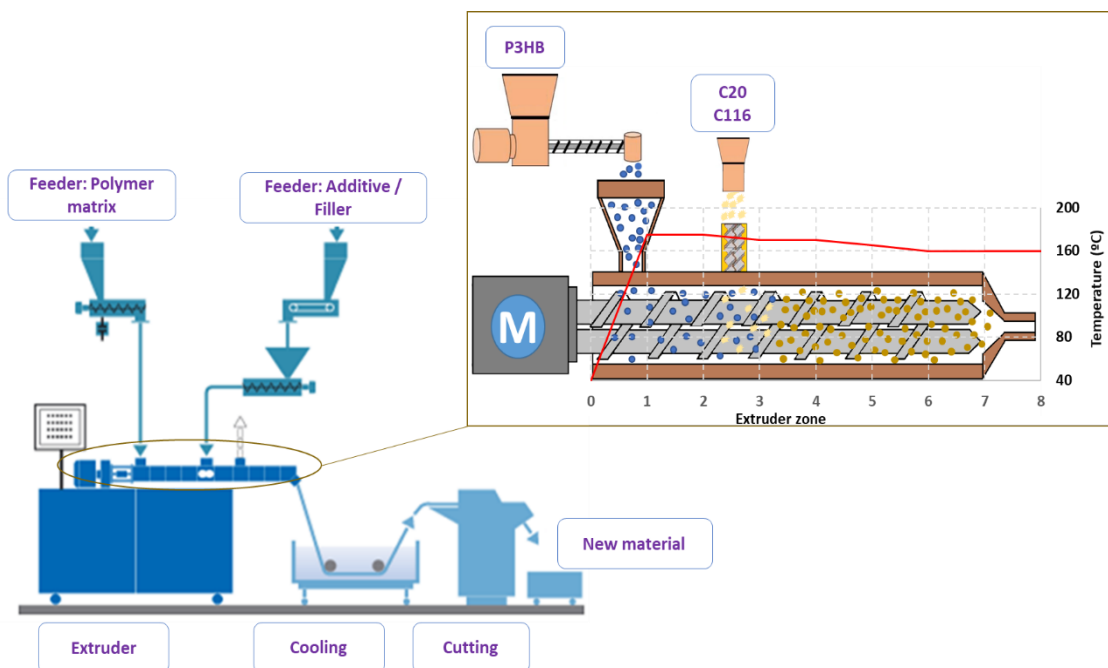


**Figure 5.1.** Schematic diagram of Twin-Screw Extruder for compounding.

### 5.2.3 Conventional injection and micro-injection molding

A standard Engel e-motion 200/55 was used to obtain the dumbbell samples by conventional injection molding tests. This equipment has a 550 kN of clamping force and is equipped with a screw of 25 mm of diameters. The profile of temperature within the injection unit of 180/160/155/150 °C with a 60 °C of mold temperature and 20 s of cooling time. The dimension of the dumbbell samples is 17.0 cm × 2.0 cm × 0.4 cm (tested zone 8.0 cm × 1.0 cm × 0.4 cm).

On the other hand, a standard Arburg allrounder 170 U was used for the conventional micro-injection molding tests to obtain the dumbbell samples. This equipment has 150 kN of clamping force and is equipped with a screw of 18 mm of diameter. A similar profile in the injection unit was used to obtain the samples: 180/170/160 °C with a 60 °C of mold temperature and 15 s of cooling time. The dimension of the dumbbell samples is 3.5 cm × 0.6 cm × 0.1 cm (tested zone 1.2 cm × 0.2 cm × 0.1 cm).

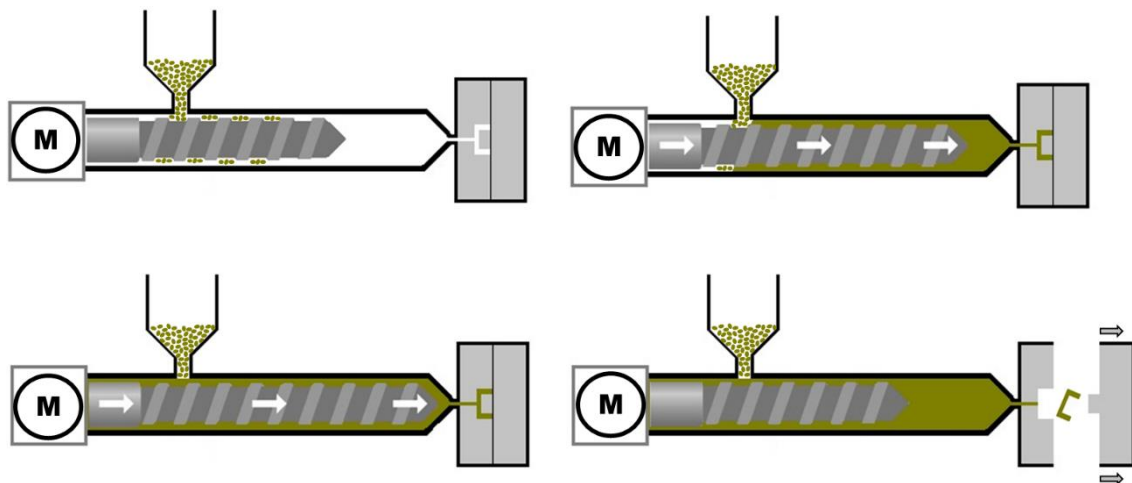


**Figure 5.2.** Schematic diagram of injection molding with their 4 steps during the process.

### 5.2.4 Ultrasonic micro-molding

First USM prototypes (**Figure 5.3**) were constituted by a controller that regulated the processing parameters (force applied to compact and push the polymer through the feed channels to the mold, amplitude of the ultrasonic wave and oscillation time), a transducer that converted the electrical signal to an undulatory movement, a pneumatic pressure system, a thermally controlled mold and an acoustic unit that was composed of a booster able to amplify or reduce the wave amplitude and a sonotrode that transferred the

vibration energy to the material while provided the force required to transfer it into the mold.

The ultrasonic micro-molding process has several steps: a) Load of the polymer in the plasticizing camera while the sonotrode is in the feeding position and the mold is closed; b) Polymer compaction by the sonotrode that applies the selected force; c) Flow of the polymer towards the mold cavities due to the sonotrode vibration at a selected amplitude that is regulated by the booster; d) Stop of the sonotrode vibration while the mold is cooled and the compaction force is kept; e) Opening of the mold, ejection of the processed specimen and return of the sonotrode to the feeding position.

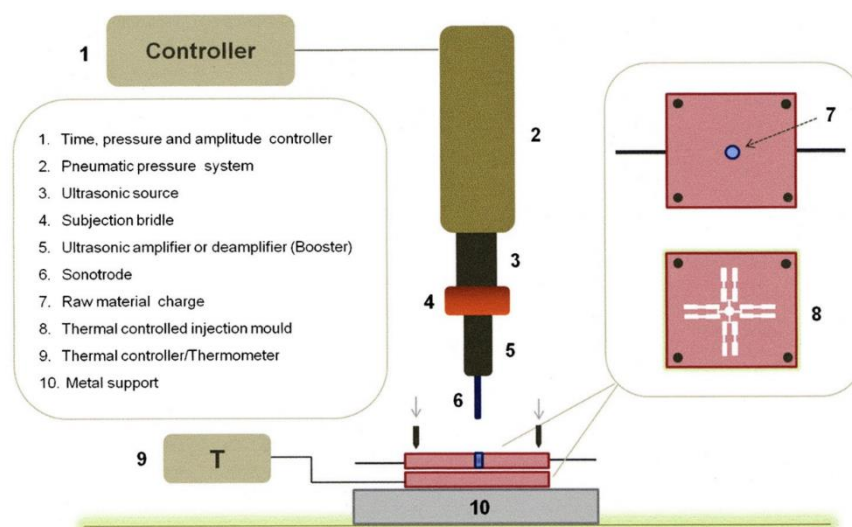


**Figure 5.3.** Representative scheme of an ultrasonic molding process (USM).

### 5.2.5 Ultrasonic micro-molding equipment

USM experiments were performed with the Sonorus 2G<sup>®</sup> prototype (Ultrason S.L., Barcelona, Spain) (**Figure 5.4a**), which incorporates two main modifications with respect to the former prototype [27]: a) A robust clamping unit able to deliver a 150 kN in order to avoid the formation of burrs; b) A nodal point ultrasonic molding configuration based on a specific design that allows to face the nodal point of the sonotrode (i.e., the position in which the longitudinal amplitude is equal to zero) with the feeding channel to the mold (**Figure 5.4b**). The USM process can be separated in four steps: Feeding, where the feedstock is fed through the parting line at the beginning of each cycle; Melting/injection, polymer pellets are compacted by means of an additional plunger that push them against the sonotrode and allows a perfect sealing of the plasticizing camera; Cooling, as in injection molding, the part must stay in the mold cooling down until it can be ejected

without deformation; Ejection, the plunger and the ejector system push the part out of the tool.

The USM apparatus was equipped with a Branson® DCX 30 kHz ultrasonic generator (1500 W), a converter from Branson® model CR 30 kHz at 1500W max, a focused Langevin piezoelectric transducer that can deliver 15 μm of peak-to-peak amplitude when it is working at 100% of gain, a green booster 1:1 (amplitude ratio) from Branson®, a sonotrode operating in longitudinal vibration mode designed by Eurecat, an electric servomotor control (Berneker and Rainer) with software from Ultrason S.L. (Barcelona, Spain) and a thermally controlled mold. This mold was designed to prepare one test specimens of dimensions 3.5 cm × 0.6 cm × 0.1 cm (tested zone 1.2 cm × 0.2 cm × 0.1 cm) and equipped with an ejection system to easily release the molded sample.

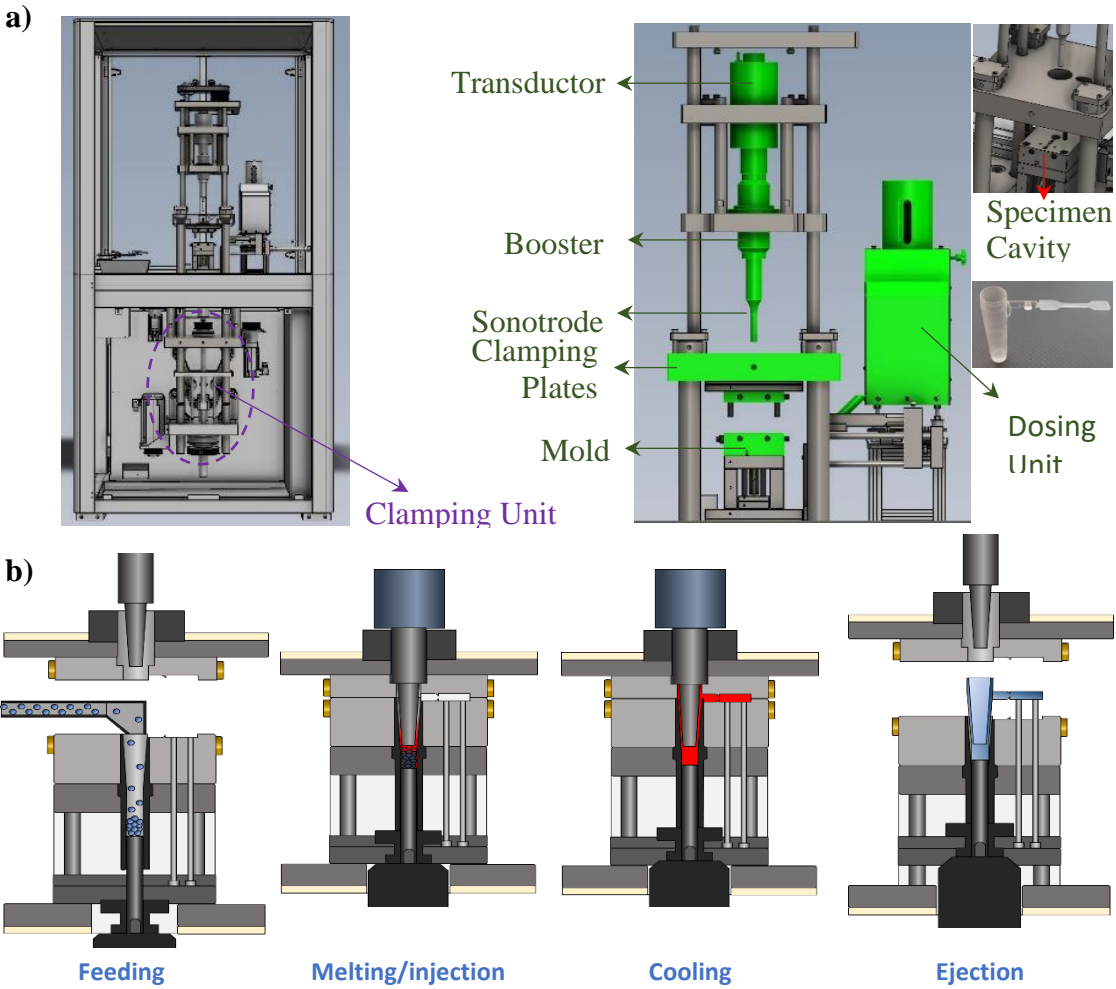


**Figure 5.4.** a) Sonorus 2G® prototype including the clamping unit at the bottom (left) and detail showing the main USM components (right). The inset shows the mold and the cavity for the designed specimen geometry. Courtesy of the firm ULTRASON S.L. b) Nodal point ultrasonic configuration (feeding, melting/injection, cooling and ejection steps).

The use of a new described technology is related to a specific procedure and methodology to obtain the processing window for each tested material. In a first step it is necessary to consider the parameters given in the technical data sheet to processing the material in a conventional injection molding equipment. Information such as melt flow index, temperature profile and mold temperature can be a relevant information to start the design of experiments. Following the manufacturer recommendations, the P3HB was dried at 60 °C more than 2 h, and the mold was preheated up to 60 °C. A packing time of 4 s and a cooling time of 15 s was found for neat P3HB and was maintained the same value for their nanocomposites. An amount of 2 g was needed to be introduced into the plasticizing chamber for each injected sample. The new configuration of the Sonorus 2G allows to define a switchover force, defined as a force reached by the plunger at the end of the filling step, not considering the ultrasonic time as a process parameter as in a traditionally ultrasonic molding [22-26]. The switchover force allows a compensation in the ultrasonic time for each weight variability in the sample [27]. A value of 7 kN was used as the switchover force in the present work. The optimal process window was defined mainly by two parameters, the velocity of the plunger and the ultrasonic amplitude.

To define a narrow process window, it was made variations in velocity of 1 mm/s and 5 % in ultrasonic amplitude. For each configuration it was injected 5 specimens and discarded the configurations that have obtained a not complete sample or evident degradation. A narrow process window was defined, allowing a design of experiments more detailed. 15 samples were obtained for each configuration where the first 5 were discarded to ensure the stabilization machine temperature.

### **5.2.6 Measurements**

Molecular weight was estimated by size exclusion chromatography (GPC) using a liquid chromatograph (Shimadzu, model LC-8A, Tokyo, Japan) equipped with an Empower computer program (Waters, company, city, country, year). The polymer was dissolved and eluted in 1,1,1,3,3,3-hexafluoroisopropanol (HFIP) containing  $\text{CF}_3\text{COONa}$  (0.05 M). The flow rate was 1 mL/min, the injected volume 20  $\mu\text{L}$ , and the sample concentration 2 mg/mL. A PL HFIP gel column ((Polymer Lab, Agilent Technologies Deutschland GmbH, Böblingen, Germany)) and a refractive index detector (Shimadzu RID-10A) were employed. The number and weight average molecular weights were determined using polymethylmethacrylate standards.

Infrared absorption spectra were recorded, at a resolution of  $4\text{ cm}^{-1}$ , with a Fourier transform FTIR 4100 Jasco spectrometer (Tokyo, Japan). A Specac MKII Golden Gate Single Reflection Diamond ATR system (Specac, Kent, England) which can be used up to  $200\text{ }^{\circ}\text{C}$ , and a high stability 4000 series controller were also employed.

A Focused Ion Beam Zeiss Neon40 microscope (Zeiss, Oberkochen, Germany) operating at  $5\text{ kV}$  was used to obtain scanning electron microscopy (SEM) micrographs of micromolded specimens. Samples were mounted on a double-side adhesive carbon disc and sputter-coated with a thin layer of carbon by using a Mitec K950 Sputter Coater (Quorum Technologies Ltd., Ashford, UK).

Tensile deformation tests were performed using the Zwick Roell Z050 Universal Tester (Barcelona, Spain) equipped with a cell charge of  $500\text{ N}$  and testXpert 8.1 software (Zwick, Ulm, Germany) under UNE EN 527 at a velocity of  $50\text{ mm/min}$ . Five specimens were tested for each processing condition.

Calorimetric data were recorded by differential scanning calorimetry (DSC) using a TA instrument (New Castle, DE, USA) Q20 series equipped with a refrigerated cooling system operating from  $-40$  to  $400\text{ }^{\circ}\text{C}$ . Experiments were performed under a flow of dry nitrogen with a sample of ca.  $3\text{ mg}$ . The instrument was calibrated for temperature and heat of fusion using an indium standard. Tzero technology required two calibrations, with empty pans and sapphire discs. Thermal characterization of polymers was carried out following a protocol consisting of three runs: a heating run of the as-molded sample, a cooling run after keeping the sample in the melt for  $1\text{ min}$  and a second heating run of the nonisothermally crystallized sample. All scans were done at  $10\text{ }^{\circ}\text{C/min}$ . Thermogravimetric analysis (TGA) and differential thermogravimetric analysis (DTGA) data were acquired with a Q50 thermogravimetric analyzer of TA Instruments (New Castle, DE, USA) under a flow of dry nitrogen with approximately  $5\text{ mg}$  samples and at a heating rate of  $20\text{ }^{\circ}\text{C/min}$ .

The spacing between layers of nanoclays within the polymer was studied by Wide-Angle X-ray scattering (WAXD) using a Bruker D8 Advance model with  $\text{Cu K}\alpha$  radiation ( $\lambda=0.1542\text{ nm}$ ) and Bragg-Brentano geometry, theta-2theta. A one-dimensional Lynx Eye detector was used. The samples were processed at  $40\text{ kV}$  and  $40\text{ mA}$ , with a 2-theta range of  $2^{\circ}$ -  $40^{\circ}$ , measurement steps of  $0.02^{\circ}$  and time/step of  $2$  to  $8$  seconds.

Deconvolution of the WAXD peaks was performed with the PeakFit v4 program from Jandel Scientific Software.

The distribution of the Cloisites 20 and 116 within the polymer matrix was complemented by observation of fine sections with a Philips TECNAI 10 electron microscope (Philips Electron Optics, Eindhoven, Netherlands) at an acceleration voltage of 100 kV. A Sorvall Porter-Blum microtome (Sorvall, New York, USA) equipped with a diamond knife was used to cut the sample into thin sections which were subsequently collected in a container filled with water and lifted onto wire racks copper with carbon coated.

## 5.3 Results and discussion

### 5.3.1 Optimization of processing parameters

A narrow processing window was obtained for USM technology by a design of experiments where the amplitude and the velocity of plunger (speed of injection molding) were the main tested parameters. It was considered the recommendations of the material producer such the mold temperature (60 °C) to carry out several combinations with both parameters recording the temperature and the pressure at the filling step as described in a previous work [27]. In a first step, the piece filling was the failure test, rejecting the conditions that have not a complete filled sample. It was not considered the conditions where presents an evident degradation of the material that could be visually detected. The repeatability was also be considered to discard or not a combination of processing parameters. In a final step, the recorded temperature and pressure done by located sensors at the mold cavity were the valuable information to evaluate the repeatability and the good conditions to the material process. Four conditions were detected as the optimal combination of amplitude a plunger velocity. These conditions were evaluated for the neat polymer and a selected nanocomposite with 5% of Cloisite 20. **Table 5.2** presents the parameters combinations relating the mechanical properties tensile strength (TS) and Elongation at break (Eb) with the temperature and pressure recorded for both materials.

These four processing conditions were compared to choose the optimal condition from a mechanical point of view, where the best combination was for 36 % of amplitude and 2,5 mm/s for the plunger velocity for both materials, P3HB and their composite with 5 % of Cloisite 20. These process conditions were selected to carry out the present study with two different nanoclays and three different amounts of the nanoclays.



**Table 5.2.** Processing windows for P3HB (A, B, C and D) and for P3HB with 5 % of Cloisite 20 (E, F, G, and H) and mechanical properties related to the measured temperature and pressure.

<b>Group</b>	<b>Amplitude %</b>	<b>Vel. Plunger mm/s</b>	<b>TS (MPa)</b>	<b>SD</b>	<b>Eb (%)</b>	<b>SD</b>	<b>T (°C)</b>	<b>SD</b>	<b>P (bar)</b>	<b>SD</b>
A	0,4	2,5	13,4	3,8	1,39	0,54	162	15,6	354	23,1
B	0,4	2	14,9	3,5	1,49	0,69	139	17,0	394	10,7
C	0,36	2,5	18,5	3,2	2,00	0,56	142	14,5	352	30,6
D	0,36	2	16,3	2,5	1,72	0,26	161	30,9	387	7,5
E	0,4	2,5	14,8	1,9	1,46	0,19	158	8,5	395	10,7
F	0,4	2	18,1	0,9	1,76	0,21	165	21,7	395	15,4
G	0,36	2,5	20,9	1,3	2,15	0,27	138	12,9	394	12,1
H	0,36	2	18,6	4,5	1,87	0,67	145	26,1	382	7,0

### 5.3.2 Molecular weight

Capability of USM to render micropieces with a minimum degradation together to the capacity to fill completely the mold and a guaranteed repeatability of results are probably the most important requirements that should be accomplished by the new technology.

GPC measurements gave a clear idea about how the ultrasonic parameters (energy/wave amplitude, pressure, and time residence) affect the molecular weight. **Figure 5.5** shows three representative chromatographs of the initial pellet, a specimen processed under the most favorable experimental conditions and a specimen with clear evidence of degradation. It is remarkable that P3HB can be processed without a significant change of the molecular parameters as summarized also in **Table 5.3** where the data corresponding to samples processed under different conditions (amplitude, flow rate) are compared.

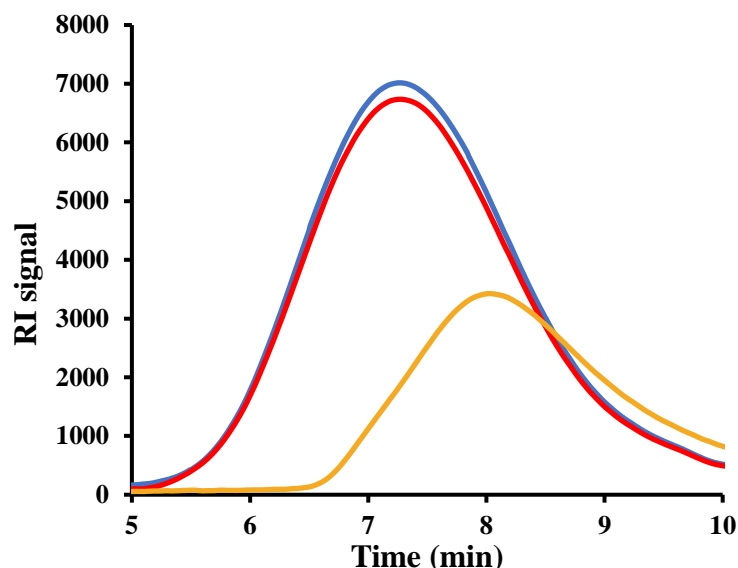


**Figure 5.5.** GPC curves corresponding to the initial P3HB pellets (blue), P3HB sample processed under optimal conditions (i.e., amplitude of 36 % of amplitude, a velocity of plunger of 2.5 mm/s) (red), and sample processed under non optimal conditions (i.e., amplitude of 80 % of amplitude, a velocity of plunger of 4 mm/s) (orange).

**Table 5.3.** Average molecular weights and polydispersity index of representative USM processed samples of P3HB and the initial pellet as a control. For the sake of completeness data for a micro-injected P3HB sample is also provided.

Sample	$M_n$	$M_w$	PI
P3HB (Pellet)	58,700	135,400	2.3
P3HB (Sonus) <sup>a</sup>	57,000	134,000	2.3
P3HB (Sonus) <sup>b</sup>	43,308	90,768	2,1
P3HB (Sonus) <sup>c</sup>	40,811	90,605	2,2
P3HB (Sonus) <sup>d</sup>	33,739	71,031	2,1
P3HB (Micro-injection)	41,182	85,466	2,0

<sup>a</sup>Processing conditions: amplitude = 36%, V. plunger = 2,5 mm/s

<sup>b</sup>Processing conditions: amplitude = 40%, V. plunger = 4 mm/s

<sup>c</sup>Processing conditions: amplitude = 43%, V. plunger = 4,5 mm/s

<sup>d</sup>Processing conditions: amplitude = 45%, V. plunger = 5 mm/s

### 5.3.3 Chemical characterization

To confirm that the chemical structure of the polymer micromolded by different technologies keeps the FTIR spectrum of a P3HB before being processed, micro-injected samples obtained under optimal and not optimal condition of nodal point USM was compared to the raw material and the conventional micro-injected samples (**Figure 5.6**). Typical bands of a P3HB were the reference to this comparison: -CH appears at 2974

$\text{cm}^{-1}$  and  $2933 \text{ cm}^{-1}$ ,  $\text{-C=O}$  appears at  $1719 \text{ cm}^{-1}$  and  $\text{-C-O}$  appear at  $1277 \text{ cm}^{-1}$  and  $1054 \text{ cm}^{-1}$ . Notes that the initial P3HB and the optimal micro-injected sample by USM technology have not a relevant difference. It is not the case of the non-optimal micro-injected sample by USM, where the FTIR reveals a change in the molecular structure of the polymer. The most significant change can be observed for the band at  $1719 \text{ cm}^{-1}$  ( $\text{-C=O}$ ), appearing a new band at higher wavenumber. More phenomena occur at lower wavenumber, that are not relevant for the present work. It can be appreciated the initial step of this phenomena changing the band at  $1719 \text{ cm}^{-1}$  for the conventional micro-injected sample. Similar results were found with molecular weight measurements and variations on mechanical properties.

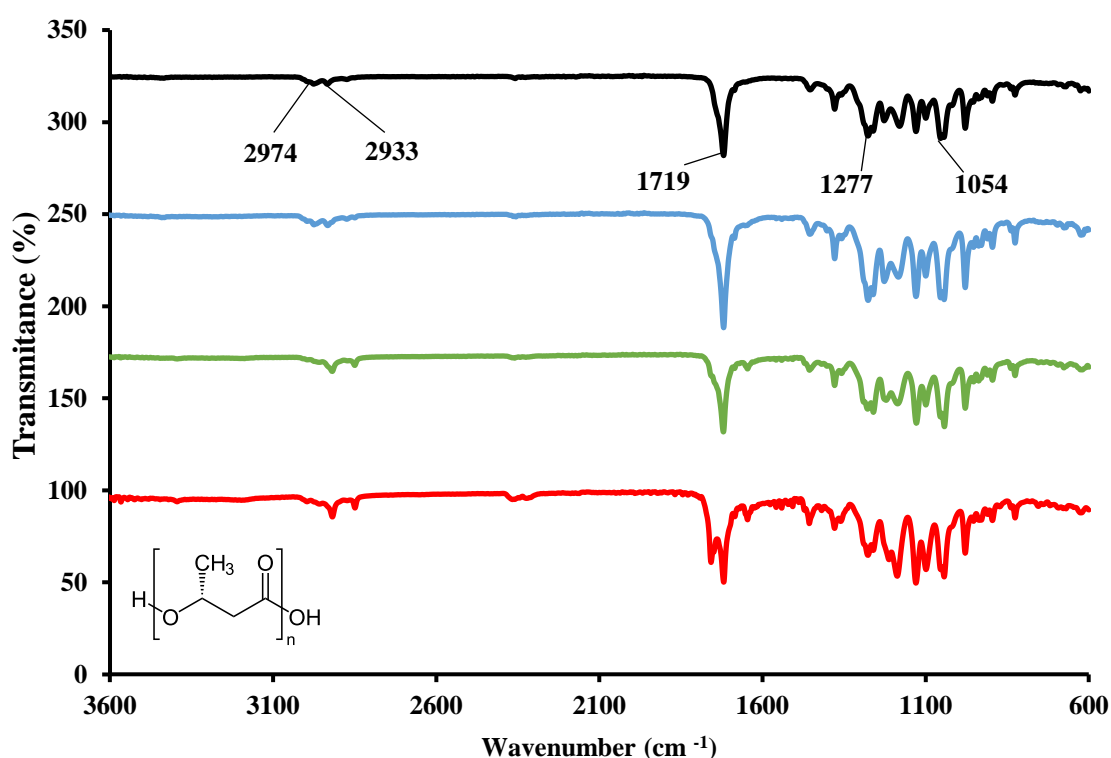


**Figure 5.6.** FTIR spectra of raw P3HB (black lines), for molded P3HB specimens obtained by the USM technology (blue lines) and by conventional micro-injection (green lines), and sample micro-injected under non optimal conditions (red lines).

### 5.3.4 Geometry and morphology of processed specimens

Micro-injected samples of P3HB were obtained by two different technologies using the same configurable mold, therefore the specimens with the same geometry can be compared between them. The homogeneity and morphology of both processed samples were evaluated by SEM (**Figure 5. 7** and **8**). The cross-section of both samples was evaluated, where a smoother surface is easily observed for the USM micro-injected

sample. SEM micrograph magnification of a cross-section for a P3HB specimen processed by USM technology reveals a spherulitic aggregates with radial lamellae (Figure 5.8)

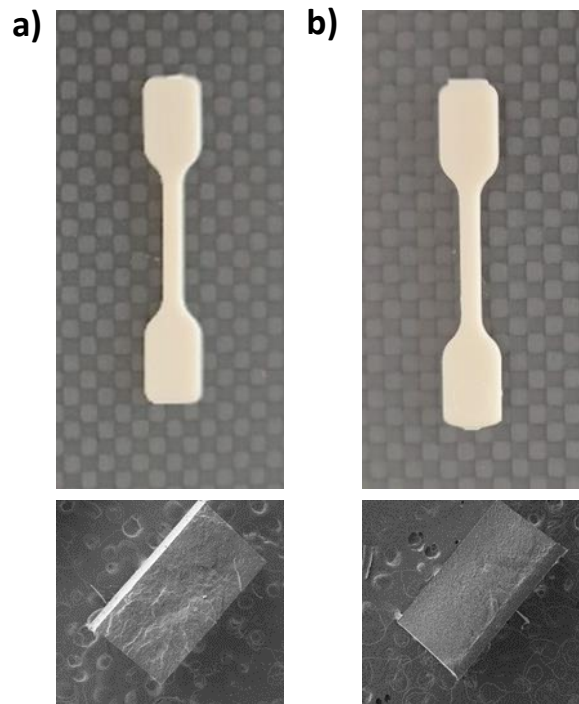


**Figure 5.7.** SEM micrograph showing different low magnification images of micro-injected (a) and USM (b) P3HB specimens. Outer (top) and cross-section) bottom images are provided.

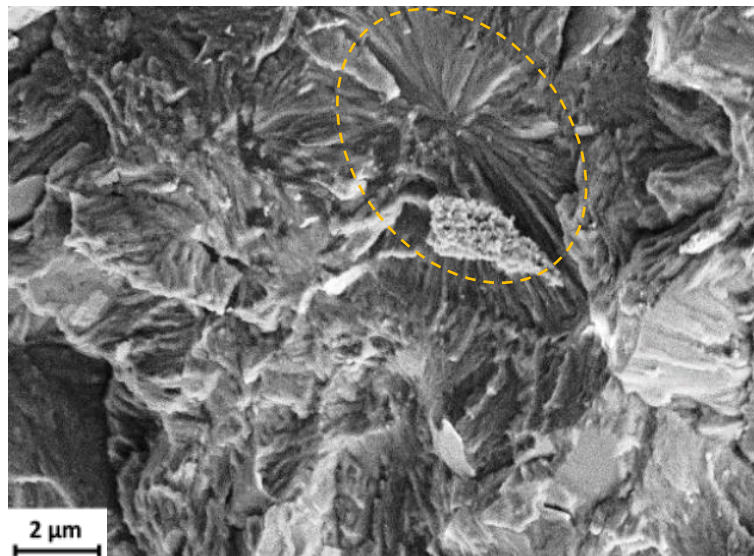


**Figure 5.8.** SEM micrograph showing a cross-section of an USM micro-molded P3HB specimen where spherulitic aggregates with radial lamellae can be envisaged (orange dashed ellipsoid).

### 5.3.5 X-ray diffraction patterns of P3HB processed samples

X-ray diffraction profiles of processed samples fully corresponded to the reported crystalline structure for the  $\alpha$ -form of P3HB. This is defined by an orthorhombic unit cell with parameters  $a = 0.576$  nm,  $b = 1.320$  nm and  $c = 0.596$  nm, a  $P2_12_12_1$  space group and a  $T\bar{G}\bar{G}T$  molecular conformation [28,29]. Main peaks correspond to the 020 and 110 reflections and appear at 0.660 nm and 0.445 nm. The structure is highly stabilized through the intermolecular hydrogen bonding interactions that are established between C=O and CH<sub>3</sub> groups of neighboring chains along the  $a$  crystallographic axis [30,31]. A second crystalline structure corresponding to a planar zig-zag conformation has also been reported when samples were submitted to stretching [29,32]. This minority structure ( $\beta$ -form) can be well distinguished from the  $\alpha$ -form by the presence of reflections at 0.480 nm and 0.460 nm. No traces of such reflections were detected in the different patterns of processed specimens.

Scarce differences between profiles were observed due to their similar and high crystallinity (as then shown by the DSC analysis). Thus, peak sharpness may show some changes due to the size of lamellar crystals [5]. This effect was clearer in the  $q$  range (i.e.,  $q = 2\pi/d$ , being  $d$  the Bragg spacing) from  $14 \text{ nm}^{-1}$  to  $18 \text{ nm}^{-1}$  (**Figure 5.9b**). Note the different resolution between the profiles of the initial P3HB pellet and the USM specimen, which mainly reflect a slight increase of crystallinity and crystal size due to the aging process experimented by the initial pellet during its storage. Resolution was also increased when the processed specimen was recrystallized from the melt, a feature that will be later discussed.

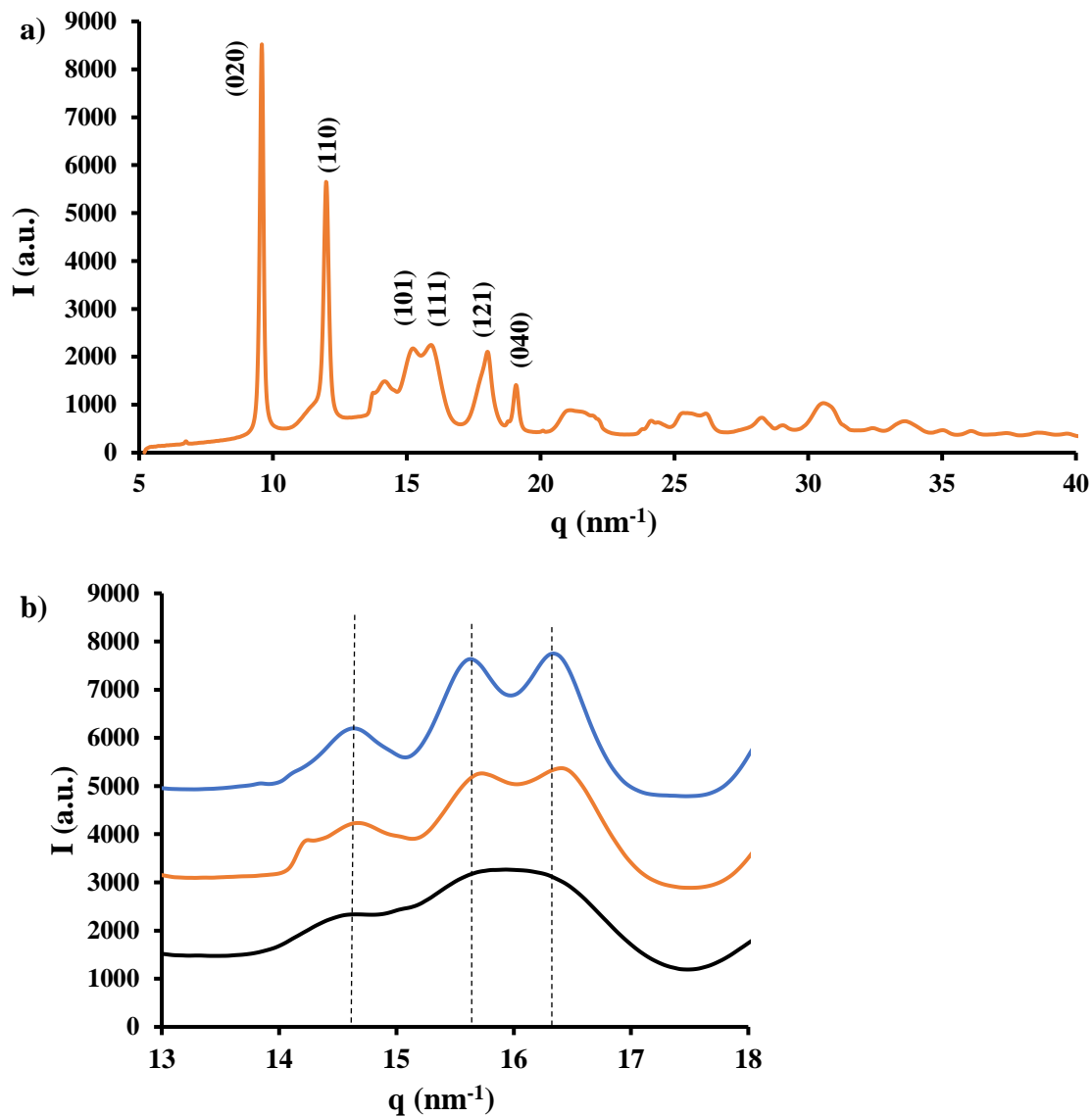


**Figure 5.9.** a) X-ray diffraction profile of an USM processed specimen of P3HB. b) X-ray diffraction profiles showing the region between 13 and 18 which is highly susceptible to the aging process. Melt extruded sample (blue), USM processed sample (black) and USM processed sample after an aging process (orange).

### 5.3.6 Thermal properties and crystallinity of micro-molded specimens

Micro-molded specimens by both conventional micro-injection and USM showed similar thermal properties as depicted in **Figure 5.10**. Thus, the first heating run was characterized by a main peak close to 171-172 °C and a shoulder around 155 °C that were typically observed for P3HB [28] and that were associated to two populations of lamellar crystals since only a single structure has been postulated for P3HB [29]. Melting peaks had only minor differences concerning the shoulder which was slightly more

defined in the micro-injected samples and reflected the formation of more thermally stable thinner crystals and a lower susceptibility to experiment a reorganization process during heating. It is noticeable that in both cases the melting enthalpy was close to 42 J/g and that consequently the same degree of crystallinity was attained (i.e., a value of 29.4 % is deduced taking into account the reported estimated enthalpy of 143 J/g for a 100 % crystalline sample [30]). Samples well-crystallized during the corresponding cooling rate with an exothermic peak temperature at 116-117 °C and an enthalpy of 42 J/g. The behavior observed in the second heating run was different to that detected in the first run due two factors: the different cooling rate of the sample in the corresponding mold and that experimented in the DSC; and the aging process at room temperature that increased the crystallinity of the sample. Note that melting enthalpies slightly increased to 47 J/g (i.e., crystallinity of 32.8 %). A slight difference was also detected between the two micro-molded specimens suggesting minimum changes on the molecular structure. Note that a shoulder around 171 °C (reorganized crystals) was only observed in the micro-molded specimen. It is also remarkable that the DSC melt crystallized samples showed the major melting peak at a temperature of 165-166 °C (i.e., a greater value than the temperature of the shoulder observed in the first heating run). This feature, suggest that crystallization took place at a higher temperature than in the mold and consequently thicker lamellae with lower capacity to be reorganized were formed.

**Figure 5.10** shows also the thermal behavior of samples obtained by conventional injection. In this case, macro-specimens with a thickness of 4 mm (i.e., greater than 1 mm of the micro-molded specimens) were obtained and obviously this different molding geometry has a remarkable impact on the final crystallinity. Thus, melting enthalpies determined for the first and second heating runs were close to 73 J/g (i.e., a crystallinity of 51.0 % could be estimated).

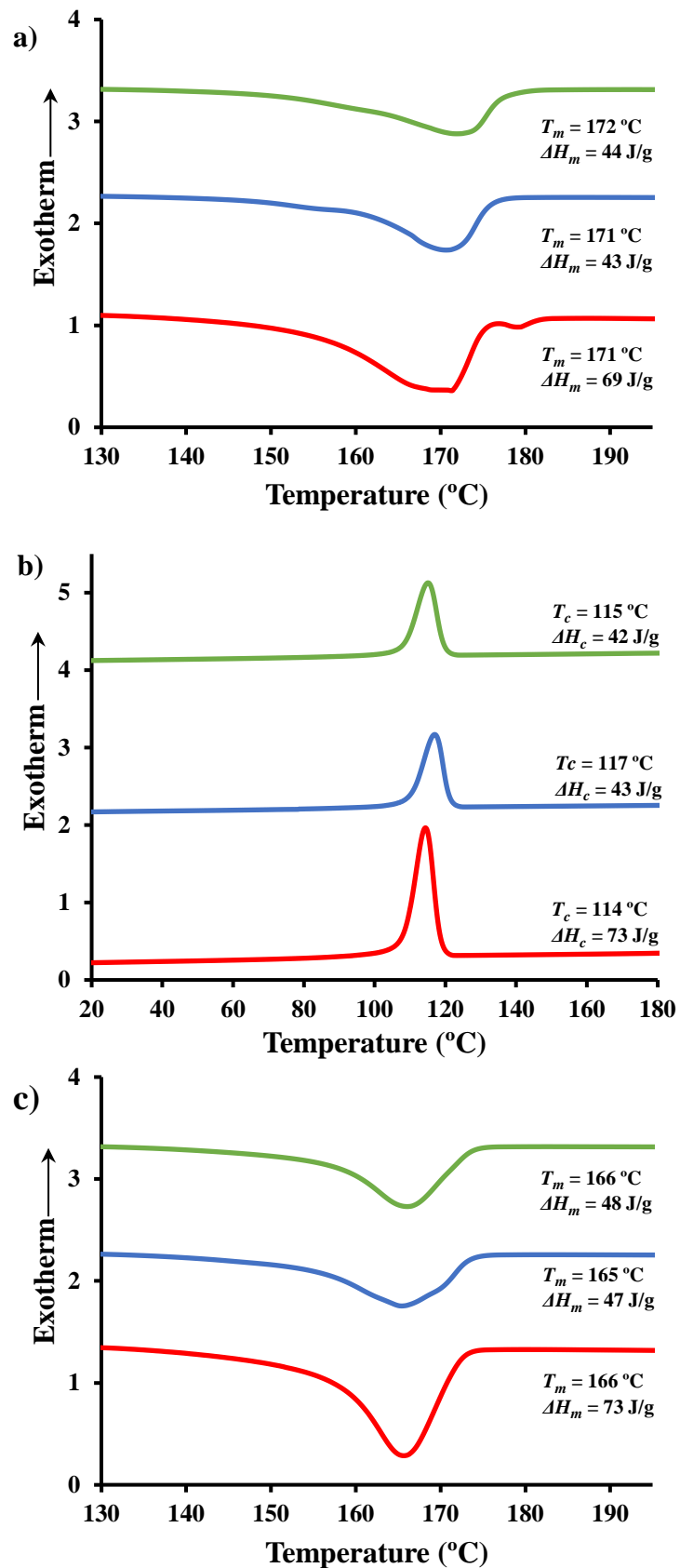


**Figure 5.10.** DSC first heating (a), cooling (b) and second heating (c) runs for injected P3HB specimens (red lines) and micro-molded P3HB specimens obtained by conventional micro-injection (blue lines) and by the USM technology (green lines).



### 5.3.7 USM processing of C20/P3HB and C116/P3HB nanocomposites. Molecular weight distribution

The two studied types of nanocomposites could be USM processed for the compositions of 3 wt.%, 5 wt.% and 8 wt.% using the same parameters determined for the neat polymer. Representative GPC curves are given in **Figure 5.11**, whereas data for all compositions are summarized in **Table 5.4** in order to avoid dispersion of data as consequence of a potential inhomogeneity of the processed samples, specimens were previously dissolved in HFIP and then aliquots containing 5 mg were evaporated to proceed to the GPC analysis. It is noticeable that minimum and moderate variations on the molecular weight parameters were observed for loads of 3 wt.% for C20 and C166 clays, respectively. Thus,  $M_w$  values decreased by 5.4 % and 23.7 %, respectively. The increase on the clay content had slight effects in the case of C20. Thus,  $M_w$  values decreased by 5.4 %, 6.3 % and 11.5 % for clay contents of 3 wt.%, 5 wt.% and 8 wt.%.

Cautions should be taken for C116 since for example  $M_w$  decreased by 35.7 wt.% (i.e., from 135,400 g/mol to 87,000 g/mol) at the highest clay concentration. Nevertheless, it should also be pointed out that a remarkable degradation was derived from the initial compounding process since for example  $M_w$  decreased to 97,000 g/mol (i.e., 28 %) for extruded pellets incorporating 8 wt.% of C116. Note that accordingly the Sonorus micro-molding process only caused an additional decrease of  $M_w$  of 10 % (i.e., from 97,000 g/mol to 87,000 g/mol).

**Table 5.4** also indicates that C20 nanocomposites could be obtained with minimum degradation by micro-injection, but it was not the case of C166 nanocomposites. Molded C166/P3HB specimens could not be obtained due to the drastic molecular weight reduction and flowability of the material that emerged from the nozzle ( $M_w$  of 33,000 g/mol). The open flow, different pressure distribution and fast cooling (**Figure 5.11**) allows to minimize degradation in the extrusion/compounding process with respect micro-injection. In any case, micromolding of C116/P3HB nanocomposites highlight the advantages of the USM technology and especially if a direct compounding in the USM equipment could be performed (i.e., avoiding the intrinsic degradation caused by the extrusion process).

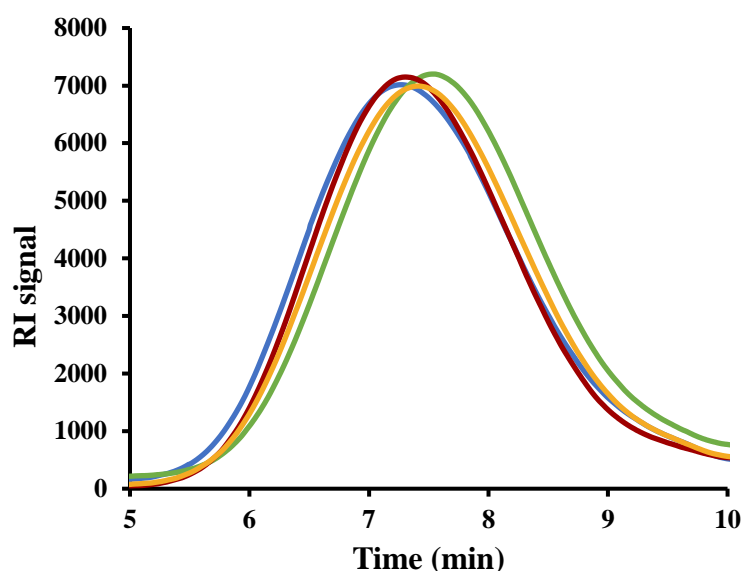


**Figure 5.11.** GPC curves corresponding to the initial P3HB pellet (blue), C20/P3HB nanocomposite containing 3 wt.% (garnet) and 8 wt.% (orange) of C20 clay and 3 wt.% (green) of C166. All samples were processed under optimal conditions (i.e., amplitude of 36 % of amplitude and a velocity of plunger of 2.5 mm/s). Values of the weight average molecular weight are indicated in all cases.

**Table 5.4.** Average molecular weights and polydispersity index of representative USM processed samples of P3HB and the initial pellet as a control. For the sake of completeness data corresponding to micro-injected pieces containing 5 wt.% of C20 and C166 are also given.

Sample	$M_n$	$M_w$	PI
P3HB (Pellet)	58,700	135,400	2.3
P3HB (Sonus)	57,000	134,000	2.3
PHB3C20	55,600	128,000	2.3
PHB5C20	54,900	126,800	2.3
PHB5C20 <sup>a</sup>	51,182	110,863	2.1
PHB8C20	50,200	119,800	2.4
PHB3C116	45,900	103,300	2.3
PHB5C116	42,900	96,100	2.2
PHB5C116 <sup>a</sup>	-	-	-
PHB8C116	41,000	87,000	2.1

<sup>a</sup>Conventional micro-injected sample.

### 5.3.8 Morphology of C20/P3HB and C116/P3HB nanocomposites

Direct observation of morphology and distribution of nanoclays within the P3HB matrix can be observed by TEM (**Figure 5.12**) and SEM measurements (**Figure 5.13**).

Micrographs at different magnifications of representative nanocomposites with 5 wt.% of C20 and C116 reveals a good dispersion of nanofillers in both cases (**Figure 5.12**). Orientation of sheet nanostructures clearly followed the direction of the melt flow during the process. It can be observed a large number of exfoliated clays, even for non-modified nanoclays (C116). The microinjected samples by USM technology of these nanocomposites were also measured by SEM (**Figure 5.13**), where it can be appreciated the presence of the exfoliated nanoclays in both cases. The results suggest that the exfoliation of nanoclays were obtained during the compounding extrusion process, and it can be maintained during the USM.

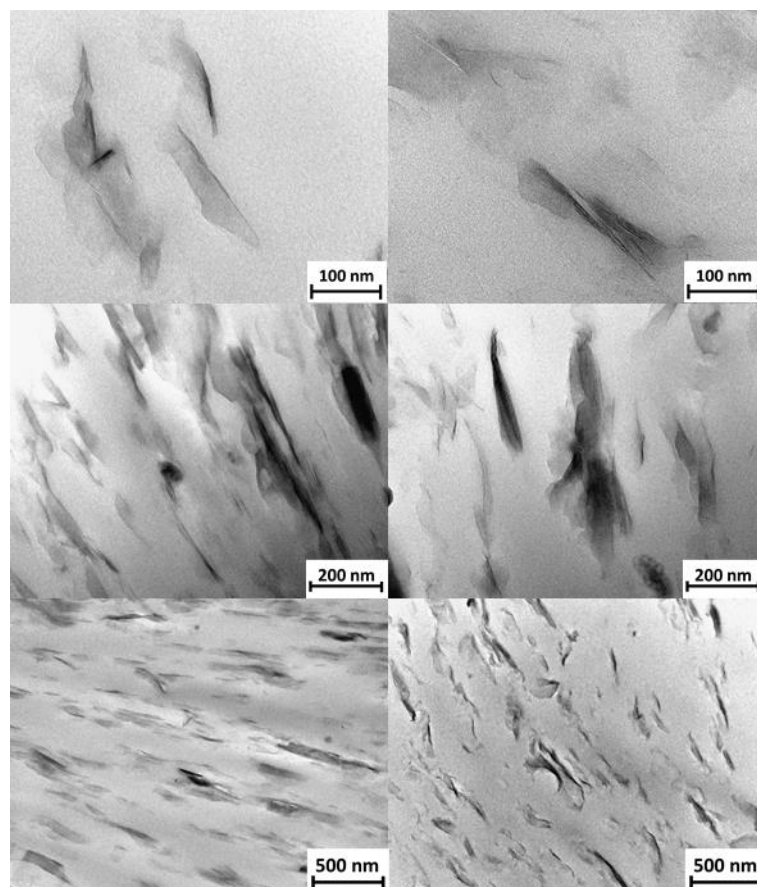


**Figure 5.12.** TEM micrographs at increasing magnification from top to the bottom of C20/P3HB (left) and C116 (right) compounded nanocomposites with clay content of 5 wt.%.

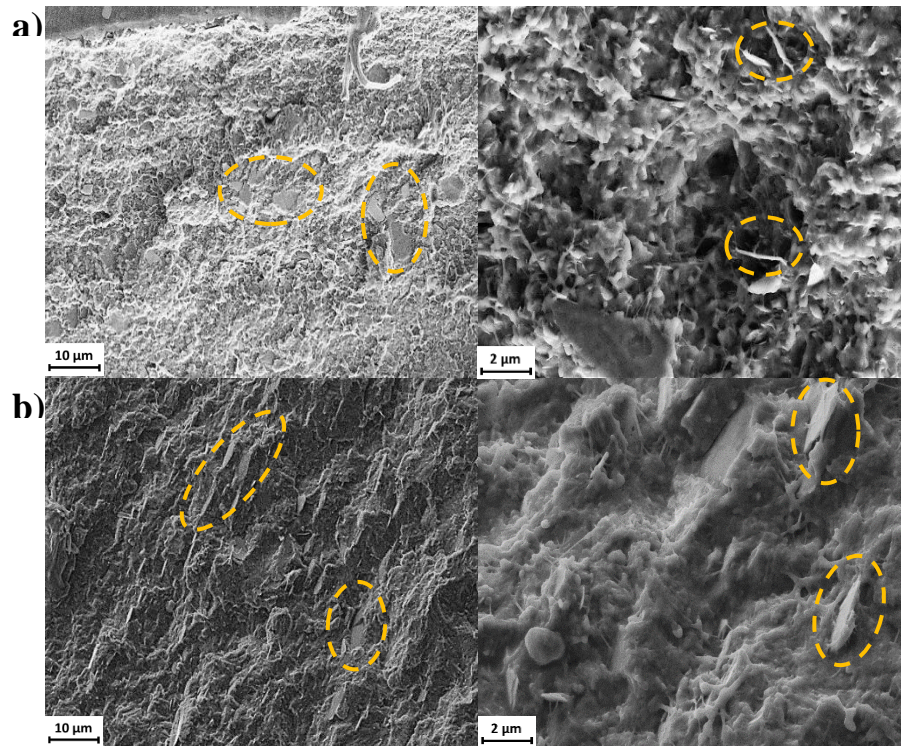


**Figure 5.13.** High (right) and low (left) magnification SEM micrographs of cross-sections C20/P3HB (a) and C116/P3HB (b) nanocomposite specimens with a clay content from 5 wt.% and processed by the USM technology. Dashed ellipsoids point out the presence of exfoliated clays.

### 5.3.9 X-ray diffraction of C20 and C116 nanocomposites

X-ray diffraction profiles of USM nanocomposites were in full agreement with the  $\alpha$ -form of P3HB (**Figure 5.14**). No additional peaks associated to the stacking of clays were detected for all assayed compositions (3-8 wt.%). These reflections should appear at 0.069, 0.066 and 0,063 nm ( $q = 14.41, 15.13$  and  $15.72 \text{ nm}^{-1}$ ) for C20 and 0.071, 0.065 and 0.064 nm ( $q = 13.94, 15.16$  and  $15.67 \text{ nm}^{-1}$ ) for C116 clays, respectively, or at higher spacings if intercalated nanocomposite structures were attained. Profiles were completely flat in this region suggesting that exfoliated nanocomposites were obtained in the former melt compounding process and that this exfoliated arrangement was kept during USM and even during micro-injection (not shown). **Figure 5.14b** shows also that the above explained differences in the region between 13 nm and 18 nm were also observed for the

prepared nanocomposites. The presence of the clay influenced on the profile of the extruded nanocomposite and specifically the peak resolution was lower than detected for the extruded neat polymer. Therefore, the presence of the clay led to smaller P3HB crystals, a feature that was found for both C20 and C116 derivatives. Additionally, USM specimens had a lower resolution that slightly increased after melt crystallization.

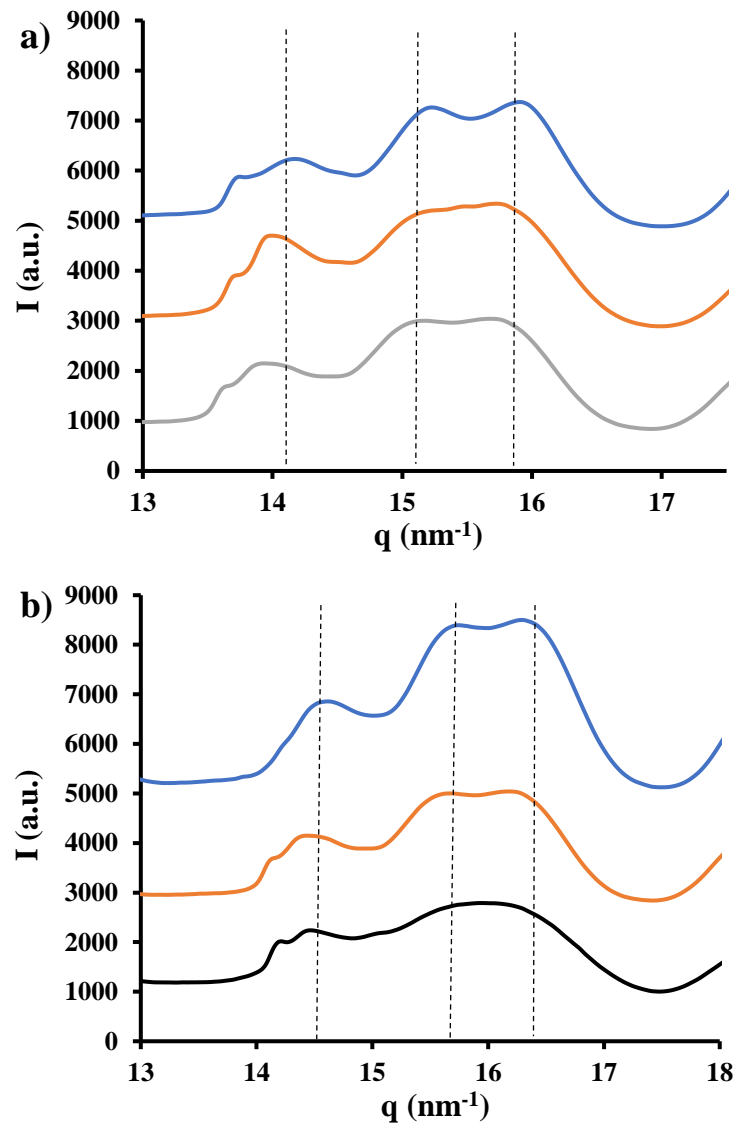


**Figure 5.14.** a) X-ray diffraction profile of an USM processed specimen of P3HB (blue) with 5 wt.% of C20 (orange) and C116 (gray) nanoclays. b) X-ray diffraction profiles of C116/P3HB nanocomposites with a clay content of 5 wt.% showing the region between 13 and 18, which is highly susceptible to the aging process. Melt extruded sample (blue), USM processed sample (black) and USM processed sample after an aging process (orange).

### 5.3.10 Thermal stability of P3HB clay nanocomposites

**Figure 5.15** shows representative TGA and DTGA curves of the neat polymer and different nanocomposites prepared all by USM. Different points can be commented:

- a) All samples are thermally stable up to a temperature of 195 °C, which appears as a common onset temperature. However, the decomposition rate is clearly different in function of the added clay.
- b) DTGA peak temperature increases in the order C116 nanocomposite < C 20 nanocomposite < neat P3HB. The result is clear and appears in contradiction with the stabilization effect caused by nanoclays in the P3HB matrix [32]. However, it should be pointed out that different clays are considered (i.e., C25 and Nanofil 757 were used in the previous work).
- c) The rather rapid degradation of the C116 nanocomposite and the closeness between melting and onset degradation temperatures highlighted the great difficulty to process the corresponding nanocomposites.
- d) USM provides rather homogeneous samples since difference between distal and proximal parts are minima as shown for the C116 nanocomposite, which is that more sensitive to degradation.
- e) The increase on the clay content basically influenced on the char yield which becomes in full agreement with the loaded percentage. Namely, values of 5 wt.% and 8 wt.% were found at temperatures of 420 °C. Therefore, TGA analysis becomes a verification process of the loading process.

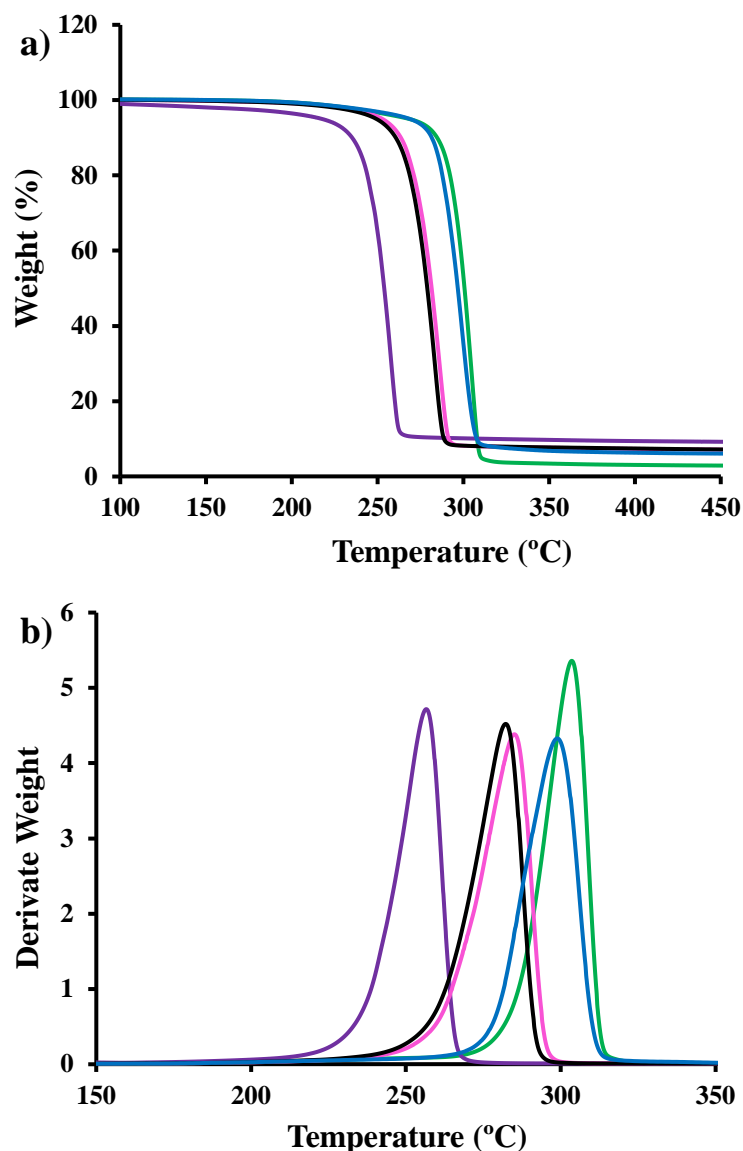


**Figure 5.15.** TGA (a) and DTGA (b) curves of different USM processed samples: neat P3HB (green), distal (black) and proximal (pink) parts of nanocomposites with 5 wt.% of Cloisite 116, proximal part of the nanocomposite with 5 wt.% of Cloisite C20 (blue) and proximal part of 8 wt.% (lilac) of Cloisite 116.

### 5.3.11 Calorimetric properties and crystallinity of C20/P3HB and C116/P3HB nanocomposites

**Figure 5.16, 5.17 and 5.18** compares the DSC traces (i.e., first heating, cooling and second heating) of C20/P3HB nanocomposites with different clay content and different micromolding technology (i.e., conventional micro-injection and USM).

Basically, properties were always very similar and even comparable with those observed for the neat sample. A detailed inspection allows to deduce some specific trends:

- a) In first heating: The increase of the clay content led to a slight decrease on the melting enthalpy (from 42 J/g to 40 J/g for clay contents of 0 wt.% and 8 wt.%, respectively). This variation was detected for both kinds of micro-molded specimens and suggests an effect of the exfoliated clay that hinders the crystallization process. Note that this is highly favored for P3HB samples and consequently the change is scarce. The increase of the clay content affected also to the melting temperature which varied from 172 °C to 170 °C. Probably the most remarkable point is the decrease on the temperature at which fusion is completed with the clay content, Thus, this temperature was around 184 °C for the neat sample and decreased up to 177 °C for the nanocomposite with an 8 wt.% of the clay. Although this effect is moderated, it should be concluded that the incorporation of the clay favors the processing of the sample and has a favorable impact in terms of not increasing (and even decreasing) the final crystallinity,
- b) Cooling traces were again highly similar for the two kinds of micro-molded specimens, but clearly revealed a slightly favored crystallization for a 3 wt.% clay content (even with respect to the neat P3HB). Thus, the crystallization peak temperature increased from 115 °C to 117 °C, while the enthalpy remained constant at the value of 42 J/g. The increase of the clay content was coherent with the indications of the previous point and therefore the crystallization peak temperature decreased to 114 °C and the enthalpy to 40 J/g.

The most remarkable difference with respect the neat polymer was found when the traces for the second heating were analyzed. Specifically, the intensity of the shoulder at 171 °C increased with the clay content and even the effect was more pronounced for the micro-injected specimens. Again, an aging effect was detected, and the melting enthalpy was always ca. 4-5 J/g higher that the crystallization enthalpy.



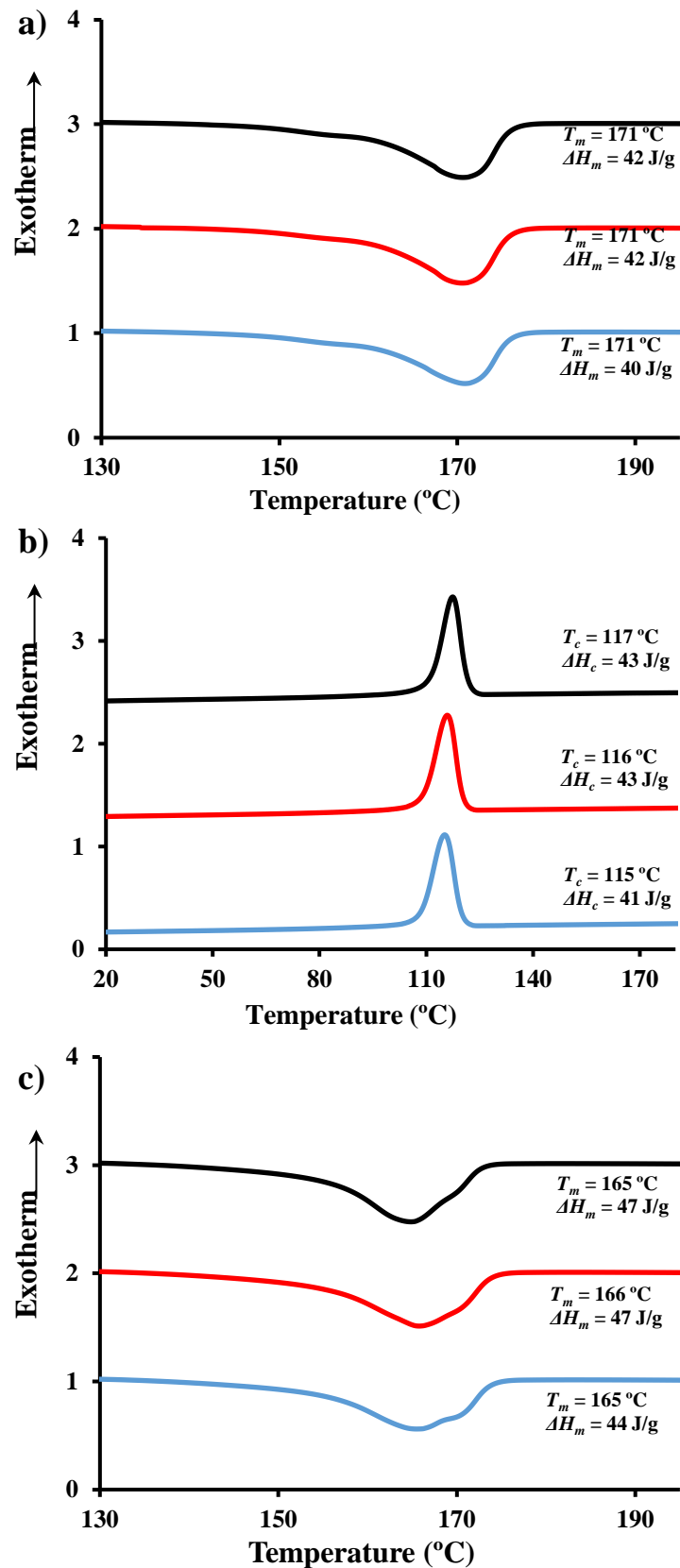


**Figure 5.16.** DSC first heating (a), cooling (b) and second heating (c) runs for micro-molded C20/P3HB specimens obtained by conventional micro-injection. The nanocomposite wt.% increase from the top to the bottom profile: 3 wt.% (black), 5 wt.% (red) and 8 wt.% (blue).

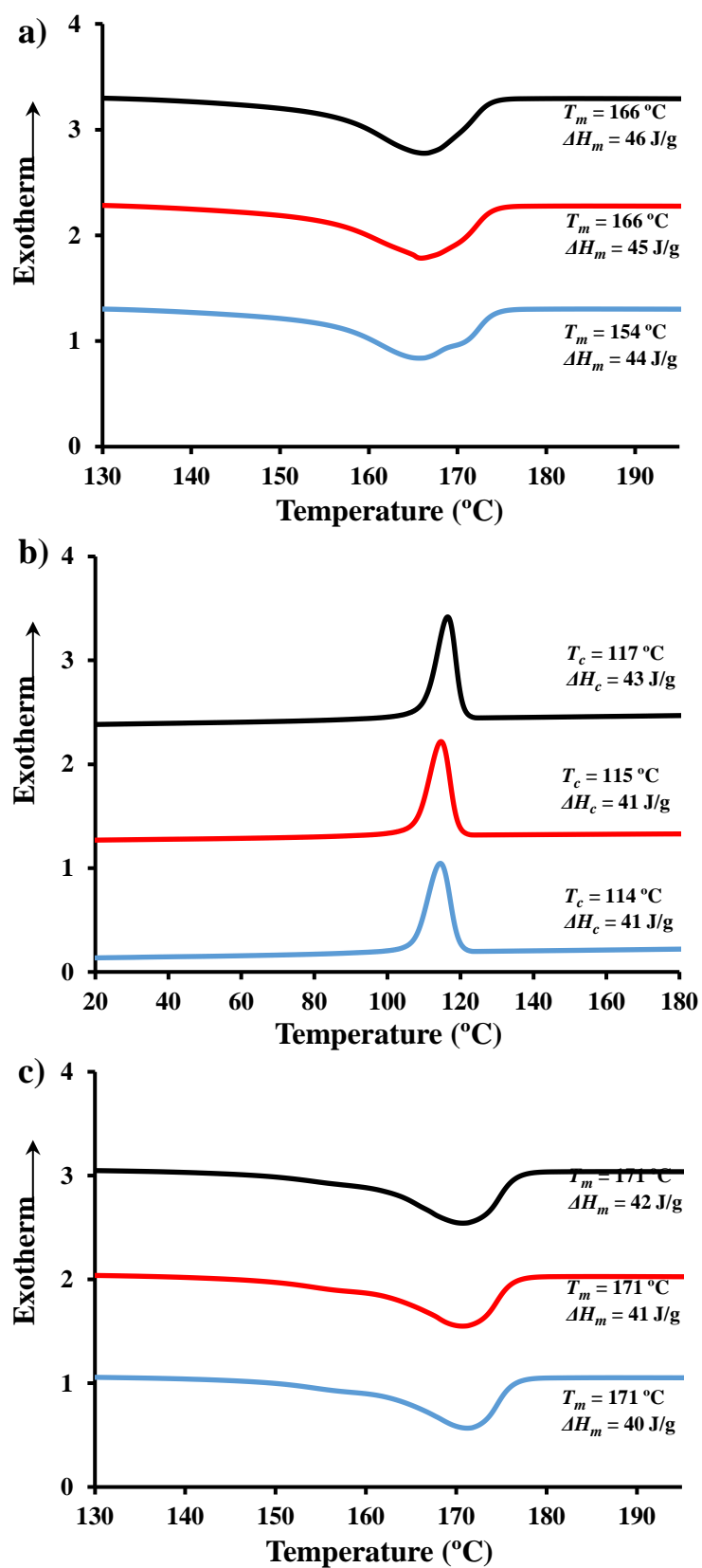


**Figure 5.17.** DSC first heating (a), cooling (b) and second heating (c) runs for micro-molded C20/P3HB specimens obtained by USM technology. The nanocomposite wt.% increase from the top to the bottom profile: 3 wt.% (black), 5 wt.% (red) and 8 wt.% (blue).

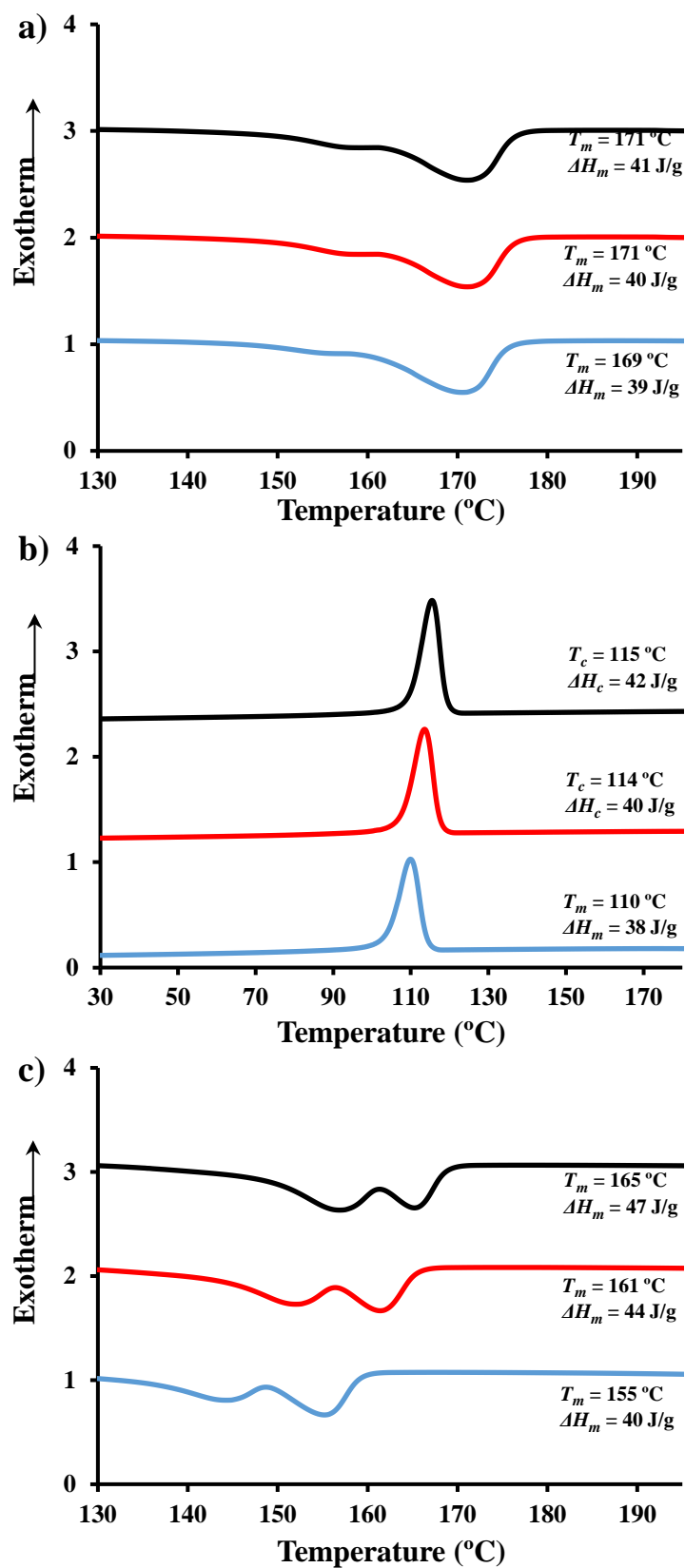


**Figure 5.18.** DSC first heating (a), cooling (b) and second heating (c) runs for micro-molded C116/P3HB specimens obtained by USM technology. The nanocomposite wt.% increase from the top to the bottom profile: 3 wt.% (black), 5 wt.% (red) and 8 wt.% (blue).

The most impacting result concerns to the suitability of USM to get C116/P3HB nanocomposites for all assayed compositions. This was not possible by the micro-injection process due to the higher temperature at which the sample was exposed, the higher residence time and even to the narrow feeding channel that caused problems in the flow of the polymer melt. Extrusion of the C116/P3HB was not problematic due to the different geometry of the extruder nozzle and the rapid cooling of the extruded thread (**Figure 5.1**).

**Figure 5.16, 5.17 and 5.18** shows also the characteristic DSC traces for the different C116/P3HB nanocomposites. First heating and cooling runs indicates similar trends to those previously commented (e.g., easier crystallization for the sample with a clay content of 3 wt.% and hindered process with respect to the neat polymer for the 8 wt.% content). However, a remarkable peculiar behavior was observed for the second heating run performed with the melt crystallized sample. Note that two melting peaks around 163-155 °C and 156-144 °C were observed. The second one could be related with the low temperature shoulder observed in the first heating run of P3HB, whereas the second one fits with the major peak observed for melt crystallized samples. Heating runs showed also clear differences according to the clay content and specifically both peaks shifted to lower temperature when the clay percentage increased while the ratio between the enthalpies of the second and first peak increased. Probably this behavior can be justified considering a hindered crystallization caused by the clay and the formation of less stable crystals (i.e., more susceptible to recrystallization). Some degradation effects could not be excluded considering the lower thermal stability and the high difficulty to be processed showed by the C166/P3HB nanocomposites.

### **5.3.12 Isothermal crystallization of C20/P3HB nanocomposites: Lamellar thickening and equilibrium melting temperature**

The dependence between the melting temperature and the crystallization temperature was further analyzed for the representative C20/P3HB blend (5 wt.% of clay) by isothermal crystallizations performed at different temperatures. The crystallization temperature range was between 125 °C and 135 °C in order to crystallize the samples in a reasonable time (i.e., 32 min to complete crystallization for the higher temperature experiment and 1.5 min to start crystallization for the lower temperature experiment).

**Figure 5.19a** shows the corresponding crystallization curves, while **Figure 5.19b** shows the subsequent heating curves. It is clear that the melting peak temperature progressively increased as the samples was crystallized at a higher temperature. Thus, differences on the crystallization temperature of only 10 °C caused an increase of the time required to get the exothermic peak of 12 min, and on the melting peak of 6 °C (i.e., from 160 °C to 166 °C).

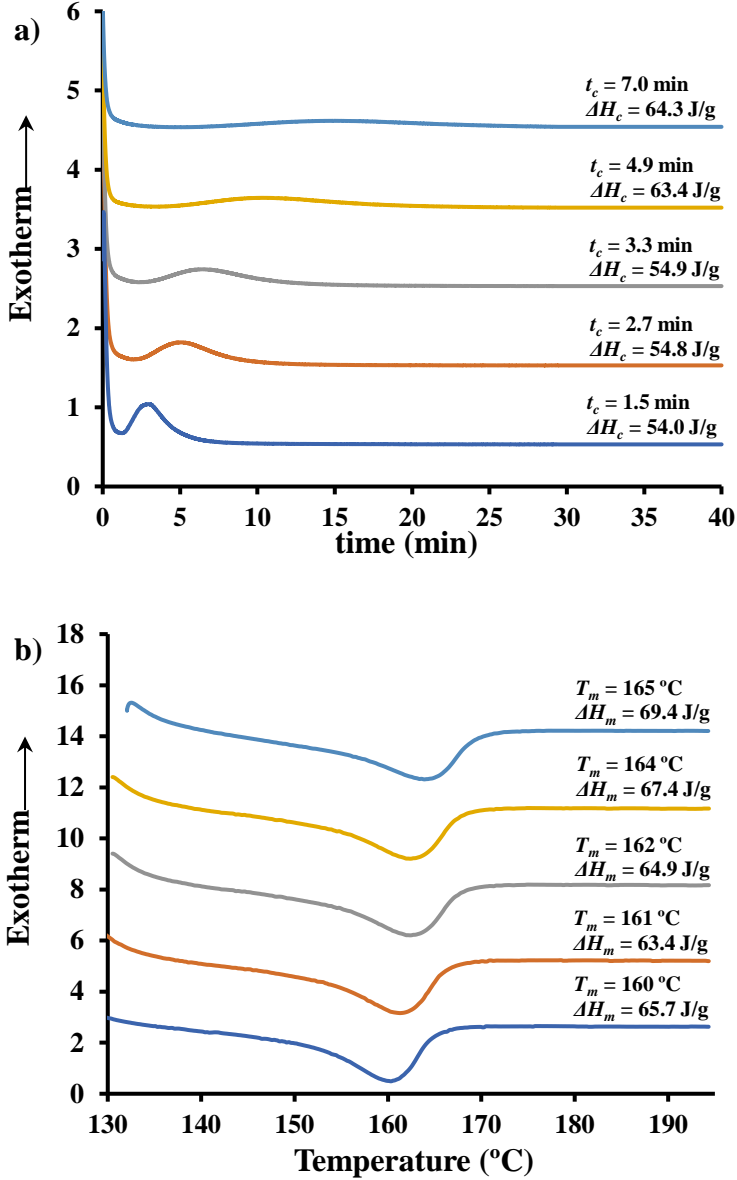


**Figure 5.19.** a) Isothermal crystallization DSC curves for C20/P3HB nanocomposite containing 5 wt.% of the clay. b) DSC heating curves of the above melt crystallized samples.

The Hoffmann-Week representation [33] (**Figure 5.20**) allows to determine the expected equilibrium melting temperature associated with an infinitum lamellar thickness. The

obtained value becomes in full agreement with the temperature of 197 °C that was reported for P3HB [33]. Therefore, the incorporation of the nanoclay has not an influence on the thermodynamic equilibrium condition and the observed variations on the melting peaks can be justified according to the increase of the lamellar thickness induced by higher crystallization temperatures. The layered disposition of the clay seems that not have influence on the full formation of the polymer structure.

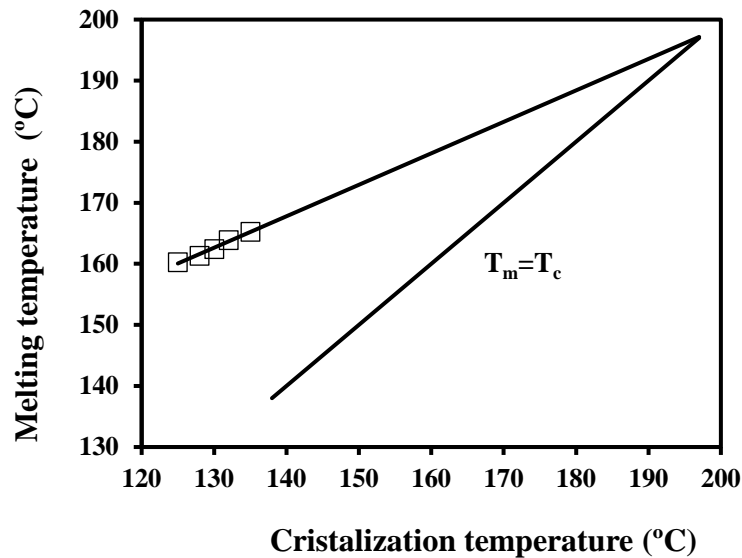


**Figure 5.20.** Hoffman-Week plot for the C20/P3HB nanocomposite containing 5 wt.% of clay.

### 5.3.13 Influence of processing on the mechanical properties of neat P3HB and nanocomposites loaded with the C20 and C116 clays.

P3HB specimens were characterized by their great stiffness (i.e., great modulus and reduced elongation at break). The aging of specimens had repercussions on mechanical properties since the increased crystallinity led to an increase of the modulus and a decrease of the elongation as shown in **Figure 5.21** were stress-strain curves are reported for storage periods of 1 day, 1 months and 1 year. Due to this variation all measurements were carried out after only one day of storage. A second issue affects the repeatability of the assays as shown in **Figure 5.22** and the standard deviations summarized in **Table 5.5** for representative samples. It is remarkable that despite the low values of  $e$ , a considerable dispersion of values was observed for USM specimens processed without the nodal point technology. By contrast, new USM prototypes dotted

with this configuration led to specimens with highly homogeneous properties. Comparison between USM and micro-injected pieces also revealed some advantages for USM processing (**Table 5.5**) in terms of a slightly lower standard deviations, higher modulus (e.g., 1560 MPa versus 1390 MPa) and higher maximum strength (i.e., 31.7 MPa versus 25.9 MPa). The absence of the nodal point technology caused local degradation and formation of cracks and irregularities in some processed specimens that led to a significant decrease of properties (e.g., modulus of 1170 MPa and maximum strength of 21,1 MPa).

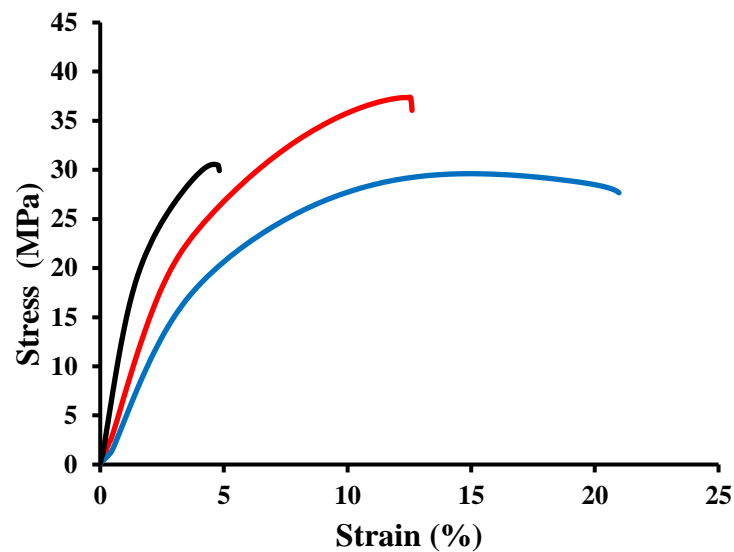


**Figure 5.21.** Stress-strain curves for neat P3HB specimens processed by USM with the nodal point configuration. Samples differ in the storage time: 1 day (blue), 1 month (red), 1 year (black).

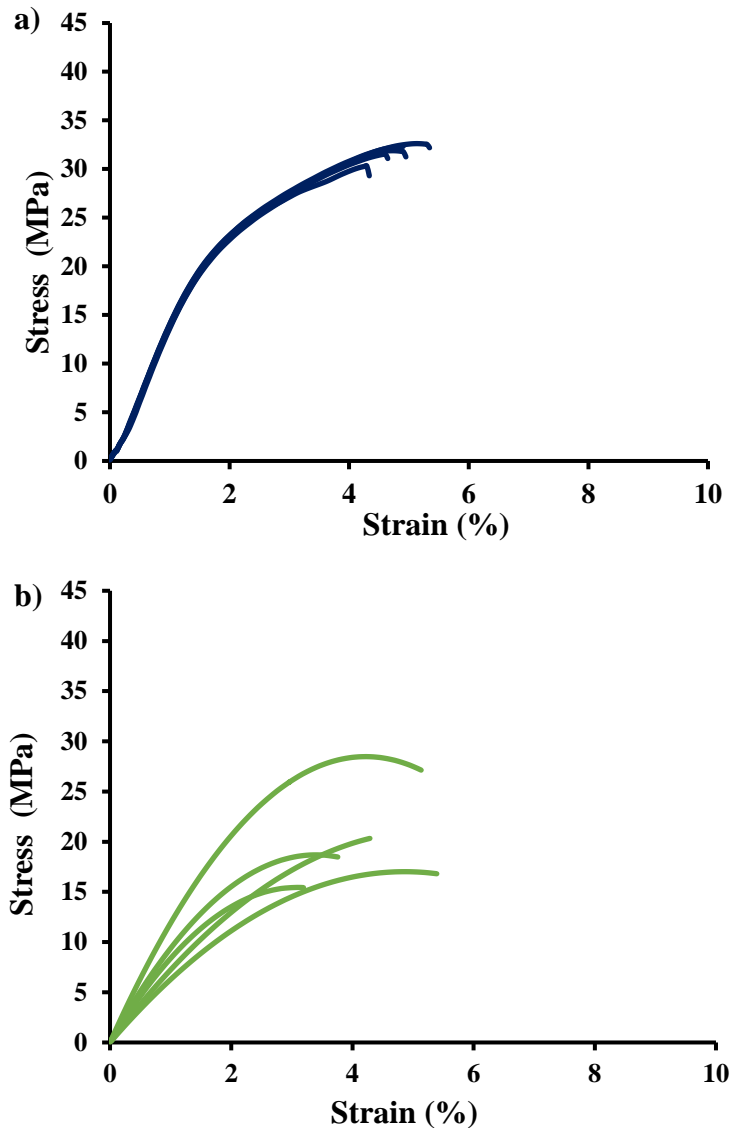


**Figure 5.22.** a) Stress-strain curves for neat P3HB specimens processed by USM with (a) and without (b) the nodal point configuration.

Nanocomposites showed a regular increase of modulus with the weight percentage of incorporated clay. Thus, modulus regularly increased from 1850 MPa to 2140 MPa for USM processed specimens when the C20 clay content changed from 3 wt.% to 8 wt.%. However, the presence of nanoclays led to a decrease of the elongation at break and the initial value of 6% for the neat polymer decreased to 3.1% - 2.7 % for C20 clay loads of 3 wt.% - 8 wt.%. The repercussion on the maximum strength was a balance between the improvement of modulus and the worsening of elongation. Thus, the strength for C20 nanocomposites increased with the clay content (from 27.9 MPa to 29.2 MPa), but this strength was always lower than determined for the neat polymer (31.7 MPa).



A similar evolution was observed for the micro-injected specimens, but it is significant that all properties were always worse than determined for the USM processed specimens. For example, modulus increased only from 1480 MPa to 1570 MPa and the elongation at break could reach a value of only 1.8% for a 8 wt.%. Note the high difference between the highest modulus (i.e., 2140 MPa and 1570 MPa) determined for USM and micro-injected specimens with a 5 wt.% of C20. This difference may reflect a better dispersion of the clay in the polymer matrix or even a lower degradation for USM processed specimens since similar degrees of crystallinities were attained.

Similar changes (i.e., regular modulus increase from 1840 MPa to 2190 MPa) were detected for nanocomposites derived from C116 and USM processed. In this case the values of modulus were maintained probably as consequence of the higher stiffness of the clay, but both maximum strength and elongation decreased with the clay content as a result of the enhanced molecular degradation. It is remarkable that specimens could not be obtained by micro-injection and that properties were also worse when the USM was performed without the nodal point configuration (**Figure 5.23**) as can be deduced considering the results attained with a 5 wt.% (i.e., decrease of modulus, maximum strength and elongation from 2010 MPa, 26.2 MPa and 2.3% to 1132 MPa, 19.5 MPa and 2.0 %, respectively).

**Table 5.5.** Young modulus, maximum strength, and break elongation for processed specimens of P3HB and its nanocomposites with C20 and C116 clays.

Sample	E (MPa)	$s_{max}$ (MPa)	Eb (%)
P3HB <sup>a</sup>	1560	31.7	5
P3HB <sup>b</sup>	1390	25.9	6
P3HB <sup>c</sup>	1170	21.1	5.1
PHB3C20 <sup>a</sup>	1850	27.9	3.1
PHB5C20 <sup>a</sup>	1990	29.2	3.2
PHB8C20 <sup>a</sup>	2140	29.2	2.7
PHB3C20 <sup>b</sup>	1480	26.2	2.6
PHB5C20 <sup>b</sup>	1270	24.9	2.4
PHB8C20 <sup>b</sup>	1570	25.2	1.8
PHB5C20 <sup>c</sup>	1320	27.6	3.7
PHB3C116 <sup>a</sup>	1840	27.5	2.5
PHB5C116 <sup>a</sup>	2010	26.2	2.3
PHB8C116 <sup>a</sup>	2190	20.6	1.3
PHB5C116 <sup>b</sup>	-	-	-
PHB5C116 <sup>c</sup>	1132	19.5	2.0

<sup>a</sup>USM using the nodal point configuration.

<sup>b</sup>Conventional micro-injection.

<sup>c</sup>USM without the nodal point configuration

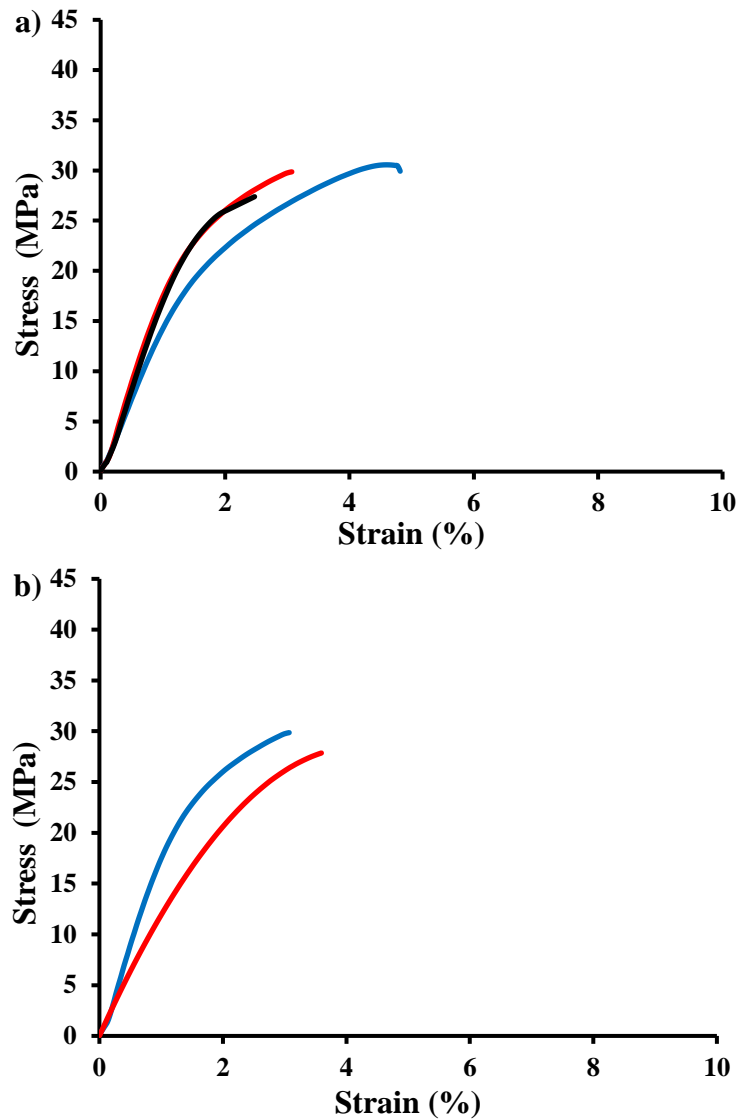


**Figure 5.23.** a) Stress-strain curves for neat P3HB (blue), PHB5C20 (red) and PHB5C166 (black) specimens processed by USM and using the nodal point configuration. b) Comparison of stress-strain curves for PHB5C20 specimens processed by USM with (blue) and without (red) the nodal point configuration and by conventional micro-injection (black).

## 5.4 Conclusions

P3HB can easily improve their properties by adding nanoclays. The incorporation of 3, 5 and 8 wt.% of an organomodified clay (C20) and non-modified clay (C116) by compounding extrusion were carried out to obtain different nanocomposites to be used as a raw material for two technologies of microinjection molding, conventional and USM. Mechanical properties were expected to be improved in both cases, but the results reveal chemical changes in the structure of P3HB for conventional microinjected samples that

reduce the material performance in comparison with the results showed by the USM technology with nodal point. FTIR and GPC measurements confirm the mentioned change that can be the reason of worse results for conventional microinjected samples. It was also seen that the conventional process cannot mold nanocomposites with C116, in contrast to the USM technology.

Not a significant difference can be observed in crystallinity studies of comparison between P3HB micro injected sample obtained by USM and conventional technology. Nevertheless, a conventional injected sample (not micro) was also compared, and it reveals a pronounced difference compared to the micro-injected samples (i.e.,  $\Delta H_m = 73$  J/g versus 47-48 J/g of micropieces). This different molding geometry has a remarkable impact on the final crystallinity.

Nanocomposites processed by USM technology reveals benefits:

- Higher values of mechanical properties and stability.
- Good homogeneity of cross-section seen by SEM.
- X-Ray studies suggest that exfoliated nanocomposites were obtained in the former melt compounding process and that this exfoliated arrangement was kept during USM process. The results were confirmed by TEM and SEM micrographs.
- FTIR and GPC presents no change of chemical structure of microsamples

USM technology was demonstrated to be an optimal option to obtain micropieces with improved properties for nanocomposites with treated and untreated nanoclays.

## 5.5 References

1. Visakh, P.M.; Polyhydroxyalkanoate (PHA) based blends, composites and nanocomposites. In Polyhydroxyalkanoates (PHAs), their Blends, Composites and Nanocomposites: State of the Art, New Challenges and Opportunities, RSC Green Chemistry, Cambridge, UK 2015, Ch. 1, 1-17.
2. R. G. Hill. Biomedical Polymers. In Biomaterials, Artificial Organs and Tissue Engineering. Woodhead Publishing Series in Biomaterials, Cambirdge, UK 2005, Ch. 10, 97-106.

3. Bugnicourt, E.; Cinelli, P.; Lazzeri, A.; Alvarez, V. *Express Polym. Lett.*, 8, 791–808, 2014.
4. Han, L.; Han, C.; Cao, W.; Wang, X.; Bian, J.; Dong, L.; *Polym. Eng. Sci.*, 52, 2, 250–258, 2012.
5. Czerniecka-Kubicka, A.; Frącz, W.; Jasiorski, M.; Błażejowski, W.; Pilch-Pitera, B.; Pyda, M.; Zarzyka, I. *J. Therm. Anal. Calorim.*, 128, 1513–1526, 2017.
6. Larsson, M.; Markbo, O.; Jannasch, P. *RSC Adv.*, 6, 44354-44363, 2016.
7. Puglia, D.; Fortunati, E.; D’Amico, D.A.; Miri, V.; Stoclet, G.; Manfredi, L.B.; Cyras, V.P.; Kenny, J.M. *J. Polym. Environ.*, 24, 12–22, 2016.
8. Han, C.C.; Ismail, J.; Kammer, H.W. *Polym. Degrad. Stab.*, 85, 947–955, 2004.
9. Baltieri, R.C.; Innocentini Mei, L.H.; Bartoli, J. *Macromol. Symp.*, 197, 33–44, 2003.
10. Yu, L.; Dean, K.; Li, L. *Prog. Polym. Sci.*, 31, 576–602, 2006.
11. Erceg, M.; Kovacic, T.; Klaric, I. *Polym. Degrad. Stab.*, 90, 313–318, 2005.
12. Hablot, E.; Bordes, P.; Pollet, E.; Averous, L. *Polym. Degrad. Stab.*, 93, 4131, 2008.
13. Puglia, D.; Fortunati, E.; D’Amico, D.A.; Manfredi, L.B.; Cyras, V.P.; Kenny, J.M. *Polym. Degrad. Stab.*, 99, 127–135, 2014.
14. Sacristán, M.; Plantá, X.; Morell, M.; Puiggali, J. *Ultrason. Sonochem.*, 21, 1, 376–386, 2014.
15. Yang, Y.J.; Huang, C.C.; Lin, S.K.; Tao, J. *J. Polym. Eng.*, 34, 7, 673–681, 2014.
16. Isayev, A.I.; Kumar, R.; Lewis, T.M. *Polymer (Guildf)*, 50, 1, 250–260, 2009.
17. Levy, A.; Le Corre, S.; Villegas, I.F. *J. Mater. Process. Technol.*, 214, 7, 1361–1371, 2014.
18. Sortino, M.; Totis, G.; Kuljanic, E. *Procedia Eng.*, 69, 1296–1305, 2014.
19. Janer, M.; Planta, X.; Riera, D. *Ultrasonics*, 102, 106038, 2020

20. Masato, D.; Babenko, M.; Shriky, B.; Gough, T.; Lucchetta, G.; Whiteside, B. *Int. J. Adv. Manuf. Technol.*, 99, 1-4, 113–125, 2018.
21. Grabalosa, J.; Vazquez, E.; Ferrer, I.; Elias-Zúniga, A.; Sirera, E.; Rivillas, F. *Proceedings of the 2nd International Conference on Design and Processes for Medical Devices*, 52–56. 2014
22. Planellas, M.; Sacristán, M.; Rey, L.; Olmo, C.; Aymamí, J.; Casas, M.T.; del Valle, L.J.; Franco, L.; Puiggali, J. *Ultrason. Sonochem.*, 21, 4, 1557–1569, 2014.
23. Olmo, C.; Franco, L.; del Valle, L.J.; Puiggali, J. *Appl. Sci.*, 10, 3106, 2020.
24. Olmo, C.; Amestoy, H.; Casas, M.T.; Martínez, J.C.; Franco, L.; Sarasua, J.R.; Puiggali, J. *Polymers*, 9, 322, 2017.
25. Díaz, A.; Casas, M.; Puiggali, J. *Appl. Sci.*, 5, 4, 1252–1271, 2015.
26. Díaz, A.; Franco, L.; Casas, M.T.; del Valle, L.J.; Aymamí, J.; Olmo, C.; Puiggali, J. *J. Polym. Res.*, 21, 584, 2014
27. Janer, M.; López, T.; Planta, X.; Riera, D.; *Ultrasonics*, 114, 106418, 2021
28. Cornibert, J.; Marchessault, R. H. *J. Mol. Biol.*, 71, 3, 735-756, 1972
29. Yokouchi, M.; Chatani, Y.; Tadokoro, H.; Teranishi, K.; Tani, H. *Polymer*, 14, 267-272, 1973.
30. Sato, H.; Nakamura, M.; Padermshoke, A.; Yamaguchi, H.; Terauchi, H.; Ekgasit, S.; Noda, I.; Ozaki, Y. *Macromolecules*, 37, 10, 3763-3769, 2004.
31. Hu, Y.; Zhang, J.; Sato, H.; Futami, Y.; Noda, I.; Ozaki, Y. *Macromolecules*, 39, 11, 3841-3847, 2006.
32. Orts, W. J.; Marchessault, R. H.; Bluhm, T. L.; Hamer, G. K. *Macromolecules*, 23, 26, 5368-5370, 1990.
33. Li, X.; Yin, J.; Yu, Z.; Yan, S.; Lu, X.; Wang, Y.; Cao, B.; Chen, X. *Polymer Composites*, 30, 9, 1338-1344, 2009.

# ———— Part II ————

# 6.

**PROCESSING AND PROPERTIES  
OF POLYMER NANOCOMPOSITES  
AND NANOCOATINGS AND THEIR  
APPLICATIONS IN THE  
PACKAGING, AUTOMOTIVE AND  
SOLAR ENERGY FIELDS**





# 6. PROCESSING AND PROPERTIES OF POLYMER NANOCOMPOSITES AND NANOCOATINGS AND THEIR APPLICATIONS IN THE PACKAGING, AUTOMOTIVE AND SOLAR ENERGY FIELDS

## 6.1 Introduction

For the last decades, nanocomposites materials have been widely reported in the scientific literature to provide substantial properties enhancements, even at low nanoparticles content. In nanotechnology, polymer nanocomposites are defined as solids consisting of a mixture of two or more phase separated materials, where one or more dispersed phase is in nanoscale and a polymeric major phase. Materials can be referred to as nanoscaled when their size, meaning at least one of the three external dimensions range from approximately 1 nm to 100 nm [1]. Nanocomposites can be processed by conventional wet and dry processing techniques, yet in adjusted conditions vs. their neat counterparts. Polymer nanocomposites and nanoparticles can also be applied as nanocoatings, meaning a deposited nanoscale layer on selected substrates to reach specific surface behavior [2,3].

There are a number of nanoparticles that have been reported to be used in the formulation of nanocomposites and which definition can be consulted in many extensive prior literature [4]. Those are generally divided in fibers (1D) platelets (2D) or particles (3D) depending on the number of dimensions they display in the nanoscale [5] and they generally differ from the microparticles commonly used in the composite sectors by a greater surface area. Among the polymeric matrix nanocomposites, since they are readily industrially available and low cost, nanoclays are among the most studied scientifically but are also the object of a number of commercial trials since the first work categorized as nanocomposites from Toyota leading to using nylon 6-clay hybrids in car equipment in 1989 [6]. Nano-oxides like  $\text{TiO}_2$ ,  $\text{ZnO}$ ,  $\text{SiO}_2$  are also extensively used in the literature and commercial applications to provide respectively for example self-cleaning properties, UV protection or tailored rheological behavior. Carbon nanotubes and more recently Graphene are gaining greater attention since their excellent intrinsic properties and

unique structures open up new prospects as their production processes become more efficient, leading to greater availability and lower costs.

The nanocomposite performance depends on a number of nanoparticles features such as the size, aspect ratio, specific surface area, volume fraction used, compatibility with the matrix and dispersion. In fact, although a long time has gone in the nanocomposites' era, the dispersion state of nanoparticles remains the key challenge in order to obtain the full potential of properties enhancement (flame retardance, mechanical, barrier, thermal properties, etc.) at lower filler loading than for microcomposites. Not only can the nanoparticles themselves explain the observed effects, the impact of the interface between the matrix and particle also plays a very important role. Indeed, the extremely high surface area leads to change in the macromolecular state around the nanoparticles (e.g., composition gradient, crystallinity, changed mobility, etc.) that modifies the overall material behavior [7].

The nanoparticles dispersion can be characterized by different states at nano-, micro- and macroscopic scales. For example, nanoclay based composites can show three different types of morphology: immiscible (e.g., microscale dispersion, tactoid), intercalated or exfoliated (miscible) composites [8]. The affinity between matrix and filler increases from tactoid over intercalated to exfoliated clays [9].

The dispersion and nanocoating thickness are generally characterized off line through the use of electronic microscopy [10,11], X-ray diffraction, etc [12]. As opposed to standard composites, nanocomposites present the advantage to be potentially transparent although the optical properties can be highly affected by the nanocomposite morphology.

Several strategies have been used to improve dispersion quality, including either chemical or physical approaches. Surface modification to enhance the compatibility of the matrix and fillers is often used, for example through the grafting of organosilanes, or through the use of long chains alkyl ammonium clay platelets intercalating ions [13,14]. Alternatively, when applicable, in situ polymerization may be preferred to reach a good dispersion state that is sometimes difficult to reach when processing nanocomposites in highly viscous media [15,16].

In terms of physical methods, besides the use of mechanical mixing methods (high speed mixer, extruder, etc.), the application of ultrasonic vibrations has been reported to be effective in enhancing the dispersion state of nanoparticles both in solutions and melt polymers [17]. Electromagnetic fields application or high shear [18]/compression in one direction are also reported methods that can help in orientating the nanoparticles to create a structure that can, for example, maximize the gas tortuosity to limit the permeation across a packaging, reduce the flammability or increase the mechanical properties in a given direction.

Nanocoatings in turns allow maximizing the concentration in nanofillers on the surface of a material to create a specific effect while requiring a lower amount of nanoparticles than when dispersed in the bulk.

Nanocoatings can be applied by different technologies such electro spray that can apply nanoparticles-based layers as opposed to established processes such as chemical or physical vapour deposition that rather allow the application of a continuous layer on an atomic scale. Electro spray present the advantage to work at atmospheric pressure and is therefore easily integrated in continuous production lines. Nanocoatings allow surface functionalization to provide specific properties such as antimicrobial [19], self-healing [20], flame retardant [21], gas barrier [22], which are of interest for textiles [23], solar panels [24], packaging [22] and automotive fields [25] among others.

This review gives an insight on the application of nanocomposites and nanocoatings with a special focus on their prospects for:

- food and cosmetic packaging
- solar energy, especially organic photovoltaics
- automotive structural parts

In terms of packaging, different properties can be enhanced through the use of nanocomposites such as the gas barrier, antimicrobial properties, etc. The most frequently tested nanofillers are nanoclays montmorillonite (MMT) and kaolinite, carbon nanotubes (CNT) and graphene nanoplates (GNP) [26]. The improvement of barrier properties could more especially benefit biopolymers which generally have limited intrinsic barrier properties. Additionally, surface coatings can be used for modulating

surface affinity of the packaging towards different liquids and pastes, e.g., to obtain water repellent paper-based packaging [27] or easy-to-empty features [28].

In terms of automotive applications, mechanical and electronic properties, thermal isolation, wear resistance and flame retardance are of interest among other improvements that can be provided by nanocomposites. In terms of mechanical reinforcement, whereas standard toughening additives and fillers normally lead to opposite variation of toughness and stiffness, the specific effect of nanoparticles allowing to improve both can benefit in the design of parts that comply similar structural functions at lower weight than micro-composites or neat polymers. Lighter but stronger materials allow optimal fuel consumption and increased safety.

In terms of solar energy, contributing to the multifunctionality and efficiency of solar panels, nanocomposites and nanocoatings are of relevance either in the photoactive layers, in protective layers, or on the surface of the solar panels. Energy harvesting by fullerenes have already been reported in the organic photovoltaic (OPV) industry [29]. As for packaging, for the outer layer, the use of nanostructured materials has been found to improve humidity, gas and UV barrier properties of solar cells in general. Nanotexturized surfaces and nanocoatings have been developed to provide self-cleaning effects to solar panels [30], therefore minimizing the requirements for maintenance while maximizing the energy yield.

In the subsequent sections, we review the different processing technologies that are used for nanocomposites conversion (including wet chemical and thermoplastic processing), as well as the common and new nanodeposition approaches with a specific focus on electrospray. The limitations and required process improvements are then discussed showing the challenges in nanoparticles dispersion.

In a following section, the different properties that can be enhanced using nanocomposites are reviewed, including barrier, mechanical, electrical/electronic, microwave absorbing properties and flammability resistance. Processability and compatibilization issues are also commented. The surface properties resulting from nanocoatings are then reported. The polymer nanocomposites applications are covered with a main focus on packaging, solar panels, and automotive sectors as well as a few words on other applications of interest.

Finally, the review gives some insights on safety and regulatory aspects that would influence the market uptake for new nanocomposites.

## 6.2 Processing

### 6.2.1 Nanocomposites

Several techniques have been developed for the preparation of polymer nanocomposites. The most important techniques are:

- Intercalation of the polymer
- In-situ intercalative polymerization
- Melt intercalation
- Direct mixture of polymer and particulates
- Template synthesis
- In-situ polymerization
- Sol-gel process

Intercalation processes is used for preparation of polymer-based nanocomposites, which contain layered silicates, as shown in **Figure 6.1**. In this method, a solvent is used in which the polymer or pre-polymer is soluble, and the silicate layers are swellable. Nanocomposites prepared with this method have structures ranging from intercalated to exfoliated, depending on the degree of penetration of the polymer chains into the silicate galleries. Hence, this has become a standard method for the preparation of polymer-layered silicate nanocomposites [31,32].

When the polymer is unable to intercalate between the silicate sheets, a phase-separated composite is obtained, which have the same range of properties as that of traditional microcomposites (**Figure 6.1**). On the other hand, when polymer matrix enters between the layered silicates then intercalated nanocomposites structure occurs in a crystallographically regular fashion, regardless of the clay to polymer ratio. A well-ordered multilayer morphology built up with alternating polymeric and inorganic layers is generated. Normally, only a few molecular layers of polymer can be intercalated in these materials [31].

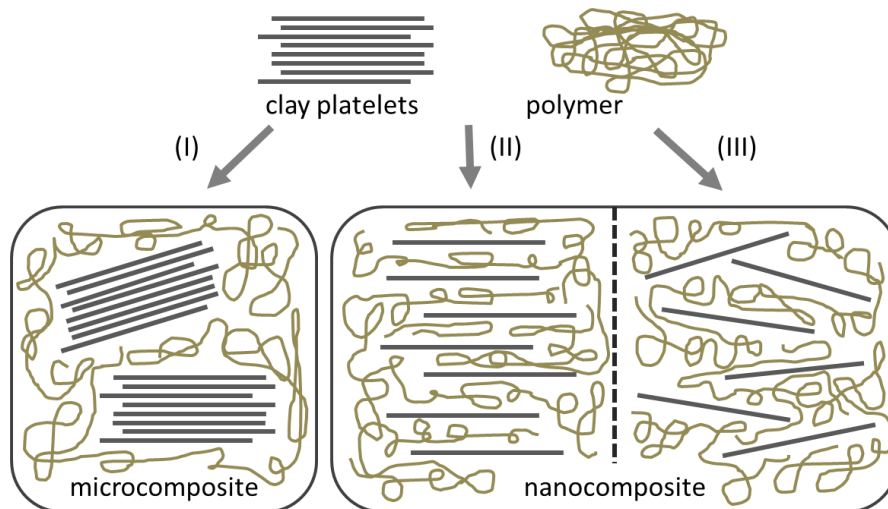


**Figure 6.1.** Different types of composites arising from the interaction of layered silicates and polymer. (I) Phase separated microcomposite, (II) intercalated nanocomposites and (III) exfoliated nanocomposites. Adapted from [31].

In-situ polymerization method encasing the layered silicate within the monomer solution, polymer formation starts between intercalated layered sheets by heat or radiation, suitable initiator or catalyst [15,16]. In the melt intercalation method, a mixture of the polymer and layered host are annealed above the softening point of the polymers statistically or under the shear. Diffusion of polymer chains from bulk polymer melt into the galleries between the host layers during the annealing process (**Figure 6.2**) [33,34].

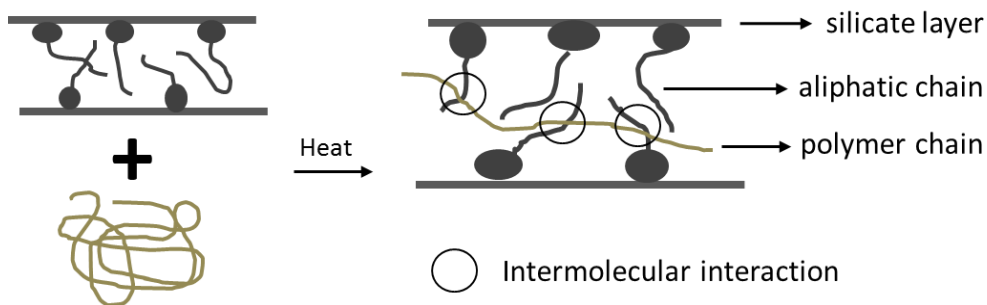


**Figure 6.2.** Melt intercalation synthesis of polymer/clay nanocomposite. Adapted from [27].

In the template method, a template is used to form nanocomposite materials of particular shape for example layered, hexagonal shape, etc. The soluble polymer acts as a template for the formation of layers. This method is widely used for the synthesis of mesoporous materials but less developed for the formation of layered silicates [35,36]. In the direct mixing method, polymer or monomers are directly mixed with reinforcing phase [37]. In

the in-situ polymerization method inorganic particles are dispersed into a precursor of the polymer matrix (monomer) and then polymerization of the mixture is done by addition of appropriate catalyst. In this method, simultaneous formation of nano particle and polymerization process occur [38,39].

Carbon-nanotubes (CNTs)-reinforced polymer nanocomposite materials are generally prepared by different methods, including direct mixing, solution mixing, melt-mixing and in-situ polymerization. Similarly, different processing techniques, mostly chemical and electrochemical methods, have been employed for the preparation of conducting polymer nanocomposites [40].

Despite the successful use of these different methods for the preparation of polymer-based nanocomposites, information on various factors is still lacking, such as the use of an appropriate method for a specific matrix reinforcement combination or the maximum amount of reinforcements to give optimum property combinations and lower the cost of the processes, etc. Therefore, it is still necessary to look into these aspects including the use of simulation and modelling techniques.

The most important requirements for a polymer-based compound reinforced by nanoparticles are the combination of an optimum surface tension (caused by a good compatibility/interaction of the particle surface with the matrix) with a maximum dispersion of the separated/exfoliated particles.

The physical requirements to achieve it are:

- similar to equal surface energy of polymer and particle surface
- low agglomeration energy
- low polymer viscosity
- high mixing efficiency in the process.

Due to the relatively high viscosity of polymers even at high temperatures, the best results can be generated by pre-dispersing surface-treated, i.e., organomodified particles in higher concentration (20–50 wt. %) before “diluting” this masterbatch in the viscous matrix using a twin screw extruder with high throughput.

Based on these requirements and the cost-performance ratio, there are three different ways for the production of nanoparticle-based composite concentrates to achieve an

optimum, i.e., homogeneous, pre-dispersion and exfoliation of the particles/platelets in a thermoplastic polymer matrix:

- **In-Situ:** The monomer is introduced between particle agglomerates or clay platelets by previous homogeneous mixing of the particles with the monomer or swelling of the agglomerates in the monomer and then polymerizing the monomers in between the particles (high solid content).
- **Direct:** Polymerization and incorporation between nanoparticle agglomerates are performed together simultaneously. The polymerization is started after premixing the components by using temperature to initiate polymerization (e.g., radical initiators) or by a catalyst.
- **Co-Precipitation:** Nanoparticles and low viscous solutions of the polymer are mixed together to form a homogeneous solution, then the finely dispersed polymer plus nanoparticle mixture is co-precipitated by adding another non-miscible solvent or by evaporating the solvent.

### 6.2.1.1 Wet Chemical Processing

In wet processing techniques, solutions or suspensions are used for the formation of thin layer films, resulting in either stand-alone films (casting) or coatings on different substrates. When polymer based coatings are applied to a substrate via lacquering or spraying, which are the mainly applied techniques, the rheological properties of the coating formulation are decisive [41]. Drying techniques vary from ambient conditions drying to conventional hot air drying, infrared to microwave energy drying, while each method influences the film or coating properties [42]. Compared to extruded coatings, the applicable coating weight can be much lower, maintaining the desired barrier properties [43].

The use of nanoparticles in coating dispersions can bring many advantages to the resulting coating properties. Compared to multilayer films, nanocoatings demand lower material usage [27], being both an economic as well as ecological advantage. Additionally, surface coatings can be used for modulating repellent properties on various surfaces, e.g., for water repellent paper-based packaging [27] or easy-to-empty features [28]. For paper coatings, the most used nanomaterials are nanoclays, inorganic pigments, minerals, ceramics and starch [43].



### 6.2.1.2 Thermoplastic Processing

Thermoplastic “dry” processing of polymers is mainly performed via extrusion, one of the most important polymer processing techniques. Extrusion allows melting a polymer with a high energy input during short time. Due to the supply of heat and energy input caused by friction between the screws, the mass melts, becomes formable and is pressed through the extruder die [44]. During the whole process, the mass can be compressed, mixed, plasticized, homogenized, chemically transformed, degasificated or gasificated [45,46]. When incorporating nanoparticles into polymeric compounds, different types of nanocomposites are possible. When processing the mostly desired exfoliated nanocomposites, the dispersion quality mainly depends on the extruder and screw configuration [47]. Exfoliation is favored at high shear rates [9], while longer residence time favors a better dispersion [47]. Also, the location where the nanoclay is introduced has been shown to be an important factor [48]. However, the major factor whether a good dispersion or exfoliation is possible is the thermodynamic affinity between the nanoclay/nanoparticle and the polymer matrix [8]. When attractive interactions between the matrix and nanoclays are not sufficient, intercalation is reached, while exfoliation can be obtained when strong attractive interactions are present [49]. **Figure 6.3** shows how exfoliation can be achieved via extrusion/melt processing [8].

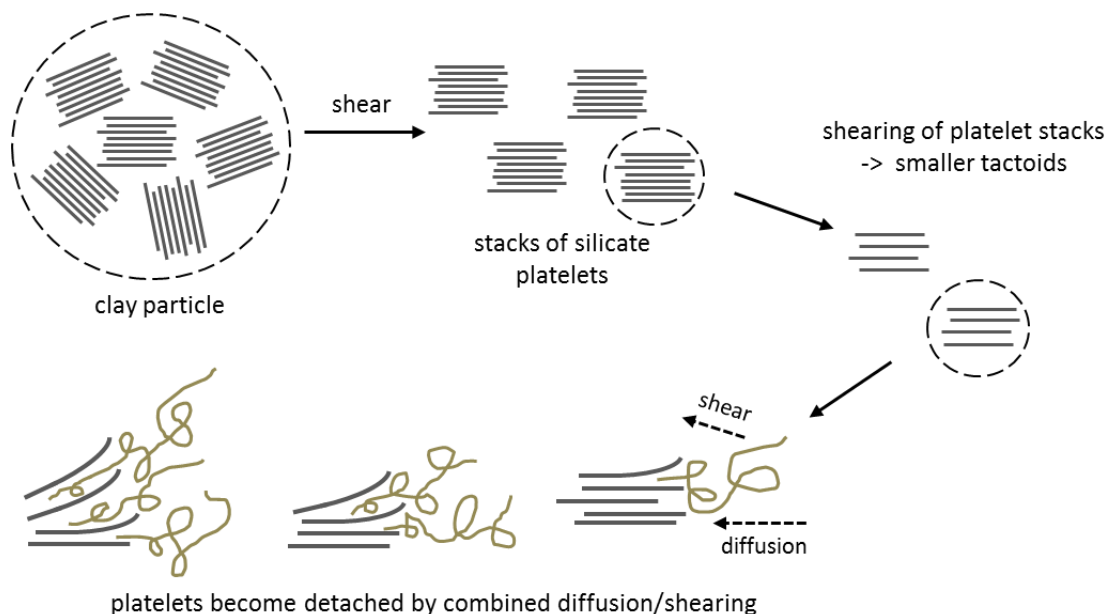


**Figure 6.3.** Mechanism of clay dispersion and exfoliation during melt processing. Adapted from [48,50].

The most widely used melt processes especially in packaging and automotive fields are injection molding, film extrusion and extrusion coating. Since many different process parameters have a direct influence on the processed materials, Taguchi methods are commonly used in plastic injection molding industry as a robust optimization technique for applications from product design to mold design; and from optimal material selection to processing parameter optimization. Villmow et al. [51] studied the influence of injection molding parameters on the electrical resistivity of nanocomposites formed by polypropylene (PP) and carbon nanotubes (CNT) using a four-factor factorial design maintaining pressure, injection velocity, mold temperature and melt temperature. Sample with lower melt temperature and higher injection velocity shown a better dispersion compared with those injection molded at low velocity and high melt temperature [51]. Chandra et al. [52] summarized their research on polycarbonate (PC) and CNT nanocomposite in order to achieve homogeneous distribution of CNT and to obtain high electrical conductivity the nanocomposites should be processed at high melt temperatures and low injection speeds to ensure proper and uniform electrical conductivity [52]. Recently, the F. Stan group has undertaken a study about the influence of the process parameters in the nanocomposite (PP/CNT) to improve the mechanical properties. The injection molding parameters affect the degree of crystalline morphology of the molded polymers. Therefore, these effects could affect the physical and mechanical properties of the injection molded parts. On the other hand, the effect of crystallinity on the mechanical properties is less significant than the effect of the CNT. Their research work concluded that the most significant injection molding parameter is the injection pressure [53].

Additionally, the use of compatibilizers can change the optimal parameters for the process. Constantino et al. studied the microstructure of the same nanocomposites PP/nanoclay produced by a non-conventional method of extrusion, SCORIM (Shear Controlled Orientation in Injection Molding). This method is based on the concept of in-mold shear manipulation of the melt during the polymer solidification phase. The degree of clay exfoliation not only depends on the affinity and compatibility of the organoclay with the matrix, but also on the shear stress which is an extrinsic factor dependent on processing conditions and clay loading. High shear rate induced a thicker skin, while high temperature induced a thinner skin [18]. An interesting work was made by P.F. Rios, comparing the behavior of different polymers with the same nanofiller. He studied the influence of injection molding parameters in high-density polyethylene (HDPE),

polyamide 6 (PA6), polyamide 66 (PA66), polybutylenterephthalat (PBT) and polycarbonate (PC) with carbon nanotubes. The main objective was to evaluate the electrical resistivity, thermal conductivity and the mechanical properties. The literature reveals how the different parameters of the injection molding process might directly affect the quality of the injected part and their properties. The formulation is important, but the process parameters can be shown to have significant role too [54].

Film extrusion applications (mono- and multilayer) are found in food packaging sector, as coating substrates, ostomy films, etc. Typically, the coextrusion technology is used to obtain a multilayer film formed by different materials or compositions [55]. An example is found in the food packaging sector, the nanoreinforcement could be clays, silicates, cellulose-based, carbon nanotubes, graphene, starch nanocrystals, chitin/chitosan nanoparticles, silica nanoparticles ( $\text{SiO}_2$ ), and others. Each one has a function into the nanocomposite film, such as antimicrobials, among which the most common for food packaging are based on silver;  $\text{O}_2$  scavengers, nanosensors (reactive nanoparticles), etc. [56]. As discussed above, each type of nanofiller can influence the optimum process parameters. All systems should be optimized to obtain a homogenous material, and in the case of multilayer film, it is necessary consider the influence of the position, a number of layers and their thickness. When it comes to improving the productivity of the line, it is important to have an adequate measurement system and control, coupled to a head rapid response [57].

Extrusion coating is commonly applied on foil, paper, or fabric with polyethylene (PE), by extruding a web directly into the nip of a pair of rolls through which the substrate is passing. The high temperature is necessary to promote surface oxidation of the resin and to ensure adequate adhesion to the substrate [58]. The use of nanoparticles in extrusion coatings can generate or enhance properties like water vapor barrier, mechanical or heat sealing.

### **6.2.2 Nanodeposits**

Nanostructured coatings or nanocoatings consist in the covering of materials with a layer of materials at the nanometer scale according to the definition mentioned above, or covering of a nanoscale entity, to form nanocomposites and nanostructured materials using conventional or novel procedures such as vapor deposition, plasma-assisted/ion-beam-assisted techniques, chemical reduction, pulsed laser deposition, mechanical

milling, magnetron sputtering, self-assembly, layer-by-layer coating, dip coating, sol-gel coating, TUFT (tubes by fiber templating) process, electrochemical deposition, sol-gel techniques or electro-hydrodynamic processing (comprising electrospraying and electrospinning techniques) [23,59]. Nanocoatings have been demonstrated to be highly applicable in the functionalization of surfaces to provide specific properties such as antimicrobial [19], self-healing [20], flame retardant [21], gas barrier [22], etc. Much research has already been carried out in the biomedicine [60-63], sensors and electronics [64,65], textiles [23], solar panels [24], lithium-ion batteries [66], construction materials [67-69], packaging [22] and automotive fields [25], among others.

### **6.2.2.1 Common Processing**

The most common technologies for the roll-to-roll deposition of thin layers belong to the class of gas phase processes. These processes allow to coat flexible substrates with nano-scale inorganic or polymeric layers with thicknesses in the nanometer region up to some hundreds of nanometers [70].

Depending on the deposition mechanisms, gas phase processes can be classified as physical vapor deposition (PVD) or chemical vapor deposition (CVD). PVD processes are performed in a high vacuum and are based on the transfer of the solid coating material into the gas or vapor phase followed by the condensation on top of the substrate [71]. Typical materials to be deposited are metals and metalloids as well as their oxides, nitrides and carbides. The deposition of compounds is possible by reactive processes which are based on a chemical reaction between the material and process gases like O<sub>2</sub>, N<sub>2</sub> or hydrocarbons, respectively.

The gaseous phase of the coating material is obtained either by evaporation due to electrical resistance heating or electron beam irradiation or by sputtering [71]. In the latter process, atoms of the solid coating material are released due to the impact of atoms of the process gas which were ionized and accelerated by an electrical field. The quality and barrier properties of the deposited layer can be improved by a magnetic field application during the process (magnetron sputtering) [72]. The fabrication of thin metal films on polymeric surfaces via PVD are commonly used techniques for the class of metal-polymer nanocomposites [73].

CVD processes are based on chemical reactions of gaseous precursors on the substrate surface [71,72]. The reactions are activated either by heat or by a plasma (PECVD = plasma enhanced CVD). These processes allow the deposition of inorganic or polymeric materials, e.g.,  $\text{SiO}_x\text{C}_y\text{H}_z$  [72], graphene [74] and parylene [75].

ALD (atomic layer deposition) is a modified version of a CVD process [71,76]. It allows the deposition of nearly defect free barrier layers which are well suited for the encapsulation of organic electronic devices.

The largest amount of layers produced by PVD or CVD processes on flexible substrates is used in food packaging technology [71]. The layers significantly reduce the permeation of oxygen and water vapor through packaging films and therefore increase the shelf life of packaged products. However, vacuum deposited layers are not completely tight since they contain defects formed during the deposition process (**Figure 6.4**) or due to mechanical stress [70,71]. The protection of vacuum insulation panels, flexible photovoltaic modules and organic light emitting diodes (OLEDs) against environmental influences therefore requires the combination of these layers with polymeric materials in complex multilayer structures exhibiting a high barrier performance [77-79].

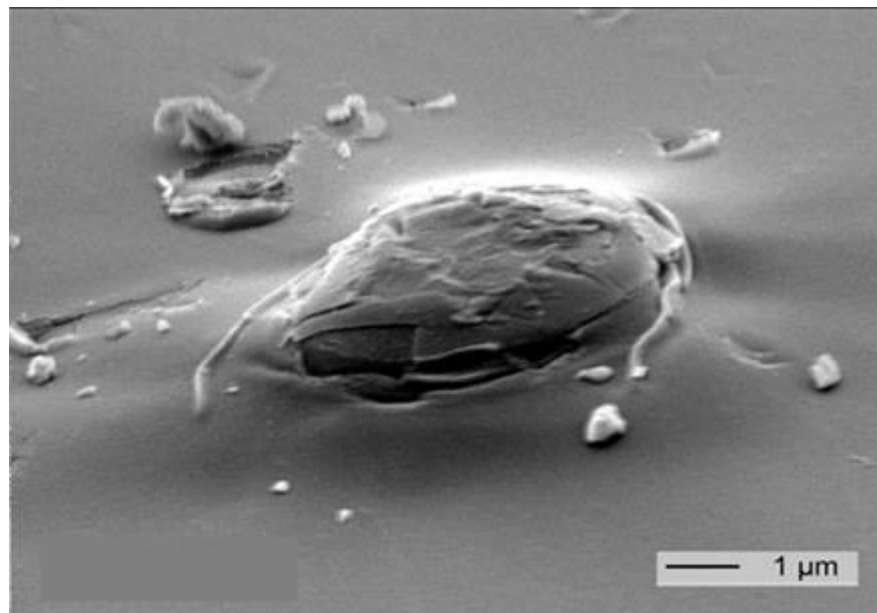


**Figure 6.4.** Surface of a polyethylene terephthalate film with particle, partially covered by a  $\text{SiO}_x$  layer [80].

Further applications of vacuum processing of polymer films cover the deposition of electrical conducting layers as transparent electrodes or to obtain antistatic properties as well as the modification of their optical properties [71].

### **6.2.2.2 Electrospaying**

Electro-hydrodynamic processing is a micro and nanofabrication technology comprising electrospinning and electrospaying [81,82]. Electrospinning is a process that produces continuous polymer fibers with diameters generally in the submicrometer range through the action of an external high-voltage electric field imposed on a polymer solution or melt. The electrospun nanostructures morphology is affected by the solution properties (mainly by the viscosity, surface tension and conductivity of the polymer solution) and by the process parameters (voltage, flow rate of the solution, tip-to-collector distance). Under certain conditions, capsules in the micro and nanoscale range can be obtained by adjusting the solution properties and the process parameters (e.g., lowering the polymer concentration and/or increasing the tip-to-collector distance), this particular process is generally known as electro-hydrodynamic atomization or electrospaying. Thus, electrospaying is a cost-effective technique that uses a uniform electro-hydrodynamic force to break up the liquids into fine particles. The injector is usually made in the form of a metal capillary, which is biased by a high voltage. When the electric repulsion in the solution or suspension exceeds the liquid surface tension a jet of droplets is produced [83-85].

The electro-hydrodynamic processing (EHDP) techniques are of particular interest as an alternative to conventional deposition and coating techniques since the latter ones require a controlled pressure and temperature environments. Compared to other deposition techniques, electrospay deposition (ESD) offers the advantage of a high deposition efficiency (up to 80%) and a reduction of the process steps [84]. The EHDP has been applied in several fields, mostly at a lab or a pilot scale. Although there have been some industrial efforts to scale up the electrospinning process, it has only been more recently that both techniques, i.e., electrospinning and electrospaying, have been scaled up via multinozzle injectors to an industrial level through companies such as Bioinicia S.L.

## 6.2.3 Limitations and Process Improvements

One of the major problems when processing nanocomposites is the aggregation of nanoparticles, which is followed by an insufficient dispersion in the desired formulations. The agglomeration and aggregation take place due to specific surface area and volume effects [86]. To characterize the dispersion quality, there are different techniques used for structure characterization of nanocomposites, naming X-ray diffraction (XRD), Scanning electron microscopy (SEM), Transmission electron microscopy (TEM), Infrared spectroscopy (IR) or Atomic force microscopy (AFM) [12]. For nanoparticles, TEM is the preferred method to examine the dispersion since polymer structure, void size and shape, filler size, shape and distribution, local crystallinity as well as crystal size can be determined. The degree of intercalation or exfoliation for particles presenting a specific layered organization such as clays can be characterized by XRD [26] and small angle neutron scattering can be used to characterize the fractal organization of amorphous particles like fumed silica [87]. Finally, recent efforts have been reported to monitor nanoparticles dispersion and nanocoating thickness distribution in-line during their processing [88].

### 6.2.3.1 Dispersion Quality and Reaggregation

#### Particle Surface Modification

Most of the inorganic minerals have hydrophilic surfaces and are therefore not compatible with mainly hydrophobic polymer matrices. The aim of fillers surface modification is consequently their hydrophobization to enhance their compatibility with the polymer in order to enable intercalation or exfoliation. The resulting organophilic and hydrophobic clays, the layers of which have lower surface energy, contribute to polymer diffusion between the layers and finally clay platelets delamination [89]. This introduction of organic coatings can be carried out using physical and chemical interactions between filler and modifier.

Physical methods are performed either with low molecular weight surfactants or high molecular weight polymers. Surfactants generally include at least one polar group and an aliphatic chain. The modification is based on preferential absorption of the polar group to the high energy surface of the filler particles [90]. This exchange of inorganic surface cations with organic cations has been widely used for surface modifications of inorganic

clays and conventionally realized with long-chain alkyl ammonium salts [89]. Another characteristic example is the treatment of calcium carbonate with stearic acid, forming a basic salt and decreasing the fillers surface tension and thereby influencing the composite properties [91]. The other technique displays a filler encapsulation with preformed or in-situ-formed polymers, developed by solution or emulsion polymerization, respectively [90].

To avoid modifier desorption from the particle surface, covalent bonds displaying chemical techniques can be used to improve interfacial interactions between the filler and matrix. Chemical surface modifications are mainly achieved via coupling agent treatments such as silane [86], titanate and zirconate to improve the adhesion between the polymer and particles, although here less information is available for nanoparticles than for microfillers [90]. Chemical grafting of macromolecules onto inorganic particles can be achieved through covalent bonding with the hydroxyl groups on the unmodified particle surface [86,90]. Compared to surfactants and coupling agents, this technique shows several advantages due to a wider selection of grafting monomers, enabling a tailor made nanocomposite structuring [90].

Beside conventionally used modifications with alkyl ammonium ions (mainly used for clays), advanced surface modifications of the fillers include modifications with reactive groups, initiator molecules or monomer molecules and several others approaches [89].

### **Ultrasonic Oscillations**

Additional improvement of nanocomposite dispersion quality can be achieved via ultrasonic treatment. Ultrasonic cavitation transfers high amounts of energy, being able to disrupt physical and chemical interactions. Therefore, it has been widely used for dispersing, emulsifying, crushing and activating particles [17]. Additionally, ultrasound energy is able to break C–C bonds, leading to long-chain radicals formation. Those radicals might build chemical bonds on the clay surface in nanocomposite systems [49], and therewith enhance the polymer/filler compatibility but also that of immiscible polymers in general [92]. There are several studies on the use of ultrasonic oscillations for nanocomposite preparation [17,49,93,94]. Isayev et al. used high power ultrasound to break up silica agglomerates in ethylene propylene diene monomer rubber (EPDM), significantly reducing the agglomerate size [94]. Xia et al. ascertained reduced aggregation of nanosilica particles and also a redispersion in aqueous systems under



ultrasound [17]. Lapshin et al. developed an ultrasound aided extrusion process for polyolefin-clay nanocomposites using MMT clays modified with quaternary ammonium salts in different polyolefin matrices. They detected increased basal spacing and even individual dispersed clay layers after ultrasonic treatment proved by TEM images [49].

### **Mechanical Alloying**

This technique generally influences the particle size and shape for the synthesis of nanoparticles to prevent excessive aggregation at the following preparation of nanocomposites. Surfactant-assisted mechanical milling and alloying lowers the tendency to agglomerate by giving a steric barrier and also lowering the surface tension [95]. The milling process for crystalline nanoparticles with high energy ball milling can be divided into three stages. First, the particles undergo deformation localization in the shear bands, followed by a grain structure in nano-dimensions. The third stage is characterized by a random orientation of the grain and a peel off of single crystal nanoparticles [96]. With the aid of surfactants, hydrophobic surfaces can be obtained during the process prevent the newly formed fine particles from aggregation and determine size and shape of the final product, depending on the surfactant, grinding material and process, respectively [95]. Nandhini et al. produced nanocarbon with sizes ranging from 80 to 500 nm from graphite using sodium dodecyl sulphate/sodium dodecyl benzene sulfonate as surfactant in a high energy ball milling process [97]. Calcium carbonate particles of about 40 nm size could be obtained from a one-step grinding process, showing enhanced dispersion and grinding of particles when poly (acrylic acid, sodium salt) was used as surfactant [98]. Therefore, high energy ball milling can be applied for the production of various nanopowders that show good properties for the utilization in nanocomposites [99].

## **6.3 Material Properties**

### **6.3.1 Nanocomposites**

The development of polymer nanocomposites is currently one of the most active areas in the field of nano-enabled materials. As discussed, the simplest process strategy is just adding appropriate nanoparticles to a polymer matrix to enhance its performance often dramatically by simply capitalizing on the nature and properties of the nanoscaled filler. This strategy is particularly effective in yielding high performance composites [32,100-111], when good dispersion of the filler is achieved then the properties of the nanoscale

fillers are substantially better than those of the matrix. That is why mainly very hard and stiff materials (minerals: oxides and silicates, carbon nanotubes) are used to optimize the main disadvantages of standard polymers [112] compared with the main competitive metal and glass materials: low modulus, insufficient creep resistance, low hardness/low scratch resistance, insufficient barrier properties, high flammability-low temperature resistance.

Nanofillers can significantly improve or adjust most of the different properties of the polymer base materials in which they are incorporated, sometimes also in synergy with conventional fillers and/or additives.

### 6.3.1.1 Barrier Properties

Traditional packaging materials include metallic materials, ceramic (glass), cellulosic (paper and cardboard) and polymers. Due to the low weight, low cost, easy processability and the diversity of the chemical and physical properties of organic polymers, these are the most employed materials nowadays in the food packaging sector (around 40% of market share) [113]. The most frequently polymers employed for food packaging include polypropylene (PP), polyethylene terephthalate (PET), various types of polyethylene (LDPE, HDPE, etc.), polyvinyl chloride (PVC) and polystyrene (PS). Although polymeric materials have revolutionized the packaging sector and exhibit many advantages over traditional materials, their main disadvantage is their inherent permeability to gases and other small molecules. **Figure 6.5** compares the permeability to oxygen and water vapor for different polymeric materials.

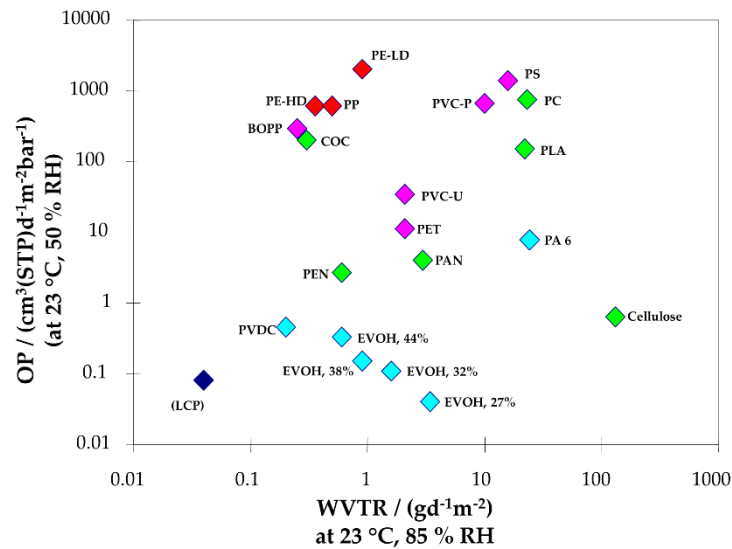


**Figure 6.5.** Comparison of oxygen permeability (OP) and water vapor transmission rate (WVTR) properties for different polymers normalized to 100  $\mu\text{m}$  thickness [114].

In general, the permeability of moisture or oxygen through polymers depends on various interrelated factors, which include:

- Structural characteristics and polarity of the polymeric chains
- Hydrogen bonding features and other intermolecular interactions
- Polydispersity and molecular weight
- Degree of cross-linking or branching
- Synthesis method and processing technology
- Crystallinity

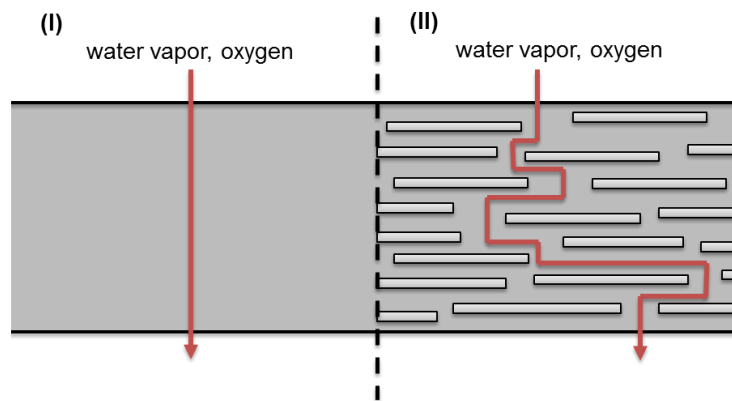
The permeability to a specific molecule can be affected by the presence of others. For example, ethylene vinyl alcohol (EVOH), provides excellent barrier properties to oxygen in dry conditions. However, in very humid conditions (e.g., >75% relative humidity), its oxygen transmission rate can be increased by one order of magnitude, due to the swelling of the polymer by the presence of water molecules [115-119].

Because there is no pure polymer that exhibit all the required barrier and mechanical properties for every packaging application, polymer blends or complex multilayer systems are widely used. For example, to provide a high barrier to oxygen in a very humid

environment, a material such as EVOH, which is sensitive to water, but very high barrier to oxygen, can be sandwiched between two layers of a hydrophobic polymer like PE [55,119,120]. Direct blending of polymers is also a used strategy to achieve desired barrier properties that cannot be obtained with monolayers of polymers [120-122]. Unfortunately, while polymer blending and multilayer films have afforded packaging materials with good barrier properties, these systems present high production costs, require the use of special adhesives that complicates their regulation, and are very difficult to recycle. Therefore, there still a great interest in the polymer industry to generate monolayer films with improved mechanical and barrier properties.

Polymeric nanocomposites are the latest materials aimed at solving the aforementioned problems [123]. Polymeric nanocomposites are prepared by dispersing nanoscale fillers throughout a polymeric matrix. In the literature, it many examples of polymeric nanocomposites containing as fillers layered materials such as clays, silicate nanoplatelets or graphene (Section 6.4.1.1), SiO<sub>2</sub> nanoparticles [124], carbon nanotubes [125], starch nanocrystals [126], cellulose nanofibers and nanocrystals [127-130], chitosan nanoparticles [131,132] and other nanomaterials can be found.



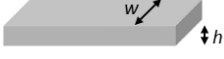
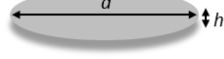
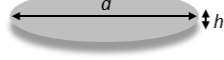
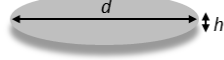
The dispersion of nanofillers into the polymer matrix affects the barrier properties of a homogeneous film in two ways. The first way is by the creation of a tortuous path for the diffusion of gas [133]. Due to the impermeable nature of the nanofillers, the molecules of gas must diffuse around them instead of taking a straight path perpendicular to the surface of the film. As a result, the mean path for the diffusion of the gas through the film is longer with the presence of nanofillers **Figure 6.6.** [134].



**Figure 6.6.** “Tortuous pathway” created by incorporation of exfoliated clay nanoplatelets into a polymer matrix film. In a film composed only of polymer (I), diffusing gas molecules on average migrate via a pathway that is perpendicular to the film orientation in a nanocomposite (II), diffusing molecules must navigate around impenetrable particles/platelets and through interfacial zones which have different permeability characteristics than those of the virgin polymer. Adapted from [134].

Taking into account this mechanism, it is evident than among all the different shapes of nanomaterials (spheres, fibers, rods, tube, plates), layered nanomaterials (2D) are the most appropriate ones to improve the barrier properties and therefore this type of materials is the most studied for this application (Section 6.4.1.1). Different models to predict barrier properties of nanocomposites depending on the filler geometry and the ratio have been proposed and are listed in **Table 6.1**.

**Table 6.1.** Models for predicting barrier properties of platelet filled nanocomposites [8].

Model	Filler Type	Particle Geometry	Formulas	Reference
Nielsen	Ribbon <sup>a</sup>		$(P_0/P)(1 - \phi) = 1 + \alpha\phi/2$	[135]
Cussler (Regular array)	Ribbon <sup>a</sup>		$(P_0/P)(1 - \phi) = (1 + \alpha\phi)^2/4$	[136]
Cussler (Random array)	Ribbon <sup>a</sup>		$(P_0/P)(1 - \phi) = (1 + \alpha\phi/3)^2$	[136]
Gusev and Lusti	Disk <sup>b</sup>		$(P_0/P)(1 - \phi) = \exp[(\alpha\phi/3.47)^{0.71}]$	[137]
Fredrickson and Bicerano	Disk <sup>b</sup>		$(P_0/P)(1 - \phi) = 4(1 + x + 0.1245x^2)/(2 + x)^2$ where $x = \alpha\phi/2\ln(a/2)$	[138]
Bharadwaj	Disk <sup>b</sup>		$(P_0/P)(1 - \phi) = 1 + 0.667\alpha\phi(S + (1/2))$ where $S = \text{orientation factor (from } -1/2 \text{ to } 1)$	[139]

<sup>a</sup> For ribbons, length is infinite, width,  $w$ ; thickness,  $t$ ; aspect ratio,  $a = w/h$ ; <sup>b</sup> For disks, circular shape of diameter  $d$  and thickness  $t$ ; aspect ratio,  $a = d/h$ .

Beside nanofiller content and aspect ratio, the state of exfoliation significantly affects barrier properties of nanocomposites [140]. Exfoliation levels are, however, not included and have to be taken into account when using such models.

A second way in which nanomaterials can influence the barrier properties is by causing changes in the polymeric matrix itself. If the interactions nanomaterial-polymer are favorable, the polymer chains in the proximity to the nanomaterials can be partially immobilized. Therefore, the gas molecules that migrate through these interfacial areas will have attenuated movement. The effect of the interfacial region is especially important in polymeric matrices that exhibit very high permeability to gases, such as polyolefins [141].

In any case, every nanomaterial-polymer system is different, and the properties can only be predicted in general terms. The consideration mentioned above demonstrate why the nanomaterials have been successful as fillers for improving barrier properties of polymers. Compared to micrometric fillers, the nanoscale fillers have much higher aspect ratios and, due to this higher surface area to volume ratios, the interfacial volume in a nanocomposite film is much higher than that of a polymer microcomposite formulated from the same materials.

### **6.3.1.2 Mechanical Properties: Reinforcement and Light Weighting vs. Conventional Composites**

Nano fillers are used in polymer matrix to improve mechanical properties such as stiffness, strength via reinforcement mechanism [142-144]. In case of fumed silica, different reinforcement effects were reported depending on the nanoparticles dispersion state, surface area, polydispersity, and organo-modification, possibly leading to their grafting to the matrix [145]. It is proved that properly dispersed and aligned clay platelets are very effective to improve stiffness of polymer matrix material. By comparing the increase in the Young's modulus,  $E$ , of injection molded composites based on nylon 6, relative to the modulus of the neat polyamide matrix,  $E_m$ , when the filler is an organoclay versus glass fibers [142]. In this example (**Figure 6.7**), increasing the modulus by a factor two relative to that of neat nylon 6 requires approximately three times more mass of glass fibers than that of MMT platelets. Thus, the nanocomposite has a lightweight advantage over the conventional glass fiber composite. Furthermore, if the platelets are aligned in the plane of the sample, the same reinforcement should be seen in all directions within

the plane, whereas fibers reinforce only along a single axis in the direction of their alignment [144]. In addition, the surface finish of the nanocomposite is much better than that of the glass fiber composite owing to nanometer size of the clay platelets compared to the 10–15  $\mu\text{m}$  diameter of the glass fibers.

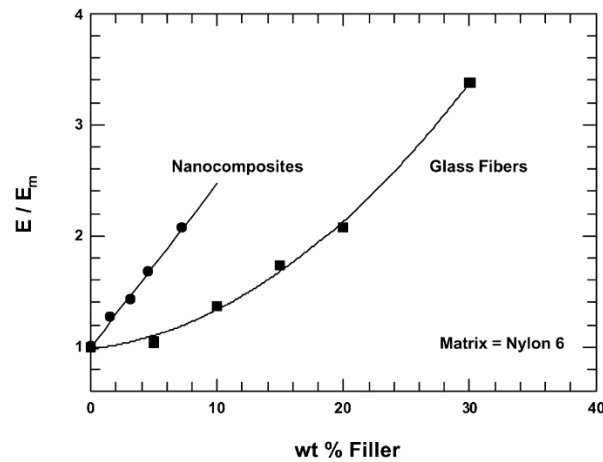


**Figure 6.7.** Comparison of modulus reinforcement (relative to matrix polymer) for nanocomposites based on montmorillonite (MMT) versus glass fiber for a PA 6 matrix [142].

The modification of the polymer matrix with clay seems to be a proper mean to increase the mechanical stability of the polymer melt. This effect is advantageous for some polymer processing techniques like blown film manufacturing or extrusion blow molding. Due to their ability to act as a nucleating agent, clay particles may induce changes in the crystallinity (morphology and crystal type) of the matrix polymers like PA6 or PP [146,147].

Several characteristics of polymers can be influenced by the size and geometry of the nanoparticles, e.g., the Young's and shear moduli [148-154], the thermal expansion coefficient [148,150,155], the thermal [156,157] and the electrical conductivity [158]. Furthermore, it was shown that, even when the polymer matrix evolves from the glassy state to a rubbery state, the influence of nano-reinforcement on the thermo-mechanical response is still observable [159-162]. It can be concluded that polymer nanocomposites are favorable in many industrial domains such as aerospace, automobile, and electronic packaging, where they act as multifunctional structures.

The interface is an important characteristic for nanocomposites. Therefore, a lot of energy has been invested to describe the mechanical response and determine its effective stiffness and volume fraction (or thickness) [148,149,151,152,156,157,160–173].

However, up to now, problems in the experimental visualizations in nanoscale hindered from understanding the exact thickness and properties of the interphase region. Consequently, the dimension of interphase layer in nanocomposites was mostly analyzed by indirect methods. For example, the glass transition temperature was determined for the continuous polymer and additionally for the interphase by DSC (differential scanning calorimetry) by Mortezaei et al. [171]. In comparison, thermally stimulated depolarization currents (TSDC) were used by Fragiadakis et al. [172]. Based on that, they calculated the dielectric strength of the corresponding relaxation. This they connected with the degree of crystallinity of the bulk polymer and then calculated the interfacial region. AFM (atomic force microscopy) was used by Bhuiyan et al. [165-166] in order to estimate the morphological changes of the regions around the particle surface.

Apart from measurements, mechanical design and modelling have been used to understand and investigate the reinforcing effect of the intermediate medium between nanoparticles and the surrounding polymer. Therefore, nanocomposites have been considered as a three phase multi-inclusion using a continuum model. The third phase is the densified polymer region of the nanoparticle, which is represented as an independent and different material. Consequently, it shall be possible to characterize the material first by experiments. In the next step, the constitutive equation of the micromechanics model or the numerical solution of the finite element shall be fed with information about the particles and the homogeneous phase. Information about the third phase—the interphase—can then be extracted by solving the equations inversely.

As mentioned before, DSC can be used for evaluating nanocomposites. However, the degree of crystallinity and crystallization rate can be affected by crystallization in narrow spaces. If the space is so narrow, that the spherulitic growth is restricted, primary nuclei are not available for heterogeneous crystallization. Consequently, homogeneous nucleation appears. This can lead to a low crystallization rate, degree of crystallinity and melting point. This was witnessed in phase separated block copolymers [174,175] and polymer blends [176]. Moreover, restricted crystallization of linear polyethylene in nanoporous alumina led to homogeneous nucleation for pore radii of 31–55 nm but heterogeneous nucleation for 7.5–24 nm pores [177]. Syndiotactic polystyrene [178] as well as linear polyethylene [179] showed decreased crystallinity versus bulk crystallization in nanoporous alumina. By adding nano-particle incorporation in a polymer, parallels to



confined crystallinity, nucleation effects and disruption of attainable spherulite size appear.

With the incorporation of inorganic and nano particles, nucleation of crystallization can appear. At nano scale, the nanoparticle can replace for the lack of primary nuclei consequently rivalling with the confined crystallization. At higher nanoparticle concentration, lower crystallization kinetics can be obtained due to the higher viscosity (lowered chain diffusion rate). Here it becomes obvious, that the crystallization process underlies multiple factors and is affected by many causes. At low concentrations, nucleation of crystallization was observed by the onset temperature of crystallization ( $T_c$ ) and crystallization half-time. This was visible in several composites, such as poly-(3-capro-lactone)-nanoclay [180], polyamide 66-nanoclay [181,182], polylactide-nanoclay [183], polyamide 6-nanoclay [184], polyamide 6.6-multi-walled carbon nanotube [185], polyester-nanoclay [186], poly(butylene terephthalate)-nanoclay [187], polypropylene-nanoclay (sepiolite) [188] and polypropylene-multi-walled carbon nanotube [189]. At higher concentrations, rather a delay of the crystallization rate has been monitored. This was even seen in such composites, where nucleation appeared at low concentrations [181,185,187,189–191]. The reason for the retardation of crystallization at higher concentration can be reasoned with diffusion constraints.

Similar effects were observed in a trial, where unmodified and organically modified clay were mixed in maleic anhydride grafted polypropylene [192]. The unmodified clay led to nucleation. In comparison, exfoliated clay led to a lower crystallization rate. While nucleation appears in many composites, the crystallization rate is commonly lowered predominantly at higher concentrations.

As mentioned before, changes in nano composites can be monitored via the glass transition temperature  $T_g$  before and after adding nano particles. However, not only increases but also decreases were observed. The reason for this is the different interactions between polymer and particle.

The  $T_g$  of a polymer is influenced when the chain is surrounded from another phase for several nanometers. An extreme case of this is where the other phase is air (or vacuum). Then the glass transition temperature of the polymer at the interphase or also in thin films (<100 nm) can be minor compared to the  $T_g$  in the bulk material [193]. This can also be reflected as a confinement effect. A specific experimental example was reported where

poly (2-vinyl pyridine) showed an increase in  $T_g$ , poly(methyl methacrylate) (PMMA) showed a decrease in  $T_g$  and polystyrene showed no change after the addition of silica nanospheres. These dissimilarities were related to surface wetting [194]. The  $T_g$  decrease for PMMA was explained by the free volume existing at the polymer interface due to poor wetting. In most publications only modest transformations are described ( $<10$  °C) as noted in various examples tabulated in **Table 6.2**. In some cases, the organic modification of clay can result in a decrease in  $T_g$  due to plasticization [195]. It should be noted that the values noted in **Table 6.2** involved relatively low levels of nanoparticle incorporation ( $<0.10$  weight fraction and even lower volume fraction) and larger changes in  $T_g$  could be expected at much higher nanofillers volume fraction.

**Table 6.2.** Glass transition changes with nano-filler incorporation. SWCNT = single-walled carbon nanotubes; MMT = montmorillonite; MWCNT = multi-walled carbon nanotubes.

Polymer	Nanofiller	$T_g$ Change	References
Polystyrene	SWCNT	3	[158]
Polycarbonate	SiC (0.5–1.5 wt %) (20–60 nm particles)	No change	[160]
Poly(vinyl chloride)	Exfoliated clay (MMT) ( $<10$ wt %)	1 to 3	[161]
Poly(dimethyl siloxane)	Silica (2–3 nm)	10	[162]
Poly(propylene carbonate)	Nanoclay (4 wt %)	13	[163]
Poly(methyl methacrylate)	Nanoclay (2.5–15.1 wt %)	4–13	[164]
Polyimide	MWCNT (0.25–6.98 wt %)	4 to 8	[165]
Polystyrene	Nanoclay (5 wt %)	6.7	[166]
Natural rubber	Nanoclay (5 wt %)	3	[168]
Poly(butylene terephthalate)	Mica (3 wt %)	6	[169]
Poly lactide	Nanoclay (3 wt %)	1 to 4	[159]

### 6.3.1.3 Viscosity = Processability vs. Mechanical Properties

Above a certain value for the molar mass  $M_c$ , the zero shear viscosity of polymer melts relates to the molar mass to the power of 3.4 [196,197]. The relation can be explained by a network due to entanglement, where macromolecules are crosslinked. This network can be described by an average molar mass which is embedded between two crosslinks. Although low viscosities, i.e., small molar masses, are favored for processing, higher molar masses lead to better mechanical characteristics like toughness and strength. Introducing nano particles into the polymer might be a solution to fulfil both requirements: mechanical stability and simple processability.

Nevertheless, many hurdles are yet to be overcome, especially regarding the dispersion and the processing of these materials. Mackay et al. [198,199] described a reduction of the viscosity of nanoparticle-filled polymer melts over a large concentration range. However, this does not follow the idea of Einstein, according to which the viscosity should increase with volume fraction and the viscosity of the polymer. Comparably, Merkel et al. [200] reasoned the reduction of the viscosity by the reduced free volume induced around the nanoparticles. This leads to a strong decline in the glass transition temperature. This may affect the eventual characteristics. Contradictorily, Kharchenko et al. [201] described a rising viscosity of carbon nanotube-filled polymer materials, even at low concentrations. Similar was reported [202] where the goal was reached and processing as well as mechanical properties of PP were improved by the addition with silica nanoparticles. Therefore, newly modified porous, semi-crystalline PP powders developed [203].

#### **6.3.1.4 Polymer Blend Compatibilization**

For the compatibilization of polymer blends, two factors should be addressed firstly. This is the interfacial tension between the phases which should be reduced and the avoidance of coalescence of the nanoparticles. One solution to address this, is the addition by graft or block copolymers. Its constituents should be equal to or at least compatible with the blend components. Observations have been reported, in which the incorporation of nanoparticles even prevented the coalescence after shear mixing. Examples can be found in literature [204-208].

One reason for such observations might be that the nanoparticles accumulate at the interface. This avoids coalescence by a barrier-type mechanism. Another explanation might be that nanoparticles behave like graft or block copolymers, which accumulate at the interface and are bound by physical [209] or chemical interactions [206].

#### **6.3.1.5 Flammability Resistance**

More and more applications in the fields of buildings, transports or even aeronautics require enhanced fire retardant properties. Some car manufacturers also follow specific standards regarding flammability of car equipment [210]. It has become an area of increased research for sustainable alternatives due to toughening of safety standards, especially regarding halogenated compounds. Therefore, many studies are currently carried out in order to develop new environmentally friendly/halogen-free fire retardant

additives or to increase their efficiency [211]. The target of fire retardant additives is to reduce heat released below the self-sustaining level of the fire. The mechanisms of action that can be involved in the enhancement of the fire resistance can be: (i) formation of a ceramic-like protective shield; (ii) decrease of heat transfer inside the material; (iii) creation of a physical barrier to oxygen propagation; (iv) modification of the degradation mechanism. The problem arising for most conventional fire retardant compounds is the large amount needed (typically up to 60 wt.%), so that mechanical properties are affected. An increasing attention is paid to other routes such as addition of nano-fillers [212], allowing an enhancement of the fire resistance and of the mechanical properties at the same time. Several studies were realized about the effect of clays into various polymers showing a large increase of the fire resistance [213-215]. While nanofillers are often insufficient to meet standards for flame retardancy, the most promising approaches is often pointed to consist in the combination of standard flame retardant additives and nanofillers. The impact of dispersion on the flammability of a material is driven by the barrier to oxygen permeation that can prevent further feeding the combustion, as well as by a charring effect when nanoparticles form a cohesive surface protective layer to stop fire propagation [7]. Likewise, continuous nanoparticles coatings, e.g., flame retardant paints, could have similar effect.

### **6.3.1.6 Electrical Properties—Electronics**

Polymer nanocomposite can show conductive properties for electronic and electrical applications. The electrical conductivity of carbon nanotubes in insulating polymers has also been an important topic of interest. The potential applications include transparent conductive coatings, supercapacitors, electromechanical actuators and various electrode applications [216,217]. Nano composite based polymer with various nanoscale filler inclusions have been investigated for sensor applications including gas sensors, biosensors and chemical sensors. The nanofillers employed include metal oxide nanowires, carbon nanotubes, nanoscale gold, silver, nickel, copper, platinum and palladium particles [218]. However, most metal-polymer nanocomposites using gold or silver nanoparticles, for example, are rather generated from a deposition process [73], yet still their electrical properties and possible scope of application stay the same. With carbon nanotubes, the electrical resistance was found to be significantly changed by exposure to specific gases such as nitrogen dioxide and ammonia [154]. A nanocomposite of single wall CNT/polypyrrole yielded gas sensor sensitivity similar to

SWCNT alone [158]. The sensing capability of these nanocomposites can be based on conductivity changes due to gas or chemical interactions between nanofiller or the conjugated polymer [160].

In order to fulfil the potential applications of conducting polymer (CP) nanotubes and fibers, it is necessary to understand the electronic transport properties of individual polymer tubes/fibers. For template prepared nanofibers, the easiest and usual way is to leave the synthesized polymer fibers inside the pores of the template membrane and measure the bulk resistance across the filled membrane by a two-probe method. The measured membrane resistance can be used to estimate the conductivity of a single fiber. It was found that at room-temperature, conductivity of 30-nm polypyrrole and poly(3-methylthiophene) fibers are much higher than in conventional forms of the analogous polymer [161,162].

### **6.3.1.7 Microwave Absorbing Property**

Conducting polymer in the form of new microwave absorbing materials have been explored due to their lower density and their easy processability. In general, traditional films or pellets of doped polyaniline and polypyrrole exhibit an electrical loss in the microwave frequency ( $f = 1\text{--}18$  GHz) [167,169]. This may arise from an enhanced chain ordering induced by the tubular morphology [170]. It was found that the doped polyaniline with fiber-like morphology has better electromagnetic wave absorbing property than that of polyaniline with particle-like morphology [171].

## **6.3.2 Nanodeposits**

### **6.3.2.1 Repellence to Selected Liquids**

The use of repellent surfaces can be of great interest for many applications such as anti-fouling, self-cleaning, anti-smudge or low-drag for different industries. Hydrophobic surfaces are those capable of repelling water, oleophobic surfaces are capable of repelling oils. To achieve super hydrophobicity or superoleophobicity, the contact angle of water or oil, respectively, must be higher than  $150^\circ$  and rolling or sliding angles should be small [219]. Superomniphobic, also called superamphiphobic, surfaces are those with contact angles greater than  $150^\circ$  and low contact angle hysteresis (generally below  $10^\circ$ ) for liquids with low and high surface tension values [220]. Compared to a

superhydrophobic surface, it is more difficult to create a superoleophobic or superamphiphobic surface because the surface tensions of organic liquids are appreciably lower than that of water [221]. Nevertheless, surface roughness, surface energy and the structure of the solid substrate should be adjusted to create superoleophobic as well as superhydrophobic surfaces and the strategy is similar for the creation of both.

Normally, superhydrophobic surfaces are obtained by mimicking those occurring naturally in plant leaves, like lotus or elephant ear [222], having an optimal combination of surface roughness and low surface energy. The surface roughness should have a hierarchical structure at the micro- and nano-scale, which for lotus leaves are built by convex cells and a much smaller super-imposed layer of hydrophobic three-dimensional wax tubules [223] and in the case of elephant ear arise from micro-bumps formed by convex surface papillae and low surface energy resulting from the formation of a crystalline wax film [224]. It is well known that those micro- and nano-scaled surface structures are of critical importance to the surface water repellence, so the use of nanoparticles is one easily accessible alternative to mimic the multilayered structures of the natural prototypes of non-wettable surfaces [225]. Different nanoparticle composites based on  $\text{SiO}_2$ ,  $\text{TiO}_2$ ,  $\text{Al}_2\text{O}_3$ ,  $\text{Fe}_2\text{O}_3$  and Au have been used. Among them,  $\text{SiO}_2$  nanoparticles are the most commonly used [226-230] due to their simple synthesis procedure, easy modification and compatibility with superhydrophobic surface coatings.

Self-cleaning surfaces can be achieved by two different approaches: creating a superhydrophilic surface or creating a superhydrophobic surface. In the first approach water completely covers the surface with a continuous film and washes away any dirt [231]. This can be achieved by incorporating photocatalytic chemicals as  $\text{TiO}_2$ , with a contact angle with water below  $1^\circ$  and which under UV light generates activated oxygen that decompose the organic materials on the surface, having a dual effect. In the second case, over a superhydrophobic surface, the rolling droplets pick up dust particles, easily removing them from the surface, thus achieving the self-cleaning effect.

Synthetic hydrophobic coatings often employ heavily fluorinated species due to the high surface energy of these materials when in contact with water. In many cases superhydrophobic coatings are created by combining perfluoroalkyl substituents on a nanoparticle (generally  $\text{SiO}_2$ ), having significant flexibility through a range of particle sizes and surface functionalizations [232].

When preparing superhydrophobic coatings for solar panels (and also for windshields for automobiles, safety goggles, etc.), high transparency is also needed. To achieve this goal, the coating must be composed of low-light absorbing materials with refractive indices spanning the refractive indices of air to that of the substrates [233]. Among the conventional transparent materials, silica has the lowest refractive index, absorbing minimal visible light. Li et al. prepared a superhydrophobic coating based on a nanoscale porous structure spontaneously assembled from branched silica nanoparticles [234].

Different methods and processes have been used for the production of super hydro/oleo/amphiphobic surfaces based on nanoparticles. The hierarchical structure in the micro- and nanoscale consists of more than one layer of protrusions on the surface, with the bigger particles at the bottom and the smaller particles on the surface. One alternative is the use of nanoparticle-assisted lithographic techniques, which rely on masks to create geometric patterns on surfaces, adjusting the roughness by changing the etching duration and the lattice space of nanoparticles with different sizes. Chemical [235] or reactive-ion etching [236] processes have been studied to remove the polymer matrix.

Layer by layer (LBL) deposition is a process of constructing multilayered films based on alternating the charge of a substrate, with no need of a special environmental chamber to control the reaction conditions unlike plasma treatment or chemical vapor deposition (CVD). To create the roughness structures for desired surface wettability nanoparticles are often added into the solutions. Cao and Gao [237] fabricated transparent superhydrophobic and highly oleophobic coatings through LBL assembly of 20 nm silica nanoparticles and sacrificial 60 nm polystyrene nanoparticles, that were removed afterwards by calcination.

Self-assembly processes, in which the interactions among the components in solutions spontaneously form an organized distribution, have also been used. Particularly, to organize nanoparticles in a molecular way, self-assembled monolayers (SAMs) designed to have a specific and favorable interaction with the solid substrate of interest are used [238]. Lassiaz et al. fabricated a stable hydrophobic surface by using the reaction of octylphosphonic acid with the surface of alumina nanoparticles [239].

Electro-hydrodynamic techniques (electrospinning and electrospraying) have also been used to create superhydro/oleo/amphiphobic surfaces, as is well described by Sas in a

review of the topic [240]. Electrospinning can produce fibers with various diameters and a low fiber diameter introduces one degree of roughness to the electrospun materials. By tuning the electrospinning parameters, post-treatments steps or using some additives in the polymer solution, the second scale of roughness needed for superhydrophobicity is created. Polystyrene (PS) and their copolymers are the most frequently used due to their low surface energy, low cost and easiness of use for electrospinning. Nanoparticles like polytetrafluoroethylene [241], titania or graphene [242] can also be added to increase PS roughness. Other non-fluorinated [243] and fluorinated [244] polymers have also been used to fabricate superhydrophobic surfaces. Hydrophilic polymers can also be coated by annealed electrospun nanostructured fibers of hydrophobic silanes to achieve a hydrophobic surface and reduce moisture sensitivity [245]. However, the challenge of achieving such electrospayed superhydrophobic and especially superamphiphobic surfaces with strong adhesion to the substrate and with non-intended migration, using application complying materials remains a challenge; this challenge is even greater when it comes to food packaging applications.

Other non-conventional approaches have been used to create this type of surfaces. Deng et al. [246] created a super amphiphobic coating by depositing a soot layer onto a glass slide held above the flame of a candle. The resulting soot consisted of carbon particles with a typical diameter of 30 to 40 nm, forming a loose, fractal like network. This layer exhibited superamphiphobic behavior but was extremely fragile. It had to be coated by a silica shell using CVD techniques. In a latter study, a paraffin wax was used to fix the candle soot, creating a paraffin wax-fixed candle soot (PFCS) coating [247]. This PFCS coating method has been tested on various surfaces, such as metal, ceramic, wood, plastic and paper.

Some of these processes and materials have already been patented. Huang developed a hydrophobic and lipophobic coating material comprising nanoparticles with a determined molecule for easy clean touch screens [248]. S. C. Johnson and Son, Inc. patented the process as well the composition of a coating for producing surfaces that are self-cleaning by water which contains an aqueous mixture of nanoparticles and surface modifier [249]. Cas Guangzhou Chemistry Co. Ltd. patented a super-hydrophobic or super-amphiphobic coating based on blending nanoparticles, epoxy resin with a solvent to obtain the epoxy resin hybridization solution [250]. Ashland Licensing and Intellectual Property Llc patented a coating composition and process for generating transparent,



near-transparent, and semi-transparent super-hydrophobic coatings whose composition comprises hydrophobic nanoparticles of silsesquioxanes containing adhesion promoter and low surface energy groups [251].

Also, some technologies have been patented for producing hydro/lipo/amphi-phobic surfaces referring to packaging materials [252-254]. For example, Eka Nobel patented a paperboard packaging with hydrophobic zeolite that enhances their water-repellent capacity [255] and Bostik Findley Sa patented a system for gluing hydrophobic and oleophobic substrates that are intended for packaging [256].

### **6.3.2.2 Self-Cleaning through Photocatalysis**

To avoid the adherence of liquids, in addition to the lotus effect that nanocoatings can provide, they can also promote other self-cleaning mechanisms by, e.g., photocatalytic effect, which allows the chemical decomposition of many organic pollutants.

TiO<sub>2</sub>, the most thoroughly semiconductor investigated in the literature, seems to be the most promising compound for this purpose. As photocatalysis is an interfacial phenomenon, nanostructured TiO<sub>2</sub> surfaces exhibit superior photocatalytic activity due to a high surface area-to-volume ratio. There are common ways of applying coating with photocatalytic TiO<sub>2</sub>. Among these various deposition systems, ESD (Electrostatic Dissipative Coating) is attractive because it produces extremely fine (sub-micron), selfdispersive (non-agglomerating), highly wettable (electrowetting), adhesive droplets that yield a uniform coating on the substrate. The pigmentary properties are no longer relevant for nanostructured particles, giving therefore almost transparent composite. TiO<sub>2</sub> semiconductor provides the best compromise between catalytic performance and stability in aqueous media [257,258].

Among the different phases, TiO<sub>2</sub> anatase is one of the most promising photocatalyst because of its high oxidative power, abundance and chemical stability. Under UV-illumination, it generates electron-hole pairs able to degrade organic matter or even microorganisms. Unfortunately, it can only absorb UV light (about 5 % of solar light) which is a key drawback for its widespread application. As a consequence, efforts have been devoted to extending the light absorption of TiO<sub>2</sub> to the visible region. Tudor et al. have developed nanostructured anatase (particle sizes < 20 nm) doped with Ag through hydrothermal process to obtain photocatalytic materials with sensitivity in the visible

region of solar spectrum [259]. Further benefiting from its antimicrobial capacity, self-cleaning active textiles could be manufactured applying by electrospray this specifically doped nano-TiO<sub>2</sub> on fabrics [260]. Another recently studied application using the photocatalytic effect of such nanocomposites is the incorporation of active TiO<sub>2</sub> nanostructures in poly (methyl methacrylate) (PMMA) for the removal of dyes, phenols and bacteria from water [261]. This approach benefits from the lack of need for a recovery of the active nanoparticles after water treatment due to their immobilization.

## 6.4 Applications of Polymer Nanocomposites

### 6.4.1 Packaging

#### 6.4.1.1 Barrier Materials

As indicated above in Section 6. 3.1.1, the most studied and promising materials used to improve the barrier properties of polymeric nanocomposites destined to packaging are layered nanomaterials. Two main types of layered nanomaterials have been studied as nanofillers to decrease the permeability to gases of polymers: layered silicates (such as nanoclays) and graphene based materials (graphene and graphene oxide). Nanoclays have been extensively investigated over the last decades because of their excellent barrier properties, low price and food contact compatibility [134]. The use of graphene in nanocomposites is much more recent, but several examples in literature have shown that it can be a strong candidate for gas-barrier materials [262]. A description of the most representative polymeric nanomaterials for packaging based on these two types of layered materials is shown in the following paragraphs.

#### Clay Nanocomposites

By far the most studied nanoscale fillers for polymeric nanocomposites destined to packaging are nanoplatelets composed of clays or other silicate materials. Nanoclays popularity's for packaging application is due to their low cost, stability, effectiveness and benignity. Montmorillonite  $[(\text{Na,Ca})_{0.33}(\text{Al,Mg})_2(\text{Si}_4\text{O}_{10})(\text{OH})_2 \cdot n\text{H}_2\text{O}]$ , a layered phyllosilicate composed of anisotropic layers separated by water molecules, is the typical clay used for polymeric nanocomposites (**Figure 6.8**). The platelets have an average thickness of ~1 nm and lateral dimensions ranging from tens of nanometers up to several microns. Each platelet contains a layer of magnesium or aluminum hydroxide octahedra

sandwiched between two layers of silicon oxide tetrahedra. Each face of the platelet has net negative charge, which is compensated by interlayer cations ( $\text{Ca}^{2+}$ ,  $\text{Mg}^{2+}$ ,  $\text{Na}^+$ , etc.).

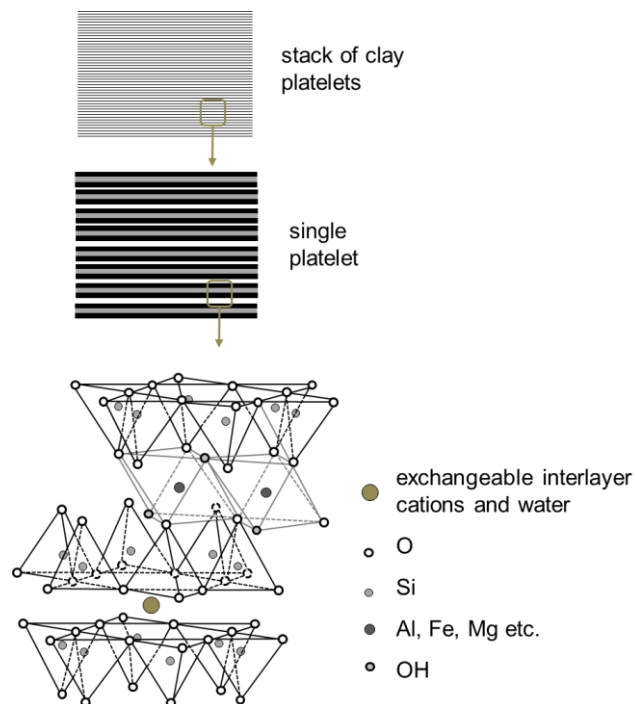


**Figure 6.8.** Structure of montmorillonite (phyllosilicate clay). Adapted from [134].

Individual layers of montmorillonite have surface areas in excess of  $750 \text{ m}^2/\text{g}$  and aspect ratios in the order of 100–500 [26]. These structural characteristics contribute to the excellent utility of montmorillonite as nanofiller in composites, significantly increasing the mechanical and barrier properties of the polymer with a few percent addition into the matrix. Montmorillonite is not the only layered silicate used in polymeric nanocomposites. Related clays such as saponite, hectorite and kaolinite have also been used and have shown properties improvements [263].

During the last two decades, hundreds of polymer-clay nanocomposites have been described, and nanoclays have been incorporated into every important class of polymer, both synthetic and natural. Some representative examples of clay nanocomposites whose polymeric matrices are typically used in packaging are provided in **Table 6.3**, along with selected moisture and oxygen permeability data. This table shows just some examples that have been studied. A more comprehensive list can be found in the literature, consulting any of the numerous specific reviews on the subject [12,264].

**Table 6.3.** Examples of polymer-clay nanocomposites and their barrier improvements. Permeabilities are expressed as improvement ratios: the ratio of the gas permeability or transmission rate of the virgin polymer to the gas permeability or transmission rate of the polymer-clay composite, measured at the same conditions [134].

Polymer Matrix	Filler	Clay (wt %)	$P(O_2)$	$P(H_2O)$	References
PS	Modified montmorillonite	16.7	2.8		[265]
PET	Modified montmorillonite	5	15.6	1.2	[266]
	Modified montmorillonite	5	2.23	1.15	[267]
EVOH	Kaolinite	5	3–4	1.2	[268]
	Montmorillonite	5	1.16	1.21	[267]
PLA	Modified montmorillonite	5	1.2–1.9	1.7–2	[269]
	Mica	4	2.8		[270]
PHB	Kaolinite	5	1.26	1.06	[267]
HDPE	Modified montmorillonite	4	1.2–1.7		[271]
	Modified montmorillonite	5	2.8–2.9	1.8–2.4	[272]
LDPE	Modified montmorillonite	4.76	2.2		[273]

### Graphene Based Nanocomposites

Recently, graphene has received significant attention and has become one of the most studied materials due to its superior properties. Graphene, a monolayer of graphite, has not only excellent mechanical, electronic and optical properties [274], but also is considered an ultrathin, perfect two-dimensional (2D) barrier against gas diffusion [275], since the electron density of aromatic rings in graphene is high enough to repel the penetration of atoms or molecules [276].

When compared with clays, graphene nanoplatelets can have some advantages as two-dimensional nanofillers for polymer nanocomposites. Polymers incorporating graphene show not only enhanced gas barrier properties but also reinforced mechanical strength and improved thermal properties and electrical conductivity when properly dispersed in the polymer matrix [277]. As compared with other nanocarbon forms, such as fullerenes or carbon nanotubes, graphene has a higher surface-to-volume ratio (aspect ratio) and so will be able to achieve the longest gas-diffusion pathway, even at low loadings. The main drawback when using this promising material is that the synthesis of defect-free, large-area, monocrystalline graphene at large scale is still challenging and too expensive for packaging application [278]. One alternative for the use of the gas-barrier properties of graphene in mass production is to use graphene oxide (GO) or its reduced form, reduced graphene oxide (rGO). GO, which consist of oxygen-containing functional groups on the basal plane [279], can be produced at large scale in polar solvents and can be well-dispersed with high aspect ratio in hydrophilic polymers [280].

Some representative examples of graphene-based nanocomposites targeting to improve gas barrier properties for food packaging are presented in **Table 6.4**. Polymer nanocomposites are mainly produced by solution mixing and melt processing.

**Table 6.4.** Representative examples of graphene-based nanocomposites targeting to improve gas barrier properties [277].

Polymer Matrix	Type of Graphene	Preparation Method	Maximum Fraction	Reference
PS	GO	Melting	2.27 vol %	[281]
LLPDE	Functionalized graphene	Solution mixing	5 wt %	[282]
PET	Functionalized GO	Solution mixing	3 wt%	[283]
	Reduced GO	Melting	1.5 wt%	[284]
PLA	GO, graphene	Solution mixing	0.6 wt%	[285]
PP	Reduced GO	Melting	1 wt %	[286]

For graphene-nanocomposites the platelet size, stacking orientation and degree of graphene exfoliation in the polymer matrix are important factors influencing the gas transport [278]. In addition, the high mechanical strength, thermal stability and electrical conductivity allow excellent applications. However, the aggregation of graphene derivatives at high loadings, the local defects of nanocomposites during preparation and the good dispersability in the matrix are significant obstacles to overcome when preparing graphene-polymer nanocomposites.

As a further very positive perspective in terms of the use of graphene in packaging applications, graphene deposits were shown to have sufficient resilience to withstand thermoforming [287]. It was also demonstrated to extend the shelf life of beer packed in PET bottles by a factor of 2 to 5 [288]. In this study, diamond-like carbon (DLC) was deposited using a microwave plasma reactor to reach nanocoatings in the range of 50 nm thickness leading to over 10-fold decrease in the oxygen permeation. The optical properties of the coating were reported to vary from semi-transparent to fully transparent depending on the technology used.

### Other Nanoparticles with Potential in Packaging Applications

Talc qualifies as good reinforcement filler of polymeric matrices because it is a layered mineral with a high aspect ratio (particle diameter/thickness  $\approx$  20:1). This is a consequence of its platy nature, having micron-sized dimensions on length and width, with nanometric thicknesses.

The size of an individual talc platelet (a few thousand of elementary layers) can vary from approximately 1 to over 100  $\mu\text{m}$ , depending on the conditions of core formation. Van der Waals' gaps (interlayer or gallery) between the layers are formed due to stacking, which may assist in the delamination behavior of talc particles during the blending with a matrix. Layer charge is zero or very small, as there are not ions present between layers.

The effects of talc on synthetic polymers have been large studied. It was demonstrated that talc improves mechanical properties and macromolecular orientation of polypropylene [289]. Moreover, an induced crystalline structure has been reported, suggesting that talc particles act as a nucleating agent for polymer crystallization. Also, high aspect ratio platelets have been used to improve gas barrier properties.

Furthermore, even though this is not a primary goal, other nanoparticles such as pyrogenic silica have also been reported to improve the barrier properties of the matrices where they are dispersed [124]. Although non-platelet like nanoparticles lead to lower increase of tortuosity effect, their high specific surface area may lead to gas adsorption and above all, as here when dispersed in PP, they may act as nucleating agent increasing the crystallization degree of the matrix which is well known to increase barrier properties.

The electro-hydrodynamic processing (EHDP) was described in Section 6.2.2.2. Electrospaying is an efficient technique to develop nanostructured surfaces and incorporate nanofillers into the package polymer matrix, as shown in several published studies [83,290,291]. The use of EHDP is also very interesting for the incorporation of active substances (e.g., antimicrobials and antioxidants) within the package polymer matrix, for the development of active packaging [292,293].

#### **6.4.1.2 Easy-to-Empty Features**

The adherence of liquids and other viscous products result in residues in packages, which leads to needless waste at the consumer end and difficulties in the packaging recycling. For reducing the residues in packages, the main objective consists of minimizing the interaction forces between the filled good and the food contact material of the packaging [294]. In Section 6.3.2.1, different methods to provide repellent properties have been described, by creating both hydrophobic or lipophobic surfaces. It has been shown that the wettability of a solid surface is governed by its surface energy determined by chemistry and texture [295]. A typical commercial example for anti-adhesive materials is

Polytetrafluoroethylene (PTFE well-known under the tradename Teflon), usually used in non-stick cookware. The incorporating of fluorine atoms, which have a small atomic radius and high electronegativity, provide a low surface energy [296]. A smooth surface coated with densely packed fluorine atoms shows a water contact angle of approximately 120° [296], while by roughening such a surface, its water contact angle became greater than 150° [297]. However, the use of Teflon in packaging is hindered due to its high cost, high processing temperatures and low acceptability because of its fluorinated content.

Alternatively, low temperature surface modification processes have been described, since generally the polymers currently used in the packaging industry (PP, PE, PET ...) are not heat-resistant. For example, ultra-water-repellent poly (ethylene terephthalate) (PET) substrates have been fabricated by a two-step dry process. First, PET substrates were treated with oxygen plasma in order to provide a proper nanotexture, and subsequently a hydrophobic layer was coated on the nanotextured PET surfaces by means of either low-temperature chemical vapor deposition (CVD) using fluoroalkylsilane or plasma enhanced CVD using tetramethylsilane [298].

Recently, the Massachusetts Institute of Technology developed the first permanently wet slippery surface that can be used for easy-to-empty packaging (LiquiGlide). This solution is durable and makes viscous liquids slide easily [299]. The technology relies on non-wetting surface containing micro/nanotextures impregnated with lubricating liquids, which have been shown to exhibit superior non-wetting performance compared to superhydrophobic surfaces based on stable air-liquid interfaces [28,300]. For determination and comparison of the emptying behavior, depletion or tack test methods can be applied for evaluation [301].

Although the development of non-wetting surfaces has been studied for a long time, easy emptying packaging is not a widely used option nowadays, due to the higher costs of the packages compared to traditional materials. However, the last improvements made in the nanomaterials field and the focus on high added value goods will pull the market for easy-to empty packaging solutions.

### **6.4.2 Solar Panels**

Organic photovoltaic films have several advantages over conventional silicon cells. Photoactive organic materials are printed in extremely thin layers on transparent plastic

film. The patented special inks used in printing consist of formulated blends of materials which after coating create electricity when exposed to light. This technology allows lightweight and flexible semi-transparent modules. As a result, they can be used on all kinds of surfaces. A further key advantage is that the modules generate relatively constant output, for instance even if it is cloudy or artificial light is being used. In addition, they can be produced in different colors and thus adapted to the surroundings. This is a property that creates new possibilities, particularly for building design. The cost-effective production of the OPV modules is also advantageous. Since these polymer materials can be processed as liquid solutions, they are suitable for multiple printing processes: spin coating, ink-jet printing or roll-to-roll processing such as gravure and flexographic printing [302].

There are many important advantages of OPV technology, especially with respect to building-integrated photovoltaics (BIPV). OPV modules do not show the performance drop usually observed with traditional inorganic photovoltaics in diffuse lighting conditions and under elevated temperatures—typical conditions found in façades. In addition, semi-transparency and tunable colors as well as freedom of design in shape and form are attractive and often even essential features for BIPV applications. Buildings account for 40 % of energy consumption and 36 % of carbon dioxide emissions in the EU. As a consequence, the EU has set a target for all new buildings to be nearly zero-energy (NZEB) as of 2021. The achievement of the legally binding NZEB objectives will require active building envelopes since passive materials are reaching their own limits. Gray OPV-based active building elements are an important step forward to combine energy generation and the aesthetic needs of architects [303].

Nanostructures on the front of the PV can guide light into the absorbing layer, or reduce reflection. Nanostructures on the back of a PV could be used as high performance reflectors, bouncing otherwise lost light back into the PV. The light-absorbing layer itself can benefit from a sculpted nanostructure, which could change its ability to absorb light of different wavelengths, for instance. Besides lower material costs, thin-film photovoltaics (tfPV) also are flexible because they only use very thin silicon, whereas current non-thin-film PVs are rigid. This could make tfPVs easier to install; like paper, they could be spooled off a roll [304-305].

Nanoparticles are established materials for OPV, but only mainly inside the OPV itself. Fullerenes are used as electron acceptor and electron transporting material [29].



PEDOT:PSS is used as a hole selective and transporting material [306-309]. As inorganic n-type contacts,  $\text{TiO}_x$  and ZnO can be used. Also indium-doped zinc oxide (IZO) is possible [29]. An additional incorporation of metal nanoparticles such as gold or silver showed efficiency enhancement of polymeric solar cells, mainly ascribed to improved photocurrent density resulting from an excited localized surface plasmon resonance [310-312]. For the outer layer, properties like barrier and/or self-cleaning nanoparticles are developed not specifically for OPV but for solar cells in general. During their usage, OPV cells are exposed to several atmospheric degradation agents and thus they need to be protected by coatings and encapsulants. Nowadays, the following main properties are basically required for solar cells coating materials to ensure devices durability: UV, oxygen and water barrier; thermal stability, transparency, anti-reflectance, anti-soiling, flexibility, affordable cost, electrical isolation. The fouling due to dust, rains, bird faeces, etc., is a well-known issue in the industry that lead to loss of efficiency of solar panels with time. Surface-bound fog similarly scatters light and reduces optical transmission for transparent materials which is detrimental to their function [313]. The application of nanocoatings is also an interesting prospect for solar panels leading, in an easier way than the creation of organized nanostructured surfaces, to tailored repellence of liquid and other unwanted substances that deposit on the panel with time. Indeed, typical fouling (dust, dirt, rain, etc.) lead to significant losses of energy harvesting efficiency (up to 40%) and requires frequent maintenance. Therefore, a number of initiatives related to their self-cleaning are already on the market [314,315]. They employ coatings based on nanoparticles or texturation to get a lotus effect [316], or alternatively apply small electrical field to prevent dust from adhering on the surface. The Nanoshell<sup>®</sup> technology claims it allows self-cleaning for up to five years and solar efficiency gains of up to 27 % percent in wet weather since stationary rainwater on the panel limits the solar energy that is captured. Nonetheless, this later coating is applied manually post production, whereas electrospray seems an optimum route for the application of tailored coatings both on the point of view of reducing the amount needed to get a required effect (therefore saving cost) and of its easy integration within the existing process. Zhao and others described the electrospray deposition as a thin film deposition method that is uniquely suited for manufacturing organic photovoltaic cells with the desired characteristics of atmospheric pressure fabrication, roll-to-roll compatibility, less material loss, and possible self-organized nanostructures [317]. The main functionalities developed in the last reported studies focus on increasing the conductivity [318,319] and providing self-cleaning and

anti-reflective properties [219] which contribute to extending the photovoltaic cells lifespan. Although a significant number of patents regarding self-cleaning solar panels in general (none for flexible OPVs though) were returned in representation of some of the above listed technologies, none of them employed electrospray as a deposition technique. Furthermore, based on nanostructured surfaces, researchers recently developed solar cells that can harvest light from any angle, and lead to self-cleaning panels at the same time [30].

Finally, inorganic nanocoatings and nanocomposites are well known to be transparent in the visible range of the spectra to allow harvesting useful light while filtering UV-light [320] potentially resulting in increasing the lifetime of the OPVs by preventing UV weathering.

All in all, the prospects of nano in solar energy are countless, and it has been one of the key drivers contributing to huge energy efficiency enhancement of the solar panels since their creation over 50 years ago.

### **6.4.3 Automotive Parts**

The automotive sector can benefit from the utilization of nanomaterials. In this sense, the polymer nanocomposites can improve the performance of existing technologies in applications such as engines and powertrains, exhaust systems and catalytic converters, paints and coatings, tires, lighter but stronger materials, suspension and braking systems, electric and electronic equipment, or frames and body parts [321].

On the one hand, the traditional fillers used in automotive parts (talc, mica and calcium carbonate) provide a higher stiffness, increasing melt viscosity and weight, and decrease the toughness and optical clarity. The glass fiber reinforcements introduce higher stiffness, but increased costs and difficulty of fabrication. Both glass fiber reinforcement and traditional fillers must be used at high loading to enhance the properties such as high modulus, or improve the dimensional stability, and the weight, toughness and surface quality are affected.

On the other hand, the nanofillers such as nanoclays, are effective at lower concentrations (<5 %). An improvement in modulus, fire retardancy, dimensional and thermal stability has been reported [322].

Nanoclays are the dominant commercial nanomaterials. It is as strong as 7% glass filled polyamide, with a density of 1.14 g/cm is an ideal light weight substitute for PA + 30 % glass beads. Nanoclay replaces the traditional fillers at a 3:1 ratio.

Because of the low cost and enhanced physico-mechanical properties, polyolefins are becoming the most used thermoplastic in nanocomposites, exceeding earlier nylon 6/clay nanocomposites.

There is currently a growing interest to reduce the weight of the components in a car to reduce the fuel consumption. After the first nylon 6-clay nanocomposites were commercially used by Toyota in 1989 [6], General Motor followed in 2002, with a thermoplastic filled with 3 % nanoclays for a step-assist. In 2004, the Chevrolet had a body side trim with nanoclays, and with a new design part, a weight saving of 25 % was achieved. Another example with the same nanofiller was shown again for General Motors in 2005 to diminish the weight. Maserati engine bay covers were made with a nanocomposite of nylon 6 and nanoclays, reducing the weight, and increasing mechanical properties.

Nowadays, Mucell (Microcellular foaming technology for injection molding industry) is another process to reduce the weight in not structural components parts. It injects supercritical fluid in molten polymer to form microstructured foam with a solid skin layer and closed cells. As opposed to the use of nanofillers for reinforcement, this process leads to significant loss of mechanical properties and therefore of structural function. Therefore, nanofillers are still in development to reduce the weight with an improvement of other properties and a low cost.

The cost-performance ratio is the main objective for nanocomposites, due to the manufacturing cost of the nanoparticles. Besides, it is important to consider the change of design in the weight reduction with nanocomposites, as well as the improvement of material properties. The growth in research activity in terms of nanocomposites for the automotive sector continues to expand their applications.

## **6.5 Nanosafety**

As is evident in this review, there are many applications of nanotechnology that involve the use of nanoparticles in a variety of applications and products. This proliferation of

nanotechnology has prompted concerns over potential risks from engineered nanoparticles where exposure to humans and/or the environment occurs intentionally or accidentally. The seminal report highlighting the opportunities and uncertainties of nanotechnologies and the potential risks posed by nanomaterials was published in 2004 by the UK's Royal Society and the Royal Academy of Engineering [104]. This was one of the first reports to highlight the potential risks to health and the environment that may arise from exposure to nanomaterials. Since then, innumerable national and international reviews have provided a consistent view about the nature and the potential risks of nanoparticles, which may be summarized as follows:

- There are potential hazards to human health and the environment from certain types and forms of nanoparticles, but not all, and this is largely influenced by their composition and morphology;
- There is a paucity of knowledge about whether and how these potential hazards manifest as actual risks to human and environmental health, through exposure, and their significance;
- The absence of data makes it challenging for manufacturers, suppliers and users to have well-informed and effective risk management processes in compliance with their regulatory obligations.

Over the past decade, there has been a significant increase in research activity internationally, intended to fill these gaps. In Europe, this is particularly evident through the European Commission's Framework Programmes. Outputs from this research are intended to further contribute to the field's evidence base in a variety of ways. In risk assessment this through the assimilation of the wealth of scientific data on health and environmental implications of manufactured nanomaterials to be applied alongside knowledge of materials' production, application and resulting potential new exposure pathways as part of responsible innovation. Several frameworks are available for assessing and managing risks from particulate nanomaterials, all of which are based on a common risk assessment approach. For example, the International Organization for Standardization (ISO) has proposed a step-by-step approach for nanomaterial risk evaluation and management [323].

Risk assessment is an integrative approach that considers the effects that potential hazards can have should exposure occur. Undertaking a risk assessment relies on having:

- good information about the hazardous nature of materials.
- good information about the effectiveness of control approaches.
- convenient and accessible ways to monitor exposure.

Exposure is characterized by measuring concentration and duration of exposure and this exposure analysis is important for risk assessment and subsequent risk management involving exposure control plans. In an occupational setting, exposure to nanomaterials can occur for workers at all phases of the material life cycle. During the development of a new material or process, it is likely that the material will be produced under controlled conditions, typically in small quantities, and although accidental releases, for example due to spills, are a possibility although in general, relatively few people are likely to be exposed at this stage. Once the material moves through pilot-scale into commercial production, more widespread exposures can potentially occur following the manufacture of the material or in downstream activities such as recovery, packaging, transport, and storage. Some materials may be subsequently incorporated into a range of other products or may be used in other processes as a feed-stock material. In these circumstances, the quantities of materials being handled can be expected to be much larger.

Exposure to nanoparticles depends upon the formulation of nanoparticles during production, their use in products, and their potential release at during service life and at the point of recycling or disposal. Nanoparticles may be attached to surfaces (e.g., surface coatings), dispersed in solids (e.g., nanocomposites used for food packaging), suspended in liquids (e.g., TiO<sub>2</sub> in sunscreen), as a powder, or be airborne (e.g., during production of nanoparticles). Suspensions of nanomaterials may represent a risk in terms of dermal exposure (see Poland et al. for a review [324]) and the solvent used for the preparation may also play an important role in influencing exposure if it can increase penetration of the material through the skin barrier or alter its size distribution for example. Suspensions of the materials are generally considered safer in terms of inhalation. However, care should be taken if physical processes such as centrifugation, ultra-

sonication, heating and milling are applied to these suspensions which may release aerosols or dry material after solvent evaporation.

In case of nanocomposites, the nanomaterial is fully embedded within a polymer matrix. Exposure to the nanomaterial would only be possible by migration of the nanomaterial out of the polymer (based on the Fickian law of diffusion) or by degradation of the polymer. In the first case it is believed that, once the nanomaterial is incorporated into a polymer matrix, it is immobilized wherefore migration cannot take place. This was examined for a variety of nanocomposites intended to be used as food packaging plastics. However, detection of possibly migrated nanomaterials in complex matrices, like food or food simulants, is quite challenging, wherefore the results of migration studies are often not consistent and sometimes even contradictory. A comprehensive overview on this topic can be found elsewhere [325-327].

The majority of studies dealing with the exposure during polymer-nanocomposites production have intended to replicate and assess particle release during the consumer/professional use stage of the nanocomposite lifecycle, often in a worst-case scenario, and may not involve the same operational conditions and risk management measures as would be present in an industrial situation. Nevertheless, they provide a first indication of the potential for nanoparticle release during the use of such methods, which could potentially be used during the finishing of nanocomposite articles. In order to obtain some preliminary information on potential release, researchers from the US National Institute for Occupational Safety and Health (NIOSH) undertook monitoring during the cutting of a nanocomposite paper containing graphene platelets, carbon nanotubes and other ingredients, using an unventilated band saw [328]. Real-time monitoring showed a very large increase in both particle number and mass concentrations when the composite was cut, with particles detected in the size range 7–100 nm. Although further research is needed to determine whether individual nanoparticles are being released, the authors recommend that if composites are routinely being cut by a band saw, dust control measures should be implemented. In a later study at the same workplace, Heitbrink, Lo et al. investigated the release of nanofibers during cutting and sanding of composite panels containing graphite fibers and/or carbon nanotubes [329]. A ventilated enclosure was built to capture and mix the emissions. Cutting the nanocomposite with a band saw did not result in the detection of carbon nanotubes or other fibers by transmission electron microscopy (TEM); however, the number concentration of particles <560 nm increased

to over 105 particles/cm<sup>3</sup> compared to background levels of 104 particles/cm<sup>3</sup>. The authors suggest that that high number concentration and emission rates may have been caused by the formation of nano-aerosols generated by frictional heating and did not appear to be elevated by the presence of carbon nanotubes. Sanding of a composite containing carbon nanotubes, generated fiber emission rates of  $1.9 \times 10^8$  and  $2.8 \times 10^6$  fibers/second, whilst measurable fiber concentrations were generated from panels that contained graphite and carbon fibers. The authors recommend the use of either a local exhaust ventilation hood or a high velocity, low volume ventilation system during such tasks. Numerous other studies have indicated the potential for significant particle release during the machining of carbon-based nanocomposites [330,331], most noticeably during dry surface grinding [332,333], dry cutting [334,335] or dry drilling [336] with the level of release being highly dependent on the sample material, sample composition, how well the nanomaterial is bound in the polymer matrix and the energy applied to the process. Performing the same tasks under wet conditions has been shown to be an effective method for reducing the number of airborne particles [334,336]. Based on the results of these studies, the release of matrix particles with and without embedded nanomaterials is common; however, the release of dissociated or “free” nanomaterials is rare [331,337-339]. This implies that, whilst degradation occurs during such tasks, nanomaterials often remain bound to the matrix. Manual sanding of carbon-based nanocomposites appears to result in lower particle emissions overall [337,340], with results indicating that particle release may be no higher than for sanding conventional composite materials. However, studies have indicated that micro-sized particles may be produced by abrasion, including with CNTs protruding from the main core [340]. Most recently, Schlagenhaut and colleagues have published two studies investigating CNT containing epoxy-based nanocomposites [338,339]. Their first study took a novel approach to the detection of CNT by labelling them with lead ions based on surface absorption before incorporation into an epoxy resin which was then abraded using a Taber Abraser. They found that in contrast to previous studies, the poorer dispersed CNT were released to a lesser extent than found with better dispersions. This was attributed to the relatively low energy of the abrasion process used which they surmised was not sufficient to break up CNT agglomerates. They were also able to predict that if 1 g of the nanocomposite had been abraded, 40 µg would be present as protruding CNT whilst there would be 0.4 µg of free CNT [338]. Given the potential for release, it has therefore been recommended that effective personal protection and engineering controls are used for all tasks involving the

machining of nanocomposites, such as a ventilated enclosure equipped with HEPA filtration to prevent fugitive releases from contaminating the work area.

Further processing or simply aging of composites containing nanomaterials may lead to the release of particles and potential exposure. Organic polymers are particularly sensitive to UV radiation that can degrade them could lead to the release of particles. There are several studies which have evaluated the effect of sunlight (as well as other forms of weathering) on nanocomposites and one such study is that of Bernard et al. (2010) who investigated the fate of graphene oxide sheets in polymers under UV irradiation [341]. The results indicated that under UV irradiation, the polyurethane matrix showed signs of degradation. In parallel, accumulation of GFN at the surface of the composite was also recorded. A later study showed similar results after the UV weathering of an elastic CNT-polyurethane nanocomposite which contained 3 % CNT and was further processed by injection molding or extrusion before weathering through UV exposure [342]. They showed that dry weathering in a progressive way led to revealing of CNT as the matrix degraded but the nanofillers did not, leading to an accumulation at the surface. Indeed, further analysis showed that 72 % of the top 10 nm of the weathered sample consisted of CNT. These results indicate that the choice of the matrix and its ageing under sunlight may lead to accumulation of nanomaterials at the surface which could influence releases to the environment [341].

An additional key issue within risk is the nature of hazards posed by nanocomposites and in particular, the nano-fillers used. There are relatively limited numbers of studies considering the toxicity of particles released from nano-composites and those which do exist tend to focus on carbon-based nanomaterials such as carbon nanotubes (CNT). Whilst these materials do present a rather polarized view of the use of nanomaterials in composites, they can be used to inform us as to how the toxicity profile of a nanomaterial may be altered by incorporation and subsequent release.

One such study is that of Wohlleben et al. (2011) which evaluated the respiratory toxicity of particulates released after abrasion of cement and thermoplastic based nanocomposites containing CNT. Animals were instilled with respirable (<10 µm) fractions of abraded cement or thermoplastic composites with or without carbon nanotubes and their toxicity compared to that of carbon nanotubes alone. The results showed that instillation of the matrix alone induced no clinical signs of toxicity or genotoxicity and minimal inflammation in the lung which was greater for the cement (a



known respiratory irritant) yet instillation of the inhalable fraction of the nanocomposites did not lead to any differences in terms of toxicity compared to the matrix alone [337]. This was in stark contrast to instillation of carbon nanotubes at a four-fold lower dose which led to prominent lung inflammation which was abrogated by its inclusion into a composite. Similar results have been noted in a range of in vitro studies addressing CNT-polyurethane nanocomposites [342] as well as CNT containing epoxy-based nanocomposites [338,339].

Whilst these studies deal with a specific form of nanomaterial which is of course not representative of all nanomaterials (not least due to their fibrous nature which may influence release characteristics), they do show that incorporation into a composite can have a significant effect on toxicity. CNT are known to present a respiratory hazard and can induce inflammation as well as granuloma formation in the lung [343,344] and one form (not addressed within the studies above) has been classified as a possible carcinogen [345]. However, despite this intrinsic activity, the studies above show that incorporation into a variety of different composites is associated with a decrease in respiratory toxicity to the levels of the composite material alone meaning that the hazards associated with such nanocomposites may in fact be more akin to that of the base composite than the pure nanomaterial. Such observations are, however, based on a limited number of studies and do not consider many types of nanomaterials but if the overall principle noted is transferable (i.e., a net lowering of potential hazards) then this may be applied to other nanomaterials, particularly if they are of lower toxicity (e.g., TiO<sub>2</sub>).

The release of nanomaterials from coatings has been assessed in only a few studies, mainly testing the release of nanomaterials from paints and other coatings. Koponen et al. compared the effect of sanding on paints, with and without nanoparticles (carbon black and TiO<sub>2</sub>) [346]. The authors showed that although the geometric mean diameter of aerosol released during the sanding of paints was only slightly different with compared to without nanoparticles, the particle number concentration was increased during sanding of nanoparticle-containing paints [346].

To conclude, the safe use of chemicals and responsible development of processes and products are recognized as fundamental to ensuring a safe working environment through easy to implement, affordable and fit-for-purpose measures to mitigate any hazards and control exposure to nanomaterials, protecting the health of workers, consumers and the environment and supporting the commercialization of nanotechnology for societal benefit.

## 6.6 Conclusions

As seen during the last 20–30 years, significant progresses have been made in synthesis, processing, performances of polymer nanocomposites and nanocoatings. This article reviewed some key aspects on these fast-growing research areas in order to understand potential applications of polymer nanocomposites. These materials offer improved performance over bulk materials and microcomposites and hence can be used to overcome the limitations of many currently existing materials and devices. Nevertheless, a full control over their morphology (nanostructure dispersion or even orientation) is still desired to consistently reach optimal properties.

While polymer nanocomposite materials have unique behavior such as improved mechanical and gas barrier properties, even upon small addition of nanofillers, nanocoatings can tailor the surface properties where they are applied for example in terms of affinity to liquids, but also of UV, gas or flame protection. Besides packaging, automotive and solar energy, nanocomposites' applicative potential is endless; it includes bio-/chemical sensing, electronic devices, drug delivery, microwave absorbing device, orthopedic application, etc.

There are different processes for the preparation of polymer nanocomposite materials each of each has its own advantages and drawbacks; therefore, the suitable methods should be adjusted to the target application, composition, dispersion performance, etc. In terms of process improvements, ultrasonic-assisted dispersions have shown some encouraging results both in liquid media and melt plastic stream. This later also faces questioning related with the nano-safety of workers when handling nanoparticles, as well as with their use within consumer applications. While for specific nanoparticles, the amount of research performed allows us to confirm the absence of hazards, the number of parameters involved is so high that generalization to others should be avoided.

## 6.7 References

1. International Organization for Standardization (ISO). Nanotechnologies—Vocabulary. In *Part 4: Nanostructured Materials*; International Organization for Standardization: Geneva, Switzerland, 2011.

2. Schmid, M.; Benz, A.; Stinga, C.; Samain, D.; Zeyer, K.P. *Int. J. Polym. Sci.*, 637837, 2012
3. Schmid, M.; Sangerlaub, S.; Miesbauer, O.; Jost, V.; Werthan, J.; Stinga, C.; Samain, D.; Stramm, C.; Noller, K.; Muller, K. *Polymers*, 6, 2764–2783, 2014
4. Hosokawa, M.; Nogi, K.; Naito, M.; Yokoyama, T. *Nanoparticle Technology Handbook*; Elsevier Science, Oxford, UK, 2007.
5. International Organization for Standardization (ISO). Nanotechnologies—Vocabulary. In *Part 2: Nano-Objects*; International Organization for Standardization: Geneva, Switzerland, 2015.
6. Okada, A.; Usuki, A. *Macromol. Mater. Eng.*, 291, 1449–1476, 2006.
7. Bugnicourt, E. Ph.D. Thesis, Institut National Des Sciences Appliquées (INSA), Villeurbanne, France, 2005.
8. Paul, D.R.; Robeson, L.M. *Polymer*, 49, 3187–3204, 2008.
9. McAdam, C.P.; Hudson, N.E.; Liggat, J.J.; Pethrick, R.A. *J. Appl. Polym. Sci.*, 108, 2242–2251, 2008.
10. Lee, S.; Lee, B.; Kim, B.J.; Park, J.; Yoo, M.; Bae, W.K.; Char, K.; Hawker, C.J.; Bang, J.; Cho, J. *J. Am. Chem. Soc.*, 131, 2579–2587, 2009.
11. Barreca, D.; Carraro, G.; Warwick, M.E.A.; Kaunisto, K.; Gasparotto, A.; Gombac, V.; Sada, C.; Turner, S.; Van Tendeloo, G.; Maccato, C.; et al. *CrystEngComm*, 17, 6219–6226, 2015.
12. Sinha Ray, S.; Okamoto, M. *Prog. Polym. Sci.*, 28, 1539–1641, 2003.
13. Bertuoli, P.T.; Piazza, D.; Scienza, L.C.; Zattera, A.J. *Appl. Clay Sci.*, 87, 46–51, 2014.
14. Huskić, M.; Žigon, M.; Ivanković, M. *Appl. Clay Sci.*, 85, 109–115, 2013.
15. Usuki, A.; Kojima, Y.; Kawasumi, M.; Okada, A.; Fukushima, Y.; Kurauchi, T.; Kamigaito, O. *J. Mater. Res.*, 8, 1179–1184, 1993.

16. Messersmith, P.B.; Giannelis, E.P. *Chem. Mater.*, **6**, 1719–1725, 1994.
17. Xia, H.S.; Wang, Q. *J. Appl. Polym. Sci.*, **87**, 1811–1817, 2003.
18. Costantino, A.; Pettarin, V.; Viana, J.; Pontes, A.; Pouzada, A.; Frontini, P. *Proc. Mater. Sci.*, **1**, 34–43, 2012.
19. Xiao, W.; Xu, J.B.; Liu, X.Y.; Hu, Q.L.; Huang, J.G. *J. Mater. Chem. B*, **1**, 3477–3485, 2013.
20. Si, Y.F.; Zhu, H.; Chen, L.W.; Jiang, T.; Guo, Z.G. *Chem. Commun.*, **51**, 16794–16797, 2015.
21. Li, Y.C.; Mannen, S.; Cain, A.C.; Grunlan, J.C. *Abstr. Pap. Am. Chem. S*, **241**, 2011.
22. Holder, K.M.; Spears, B.R.; Huff, M.E.; Priolo, M.A.; Harth, E.; Grunlan, J.C. *Macromol. Rapid Commun.*, **35**, 960–964, 2014.
23. Joshi, M.; Khanna, R.; Shekhar, R.; Jha, K. *J. Appl. Polym. Sci.*, **119**, 2793–2799, 2011.
24. Rahman, A.; Ashraf, A.; Xin, H.; Tong, X.; Sutter, P.; Eisaman, M.D.; Black, C.T. *Nat. Commun.*, **6**, 2015.
25. Wong, K.V.; Paddon, P.A. *Recent Patents Nanotechnol.*, **8**, 181–199, 2014.
26. Arora, A.; Padua, G.W. *J. Food Sci.*, **75**, R43–R49, 2010.
27. Mihindukulasuriya, S.D.F.; Lim, L.T. *Trends Food Sci. Technol.*, **40**, 149–167, 2014.
28. Anand, S.; Paxson, A.T.; Dhiman, R.; Smith, J.D.; Varanasi, K.K. *ACS Nano*, **6**, 10122–10129, 2012.
29. Sims, L.; Egelhaaf, H.J.; Hauch, J.A.; Kogler, F.R.; Steim, R. *Compr. Renew. Energy*, **1**, 439–480, 2012.

30. Solar Cells That Can Face almost Any Direction and Keep Themselves Clean. Available online: <http://m.phys.org/news/2015-12-solar-cells.html> (accessed on 18 February 2016).
31. Alexandre, M.; Dubois, P. *Mater. Sci. Eng. R-Rep.*, **28**, 1–63, 2000.
32. Kamigaito, O. *J. Jpn. Soc. Powder Powder Metall.*, **38**, 315–321, 1991.
33. Vaia, R.A.; Giannelis, E.P. *Macromolecules*, **30**, 8000–8009, 1997.
34. Vaia, R.A.; Giannelis, E.P. *Macromolecules*, **30**, 7990–7999, 1997.
35. Tomasko, D.L.; Han, X.M.; Liu, D.H.; Gao, W.H. *Curr. Opin. Solid State Mater. Sci.*, **7**, 407–412. 2003.
36. Carrado, K.A.; Xu, L.Q. *Chem. Mater.*, **10**, 1440–1445, 1998.
37. Mbhele, Z.H.; Salemane, M.G.; van Sittert, C.G.C.E.; Nedeljkovic, J.M.; Djokovic, V.; Luyt, A.S. *Chem. Mater.*, **15**, 5019–5024, 2003.
38. Park, S.S.; Bernet, N.; de la Roche, S.; Hahn, H.T. *J. Compos. Mater.*, **37**, 465–476, 2003.
39. Xu, X.L.; Yin, Y.D.; Ge, X.W.; Wu, H.K.; Zhang, Z.C. *Mater. Lett.*, **37**, 354–358, 1998.
40. Gangopadhyay, R.; De, A. *Chem. Mater.*, **12**, 608–622, 2000.
41. Tracton, A.A. *Coatings Technology Handbook*, 3rd ed.; CRC Press: Boca Raton, FL, USA, 2005.
42. Embuscado, M.; Huber, K.C. *Edible Films and Coatings for Food Applications*; Springer: New York, NY, USA, 2009.
43. Rastogi, V.; Samyn, P. *Coatings*, **5**, 887, 2015.
44. Domininghaus, H.; Eyerer, P.; Elsner, P.; Hirth, T. *Kunststoffe: Eigenschaften und Anwendungen; mit 240 Tabellen*; Springer-Verlag GmbH: Heidelberg, Germany, 2008.
45. Braun, D. *Kunststofftechnik für Einsteiger*; Hanser: Munich, Germany, 2003.

46. Kaiser, W. *Kunststoffchemie für Ingenieure*; Hanser: Munich, Germany, 2007.
47. Dennis, H.R.; Hunter, D.L.; Chang, D.; Kim, S.; White, J.L.; Cho, J.W.; Paul, D.R. *Polymer*, **42**, 9513–9522, 2001.
48. Chavarria, F.; Shah, R.K.; Hunter, D.L.; Paul, D.R. *Polym. Eng. Sci.*, **47**, 1847–1864, 2007.
49. Lapshin, S.; Swain, S.K.; Isayev, A.I. *Polym. Eng. Sci.*, **48**, 1584–1591, 2008.
50. Fornes, T.D.; Yoon, P.J.; Keskkula, H.; Paul, D.R. *Polymer*, **42**, 9929–9940, 2001.
51. Villmow, T.; Pegel, S.; Potschke, P.; Wagenknecht, U. *Compos. Sci. Technol.*, **68**, 777–789, 2008.
52. Chandra, A.; Kramschuster, A.J.; Hu, X.; Turng, L.S. Effect of injection molding parameters on the electrical conductivity of polycarbonate/carbon nanotube nanocomposites. In Proceedings of the Annual Technical Conference (ANTEC), Cincinnati, OH, USA, 6–11 May 2007; 2171–2175.
53. Stan, F.; Sandu, L.I.; Fetecau, C. *Compos. Part B Eng.*, **59**, 109–122, 2014.
54. Rios, P.F.; Ophir, A.; Kenig, S.; Efrati, R.; Zonder, L.; Popovitz-Biro, R. *J. Appl. Polym. Sci.*, **120**, 70–78, 2011.
55. Schmid, M.; Dallmann, K.; Bugnicourt, E.; Cordoni, D.; Wild, F.; Lazzeri, A.; Noller, K. *Int. J. Polym. Sci.*, **2012**, 1–7, 2012.
56. De Azeredo, H.M.C. *Food Res. Int.*, **42**, 1240–1253, 2009.
57. Alberto, R. Fundamentos de la Tecnología de Extrusión de Película Cast. Available online: <http://www.plastico.com/> (accessed on 4 February 2016).
58. Coltelli, M.-B.; Wild, F.; Bugnicourt, E.; Cinelli, P.; Lindner, M.; Schmid, M.; Weckel, V.; Müller, K.; Rodriguez, P.; Staebler, A. *Coatings*, **6**, 1, 2015.
59. Caruso, R.A.; Antonietti, M. *Chem. Mater.*, **13**, 3272–3282, 2001.
60. Anghel, I.; Holban, A.M.; Andronescu, E.; Grumezescu, A.M.; Chifiriuc, M.C. *Biointerphases*, **8**, 2013.

61. Gurzawska, K.; Svava, R.; Yu, Y.H.; Haugshoj, K.B.; Dirscherl, K.; Levery, S.B.; Byg, I.; Damager, I.; Nielsen, M.W.; Jorgensen, B.; et al. *Mater. Sci. Eng. C Mater.*, **43**, 117–125, 2014.
62. Mattioli-Belmonte, M.; Cometa, S.; Ferretti, C.; Iatta, R.; Trapani, A.; Ceci, E.; Falconi, M.; De Giglio, E. *Carbohydr. Polym.*, **110**, 173–182, 2014.
63. Park, J.H.; Yang, S.H.; Lee, J.; Ko, E.H.; Hong, D.; Choi, I.S. *Adv. Mater.*, **26**, 2001–2010, 2014.
64. Chen, D.Y.; Singh, D.; Sirkar, K.K.; Zhu, J.T.; Pfeffer, R. *Langmuir*, **30**, 7804–7810, 2014.
65. Smietana, M.; Bock, W.J.; Szmids, J.; Pickrell, G.R. *Ceram. Trans.*, **222**, 275–286, 2010.
66. Chen, M.M.; Sun, X.; Qiao, Z.J.; Ma, Q.Q.; Wang, C.Y. *J. Alloy Compd.*, **601**, 38–42, 2014.
67. Hamedi, G.H.; Nejad, F.M. *Road Mater. Pavement*, **16**, 239–255, 2015.
68. Hsieh, C.T.; Chang, B.S.; Lin, J.Y. *Appl. Surf. Sci.*, **257**, 7997–8002, 2011.
69. Zhang, T.; Yan, H.; Peng, M.; Wang, L.; Ding, H.; Fang, Z. *Nanoscale*, **5**, 3013–3021, 2013.
70. Langowski, H.-C. Permeation of gases and condensable substances through monolayer and multilayer structures. In *Plastic Packaging*; Wiley-VCH Verlag GmbH & Co. KGaA: Weinheim, Germany, 2008; 297–347.
71. Bishop, C. *Vacuum Deposition onto Webs, Films and Foils*; Elsevier Science: Amsterdam, The Netherlands, 2011.
72. Fahlteich, J. Ph.D. Thesis, Technische Universität Chemnitz, Chemnitz, Germany, 2010.
73. Torrisi, V.; Ruffino, F. *Coatings*, **5**, 378–424, 2015.
74. Kim, H.; Abdala, A.A.; Macosko, C.W. *Macromolecules*, **43**, 6515–6530, 2010.

75. Yoon, Y.S.; Park, H.Y.; Lim, Y.C.; Choi, K.G.; Lee, K.C.; Park, G.B.; Lee, C.J.; Moon, D.G.; Han, J.I.; Kim, Y.B.; et al. *Thin Solid Films*, 513, 258–263, 2006.
76. Kääriäinen, T.; Cameron, D.; Kääriäinen, M.L.; Sherman, A. *Atomic Layer Deposition: Principles, Characteristics, and Nanotechnology Applications*; Wiley: Hoboken, NJ, USA, 2013.
77. Lewis, J.S.; Weaver, M.S. *IEEE J. Sel. Top. Quantum Electron*, 10, 45–57, 2004.
78. Miesbauer, O.; Kucukpinar, E.; Kiese, S.; Carmi, Y.; Noller, K.; Langowski, H.C. *Energy Build.*, 85, 597–603, 2014.
79. Miesbauer, O.; Schmidt, M.; Langowski, H.-C. *Vak. Forsch. Prax.*, 20, 32–40, 2008.
80. Langowski, H.-C. *Vak. Forsch. Prax.*, 14, 297–302, 2002.
81. Jaworek, A. *Powder Technol.*, 176, 18–35, 2007.
82. Wu, Y.Q.; Clark, R.L. *J. Biomat. Sci.-Polym. E*, 19, 573–601, 2008.
83. Fabra, M.J.; Pardo, P.; Martinez-Sanz, M.; Lopez-Rubio, A.; Lagaron, J.M. *J. Appl. Polym. Sci.*, 133, 42695, 2016.
84. Khan, S.; Doh, Y.H.; Khan, A.; Rahman, A.; Choi, K.H.; Kim, D.S. *Curr. Appl. Phys.*, 11, S271–S279, 2011.
85. Pérez-Masiá, R.; Lagaron, J.M.; López-Rubio, A. *Carbohydr. Polym.*, 101, 249–255, 2014.
86. Kango, S.; Kalia, S.; Celli, A.; Njuguna, J.; Habibi, Y.; Kumar, R. *Prog. Polym. Sci.*, 38, 1232–1261, 2013.
87. Bugnicourt, E.; Galy, J.; Gérard, J.; Boué, F.; Barthel, H. *Polymer*, 48, 949–958, 2006.
88. Bugnicourt, E.; Kehoe, T.; Latorre, M.; Serrano, C.; Philippe, S.; Schmid, M. *Nanomaterials*, 6, 150, 2016.



89. Mittal, V. *Optimization of Polymer Nanocomposite Properties*; Wiley-VCH Verlag GmbH & Co. KGaA: Weinheim, Germany, 2009.
90. Rong, M.Z.; Zhang, M.Q.; Ruan, W.H. *Mater. Sci. Technol.*, **22**, 787–796, 2006.
91. Fekete, E.; Pukánszky, B.; Tóth, A.; Bertóti, I. *J. Colloid Interface Sci.*, **135**, 200–208, 1990.
92. Lin, H.; Isayev, A.I. *J. Appl. Polym. Sci.*, **102**, 2643–2653, 2006.
93. Kumar, R.V.; Kolytyn, Y.; Palchik, O.; Gedanken, A. *J. Appl. Polym. Sci.*, **86**, 160–165, 2002.
94. Isayev, A.I.; Hong, C.K.; Kim, K.J. *Rubber Chem. Technol.*, **76**, 923–947, 2003.
95. Ullah, M.; Ali, M.E.; Abd Hamid, S.B. *Rev. Adv. Mater. Sci.*, **37**, 1–14, 2014.
96. Fecht, H.J.; Hellstern, E.; Fu, Z.; Johnson, W.L. *Metall. Trans.*, **21**, 2333–2337, 1990.
97. Nandhini, R.; Mini, P.A.; Avinash, B.; Nair, S.V.; Subramanian, K.R.V. *Mater. Lett.*, **87**, 165–168, 2012.
98. Cho, K.; Chang, H.; Kil, D.S.; Kim, B.-G.; Jang, H.D. *J. Ind. Eng. Chem.*, **15**, 243–246, 2009.
99. Zhang, D.L. *Prog. Mater. Sci.*, **49**, 537–560, 2004.
100. Mark, J.E.; Jiang, C.Y.; Tang, M.Y. *Macromolecules*, **17**, 2613–2616, 1984.
101. Wen, J.Y.; Wilkes, G.L. *Chem. Mater.*, **8**, 1667–1681, 1996.
102. Huang, H.-H.; Orlor, B.; Wilkes, G.L. *Polym. Bull.*, **14**, 557–564, 1985.
103. Fischer, H. *Mat. Sci. Eng. C*, **23**, 763–772, 2003.
104. The Royal Society. *Nanoscience and Nanotechnologies: Opportunities and Uncertainties*; The Royal Society & The Royal Academy of Engineering: London, UK, 2004.
105. Oriakhi, C. Nano sandwiches. *Chem. Br.*, **34**, 59–62, 1998.

106. Usuki, A.; Kawasumi, M.; Kojima, Y.; Okada, A.; Kurauchi, T.; Kamigaito, O. *J. Mater. Res.*, **8**, 1174–1178, 1993.
107. Kuchibhatla, S.V.N.T.; Karakoti, A.S.; Bera, D.; Seal, S. *Prog. Mater. Sci.*, **52**, 699–913, 2007.
108. Li, C.; Bai, H.; Shi, G.Q. *Chem. Soc. Rev.*, **38**, 2397–2409, 2009.
109. Tran, H.D.; Li, D.; Kaner, R.B. *Adv. Mater.*, **21**, 1487–1499, 2009.
110. MacDiarmid, A.G. “Synthetic metals”: A novel role for organic polymers (nobel lecture). *Angew. Chem. Int. Ed.* 2001, **40**, 2581–2590.
111. Heeger, A.J. *Chem. Soc. Rev.*, **39**, 2354–2371, 2010.
112. Manias, E. *Nat. Mater.*, **6**, 9–11, 2007.
113. Muncke, J. Food Packaging Materials. Available online: <http://www.foodpackagingforum.org/food-packaging-health/food-packaging-materials> (accessed on 4 February 2016).
114. Schmid, M.; Dallmann, K.; Bugnicourt, E.; Cordoni, D.; Wild, F.; Lazzeri, A.; Noller, K. *Int. J. Polym. Sci.*, **2012**, 562381, 2012.
115. Yam, K.L. *The Wiley Encyclopedia of Packaging Technology*; Third Edition. Wiley: Hoboken, NJ, USA, 2009.
116. Hammann, F.; Schmid, M. *Materials*, **7**, 7975–7996, 2014.
117. Zink, J.; Wyrobnik, T.; Prinz, T.; Schmid, M. *Int. J. Mol. Sci.*, **17**, 1376, 2016.
118. Schmid, M.; Reichert, K.; Hammann, F.; Stäbler, A. *J. Mater. Sci.*, **50**, 4396–4404, 2015.
119. Schmid, M.; Zillinger, W.; Müller, K.; Sänglerlaub, S. *Food Packag. Shelf Life*, **6**, 21–29, 2015.
120. Zhang, Z.; Britt, I.J.; Tung, M.A. *J. Plast. Film Sheeting*, **14**, 287–307, 1998.
121. Yeo, J.H.; Lee, C.H.; Park, C.-S.; Lee, K.-J.; Nam, J.-D.; Kim, S.W. *Adv. Polym. Technol.*, **20**, 191–201, 2001.

122. Lagaron, J.M.; Gimenez, E.; Gavara, R.; Saura, J.J. *Polymer*, *42*, 9531–9540, 2001.
123. Reig, C.S.; Lopez, A.D.; Ramos, M.H.; Ballester, V.A.C. *Packag. Technol. Sci.*, *27*, 839–866, 2014.
124. Vladimirov, V.; Betchev, C.; Vassiliou, A.; Papageorgiou, G.; Bikiaris, D. *Compos. Sci. Technol.*, *66*, 2935–2944, 2006.
125. Kim, J.Y.; Han, S.-I.; Kim, S.H. *Polym. Eng. Sci.*, *47*, 1715–1723, 2007.
126. Chen, Y.; Cao, X.; Chang, P.R.; Huneault, M.A. *Carbohydr. Polym.*, *73*, 8–17, 2008.
127. Azeredo, H.M.C.; Mattoso, L.H.C.; Wood, D.; Williams, T.G.; Avena-Bustillos, R.J.; McHugh, T.H. *J. Food Sci.*, *74*, N31–N35, 2009.
128. Bilbao-Sáinz, C.; Avena-Bustillos, R.J.; Wood, D.F.; Williams, T.G.; McHugh, T.H. *J. Agric. Food Chem.*, *58*, 3753–3760, 2010.
129. Cao, X.; Chen, Y.; Chang, P.R.; Stumborg, M.; Huneault, M.A. *J. Appl. Polym. Sci.*, *109*, 3804–3810, 2008.
130. Podsiadlo, P.; Choi, S.Y.; Shim, B.; Lee, J.; Cuddihy, M.; Kotov, N.A. *Biomacromolecules*, *6*, 2914–2918, 2005.
131. De Moura, M.R.; Aouada, F.A.; Avena-Bustillos, R.J.; McHugh, T.H.; Krochta, J.M.; Mattoso, L.H.C. *J. Food Eng.*, *92*, 448–453, 2009.
132. De Moura, M.R.; Lorevice, M.V.; Mattoso, L.H.C.; Zucolotto, V. *J. Food Sci.*, *76*, N25–N29, 2011.
133. Choudalakis, G.; Gotsis, A.D. *Eur. Polym. J.*, *45*, 967–984, 2009.
134. Duncan, T.V. *J. Colloid Interface Sci.*, *363*, 1–24, 2011.
135. Nielsen, L.E. *J. Macromol. Sci.*, *1*, 929–942, 1967.
136. Lape, N.K.; Nuxoll, E.E.; Cussler, E.L. *J. Membr. Sci.*, *236*, 29–37, 2004.
137. Gusev, A.A.; Lusti, H.R. *Adv. Mater.*, *13*, 1641–1643, 2001.

138. Fredrickson, G.H.; Bicerano, J. *J. Chem. Phys.*, *110*, 2181–2188, 1999.
139. Bharadwaj, R.K. *Macromolecules*, *34*, 9189–9192, 2001.
140. Sun, L.; Boo, W.J.; Clearfield, A.; Sue, H.J.; Pham, H.Q. *J. Membr. Sci.*, *318*, 129–136, 2008.
141. Picard, E.; Gauthier, H.; Gérard, J.F.; Espuche, E. *J. Colloid Interface Sci.*, *307*, 364–376, 2007.
142. Fornes, T.; Paul, D. *Polymer*, *44*, 4993–5013, 2003.
143. Sen, S.; Thomin, J.D.; Kumar, S.K.; Koblinski, P. *Macromolecules*, *40*, 4059–4067, 2007.
144. Vaia, R.; Giannelis, E. *Polymer*, *42*, 1281–1285, 2001.
145. Bugnicourt, E.; Galy, J.; Gérard, J.-F.; Barthel, H. *Polymer*, *48*, 1596–1605, 2007.
146. Hunter, D.L.; Kamena, K.W.; Paul, D.R. *MRS Bull.*, *32*, 323–327, 2007.
147. Hotta, S.; Paul, D. *Polymer*, *45*, 7639–7654, 2004.
148. Jang, J.S.; Bouveret, B.; Suhr, J.; Gibson, R.F. *Polym. Compos.*, *33*, 1415–1423, 2012.
149. Yu, S.; Yang, S.; Cho, M. *Polymer*, *50*, 945–952, 2009.
150. Choi, J.; Yu, S.; Yang, S.; Cho, M. *Polymer*, *52*, 5197–5203, 2011.
151. Tsai, J.-L.; Tzeng, S.-H. *J. Compos. Mater.*, *42*, 2345–2361, 2008.
152. Yang, S.; Cho, M. *Appl. Phys. Lett.*, *93*, 043111, 2008.
153. Liu, H.; Brinson, L.C. *Compos. Sci. Technol.*, *68*, 1502–1512, 2008.
154. Yang, B.; Hwang, Y.; Lee, H. *Compos. Struct.*, *99*, 123–130, 2013.
155. Goertzen, W.K.; Kessler, M. *J. Appl. Polym. Sci.*, *109*, 647–653, 2008.
156. Yu, S.; Yang, S.; Cho, M. *J. Appl. Phys.*, *110*, 124302, 2011.

157. Shin, H.; Yang, S.; Chang, S.; Yu, S.; Cho, M. *Polymer*, *54*, 1543–1554, 2013.
158. Kratochvíla, J.; Boudenne, A.; Krupa, I. *Polym. Compos.*, *34*, 149–155, 2013.
159. Harton, S.E.; Kumar, S.K.; Yang, H.; Koga, T.; Hicks, K.; Lee, H.; Mijovic, J.; Liu, M.; Vallery, R.S.; Gidley, D.W. *Macromolecules*, *43*, 3415–3421, 2010.
160. Choi, J.; Yang, S.; Yu, S.; Shin, H.; Cho, M. *Polymer*, *53*, 5178–5189, 2012.
161. Qiao, R.; Brinson, L.C. *Compos. Sci. Technol.*, *69*, 491–499, 2009.
162. Hadden, C.; Jensen, B.; Bandyopadhyay, A.; Odegard, G.; Koo, A.; Liang, R. *Compos. Sci. Technol.*, *76*, 92–99, 2013.
163. Buryachenko, V.; Roy, A.; Lafdi, K.; Anderson, K.; Chellapilla, S. *Compos. Sci. Technol.*, *65*, 2435–2465, 2005.
164. Buryan, O.; Novikov, V. *Mech. Compos. Mater.*, *38*, 187–190, 2002.
165. Bhuiyan, M.A.; Pucha, R.V.; Karevan, M.; Kalaitzidou, K. *Comput. Mater. Sci.*, *50*, 2347–2353, 2011.
166. Bhuiyan, M.A.; Pucha, R.V.; Worthy, J.; Karevan, M.; Kalaitzidou, K. *Compos. Struct.*, *95*, 80–87, 2013.
167. Ayatollahi, M.; Shadlou, S.; Shokrieh, M. *Compos. Struct.*, *93*, 2250–2259, 2011.
168. Shokrieh, M.M.; Rafiee, R. *Compos. Struct.*, *92*, 647–652, 2010.
169. Arrighi, V.; McEwen, I.; Qian, H.; Prieto, M.S. *Polymer*, *44*, 6259–6266, 2003.
170. Yang, S.; Yu, S.; Ryu, J.; Cho, J.-M.; Kyoung, W.; Han, D.-S.; Cho, M. *Int. J. Plast.*, *41*, 124–146, 2013.
171. Mortezaei, M.; Famili, M.H.N.; Kokabi, M. *Compos. Sci. Technol.*, *71*, 1039–1045, 2011.
172. Fragiadakis, D.; Pissis, P.; Bokobza, L. *Polymer*, *46*, 6001–6008, 2005.
173. Yang, S.; Cho, M. *Appl. Phys. Lett.*, *94*, 223104, 2009.

174. Loo, Y.-L.; Register, R.A.; Ryan, A.J. *Phys. Rev. Lett.*, **84**, 4120, 2000.
175. Loo, Y.-L.; Register, R.A.; Ryan, A.J. *Macromolecules*, **35**, 2365–2374, 2002.
176. Santana, O.O.; Müller, A.J. *Polym. Bull.*, **32**, 471–477, 1994.
177. Woo, E.; Huh, J.; Jeong, Y.G.; Shin, K. *Phys. Rev. Lett.*, **98**, 136103, 2007.
178. Wu, H.; Wang, W.; Yang, H.; Su, Z. *Macromolecules*, **40**, 4244–4249, 2007.
179. Shin, K.; Woo, E.; Jeong, Y.G.; Kim, C.; Huh, J.; Kim, K.-W. *Macromolecules*, **40**, 6617–6623, 2007.
180. Di Maio, E.; Iannace, S.; Sorrentino, L.; Nicolais, L. *Polymer*, **45**, 8893–8900, 2004.
181. Zhang, Q.X.; Yu, Z.Z.; Yang, M.; Ma, J.; Mai, Y.W. *J. Polym. Sci. Part B*, **41**, 2861–2869, 2003.
182. Mu, B.; Wang, Q.; Wang, H.; Jian, L. *J. Macromol. Sci. Part B*, **46**, 1093–1104, 2007.
183. Nam, J.Y.; Sinha Ray, S.; Okamoto, M. *Macromolecules*, **36**, 7126–7131, 2003.
184. Lincoln, D.M.; Vaia, R.A.; Krishnamoorti, R. *Macromolecules*, **37**, 4554–4561, 2004.
185. Li, L.; Li, C.Y.; Ni, C.; Rong, L.; Hsiao, B. *Polymer*, **48**, 3452–3460, 2007.
186. Phang, I.Y.; Pramoda, K.; Liu, T.; He, C. *Polym. Int.*, **53**, 1282–1289, 2004.
187. Wu, D.; Zhou, C.; Fan, X.; Mao, D.; Bian, Z. *Polym. Polym. Compos.*, **13**, 61–71, 2005.
188. Bilotti, E.; Fischer, H.; Peijs, T. *J. Appl. Polym. Sci.*, **107**, 1116–1123, 2008.
189. Xu, D.; Wang, Z. *Polymer*, **49**, 330–338, 2008.
190. Homminga, D.; Goderis, B.; Dolbnya, I.; Reynaers, H.; Groeninckx, G. *Polymer*, **46**, 11359–11365, 2005.
191. Chen, E.C.; Wu, T.M. *J. Polym. Sci. Part B*, **46**, 158–169, 2008.

192. Harrats, C.; Groeninckx, G. *Macromol. Rapid Commun.*, **29**, 14–26, 2008.
193. Guérin, G.; Prud'Homme, R.E. *J. Polym. Sci. Part B*, **45**, 10–17, 2007.
194. Rittigstein, P.; Torkelson, J.M. *J. Polym. Sci. Part B*, **44**, 2935–2943, 2006.
195. Pluta, M.; Jeszka, J.; Boiteux, G. *Eur. Polym. J.*, **43**, 2819–2835, 2007.
196. Siegel, R.W. *Phys. Today*, **46**, 1993.
197. Mayo, M.J.; Siegel, R.W.; Narayanasamy, A.; Nix, W.D. *J. Mater. Res.*, **5**, 1073–1082, 1990.
198. Mackay, M.E.; Tuteja, A.; Duxbury, P.M.; Hawker, C.J.; Van Horn, B.; Guan, Z.; Chen, G.; Krishnan, R. *Science*, **311**, 1740–1743, 2006.
199. Tuteja, A.; Mackay, M.E.; Hawker, C.J.; Van Horn, B. *Macromolecules*, **38**, 8000–8011, 2005.
200. Merkel, T.; Freeman, B.; Spontak, R.; He, Z.; Pinnau, I.; Meakin, P.; Hill, A. *Science*, **296**, 519–522, 2002.
201. Kharchenko, S.B.; Douglas, J.F.; Obrzut, J.; Grulke, E.A.; Migler, K.B. *Nat. Mater.*, **3**, 564–568, 2004.
202. Ren, J.; Krishnamoorti, R. *Macromolecules*, **36**, 4443–4451, 2003.
203. Jain, S.; Goossens, H.; Picchioni, F.; Magusin, P.; Mezari, B.; van Duin, M. *Polymer*, **46**, 6666–6681, 2005.
204. Li, Y.; Shimizu, H. *Polymer*, **45**, 7381–7388, 2004.
205. Khatua, B.; Lee, D.J.; Kim, H.Y.; Kim, J.K. *Macromolecules*, **37**, 2454–2459, 2004.
206. Si, M.; Araki, T.; Ade, H.; Kilcoyne, A.; Fisher, R.; Sokolov, J.C.; Rafailovich, M.H. *Macromolecules*, **39**, 4793–4801, 2006.
207. Vo, L.T.; Giannelis, E.P. *Macromolecules*, **40**, 8271–8276, 2007.
208. Zhang, Q.; Yang, H.; Fu, Q. *Polymer*, **45**, 1913–1922, 2004.

209. Wang, Y.; Zhang, Q.; Fu, Q. *Macromol. Rapid Commun.*, **24**, 231–235, 2003.
210. International Organization for Standardization (ISO). *Road Vehicles, and Tractors and Machinery for Agriculture and Forestry—Determination of Burning Behaviour of Interior Materials*; International Organization for Standardization: Geneva, Switzerland, 2013; Volume ISO 3795:1989, p. 6.
211. Stevens, M.; Bugnicourt, E.; Seignan, J. Harmonised fr regulations accelerate composites growth in public transportation. *Reinf. Plast.* 2008, **52**, 40–41.
212. Intrater, J. *Mater. Manuf. Process.*, **23**, 220–221, 2008.
213. Horrocks, A.R.; Kandola, B.K.; Nazare, S.; Padbury, S. Nanoclay-Flame retardant interactions in thermoplastic and thermosetting polymers. In *MODEST*; Villeurbanne, France, 2004.
214. Zanetti, M.; Lomakin, S.; Camino, G. *Macromol. Mater. Eng.*, **279**, 1–9, 2000.
215. Hsiue, G.H.; Liu, Y.L.; Liao, H.H. *J. Polym. Sci. Part A*, **39**, 986–996, 2001.
216. Nodoro, T.V.; Böhm, M.C.; Müller-Plathe, F. *Macromolecules*, **45**, 171–179, 2011.
217. Nodoro, T.V.; Voyiatzis, E.; Ghanbari, A.; Theodorou, D.N.; Böhm, M.C.; Müller-Plathe, F. *Macromolecules*, **44**, 2316–2327, 2011.
218. Liu, J.; Wu, Y.; Shen, J.; Gao, Y.; Zhang, L.; Cao, D. *Phys. Chem. Chem. Phys.*, **13**, 13058–13069, 2011
219. Ragesh, P.; Ganesh, V.A.; Naira, S.V.; Nair, A.S. *J. Mater. Chem. A*, **2**, 14773–14797, 2014.
220. Kota, A.K.; Choi, W.; Tuteja, A. *MRS Bull.*, **38**, 383–390, 2013.
221. Tuteja, A.; Choi, W.; Ma, M.L.; Mabry, J.M.; Mazzella, S.A.; Rutledge, G.C.; McKinley, G.H.; Cohen, R.E. *Science*, **318**, 1618–1622, 2007.
222. Bhushan, B.; Jung, Y.C. *Nanotechnology*, **17**, 2758–2772, 2006.
223. Koch, K.; Bhushan, B.; Barthlott, W. *Soft Matter*, **4**, 1943–1963, 2008.



224. Ensikat, H.J.; Ditsche-Kuru, P.; Neinhuis, C.; Barthlott, W. *Beilstein J. Nanotechnol.*, **2**, 152–161, 2011.
225. Gao, N.; Yan, Y.Y. *Nanoscale*, **4**, 2202–2218, 2012.
226. Leng, B.X.; Shao, Z.Z.; de With, G.; Ming, W.H. *Langmuir*, **25**, 2456–2460, 2009.
227. Hsieh, C.T.; Wu, F.L.; Chen, W.Y. *J. Phys. Chem. C*, **113**, 13683–13688, 2009.
228. Wang, L.F.; Yang, S.Y.; Wang, J.; Wang, C.F.; Chen, L. *Mater. Lett.*, **65**, 869–872, 2011.
229. Yang, H.T.; Jiang, P. *J. Colloid Interface Sci.*, **352**, 558–565, 2010.
230. Yang, S.Y.; Chen, S.; Tian, Y.; Feng, C.; Chen, L. *Chem. Mater.*, **20**, 1233–1235, 2008.
231. Gould, P. *Mater. Today*, **6**, 44–49, 2003.
232. Mats, L.; Bramwell, A.; Dupont, J.; Liu, G.J.; Oleschuk, R. *Microelectron. Eng.*, **148**, 91–97, 2015.
233. Perl, E.E.; McMahon, W.E.; Farrell, R.M.; DenBaars, S.P.; Speck, J.S.; Bowers, J.E. *Nano Lett.*, **14**, 5960–5964, 2014.
234. Li, F.; Du, M.; Zheng, Z.; Song, Y.H.; Zheng, Q. *Adv. Mater. Interfaces*, **2**, 2015.
235. Jiao, L.Y.; Zhang, L.; Wang, X.R.; Diankov, G.; Dai, H.J. *Nature*, **458**, 877–880, 2009.
236. Chen, L.; Yan, L.L.; Li, Q.; Wang, C.F.; Chen, S. *Langmuir*, **26**, 1724–1733, 2010.
237. Cao, L.L.; Gao, D. *Faraday Discuss.*, **146**, 57–65, 2010.
238. Cha, N.G.; Echegoyen, Y.; Kim, T.H.; Park, J.G.; Busnaina, A.A. *Langmuir*, **25**, 11375–11382, 2009.
239. Lassiaz, S.; Galarneau, A.; Trens, P.; Labarre, D.; Mutin, H.; Brunel, D. *New J. Chem.*, **34**, 1424–1435, 2010.

240. Sas, I.; Gorga, R.E.; Joines, J.A.; Thoney, K.A. *J. Polym. Sci. Part B*, *50*, 824–845, 2012.
241. Menini, R.; Farzaneh, M. *Polym. Int.*, *57*, 77–84, 2008.
242. Asmatulu, R.; Ceylan, M.; Nuraje, N. *Langmuir*, *27*, 504–507, 2011.
243. Shao, L.J.; Wu, J.; Xu, Z.K. *Chin. J. Polym. Sci.*, *27*, 115–120, 2009.
244. Singh, A.; Steely, L.; Allcock, H.R. *Langmuir*, *21*, 11604–11607, 2005.
245. Martinez-Sanz, M.; Lopez-Rubio, A.; Lagaron, J.M. *Carbohydr. Polym.*, *98*, 1072–1082, 2013.
246. Deng, X.; Mammen, L.; Butt, H.J.; Vollmer, D. *Science*, *335*, 67–70, 2012.
247. Seo, K.; Kim, M.; Kim, D.H. *Carbon*, *68*, 583–596, 2014
248. Huang, Y.H. U.S. Patent 20120219801 A1, 30 August 2012.
249. Valpey, R.S.; Jones, M.A. International Patent WO2004037944, 27 March 2004.
250. Hu, J.; Zou, H.; Liu, G.; Li, F.; Lin, S.; Zhang, G.; Tu, Y.; Hu, M. Chinese Patent CN103436138 B, 28/10/2015.
251. Kanagasabapathy, S.; Baumgart, R.J.; Dituro, M.A.; Su, W.C.; Lockwood, F.E. International Patent WO2008153687 A3, 29/01/2009.
252. Zischka, M.; Spanring, J.; Reischl, M. International Patent WO2012168433 A1, 13/12/2012.
253. Lee, J.H.; Jo, K.S.; Lee, S.W.; Park, M.Y.; Lee, S.E.; Lee, K.W.; Kim, J.H.; Lim, H.K.; Lee, S.S. International Patent WO2013012123 A1, 24/01/2013.
254. Carew, D.; Hamilton, S.P. International Patent WO2008025085 A1, 06/03/2008.
255. Lindgren, E.; Larsson, K.; Sundstrand, S.; Andersson, A. U.S. Patent 5603997 A, 18/02/1997.
256. Sajot, N.; Pollacchi, B.; Sellak, S. U.S. Patent 20080221247 A1, 11/09/2008.

257. Beydoun, D.; Amal, R.; Low, G.; McEvoy, S. *J. Nanopart. Res.*, **1**, 439–458, 1999.
258. Yoon, H.; Joshi, B.; Na, S.-H.; Yoon, S.S. *J. Electrochem. Soc.*, **159**, H823–H827, 2012.
259. Tudor, I.A.; Petriceanu, M.; Piticescu, R.-R.; Piticescu, R.M.; Predescu, C. *UPB Sci. Bull. Ser. B*, **76**, 207–215, 2014.
260. Serrano, C.; Bugnicourt, E.; Niculescu, C.; Ghituleasa, C.; Dumitrescu, I.; Sobetkii, A.; Mocioiu, A.M.; Petriceanu, M.; Piticescu, R.M. Manucoat. In Proceedings of the ANNIC 2015 Applied Nanotechnology and Nanoscience International Conference, Paris, France, 5–7 November 2015.
261. Cantarella, M.; Sanz, R.; Buccheri, M.A.; Ruffino, F.; Rappazzo, G.; Scalese, S.; Impellizzeri, G.; Romano, L.; Privitera, V. *J. Photochem. Photobiol. A*, **321**, 1–11, 2016.
262. Hu, K.; Kulkarni, D.D.; Choi, I.; Tsukruk, V.V. *Prog. Polym. Sci.*, **39**, 1934–1972, 2014.
263. Yano, K.; Usuki, A.; Okada, A. *J. Polym. Sci. Part A*, **35**, 2289–2294, 1997.
264. Rhim, J.-W.; Ng, P.K.W. *Crit. Rev. Food Sci. Nutr.*, **47**, 411–433, 2007.
265. Nazarenko, S.; Meneghetti, P.; Julmon, P.; Olson, B.G.; Qutubuddin, S. *J. Polym. Sci. Part B*, **45**, 1733–1753, 2007.
266. Choi, W.J.; Kim, H.J.; Yoon, K.H.; Kwon, O.H.; Hwang, C.I. *J. Appl. Polym. Sci.*, **100**, 4875–4879, 2006.
267. Sanchez-Garcia, M.D.; Gimenez, E.; Lagaron, J.M. *J. Plast. Film Sheeting*, **23**, 133–148, 2007.
268. Lagaron, J.M.; Cabedo, L.; Cava, D.; Feijoo, J.L.; Gavara, R.; Gimenez, E. *Food Addit. Contam.*, **22**, 994–998, 2005.
269. Thellen, C.; Orroth, C.; Froio, D.; Ziegler, D.; Lucciarini, J.; Farrell, R.; D'Souza, N.A.; Ratto, J.A. *Polymer*, **46**, 11716–11727, 2005.

270. Sinha Ray, S.; Yamada, K.; Okamoto, M.; Fujimoto, Y.; Ogami, A.; Ueda, K. *Polymer*, *44*, 6633–6646, 2003.
271. Osman, M.A.; Rupp, J.E.P.; Suter, U.W. *J. Mater. Chem.*, *15*, 1298–1304, 2005.
272. Lotti, C.; Isaac, C.S.; Branciforti, M.C.; Alves, R.M.V.; Liberman, S.; Bretas, R.E.S. *Eur. Polym. J.*, *44*, 1346–1357, 2008.
273. Dadbin, S.; Noferesti, M.; Frounchi, M. *Macromol. Symp.*, *274*, 22–27, 2008.
274. Geim, A.K.; Novoselov, K.S. *Nat. Mater.*, *6*, 183–191, 2007.
275. Bunch, J.S.; Verbridge, S.S.; Alden, J.S.; van der Zande, A.M.; Parpia, J.M.; Craighead, H.G.; McEuen, P.L. *Nano Lett.*, *8*, 2458–2462, 2008.
276. Leenaerts, O.; Partoens, B.; Peeters, F.M. *Appl. Phys. Lett.*, *93*, 193107, 2008.
277. Yoo, B.M.; Shin, H.J.; Yoon, H.W.; Park, H.B. *J. Appl. Polym. Sci.*, *131*, 39628, 2014.
278. Huang, P.Y.; Ruiz-Vargas, C.S.; van der Zande, A.M.; Whitney, W.S.; Levendorf, M.P.; Kevek, J.W.; Garg, S.; Alden, J.S.; Hustedt, C.J.; Zhu, Y.; et al. *Nature*, *469*, 389–392, 2011.
279. Dreyer, D.R.; Park, S.; Bielawski, C.W.; Ruoff, R.S. *Chem. Soc. Rev.*, *39*, 228–240, 2010.
280. Suk, J.W.; Piner, R.D.; An, J.; Ruoff, R.S. *ACS Nano*, *4*, 6557–6564, 2010.
281. Compton, O.C.; Kim, S.; Pierre, C.; Torkelson, J.M.; Nguyen, S.T. *Adv. Mater.*, *22*, 4759–4763, 2010.
282. Kuila, T.; Bose, S.; Mishra, A.K.; Khanra, P.; Kim, N.H.; Lee, J.H. *Polym. Test.*, *31*, 31–38, 2012.
283. Shim, S.H.; Kim, K.T.; Lee, J.U.; Jo, W.H. *ACS Appl. Mater. Interfaces*, *4*, 4184–4191, 2012.
284. Al-Jabareen, A.; Al-Bustami, H.; Harel, H.; Marom, G. *J. Appl. Polym. Sci.*, *128*, 1534–1539, 2013.

285. Pinto, A.M.; Cabral, J.; Tanaka, D.A.P.; Mendes, A.M.; Magalhães, F.D. *Polym. Int.*, **62**, 33–40, 2013.
286. Song, P.a.; Yu, Y.; Zhang, T.; Fu, S.; Fang, Z.; Wu, Q. *Ind. Eng. Chem. Res.*, **51**, 7255–7263, 2012.
287. NANOMASTER. Graphene based thermoplastic masterbatches for conventional and additive manufacturing processes. In *Nanomaster Periodic Report Summary*; UK, 2013.
288. Casiraghi, C.; Robertson, J.; Ferrari, A.C. *Mater. Today*, **10**, 44–53, 2007.
289. Castillo, L.; López, O.; López, C.; Zaritzky, N.; García, M.A.; Barbosa, S.; Villar, M. *Carbohydr. Polym.*, **95**, 664–674, 2013.
290. Fabra, M.J.; Lopez-Rubio, A.; Lagaron, J.M. *Food Hydrocoll.*, **55**, 11–18, 2016.
291. Rao, S.; Upadhyay, J.; Das, R. Manufacturing and characterization of multifunctional polymer-reduced graphene oxide nanocomposites, In *Fillers and Reinforcements for Advanced Nanocomposites*; Woodhead Publishing: Camebridge, UK, 2015, 157–232.
292. Wen, P.; Zhu, D.H.; Feng, K.; Liu, F.J.; Lou, W.Y.; Li, N.; Zong, M.H.; Wu, H. *Food Chem.*, **196**, 996–1004, 2016.
293. Fabra, M.J.; López-Rubio, A.; Sentandreu, E.; Lagaron, J.M. *Starch/Staerke*, **68**, 603–610, 2015.
294. Schmidt, M.C.; Loibl, F.; Muller, M.; Oehr, C.; Hirth, T. *J. Adhes. Sci. Technol.*, **26**, 2449–2467, 2012.
295. Bellanger, H.; Darmanin, T.; Taffin de Givenchy, E.; Guittard, F. *Chem. Rev.*, **114**, 2694–2716, 2014.
296. Nishino, T.; Meguro, M.; Nakamae, K.; Matsushita, M.; Ueda, Y. *Langmuir*, **15**, 4321–4323, 1999.
297. Teshima, K.; Sugimura, H.; Inoue, Y.; Takai, O.; Takano, A. *Langmuir*, **19**, 10624–10627, 2003.

298. Teshima, K.; Sugimura, H.; Inoue, Y.; Takai, O.; Takano, A. *Appl. Surf. Sci.*, **244**, 619–622, 2005.
299. LiquiGlide. Available online: <http://liquiglide.com> (accessed on 23 February 2016).
300. Smith, J.D.; Dhiman, R.; Anand, S.; Reza-Garduno, E.; Cohen, R.E.; McKinley, G.H.; Varanasi, K.K. *Soft Matter*, **9**, 1772–1780, 2013.
301. Loibl, F.; Schmidt, M.C.; Auer-Seidl, A.; Kirchner, C.; Holtz, C.; Muller, K.; Stramm, C.; Langowski, H.C. *J. Adhes. Sci. Technol.*, **26**, 2469–2503, 2012.
302. Merck. *Merck Presents Organic Photovoltaic Materials at Expo 2015 in Milan*; Merck KGaA: Darmstadt, Germany, 2015.
303. Belectric. *Gray Modules: New Dimension in Organic Photovoltaics for Buildings*; BELECTRIC OPV GmbH: Nuremberg, Germany, 2015.
304. European Commission DG, Environment News Alert Service. *Science for Environment Policy*; edited by SCU, the University of the West of England:: Bristol, UK, 2015.
305. Brongersma, M.L.; Cui, Y.; Fan, S. *Nat. Mater.*, **13**, 451–460, 2014.
306. Li, G.; Shrotriya, V.; Huang, J.; Yao, Y.; Moriarty, T.; Emery, K.; Yang, Y. *Nat. Mater.*, **4**, 864–868, 2005.
307. Kim, J.Y.; Kim, S.H.; Lee, H.H.; Lee, K.; Ma, W.; Gong, X.; Heeger, A.J. *Adv. Mater.*, **18**, 572–576, 2006.
308. Wang, E.; Wang, L.; Lan, L.; Luo, C.; Zhuang, W.; Peng, J.; Cao, Y. *Appl. Phys. Lett.*, **92**, 33307–33307, 2008.
309. Reese, M.O.; Morfa, A.J.; White, M.S.; Kopidakis, N.; Shaheen, S.E.; Rumbles, G.; Ginley, D.S. *Sol. Energy Mater. Sol. C*, **92**, 746–752, 2008.
310. Pei, J.; Tao, J.; Zhou, Y.; Dong, Q.; Liu, Z.; Li, Z.; Chen, F.; Zhang, J.; Xu, W.; Tian, W. *Sol. Energy Mater. Sol. C*, **95**, 3281–3286, 2011.
311. Chen, F.-C.; Wu, J.-L.; Lee, C.-L.; Hong, Y.; Kuo, C.-H.; Huang, M.H. *Appl. Phys. Lett.*, **95**, 013305, 2009.

312. Tang, Z.; Liu, Q.; Chen, Q.; Khatri, I.; Shirai, H. *Phys. Status Solidi A*, 211, 1179–1183, 2014.
313. Howarter, J.A.; Youngblood, J.P. *Macromol. Rapid Commun.*, 29, 455–466, 2008.
314. Gray, A. Self-Cleaning Hydrophobic Nano Coating for Solar Panel Glass Generating Great Results for Nanoshell. Available online: [http://www.pv-magazine.com/services/press-releases/details/beitrag/self-cleaning-hydrophobic-nano-coating-for-solar-panel-glass-generating-great-results-for-nanoshell\\_100005577/#ixzz3Sr9qqsGv](http://www.pv-magazine.com/services/press-releases/details/beitrag/self-cleaning-hydrophobic-nano-coating-for-solar-panel-glass-generating-great-results-for-nanoshell_100005577/#ixzz3Sr9qqsGv) (accessed on 18 February 2016).
315. Friday, L. Self-Cleaning System Boosts Efficiency of Solar Panels. Available online: <http://www.bu.edu/today/2014/self-cleaning-system-boosts-efficiency-of-solar-panels/> (accessed on 18 February 2016).
316. Bullis, K. Self-Cleaning Solar Panels. Available online: <http://www.technologyreview.com/news/420524/self-cleaning-solar-panels/> (accessed on 18 February 2016).
317. Zhao, X.Y.; Yang, W.W.; Lie, C.; Wang, X.Z.; Lim, S.L.; Qi, D.C.; Wang, R.; Gao, Z.Q.; Mi, B.X.; Chen, Z.K.; et al. *Sol. Energy Mater. Sol. C*, 134, 140–147, 2015.
318. Yoon, H.; Mali, M.G.; Kim, M.W.; Al-Deyab, S.S.; Yoon, S.S. *Catal. Today*, 260, 89–94, 2016.
319. Liu, J.; Fu, X.; Cao, D.P.; Mao, L.; Wang, J.; Mu, D.H.; Mi, B.X.; Zhao, B.M.; Gao, Z.Q. *Organ. Electron. Phys. Mater. Appl.*, 23, 158–163, 2015.
320. Ranjgar, A.; Norouzi, R.; Zolanvari, A.; Sadeghi, H. *Armen. J. Phys.*, 6, 198–203, 2013.
321. Pavlidou, S.; Papaspyrides, C. *Prog. Polym. Sci.*, 33, 1119–1198, 2008.
322. Kotal, M.; Bhowmick, A.K. *Prog. Polym. Sci.*, 51, 127–187, 2015.
323. International Organization for Standardization (ISO). *Nanotechnologies—Nanomaterial Risk Evaluation*; International Organization for Standardization: Geneva, Switzerland, 2011; Volume ISO/TR 13121:2011, p. 58.

324. Poland, C.A.; Read, S.A.K.; Varet, J.; Carse, G.; Christensen, F.M.; Hankin, S.M. *Dermal Absorption of Nanomaterials*; Danish Ministry of the Environment: Copenhagen, Denmark, 2013.
325. Störmer, A.; Bott, J.; Kemmer, D.; Franz, R. *Trends Food Sci. Technol.*, **63**, 39–50, 2017.
326. Duncan, T.V. *ACS Appl. Mater. Interfaces* 2015, **7**, 20–39.
327. Duncan, T.V.; Pillai, K. *ACS Appl. Mater. Interfaces*, **7**, 2–19, 2015.
328. Heitbrink, W.A.; Lo, L.-M.; Farwick, D.R. *Evaluation of Enclosing Hood and Downflow Room for Nanocomposite Manufacturing*; EPHB-356-16a; U.S. Department of Health and Human Services, Public Health Service, Centers for Disease Control and Prevention: Cincinnati, OH, USA, 2012.
329. Heitbrink, W.; Lo, L.-M.; Garcia, A. *Case Study: Particle Emissions from the Processes of Machining Nanocomposites*; EPHB 356-19a; National Institute for Occupational Safety and Health: Cincinnati, OH, USA, 2013.
330. Nowack, B.; David, R.M.; Fissan, H.; Morris, H.; Shatkin, J.A.; Stintz, M.; Zepp, R.; Brouwer, D. *Environ. Int.*, **59**, 1–11, 2013.
331. Froggett, S.J.; Clancy, S.F.; Boverhof, D.R.; Canady, R.A. *Part. Fibre Toxicol.*, **11**, 17, 2014.
332. Methner, M.; Crawford, C.; Geraci, C. *J. Occup. Environ. Hyg.*, **9**, 308–318, 2012.
333. Ogura, I.; Kotake, M.; Shigeta, M.; Uejima, M.; Saito, K.; Hashimoto, N.; Kishimoto, A. *J. Phys. Conf. Ser.*, **429**, 012049, 2013.
334. Bello, D.; Wardle, B.L.; Yamamoto, N.; Guzman DeVilloria, R.; Garcia, E.J.; Hart, A.J.; Ahn, K.; Ellenbecker, M.J.; Hallock, M. *J. Nanopart. Res.*, **11**, 231–249, 2009.
335. Lo, L.-M.; Dunn, K.H.; Hammond, D.; Marlow, D.; Topmiller, J.; Tsai, C.S.J.; Ellenbecker, M.; Huang, C.-C. *Evaluation of Engineering Controls in a Manufacturing Facility Producing Carbon Nanotube-Based Products*; EPHB-356-13a; U.S. Department of Health and Human Services, Public Health Service, Centers for Disease Control and Prevention: Cincinnati, OH, USA, 2012.



336. Bello, D.; Wardle, B.L.; Zhang, J.; Yamamoto, N.; Santeufemio, C.; Hallock, M.; Virji, M.A. *Int. J. Occup. Environ. Health*, *16*, 434–450, 2010.
337. Wohlleben, W.; Brill, S.; Meier, M.W.; Mertler, M.; Cox, G.; Hirth, S.; Von Vacano, B.; Strauss, V.; Treumann, S.; Wiench, K.; et al. *Small*, *7*, 2384–2395, 2011.
338. Schlagenhauf, L.; Buerki-Thurnherr, T.; Kuo, Y.Y.; Wichser, A.; Nüesch, F.; Wick, P.; Wang, J. *Environ. Sci. Technol.*, *49*, 10616–10623, 2015.
339. Schlagenhauf, L.; Kianfar, B.; Buerki-Thurnherr, T.; Kuo, Y.Y.; Wichser, A.; Nüesch, F.; Wick, P.; Wang, J. *Nanoscale*, *7*, 18524–18536, 2015.
340. Cena, L.G.; Peters, T.M. *J. Occup. Environ. Hyg.*, *8*, 86–92, 2011.
341. Bernard, C.; Nguyen, T.; Pellegrin, B.; Holbrook, R.D.; Zhao, M.; Chin, J. *J. Phys.*, *304*, 012063, 2011.
342. Wohlleben, W.; Meier, M.W.; Vogel, S.; Landsiedel, R.; Cox, G.; Hirth, S.; Tomović, Z. *Nanoscale*, *5*, 369–380, 2013.
343. Hamilton Jr, R.F.; Wu, Z.; Mitra, S.; Shaw, P.K.; Holian, *Part. Fibre Toxicol.*, *10*, 57, 2013.
344. Ma-Hock, L.; Strauss, V.; Treumann, S.; Küttler, K.; Wohlleben, W.; Hofmann, T.; Gröters, S.; Wiench, K.; van Ravenzwaay, B.; Landsiedel, R. *Part. Fibre Toxicol.*, *10*, 23, 2013.
345. Grosse, Y.; Loomis, D.; Guyton, K.Z.; Lauby-Secretan, B.; El Ghissassi, F.; Bouvard, V.; Benbrahim-Tallaa, L.; Guha, N.; Scoccianti, C.; Mattock, H.; et al. *Lancet Oncol.*, *15*, 1427–1428, 2014.
346. Koponen, I.K.; Jensen, K.A.; Schneider, T. *J. Phys.*, *151*, 012048, 2009.



# 7.

## **ULTRASOUND ASSISTED EXTRUSION TO PREPARE LIGHT AND REINFORCED POLYPROPYLENE NANOCOMPOSITES FOR AUTOMOTIVE APPLICATIONS**



# 7. ULTRASOUND ASSISTED EXTRUSION TO PREPARE LIGHT AND REINFORCED POLYPROPYLENE NANOCOMPOSITES FOR AUTOMOTIVE APPLICATIONS

## 7.1 Introduction

Plastics industry is the focus of great attention due to its environmental impact mainly caused by poor degradability of materials and their high production volume. Many measures are being considered on manufacture, origin, or even the effectiveness of polymers for different sectors. In the specific case of the automotive industry, the reduction of CO<sub>2</sub> emissions from new vehicles is an environmental priority. Cars are responsible for around 12% of CO<sub>2</sub> emissions throughout the European Union. On April 17, 2019, the European Parliament and the Council adopted Regulation (EU) 2019/631 that sets CO<sub>2</sub> emission performance standards for new passenger cars and for new light commercial vehicles in the EU for the subsequent period to 2020. This regulation indicates that the emission must be 95 g of CO<sub>2</sub>/km, an ambitious objective since in 2007, an improvement was registered to 152, and the recent data for 2018 is 120,4 g of CO<sub>2</sub>/km. A big effort has been done over the years to reduce the weight of different components that make up a vehicle, but the goal set in Europe has not yet been reached. The plastic-based components of a car represent 14% of the weight, enough to bring the attention towards this family of materials. Most of these components are reinforced with fiberglass, talc, calcium carbonate, among others, reaching their functional objectives but unfortunately increasing their weight.

The door panel of a vehicle is a component that must meet minimum mechanical properties, such as elastic modulus, flexural strength or impact strength. A typical panel weights around 1,500 g and appears a clear car component where efforts to reduce weight and keep performance are justified. A reinforced block copolymer of polypropylene (i.e., Innopol PP CS 2-9120) is a material typically employed as a door panel. This material is loaded with 20 wt.% of talc and a small percentage of an elastomer to improve its impact properties. Density of such loaded material becomes higher than neat polypropylene (PP) (i.e., 1.04 g/cm<sup>3</sup> with respect to 0,90-0,92 g/cm<sup>3</sup>) and therefore reformulations implying the use of new reinforcements, additives and polymers are plenty

justified if weight can be decreased, and mechanical properties could be maintained. Note that initial formulations are based on talc (up to 20 wt.%) due to economic reasons, capacity to improve mechanical properties, prevention of defects during injection, but its high density (2.7-2.8 g/cm<sup>3</sup>) advise against its use when a reduction of the total weight of automotive components is desirable.

The use of nanoclays may be an interesting alternative since its high surface area may provide interfacial interactions that lead to improved mechanical properties [1-4]. There are different factors that should be taken into account to get a great efficiency when nanoparticles are incorporated inside a polymer matrix: effective surface area, aspect ratio and wettability of particles, compatibility between nanoparticles and the polymer matrix, degree of dispersion of nanoparticles in the polymeric matrix and strength of interfacial interactions [5-8]. In order to improve the compatibility between the polymer matrix and the fillers polypropylene grafted with maleic anhydride will also be added.

The use of hollow glass particles is a strategy similar to the foaming of injected parts, a technology in evolution for decades [9]. A porous injected component is derived with little modification of its mechanical properties, but with a considerable density reduction. This method (Mucell process) was originated at MIT in 1980 and marketed by Trexel Inc. Addition of hollow glass spheres is an alternative to this process, which entails a technological challenge and a higher investment cost in equipment [10,11]. Selection of hollow glass spheres with low density and low diameter is interesting since a low repercussion on mechanical properties is expected.

Compounding extrusion is a transformation process widely used in industry to add reinforcements or additives to a polymeric base and get a material with specific properties. The extrusion assisted by an ultrasound system was designed at first time to improve the dispersion of nanofillers, but different approaches were developed during the last years to reach a chemical or physical effect on the polymer, to improve the compatibility between two or more polymers (blending) or the contrary effect, to decrosslink a polymer network. The ultrasonic energy has a different effect dependently on the polymer, the amplitude or energy of the applied ultrasonic waves, or even the situation of the ultrasonic source in the extruder. In the present work, the ultrasound system was located in the last phase of the extrusion process (i.e., when the pressure is maximum, and the polymer is in a molten state). In this way, energy can efficiently be transferred to the nano-reinforcements and led to a greater degree of dispersion within

the polymeric matrix. As a consequence, an improvement of mechanical properties such as elongation at break and toughness is expected [12-15]. Positive influence of ultrasounds has been reported for other properties like oxygen permeability. Note also that the die where the ultrasound system is coupled, has a decrease in pressure when the ultrasonic energy is activated as consequence of the reduced friction between the polymer and the die walls [16,17]. In addition, the applied ultrasonic energy should be carefully controlled in order to avoid polymer degradation. By contrast, some studies on ultrasound processed samples indicate the formation of long chain radicals [18], which can end up on the surface of the clay or combine with surface modifying agents (i.e., when organoclays are employed), forming a new chemical bond. Finally, it is reported the influence of ultrasounds for the improvement of the efficiency of PP-g-MA as compatibilizer agent that makes feasible to attain a higher dispersion of nanoparticles is attributed due to this effect [19,20]. The final high dispersion has also been attributed to the capacity of ultrasonic wave to promote the formation of more PP macro-radicals able to interact with maleic anhydride grafts [21,22]. Nevertheless, a negative effect of ultrasounds to the mixtures of PP and maleic anhydride in the molten state has also been reported [23].

## 7.2 Experimental section

### 7.2.1 Materials

The reference material was INNOPOL PP CS 2-9120 (Inno-Comp Ltd.), a 20 wt.% talc-filled compound based on a copolymer having predominantly polypropylene blocks together with an unspecified quantity of elastomeric blocks. Density is 1.04 g/cm<sup>3</sup> and the melt flow index (MFI) 30 (230 °C/2.16 kg).

New polymeric materials were selected with a lower density and specifically polypropylenes BF970MO (PP1) and ISPLEN PP080G2M (PP2) were employed.

BF970MO is a heterophasic copolymer from Borealis that is characterized by a density of 0.905 g/cm<sup>3</sup>, a MFI of 20, a tensile stress of 27 MPa and Charpy impact strength of 9 kJ/m<sup>2</sup>.

ISPLEN PP080G2M is a polypropylene homopolymer from Repsol that is characterized by a density of 0.905 g/cm<sup>3</sup>, a MFI of 20 and Charpy impact strength of 3 kJ/m<sup>2</sup>.

Selected nanoclays were Cloisite 20 and Garamite 1958 from BYK. The first one is a bis(hydrogenated tallow alkyl)dimethyl *ammonium* bentonite salt with a density of 1.77 g/cm<sup>3</sup> and a characteristic X-ray diffraction spacing at 3.16 nm (i.e., 001 reflection). The second nanoclay is a mixture of sheet and whiskers clays modified with an organic quaternary ammonium salt. The material has a density of 1.60 g/cm<sup>3</sup> and provides good thixotropic properties.

Scona TPPP 2112 GA, a maleic anhydride grafted polypropylene, was purchased from BYK and employed as a compatibilizer agent, with a maleic anhydride content of 0.9-1.2 wt.%.

iM30k glass bubbles with density of 0.60 g/cm<sup>3</sup> and average particle diameter of 18 µm were provided by 3M™.

### 7.2.2 Compounding extrusion

A co-rotating twin-screw extruder Coperion ZSK 18MEGAlab was employed to prepare the different masterbatches from each polymer that incorporate 20 wt.% of the corresponding filler. These will be named as MBPP2-20NCG (for Garamite 1958), MBPP2-20NCC (for Cloisite 20) and MBPP2-20GB (for glass bubbles). During this process, the compatibilizer agent was added at 2 wt.%. The ultrasound system was not used in this former step since it was considered that homogenization was enough.

### 7.2.3 Preparation of nanocomposites from the BF970MO heterophasic copolymer

Masterbatches were diluted by adding the corresponding amount of the neat copolymer in the co-rotating twin-screw extruder to get nanocomposites with clay loads of 3, 5 and 8 wt.%. In this case an ultrasonic system was mounted on the die (**Figure 7.1**). The temperature profile used during the extrusion process was 175/175/175/175/175/185/200 °C according to the processability of the base polymer. The temperature of the die was 200 °C. Samples were obtained without applying ultrasounds and applying waves with an amplitude of 45.5 µm. **Tables 7.1** and **2** show the specific extrusion parameters and the denomination of the different processed samples.



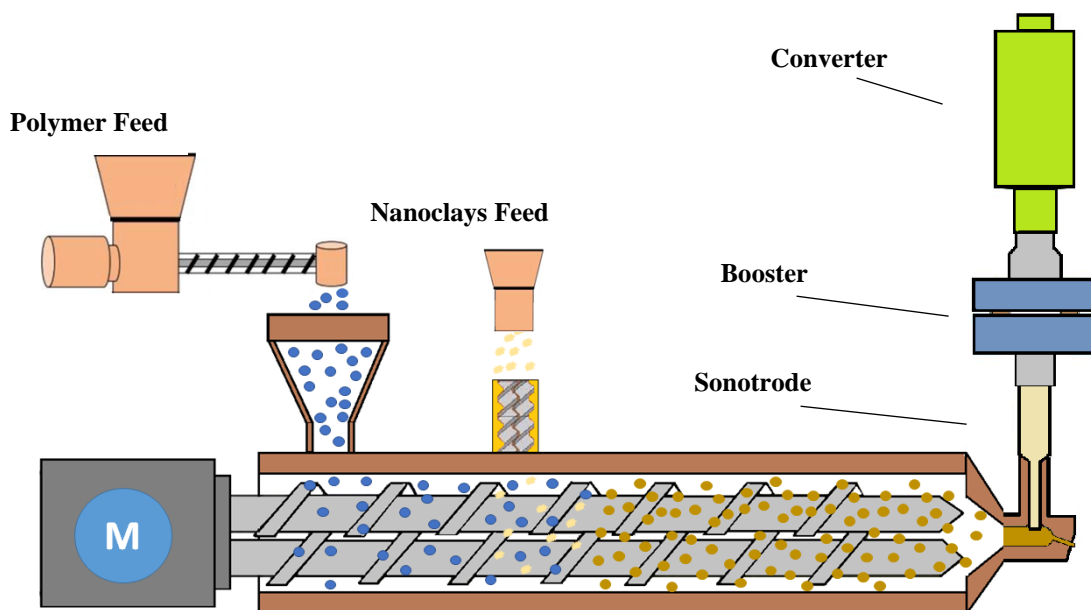


**Figure 7.1.** Scheme of the ultrasound assisted co-rotating twin-screw extruder.

**Table 7.1.** Extrusion parameters for processing PP1/Cloisite 20 nanocomposites.

	A	B	C	D	E	F	G
<b>Cloisite (%)</b>	3	3	5	5	8	8	8
<b>Flow (kg/h)</b>	9	9	9	9	9	9	7.4
<b>Screw speed (rpm)</b>	600	600	600	600	600	600	600
<b>Torque (%)</b>	62	60	60	59	60	56	61
<b>Pressure (bar)</b>	22	20	21	20	21	19	21
<b>US Amplitude (<math>\mu\text{m}</math>)</b>	0	44.5	0	44.5	0	44.5	0
<b>SME (kJ/kg)</b>	188	182	182	179	182	170	227
<b>MFI (2.16 kg, 230 °C)</b>	29.1	29.4	30.1	26.1	25.0	23.2	20.7

\*Without compatibilizer agent.

**Table 7.2.** Extrusion parameters for processing PP1/Garamite 1958 nanocomposites.

	J	K	L	M	N	O
<b>Garamite (%)</b>	3	3	5	5	8	8
<b>Flow(kg/h)</b>	7	7	7	8	7	7
<b>Screw speed (rpm)</b>	500	500	500	500	500	500
<b>Torque (%)</b>	62	59	63	58	61	60
<b>Pressure (bar)</b>	24	21	23	21	23	23
<b>US Amplitude (<math>\mu\text{m}</math>)</b>	0	44.5	0	44.5	0	44.5
<b>SME (kJ/kg)</b>	202	192	205	165	199	195
<b>MFI (2.16 kg, 230 °C)</b>	15.5	14.9	10.8	9.8	7	6.5

## 7.2.4 Preparation of nanocomposites from the ISPLEN

### PP080G2M polypropylene homopolymer

**Tables 7. 3 and 4** summarize the processing parameters for preparing PP2 samples loaded with the indicated percentages of the two nanoclays. Note that some selected

samples incorporated also 5 wt.% and 10 wt.% of glass bubbles (GB). A temperature profile of 195/210/210/220/220/230/ 230°C was applied since it was optimum for processing the base polymer. The temperature at the extrusion die was kept at 180°C.

**Table 7.3.** Extrusion parameters for processing PP2/Cloisite 20 nanocomposites.

	A'	B'	C'	D'	E'	F'	G'	H'
<b>Cloisite (%)</b>	3	3	5	5	8	8	5	5
<b>GB (%)</b>	0	0	0	0	0	0	5	10
<b>Flow (kg/h)</b>	7	6	7	6	7	6	7	7
<b>Screw speed (rpm)</b>	400	400	400	400	400	400	400	400
<b>Torque (%)</b>	66	58	62	56	61	55	61	61
<b>Pressure (bar)</b>	20	22	19	21	19	21	20	20
<b>US Amplitude (µm)</b>	0	44.5	0	44.5	0	44.5	0	0
<b>SME (kJ/kg)</b>	172	176	162	170	159	167	159	159
<b>MFI (2.16 kg, 230 °C)</b>	26.8	20.9	20.1	16	11.8	10.9	11.2	13.7

**Table 7.4.** Extrusion parameters for processing PP2/Garamite nanocomposites.

	J'	K'	L'	M'	N'	O'	Q'	R'	S'	T'
<b>Garamite</b>	3	3	5	5	8	8	5	5	8	8
<b>GB (%)</b>	0	0	0	0	0	0	5	10	5	10
<b>Flow (kg/h)</b>	6	6	6	6	6	6	7	7	7	7
<b>Screw speed (rpm)</b>	400	400	400	400	400	400	400	400	400	400
<b>Torque (%)</b>	60	60	57	60	63	60	66	64	61	68
<b>Pressure (bar)</b>	24	24	24	25	21	25	22	23	22	25
<b>US Amplitude (µm)</b>	0	44.5	0	44.5	0	44.5	0	0	0	0
<b>SME (kJ/kg)</b>	182	182	173	182	192	182	172	167	159	177
<b>MFI (2.16 kg, 230 °C)</b>	18.6	16.8	14.3	11.4	7.9	6.6	11.1	8.5	5.4	4.3

## 7.2.5 Preparation of injected samples

According to the finality of producing injected panel doors, a final step consisted on injection tests which in addition allowed evaluating the processability of the material. Further, to assess the mechanical properties of the different developed materials, standardized dumbbell specimens were obtained by injection molding for tensile and flexural tests according to ISO 527 and ISO 14125 standards. The equipment employed to obtain the dumbbell specimens was the Engel e-motion 200/55 with 55 tons of clamping force.

## 7.2.6 Measurements

The fluidity of processed specimens was tested with the Modular Flow Index equipment from CEAAT, according to the ISO 1133 standard with the test conditions of a polypropylene, weight 2.160 Kg and temperature of 230 °C.

A Focused Ion Beam Zeiss Neon40 microscope (Zeiss, Oberkochen, Germany) operating at 5 kV was used to obtain SEM micrographs of specimens. Samples were mounted on a double-side adhesive carbon disc and sputter-coated with a thin layer of carbon by using a Mitec K950 Sputter Coater (Quorum Technologies Ltd., Ashford, UK).

Tensile deformation tests were performed using the Zwick Roell Z050 Universal Tester (Barcelona, Spain) equipped with a cell charge of 500 N and testXpert 8.1 software (Zwick, Ulm, Germany) under ISO 527 at a test speed of 50 mm/min. Five specimens were tested for each processing condition. Flexural tests were performed according to ISO 14125 with method A (three points) with support spacing of 64 mm and at a speed of 5 mm/min and a stroke of 20 mm.

Calorimetric data were recorded by differential scanning calorimetry (DSC) using a TA instrument (New Castle, DE, USA) Q20 series equipped with a refrigerated cooling system operating from -40 to 400 °C. Experiments were performed under a flow of dry nitrogen with a sample of ca. 3 mg. The instrument was calibrated for temperature and heat of fusion using an indium standard. Cooling runs were performed after maintaining the sample in the melt state for 3 minutes to erase thermal history. All scans were done at a rate of 10 °C/min.

The spacing between layers of nanoclays within the polymer was studied by Wide-Angle X-ray scattering (WAXD) using a Bruker D8 Advance model with Cu K $\alpha$  radiation ( $\lambda=0.1542$  nm) and Bragg-Brentano geometry, theta-2theta. A one-dimensional Lynx Eye detector was used. The samples were processed at 40 kV and 40 mA, with a 2-theta range of 2°- 40°, measurement steps of 0.02° and time/step of 2 to 8 seconds. Deconvolution of the WAXD peaks was performed with the PeakFit v4 program from Jandel Scientific Software.

The distribution of the Cloisite 20 and 116 within the polymer matrix was complemented by observation of fine sections with a Philips TECNAI 10 electron microscope (Philips Electron Optics, Eindhoven, Netherlands) at an acceleration voltage of 100 kV. A Sorvall Porter-Blum microtome (Sorvall, New York, USA) equipped with a diamond knife was used to cut the sample into thin sections which were subsequently collected in a container filled with water and lifted onto wire racks copper with carbon coated.

Density measurements were performed using the Electronic Densimeter METROTEC MD300S (Barcelona, Spain) under ISO 1183-1:2004. Sixteen samples were tested with method A: immersion method for solid plastics (except for powders in void-free form).

## 7.3 Results and discussion

### 7.3.1 Extrusion parameters

Torque is an output value of the compounding extrusion process that allows calculating the specific mechanical energy (SME) of the screw rotation. Values are therefore indicative of the shear applied that has been applied to the processed material. In order to get comparative results for all samples prepared in this study, processing conditions were adjusted to maintain the same range of SME (i.e., materials are submitted to a similar shear during the process).

In general, the effect of ultrasounds was that the fluidity of the material increased, translating into a pressure decrease in the die for all composites based on PP1 (**Tables 7.1 and 2**), a feature that is in agreement with previous observations concerning the effect of ultrasounds [22-24]. This observation is highly positive since the increase in fluidity allows increasing both feed flow and productivity. By contrast, different results were obtained when the PP2 homopolymer was selected (**Tables 7.3 and 4**), being observed the higher pressure increase for the sample loaded with 8 wt.% of Garamite. Pressure was also slightly higher when Garamite was incorporated (i.e., 25 bar with respect to 21 bar for samples loaded with 5 wt.% of Cloisite or Garamite, respectively). Probably morphological differences between this two nanofillers (**Figure 7.2**) played a significant role. In the same way, flow rate decreased with respect to the values determined for PP1 samples (i.e., 9 Kg/h and 6 Kg/h for PP1 and PP2 samples loaded with 5 wt.% of Cloisite 20). Finally, the incorporation of glass bubbles had practically no influence since the flow rate was constant (7 Kg/h) when their content increased from 5 wt.% to 10 wt.%. Note that in this case, surface interactions between filler and polymer were less significant due to the micrometric size of the glass spheres (**Figure 7.2c**).

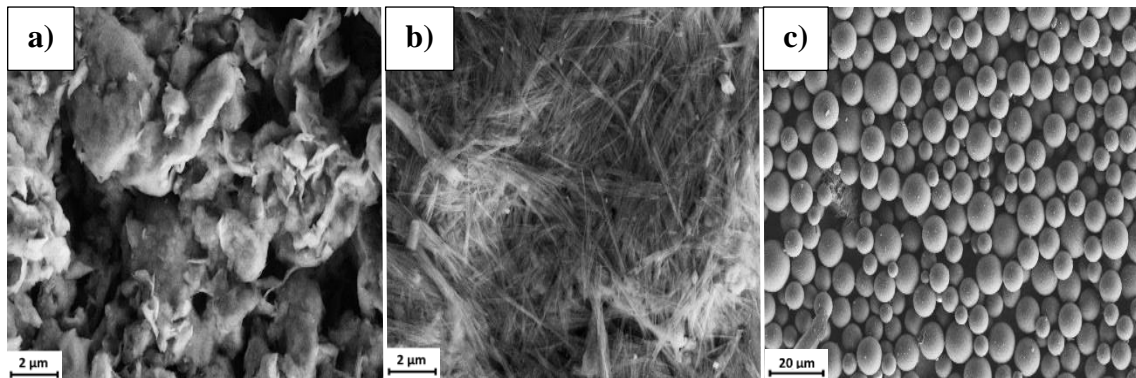


**Figure 7.2.** SEM images of Cloisite 20 (left), Garamite 1958 (center) and hollow glass spheres (right).

### 7.3.2 Rheological measurements

Before the injection molding, the MFI of each nanocompound was measured to assess the processability of the material under the same conditions. This test shows the fluidity of the polymer at a specific temperature point. The final injection process requires materials with a high fluidity and low viscosity due to the specific geometry of the molded pieces (i.e., door panels with large surface area and low thickness). A control of the MFI of the extruded nanocomposites was therefore performed (**Figure 7.3**). The MFI of the usually employed PP is 30, and around 25 for both PP1 and PP2 neat polymers. MFI measurements indicate a great influence of the added nanocomposite, a smaller effect caused by the application of ultrasounds and a distinct behavior between the two selected PPs.

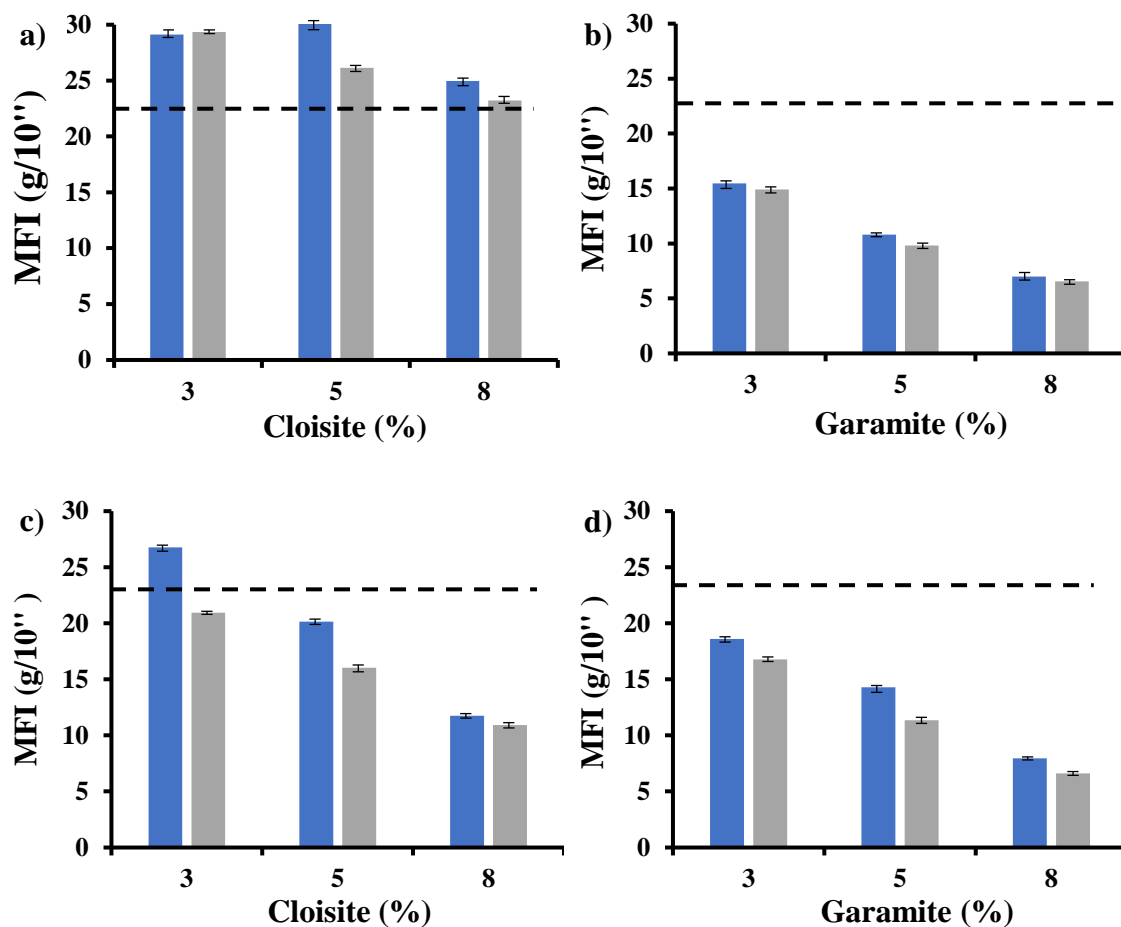


**Figure 7.3.** Melt Flow Index (g/10'') of nanocomposites obtained by extrusion without (blue bars) and with the assistance of ultrasounds (gray bars): a) PP1/Cloisite 20, b) PP1/Garamite 1958, c) PP2/Cloisite 20 and d) PP2/Garamite 1958.

The results show a clear trend of increasing viscosity when the percentage of added nanoclay was increased, with a more pronounced effect in the case of Garamite 1958 regardless of the polypropylene used. The higher viscosity values (i.e., lower MFIs) were found with both PP1 and PP2 polymers containing 8 wt.% of Garamite 1958. Thus, MFI reached a value around 5, which could still be acceptable for door panel processing even in absence of typical processing aid additives. The great effect of Garamite 1958 indicate that strong interactions could be established between the added nanoparticles and either PP1 or PP2 polymers, but some reticulation effect could not be discarded. A lower decrease of MFI was observed when Cloisite 20 was added to PP2 (i.e., a minimum value of 11 was reached for a clay content 8 wt.%). It seems that in this case weaker interactions or alternatively a reduced number of interactions were established. On the other hand, the effect that has been reported in different studies of a high viscosity reduction when

ultrasounds were applied to the molten polymer as consequence of chain breakage does not occur in any of the cases evaluated in this work [18,25,26].

The effect of the incorporation of Cloisite 20 was anomalous for the PP1 sample since MFI increased with respect the value observed for the neat polymer, probably degradation of the elastomeric phase was in this case enhanced. In all cases, the application of ultrasounds led to an additional decrease of MFI (with respect to the sample processed without the aid of ultrasonic waves), a feature that suggests an improved dispersion of nanoparticles. The ultrasonic energy applied in the die may affect nanoparticles due to cavitation and may provide a higher degree of dispersion [27-29]. Note that in any case the observed decrease is low and corresponds at maximum to 5 MFI units.

### 7.3.3 Dispersion of nanoclays

Great efforts have been performed to improve dispersion of nanoparticles during the compounding extrusion process due to the high potential benefits when structures with a high level of intercalation or even exfoliation are derived [30-34]. These involve from optimizing the surface characteristics of nanoparticles to improving the design of screws. Application of ultrasound has also been revealed as an ideal method to improve particle dispersion. Ultrasonic energy helps to avoid aggregates that would have a negative effect on the material homogeneity, and it could be a fragile area promoting a cracking failure.

The degree of dispersion of injected pieces was evaluated from TEM micrographs of thin sections (**Figure 7.4**). These revealed in all cases and oriented disposition of nanoparticles (i.e., parallel to the flow direction) and the presence of both intercalated and exfoliated structures (**Figures 7.4a** and **4b**). Inspection of pieces molded with assistance of ultrasound indicated an improved dispersion with a higher homogeneity and a greater density of exfoliated structures (**Figures 7.4c** and **4d**). Thus, ultrasound help to disaggregate some of the intercalated structures that remain after the conventional extrusion process and even eliminate the presence of bigger aggregates.

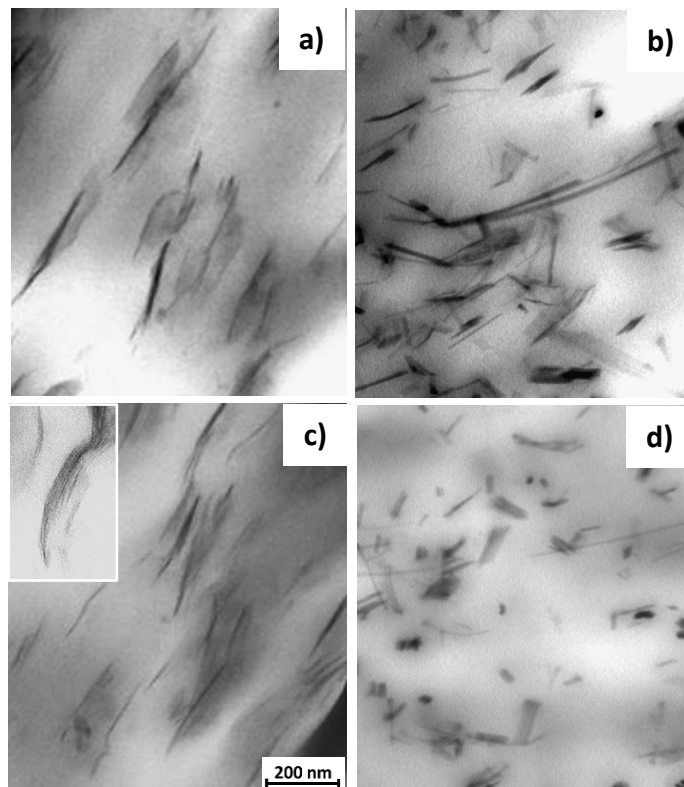


**Figure 7.4.** TEM micrographs of PP1/Cloisite 20 (a, c) and PP1/Garamite 1958 (b, d) nanocomposites incorporating 5 w.% of nanoparticles without (a, b) and with assistance of ultrasounds (c, d). Inset of (c) points out the presence of intercalated structures. Red arrows indicate the flow direction.

X-ray diffraction data is more indicative of the structure of nanocomposites since give an average information of the whole sample and not of particular details deduced from TEM micrographs. **Figure 7.5** reveals the common observed behavior for the region between  $2\theta$  values of  $2^\circ$  and  $16^\circ$  where peaks associated to intersheet nanoclay spacings are detected (i.e., 001, 002 and 003 reflections). Representative data for the studied samples are summarized in **Table 7.5**. The following conclusions can be given: a) Intersheet spacings increased with respect to those observed for the neat clay as a clear signal of the attainment of some degree of intercalation. A greater increase can be correlated with a better intercalation since the space between sheets increase; b) The intensity of clay peaks decreased (especially for the 001 reflection) when ultrasounds were applied, a feature that is compatible with a random separation between sheets of an intercalated structure or alternatively to an increase of exfoliation as also observed in the TEM micrographs. Note that X-ray profiles are comparative since the signal of PP at 0.624 nm has in all cases a comparable intensity; c) Peak shift and decrease of peak intensity slightly changed with the ratio of added nanoparticles, although slightly better results in



terms of disaggregation can be deduced for samples with a nanoparticle content of 3 wt.%; d) Results derived from Garamite 1958 are less clear due to its different morphology and lower content of clay sheets.

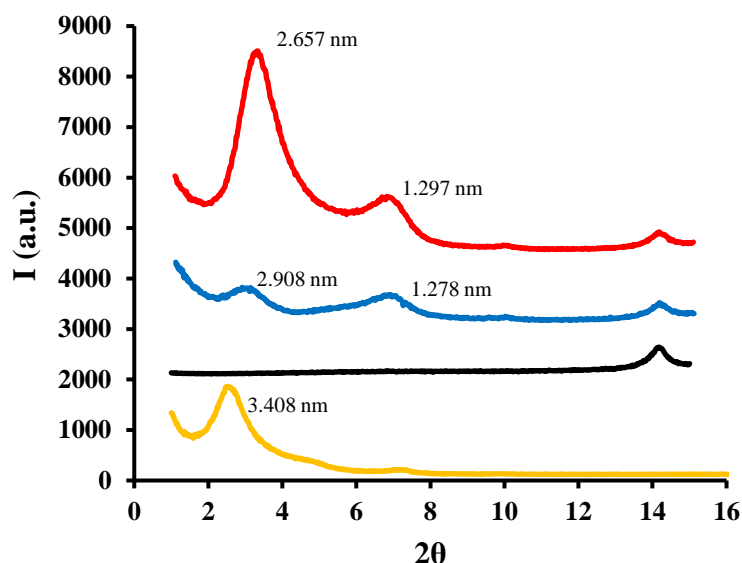


**Figure 7.5.** X-ray diffraction profiles of PP1/Cloisite 20 with a 8 wt.% content of nanoclay. All profiles have been normalized to get a similar intensity for the PP peak at  $2\theta = 14.18^\circ$ . The different profiles correspond to: Cloisite 20 (yellow), neat PP1 (black), nanocomposites obtained without (red) and with assistance of ultrasounds (blue)

**Table 7.5.** X-ray diffraction data for reference simples and representative nanocomposites studied in this work.

	Nanoclay	Filler (%)	US ( $\mu\text{m}$ )	d (nm)	d (nm)	d (nm)
<b>Cloisite</b>	-	100	-	3.408	1.230	-
<b>Garamite</b>	-	100	-	1.296	-	-
<b>PP 1</b>	-	-	-	-	-	0.624
<b>A</b>	Cloisite	3	0	2.341	1.506	-
<b>B</b>	Cloisite	3	44.5	2.376	1.481	0.624
<b>C</b>	Cloisite	5	0	2.472	1.472	0.624
<b>D</b>	Cloisite	5	44.5	2.541	1.485	0.624
<b>E</b>	Cloisite	8	0	2.657	1.297	0.624
<b>F</b>	Cloisite	8	44.5	2.908	1.278	0.624
<b>N</b>	Garamite	8	0	1.358	-	0.624
<b>O</b>	Garamite	8	44.5	1.366	-	0.624

### 7.3.4 Thermal properties of nanocomposites

Incorporation of nanocomposites can influence on thermal properties and specifically on the crystallization rate and degree of crystallinity. Depending on the type of nanocomposite structure, a nucleation effect is generally observed for an intercalated clay

disposition while a decrease of the crystal growth rate is characteristic for an exfoliated disposition due to the hindered movement of polymer chains towards the crystal surface. In any case, effects depend also on the type of polymer and for example polylactide shows an opposite behavior [35]. PP is a highly crystalline polymer and consequently a small effect is expected from the incorporation of nanoparticles. **Figure 7.6** shows heating and cooling scans for some representative polymers, whereas the corresponding numerical data are summarized in **Table 7.6**. Melting and crystallization temperatures of all nanocomposites loaded with were similar to the values found for the corresponding neat polymers regardless of being processed with or without ultrasounds. Enthalpy showed also a minimum variation for Cloisite 20 nanocomposites once the values were normalized by the real polymer content (i.e., after considering the loaded percentage of nanoparticles). Crystallinities were deduced considering the melting enthalpy for a 100% crystalline propylene (165 J/g) [36] after the indicated weight normalization. By contrast, nanocomposites loaded with Garamite revealed a certain increase of crystallinity when samples were obtained by the assistance of ultrasounds. Therefore in this case, the greater dispersion of whiskers allowed improving crystallinity as consequence of a nucleation effect. Similar trends were deduced for PP1 based nanocomposites, although in this case the crystallinity of samples was lower than found for the corresponding PP2 composites due to the presence of the elastomeric blocks.

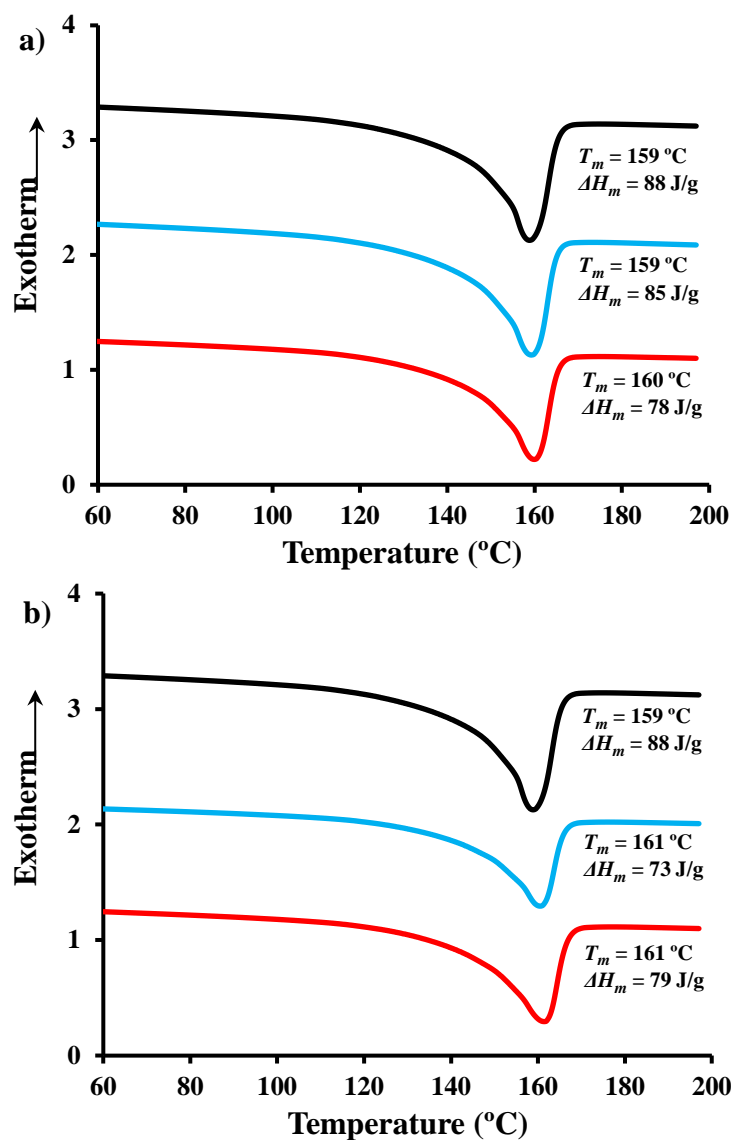


**Figure 7.6.** Second heat run of PP2 (black), PP2/Cloisite 20 nanocomposites loaded with 5 wt.% of clay and processed without (blue) and with (red) ultrasounds (a), and PP2/Garamite 1958 nanocomposites loaded with 8 wt.% of nanoparticles and processed without (blue) and with (red) ultrasounds.

**Table 7.6.** Thermal properties of processed nanocomposites.

Sample	Nanofiller %	US $\mu\text{m}$	$T_m$ °C	$\Delta H_m$ J/g	$T_c$ °C	$\Delta H_c$ J/g	$\chi_c$ %
PP2	0	0	159	88	117	102.2	53.4
C'	5	0	159	85	119	95.5	54.3
D'	5	44.5	160	78	118	90.6	49.6
E'	8	0	160	78	118	82.3	51.5
F'	8	44.5	161	76	117	83.8	50.3
N'	8	0	161	73	119	73.1	47.9
O'	8	44.5	161	79	118	86.8	52.1

### 7.3.5 Mechanical properties of nanocomposites

Elastic modulus always increased when the percentage of nano-reinforcement was increased. Furthermore, for all tested nanocomposites, modulus was further increased when ultrasounds were applied (**Figure 7.7**) as consequence of the improved dispersion in the case of Cloisite 20 since crystallinity remained practically constant. The magnitude of the modulus increment was different for Garamite 1958 than for Cloisite 20, demonstrating the higher efficiency as reinforcement of Garamite 1958, probably as consequence of the morphology of nanoparticles where components with a whisker morphology are predominant. Note also that the incorporation of whiskers increased the degree of crystallinity when ultrasounds were applied as consequence of an improved capacity of nucleation. Results also indicate that despite both neat PP1 and PP2 polymers had a similar elastic modulus, the modulus increment was always higher for the PP2 homopolymer. In summary, evaluation of modulus indicate that the best formulation corresponded to the PP2 homopolymer reinforced with 8 wt.% of Garamite 1958 and processed with the ultrasound assisted extrusion.

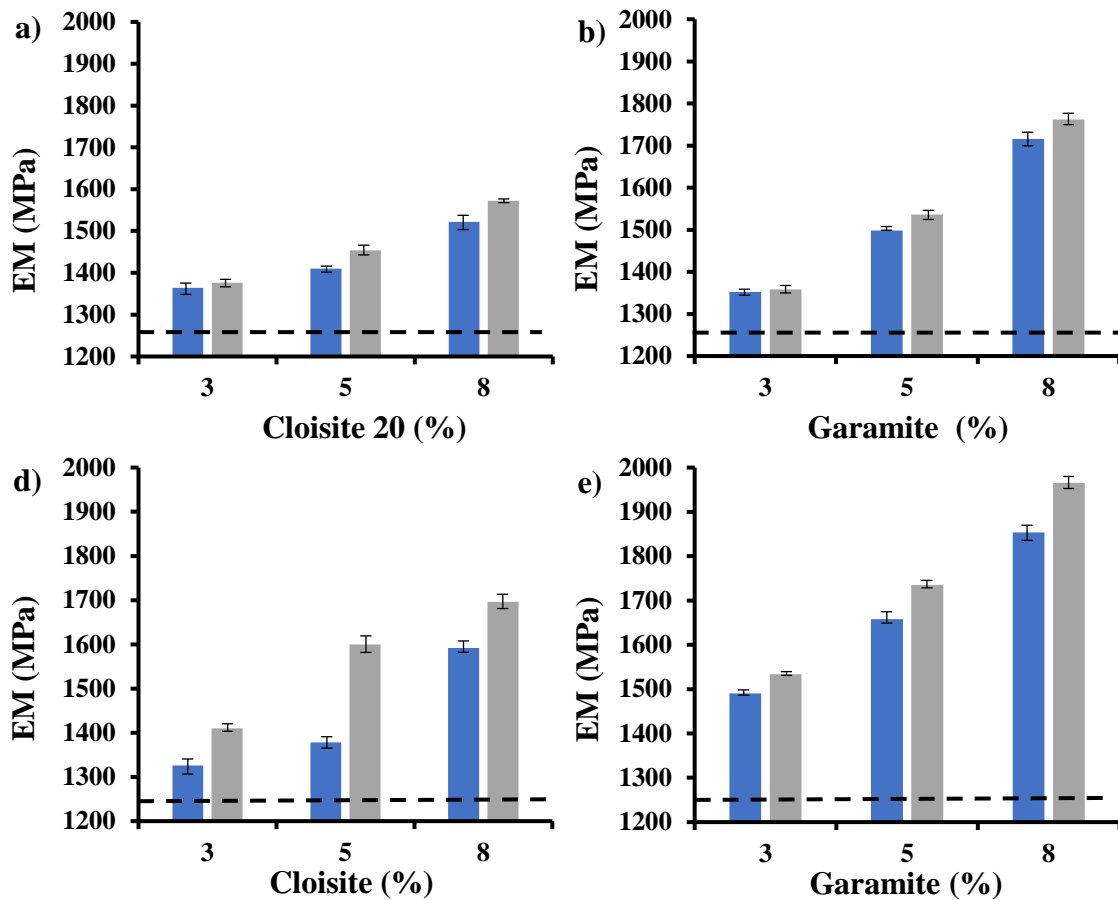


**Figure 7.7.** Comparison of elastic modulus between different nanocomposites extruded with (gray bars) and without (blue bars) ultrasounds: a) PP1/Cloisite 20, b) PP1/Garamite 1958, c) P2/Cloisite 20, d) PP2/Garamite 1958. Dashed lines indicate the values of the corresponding neat polymers.

Considering the PP2/Cloisite 20 nanocomposites it is interesting to note that the elastic modulus of the 5 wt.% nanocomposite prepared using ultrasound was similar and even slightly higher to the modulus of the nanocomposite with 8 wt.% of nanoclays but prepared without applying ultrasounds (i.e., 1600 MPa and 1,592 MPa respectively). It was therefore possible to reduce the nanoreinforcement by 3 wt.% and maintain the value of elastic modulus. On the other hand, the effect of ultrasounds was also remarkable for the PP2 nanocomposite loaded with 8 wt.% of Garamite 1958. Specifically, elastic modulus increased by 10% with respect to the nanocomposite processed without ultrasounds and reached a maximum final value of 1966 MPa.

For several decades, theoretical models have been formulated to predict the mechanical properties of composites according to their composition. We have tried to fit the

experimental data obtained for PP/Cloisite 20 nanocomposites with those derived from the formulated theoretical models. The estimation was not performed for nanocomposites based on Garamite 1958 due to complex/mixed morphology of the constitutive nanoparticles.

The most simple estimation correspond to the parallel model of Voigt, which is applied to estimate the longitudinal modulus of aligned and long fibers considering the modulus of the individual components ( $E_m$  and  $E_f$  for the matrix and the fibers, respectively) and the corresponding volume fractions ( $\phi_m$  and  $\phi_f$ ). The model gives an overestimation of the modulus of the composite,  $E_c$ , since a perfect orientation of fibers cannot be obtained:

$$E_c = E_f \times \phi_f + (1 - \phi_f) \cdot E_m \quad (1)$$

The series model of Reuss renders the lowest modulus for composites constituted by large and aligned fibers. In this case the estimation appears appropriate for the transversal

$$\frac{1}{E_c} = \frac{\phi_f}{E_f} + \frac{(1 - \phi_f)}{E_m} \quad (2)$$

The Halpin–Tsai model takes into account the geometry and orientation of the filler and the elastic properties of both components: filler and matrix. The model is based on the self-consistent field method although it has often been considered as an empirical equation. The Halpin–Tsai model is also highly appropriate for low-volume fractions of filler as is the case of the studied systems. Note that Halpin-Tsai model is the only one that takes into account the aspect ratio of the system ( $l/t$ , namely the ratio between the length and the diameter). This depends on the degree of dispersion of the filler (i.e., if it is a fully exfoliated or intercalated system). Fornes et al. [37] concluded that an intercalated compound was formed when  $l/t$  approaches 10, and an exfoliated one when it is in a range of 100-1000 (basically a value of 100 can be used for an exfoliated structure). The estimated modulus for aligned fibers (sheets for nanoclays) is given by equation 3:

$$E_c = E_m \cdot \frac{1 + \xi \cdot \eta \cdot \phi_f}{1 - \eta \cdot \phi_f} \quad (3)$$

where  $\eta$  and  $\xi$  are given by equations 4 and 5, respectively.

$$\eta = \frac{\frac{E_f}{E_m} - 1}{\frac{E_f}{E_m} + \xi} \quad (4)$$

$$\xi = 2 * l/t \quad (5)$$

Note that when  $\xi$  becomes very small ( $\xi \rightarrow 0$ ), the Halpin–Tsai model corresponds to the series model, while when it is large ( $\xi \rightarrow \infty$ ) the parallel model is derived.

For composites reinforced with fibers randomly oriented, the Halpin–Tsai model equation is more complex and follow equation (6):

$$E_c = E_m \left[ \frac{3}{8} \cdot \left( \frac{1 + \xi \cdot \eta_L \cdot \phi_f}{1 - \eta_L \cdot \phi_f} \right) + \frac{5}{8} \left( \frac{1 + 2 \cdot \eta_T \cdot \phi_f}{1 - \eta_T \cdot \phi_f} \right) \right] \quad (6)$$

$$\eta_L = \frac{\frac{E_f}{E_m} - 1}{\frac{E_f}{E_m} + 2 \cdot \frac{l}{t}} \quad (7)$$

$$\eta_T = \frac{\frac{E_f}{E_m} - 1}{\frac{E_f}{E_m} + 2} \quad (8)$$

**Figure 7.8** plots the modulus estimated for series, parallel and both oriented and random Halpin–Tsai models for nanocomposites having different clay percentages and considering both exfoliated and intercalated structures. The modulus of the clay was considered 178 GPa according to literature data. Experimental data fits in all cases better with an intercalated structure and a non-perfect uniaxial clay orientation. Note that application of ultrasounds improves the Young’s Modulus and tends the complete intercalate model. All these observations appear in close agreement with TEM observations and X-ray diffraction data.

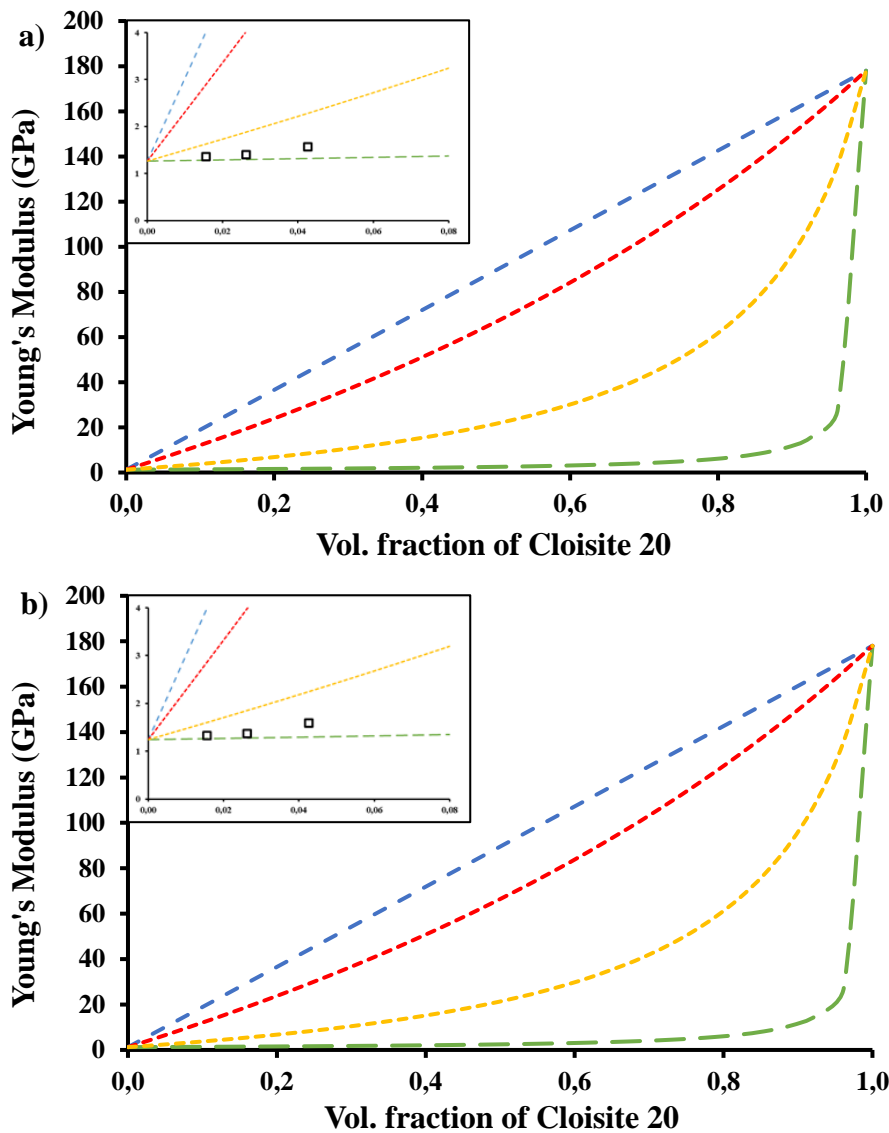


**Figure 7.8.** Young's modulus of PP1/Cloisite 20 (a) and PP2/Cloisite 20 (b) nanocomposites according to the Reuss (green), Voigt (blue), and Halpin–Tsai (for intercalated and exfoliated structures with oriented and random clay dispositions in yellow and red respectively) models. Experimental modulus are indicated in each case by the square symbols (black) into the inset.

**Figure 7.9** shows representative strength-strain curves of flexural test for the different studied nanocomposites, whereas **Tables 7.7-10** summarizes their main mechanical properties. In general elongation at break clearly decreased by adding nanoparticles and even by applying ultrasounds. This feature suggests that well dispersed particles can promote the formation of cracks diminishing therefore the tenacity of samples. It should also be pointed out the great tenacity of the neat PP2 samples that contrast with the rigidity of PP1. Thus, the effect of nanoparticle addition is emphasized for the PP2 nanocomposites. A certain degree of reticulation may also increase the rigidity, a feature



that also agrees with the significant decrease of MFIs for PP2 derivatives. In all cases the application of ultrasounds improved dispersion and slightly decreased the break elongation.

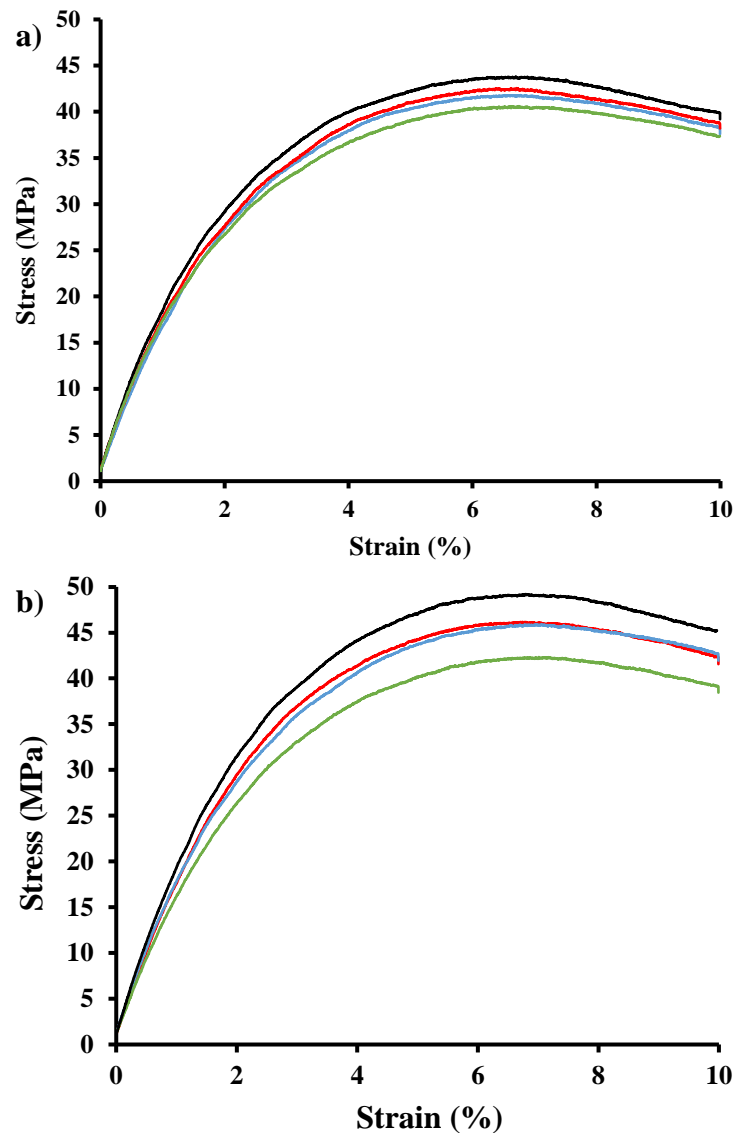


**Figure 7.9.** Stress-strain curves for representative nanocomposites loaded with Cloisite 20 (a) and Garamite 1958 (b), at 3 wt.% in green, 5 wt.% with and without ultrasounds, red and blue respectively, and 8 wt.% in black.

**Table 7.7.** Mechanical properties of PP1/Cloisite 20 nanocomposites.

	PP1	A	B	C	D	E	F	G
<b>C20 (%)</b>	<b>0</b>	<b>3</b>	<b>3</b>	<b>5</b>	<b>5</b>	<b>8</b>	<b>8</b>	<b>8</b>
<b>Amplitude (<math>\mu\text{m}</math>)</b>	<b>0</b>	<b>0</b>	<b>44.5</b>	<b>0</b>	<b>44.5</b>	<b>0</b>	<b>44.5</b>	<b>0</b>
<b>EM (MPa)</b>	1260	1364	1376	1410	1454	1522	1572	1362
<b>TS (MPa)</b>	22.3	22.9	23.5	23.0	23.8	23.0	23.9	20.8
<b>EB (%)</b>	34.6	12.4	11.2	6.6	6.1	4.3	4.1	13.6
<b>FM (MPa)</b>	1054	1190	1250	1252	1290	1292	1320	1138
<b>FS (MPa)</b>	33.9	34.2	34.6	34.0	34.4	34.0	34.3	32.6

**Table 7.8.** Mechanical properties of PP2/Cloisite 20 nanocomposites.

	PP2	A'	B'	C'	D'	E'	F'	G'	H'
<b>C20 (%)</b>	<b>0</b>	<b>3</b>	<b>3</b>	<b>5</b>	<b>5</b>	<b>8</b>	<b>8</b>	<b>5</b>	<b>5</b>
<b>GB (%)</b>	<b>0</b>	<b>0</b>	<b>0</b>	<b>0</b>	<b>0</b>	<b>0</b>	<b>0</b>	<b>5</b>	<b>10</b>
<b>Amplitude (µm)</b>	<b>0</b>	<b>0</b>	<b>44.5</b>	<b>0</b>	<b>44.5</b>	<b>0</b>	<b>44.5</b>	<b>0</b>	<b>0</b>
<b>EM (MPa)</b>	1242	1326	1410	1378	1600	1592	1696	1540	1616
<b>TS (MPa)</b>	30.6	31.0	32.5	31.4	32.7	32.2	33.6	29.0	29.2
<b>EB (%)</b>	530	376	328	15,7	16,0	10.6	12.8	7.4	6.6
<b>FM (MPa)</b>	1376	1682	1761	1770	1840	2080	2188	2050	2184
<b>FS (MPa)</b>	37.9	41.2	41.7	42.1	42.6	43.4	43.8	43.4	43.5

**Table 7.9.** Mechanical properties of PP1/Garamite 1958 nanocomposites.

	PP	J	K	L	M	N	O
<b>Garamite (%)</b>	<b>0</b>	<b>3</b>	<b>3</b>	<b>5</b>	<b>5</b>	<b>8</b>	<b>8</b>
<b>Amplitude (µm)</b>	<b>0</b>	<b>0</b>	<b>44.5</b>	<b>0</b>	<b>44.5</b>	<b>0</b>	<b>44.5</b>
<b>EM (MPa)</b>	1260	1352	1358	1498	1536	1716	1762
<b>TS (MPa)</b>	22.3	25.3	26.1	27.8	28.3	32.6	33.5
<b>EB (%)</b>	34.6	24.4	23.4	18.0	17.2	15.2	17.4
<b>FM (MPa)</b>	1054	1234	1282	1380	1442	1646	1666
<b>FS (MPa)</b>	33.9	36.1	36.5	38.0	38.7	41.4	41.7

**Table 7.10.** Mechanical properties of PP2/Garamite 1958 nanocomposites.

	PP2	J'	K'	L'	M'	N'	O'	P'	Q'	R'	S'
<b>Garamite (%)</b>	<b>0</b>	<b>3</b>	<b>3</b>	<b>5</b>	<b>5</b>	<b>8</b>	<b>8</b>	<b>5</b>	<b>5</b>	<b>8</b>	<b>8</b>
<b>GB (%)</b>	<b>0</b>	<b>0</b>	<b>0</b>	<b>0</b>	<b>0</b>	<b>0</b>	<b>0</b>	<b>5</b>	<b>10</b>	<b>5</b>	<b>10</b>
<b>Amplitude (µm)</b>	<b>0</b>	<b>0</b>	<b>44.5</b>	<b>0</b>	<b>44.5</b>	<b>0</b>	<b>44.5</b>	<b>0</b>	<b>0</b>	<b>0</b>	<b>0</b>
<b>EM (MPa)</b>	1242	1490	1534	1658	1735	1854	1966	1704	1784	2052	2054
<b>TS (MPa)</b>	30.6	33.7	34.8	36.5	36.9	39.6	40.4	35.4	34.6	39.0	37.3
<b>EB (%)</b>	530	350	342	40	67	25	29	10	8	10	8
<b>FM (MPa)</b>	1376	1662	1748	1826	1878	2088	2140	2058	2380	2440	2508
<b>FS (MPa)</b>	37.9	42.9	44.0	45.0	45.6	49.1	49.6	46.9	49.4	50.9	50.2

Interpretation of tensile strength results is more complex since depends on two parameters modulus and elongation of break that as indicated are differently influenced by the incorporation of nanoparticles. Nevertheless, some general trends can be deduced from the experimental results (**Figure 7.10**): a) Tensile strength of nanocomposites are always higher than the values determined for the corresponding neat polymers; b) Tensile strength clearly increase with the content of nanoparticles; c) The effect of Garamite is higher than that provided by Cloisite 20; d) The PP2 matrix appear more susceptible to the effect caused by nanoparticles and e) The application of ultrasound provide an additional but slight increase of the tensile strength.

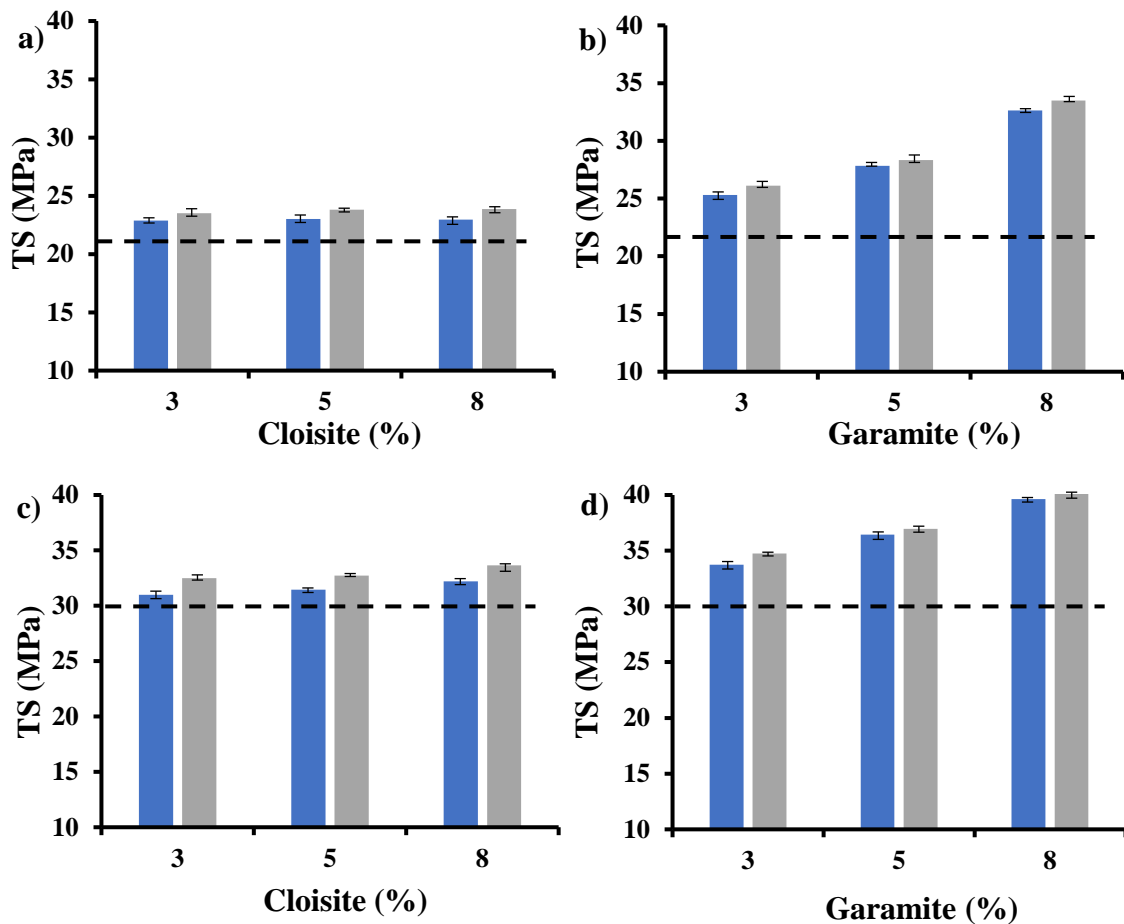


**Figure 7.10.** Comparison of tensile strength between different nanocompounds extruded with gray bars) and without (blue bars) ultrasounds: a) PP1/Cloisite 20, b) PP1/Garamite 1958, c) P2/Cloisite 20, d) PP2/Garamite 1958. Dashed lines indicate the values of the corresponding neat polymers.

**Figure 7.11** compares the modulus determined from flexural tests for the different nanocomposites. In general, the same trends observed for the strength-strain tests were observed. Basically, modulus clearly increased with the nanoparticle content and the treatment with ultrasounds. Modulus of the neat polymers were in this case different, being the maximum increase of loaded samples determined for the PP2 nanocomposites. A similar increment was observed when Cloisite 20 or Garamite 1958 were employed, a feature that contrasted with the higher increment observed when Garamite was added into the PP1 matrix.

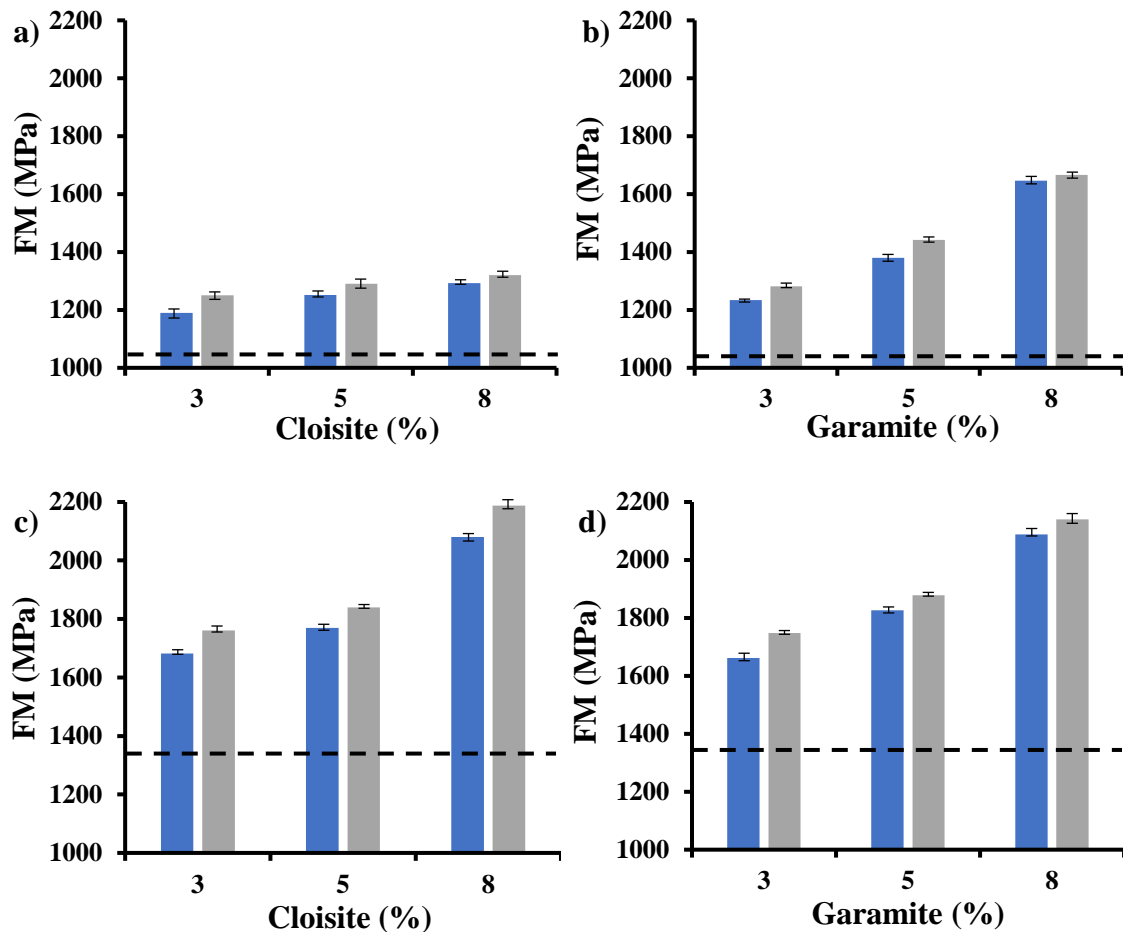


**Figure 7.11.** Comparison of tensile flexural modulus between different nanocompounds extruded with gray bars) and without (blue bars) ultrasounds: a) PP1/Cloisite 20, b) PP1/Garamite 1958, c) P2/Cloisite 20, d) PP2/Garamite 1958. Dashed lines indicate the values of the corresponding neat polymers.

Finally, flexural strength values (**Figure 7.12**) slightly increased with the nanoparticle content. Differences concerning the effect of ultrasounds were different depending on the polymer matrix. Thus, an increase and a decrease were determined for PP1 and PP2 matrices, respectively. Probably, the higher increase of rigidity of PP2, as it was previously indicated, is responsible of the peculiar behavior of its composites.

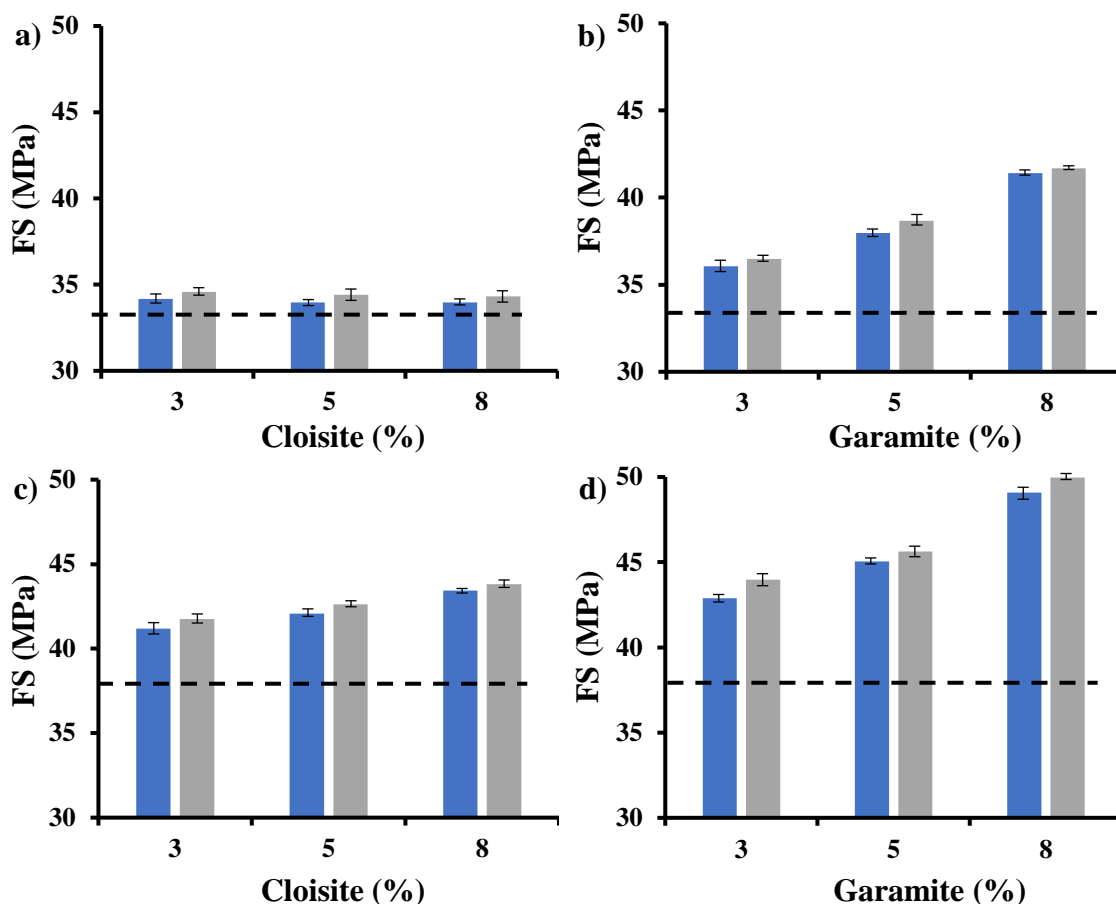


**Figure 7.12.** Comparison of flexural strength between different nanocompounds extruded with gray bars) and without (blue bars) ultrasounds: a) PP1/Cloisite 20, b) PP1/Garamite 1958, c) PP2/Cloisite 20, d) PP2/Garamite 1958. Dashed lines indicate the values of the corresponding neat polymers.

### 7.3.6 Influence of the incorporation of hollow glass spheres

Nanocomposites based on PP2 showed the higher tensile and flexural modulus and appeared appropriate for the final use. Nevertheless, the density of samples clearly increased with the addition of nanoparticles (**Figure 7.14**). Specifically, it was observed a linear increase from the value of  $0.905 \text{ g/cm}^3$  for the neat polymer to  $0.938 \text{ g/cm}^3$  or  $0.942 \text{ g/cm}^3$  for nanocomposites loaded with 8 wt.% of Cloisite 20 or Garamite 1958, respectively. Addition of hollow spheres (density of  $0.69 \text{ g/cm}^3$ ) was therefore considered to get material with lower densities than the neat polymers and to the materials currently commercialized for the considered application. To this end nanocomposites containing 5 wt.% of Cloisite 20 and 5 wt.% or 8 wt.% of Garamite 1958 were selected to evaluate the effect caused by the addition of 5 wt.% or 10 wt.% of the hollow glass spheres.

**Figure 7.13** shows a cross section of a representative specimen where spheres with different size can be detected. Spheres that were placed just in the cross section surface appear broken as consequence of the fracture of the specimen, but those located in deeper positions are intact and demonstrated that they were resistant to the previous extrusion and injection processes. Note the bad bonding between spheres and the polymer matrix that indicate a lower bonding energy between the polymer and the filler (adhesion energy) than the cohesive energy of the matrix.

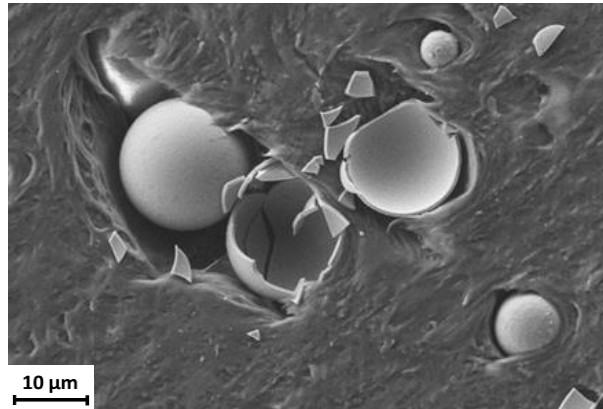


**Figure 7.13.** SEM micrographs of the fracture surface of PP2/Cloisite 20 nanocomposite incorporating 10 wt.% of hollow glass spheres.

Mechanical properties of glass loaded specimens are summarized in the previous **Tables 7.8** and **10**. The effect was similar regardless of the type of nanoclay. Thus, elastic and flexural modulus tend to increase while the elongation at break clearly decreases. Values of the tensile and flexural strength remained constant or slightly decreased. **Figure 7.14** shows also the decrease on density when hollow glass spheres were incorporated, being the density reduction between 11-13% and the save of material around 200 g for a door panel. The commercialized material has a value of  $1.04 \text{ g/cm}^3$  for a door panel with a total weight of 1470 g. Material with 5 wt.% of Cloisite 20 and 10 wt.% has a weight reduction for this piece of 13 % (1307 g) with a density of  $0.904 \text{ g/cm}^3$ . **Figure 7.14** also reveals that measured densities that could not be attained the optimal value, probably as consequence of the minor presence of some broken spheres.

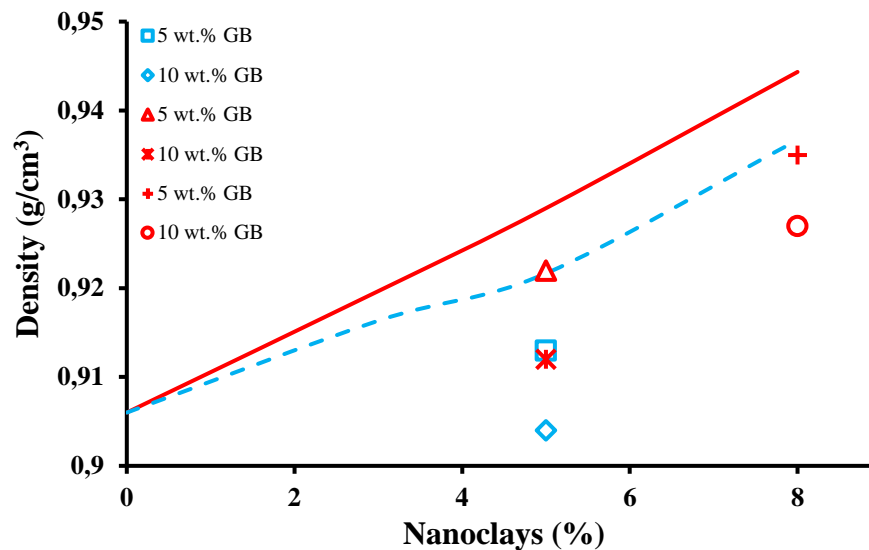


**Figure 7.14.** Variation of density with the percentage of added nanoparticles, blue for Cloisite 20 and red for Garamite 1958. Six different point with different amounts of glass spheres added to the nanocomposites.

## 7.4 Conclusions

The use of nanocomposites appears a good strategy to substitute typical reinforced composites used in automotive applications. Mechanical properties can be maintained and even improved by using lower density materials. The total weight reduction can also be enhanced by the simple addition of hollow glass spheres that are also able to keep the desired properties. The type of polypropylene (copolymer with elastomeric blocks or the homopolymer) that is selected as a matrix and the morphology of the added nanoparticles had a remarkable influence of the final properties of nanocomposites. Specifically, the extrusion process in presence of nanoparticles led to an increase on the MFI, which suggest the occurrence of some crosslinking reactions, especially when Garamite was employed. Elastic and flexural modulus tended to increase with the ratio of added nanoparticles while elongation at break decreased mainly when the homopolymer was employed. Behavior of tensile and flexural strength was more complicated due to the incidence of two parameters (modulus and elongation) than had a different response respect to the addition of nanoparticles. The Halpin & Tsai theoretical model was useful to demonstrate the presence of some ratio of intercalated Cloisite 20 structures and a certain degree of misalignment in the injected specimens.

In all cases nanocomposites having a mixture of intercalated and exfoliated clay structures were achieved. Interestingly, exfoliation/dispersion was enhanced when extrusion was assisted by the application of ultrasonic energy. The dispersion of Cloisite 20 had not a remarkable influence on the crystallinity of the samples but the incorporation of Garamite increased the crystallinity probably as consequence of the nucleation effect of constitutive nanowhiskers.

The two nanocomposites with better potential to be employed as door panel where the homopolymer incorporating 5 wt.% or 8 wt.% of Cloisite 20 or Garamite 1958, respectively. The incorporation of hollow glass spheres allowed a reduction of density close to 13% and even causing an additional improvement of modulus.

## 7.5 References

1. Alexandre, M.; Dubois, P. *Mater. Sci. Eng. R Reports*, 28, 1, 1–63, 2000.
2. Beyer, G. *Plast. Addit. Compd.*, 4, 10, 22–28, 2002.
3. Ton-That, M. T.; Perrin-Sarazin, F.; Cole, K. C.; Bureau, M. N.; Denault, J. *Polym. Eng. Sci.*, 44, 7, 1212–1219, 2004.
4. Selvakumar, V.; Manoharan, N. *Indian Journal of Science and Technology*, 7, 136–139, 2014.
5. Karak, N. *Veg. Oil-Based Polym.*, 271–309, 2012.
6. Cho, J.; Joshi, M. S.; Sun, C. T. *Compos. Sci. Technol.*, 66, 13, 1941–1952, 2006.
7. Kemaloglu, S.; Ozkoc, G.; Aytac, A. *Thermochim. Acta*, 499, 1–2, 40–47, 2010.
8. Hári, J.; Horváth, F.; Renner, K.; Móczó, J.; Pukánszky, B. *Polym. Test.*, 72, 178–186, 2018.
9. Yusa A.; Yamamoto, S.; Goto, H.; Uezono, H.; Asaoka, F.; Wang, L.; Ando, M.; Ishihara, S.; Ohshima, M. *Polym. Eng. Sci.*, 57, 1, 105–113, 2017.
10. Baumeister, E.; Klaeger, S. *Adv. Eng. Mater.*, 5, 9, 673–677, 2003.
11. Capela, C.; Costa, J. D.; Ferreira, J. A. M. *Strain*, 44, 2, 141–146, 2008.
12. Isayev, A. I.; Lapshin, S. *J. Vinyl Addit. Technol.*, 12, 2, 78–82, 2006.
13. Kumar, R. V.; Koltypin, Y.; Palchik, O.; Gedanken, A. *J. Cell. Mol. Med.*, 86, 1, 160–165, 2002.
14. Xia, H.; Wang, Q. *J. Appl. Polym. Sci.*, 87, 11, 1811–1817, 2003.



15. Isayev, A. I.; Hong, C. K.; Kim, K. J. *Rubber Chem. Technol.*, 76, 4, 923–947, 2003.
16. Swain, S. K.; Isayev, A. I. *Polymer (Guildf.)*, 48, 1, 281–289, 2007.
17. Ryu, J. G.; Kim, H.; Lee, J. W. *Polym. Eng. Sci.*, 44, 7, 1198–1204, 2004.
18. Isayev, A. I.; Wong, C. M.; Zeng, X. *Adv. Polym. Technol.*, 10, 1, 31–45, 1990.
19. Martínez-Colunga, J. G.; Sánchez-Valdés, S.; Ramos-deValle, L.F.; Muñoz-Jiménez, L.; Ramírez-Vargas, E.; Ibarra-Alonso, M.C.; Lozano-Ramirez, T.; Lafleur, P.G. *J. Appl. Polym. Sci.*, 131, 16, 1–8, 2014.
20. Sohn, C. H.; Shim, D. C.; Lee, J. W. *Macromol. Symp.*, 249–250, 580–585, 2007.
21. Chen, G.; Guo, S.; Li, H. *J. Appl. Polym. Sci.*, 84, 13, 2451–2460, 2002.
22. Wu, H.; Guo, S.; Chen, G.; Lin, J.; Chen, W.; Wang, H. *J. Appl. Polym. Sci.*, 90, 7, 1873–1878, 2003.
23. Ye, Y.; Qian, J.; Xu, Y. *J. Polym. Res.*, 18, 6, 2023–2031, 2011.
24. Chen, J.; Chen, Y.; Li, H.; Lai, S.Y.; Jow, J. *Ultrason. Sonochem.*, 17, 1, 66–71, 2010.
25. Isayev, A. I.; Kumar, R.; Lewis, T. M. *Polymer (Guildf.)*, 50, 1, 250–260, 2009.
26. Blanco, M.; Sarasua, J.A.; López, M.; Gonzalo, O.; Marcaide, A.; Muniesa, M.; Fernández, A.; *Macromol. Symp.*, 321–322, 1, 80–83, 2012.
27. Ávila-Orta, C. A. Quiñones-Jurado, Z.V.; Waldo-Mendoza, M.A.; Rivera-Paz, E.A.; Cruz-Delgado, V.J.; Mata-Padilla, J.M.; González-Morones, P.; Ziolo, R.F. *Materials (Basel)*, 8, 11, 7900–7912, 2015.
28. Gao, X.; Isayev, A. I.; Yi, C. *Polymer (Guildf.)*, 84, 209–222, 2016.
29. Sanchez-Olivares, G.; Sanchez-Solis, A.; Calderas, F.; Medina-Torres, L.; Herrera-Valencia, E.E.; Castro-Aranda, J.I.; Manero, O.; Di Blasio, A.; Alongi, J. *Polym. Degrad. Stab.*, 98, 11, 2153–2160, 2013.
30. Dennis, H. R.; Hunter, D.L.; Chang, D.; Kim, S.; White, J.L.; Cho, J.W.; Paul, D.R. *Polymer (Guildf.)*, 42, 23, 9513–9522, 2001.
31. Nevalainen, K.; Vuorinen, J.; Villman, V.; Suihkonen, R.; Järvelä, P. *Polym. Eng. Sci.*, 49, 4, 631–640, 2009.
32. Villmow, T.; Kretschmar, B.; Pötschke, P. *Compos. Sci. Technol.*, 70, 14, 2045–2055, 2010.
33. Domenech, T.; Peuvrel-Disdier, E.; Vergnes, B. *Int. Polym. Process.*, 27, 5, 517–526, 2012.
34. Luo, J. J.; Daniel, I. M. *Compos. Sci. Technol.*, 63, 11, 1607–1616, 2003.

35. Planellas, M.; Sacristán, M.; Rey, L.; Olmo, C.; Aymamí, J.; Casas, M.T.; del Valle, L.J.; Franco, L.; Puiggali, J. *Ultrason. Sonochem.*, 21,1557–1569, 2014.
36. Moore, E. P. Polypropylene Handbook. *Polymerization, characterization, properties, processing, applications*, Hanser/Gardner:Cincinnati, OH, 1996.
37. Fornes, T. D.; Paul, D. R. *Polymer (Guildf.)*, 44, 17, 4993–5013, 2003.

## CONCLUSIONS



# CONCLUSIONS

The results reported in this PhD work conclude that the ultrasonic energy can enhance the processing technologies of the compounding extrusion and micromolding of polypropylene and nanocomposites based on a biopolymer P3HB. In both cases, the main components of the ultrasound system design have revealed to be an indispensable part of the development research that ensure the success of the transformation processes. During the compounding extrusion the ultrasonic energy has demonstrated to be a useful technology to improve the dispersion of nanoclays. The ultrasonic molding showed a similar result of nanoclays dispersion accompanied by an improved mechanical property of the neat polymer and nanocomposites with highly stability of the process.

The main conclusions related to the specific objectives of this Thesis work can be summarized as follows:

## **Advances on the application of ultrasonic technologies for the melt processing of polymers**

- ! The ultrasonic energy has been reported in the literature as an effective technology to be implemented in the most important transformation process in the industry, the extrusion and the injection molding. Several designs of ultrasound system for both processes were done to optimize the synergistic effect of the ultrasonic energy.
- ! For the injection molding assisted by ultrasounds, the main approach was focused on the rheological behavior of the neat polymer, where the ultrasonic energy promoted changes on the polymeric structure.
- ! The ultrasonic molding, based on the cavitation mechanism due to ultrasonic energy, makes flow the material through the cavity of the mold without a screw (conventional injection molding) and it is not needed the application of temperature to melt the polymer. It is an early technology that has several positive reports, and it adapts the conventional method such as simulation software to optimize the injection process. The most relevant reported results are focused on the replication

surface, minimum material loss to obtain a microsample and dispersion of nanoparticles within the polymeric material.

- ! In the field of nanocomposites obtained by compounding extrusion assisted by an ultrasound system, several approaches were reported. It was revealed that the ultrasonic energy had different effects depending on the material. Results such as an increase of flowability of the treated material that reduces the pressure at die extrusion, thus increasing the productivity, were found for most of the works. The main benefits reported were found for application of blending different polymers (thermoplastic or elastomers), decrosslink (crosslinked polyethylene or elastomers) and improvement of the micro and nanofillers to enhance mechanical, thermal, or electrical properties.

### **Ultrasonic device for a polymer extruder machine**

- ! An exhaustive analyze was done for the compounding extrusion process that is assisted by an ultrasound system. The reported works describes an ultrasound system that have been concluded have not enough stability to be implemented in the industry environment. It was found that maintain the axis from the transducer to the sonotrode was the main problem to be solved to stabilize the system. A little change in the position makes fail the stability of the system.
- ! To solve the mentioned problematic a new component was designed tasking into account the nodal points of the system. The nodal point, or nodal plane, is defined as the position of the sonotrode where the longitudinal amplitude is equal to zero. the design of the new component takes advantage of the nodal plane to add a fixation of the ultrasound system that prevents movements of the axis, and therefore stabilizes the process. This component allows to the system work in continuous conditions.

### **Point nodal ultrasonic molding of polypropylene: a technology able to prepare micropieces with highly repetitive properties and good mechanical performance**

- ! The ultrasonic molding has a new approach of this technology that consider the component that fixes the ultrasound system in the nodal point, improving the

stabilization of the process. The results of this study that performs micropieces of polypropylene was evaluated under two points of view.

- ! Considering the mechanical properties by tensile test of the microsamples obtained with and without a consideration of the nodal point. An evident improvement in the stabilization of the process was revealed with the nodal point approach, that is reflected in during the tensile test behavior.
- ! Flowability of the material under optimal and non-optimal conditions of the nodal point of view. The effect of the ultrasonic energy on the polymer rheology when the system worked at non-optimal conditions (extreme conditions) was evaluated. The sample was performed but a degradation of the polymer was evident even at visual inspection. The viscosity of the polymer was reduced by half compared to the neat polymer under optimal conditions.

#### **Ultrasonic molding of poly(3-hydroxybutyrate): a high-resolution process to get micropieces with minimum material loss and degradation**

- ! Ultrasonic molding with nodal point approach was demonstrated to be an optimal process to obtain microsamples of P3HB without relevant modifications at chemical structure of the biopolymer. No degradation was observed with GPC analysis and FTIR.
- ! Same results were found for nanocomposites with organomodified an unmodified nanoclays, C20 and C116 respectively. In addition, the nanocomposites improved the mechanical properties increasing the amount of nanoclays (3, 5 and 8 wt.% were studied).
- ! X-Ray studies suggest that exfoliated nanocomposites were obtained during the compounding extrusion process, which was kept during USM process. The results were confirmed by TEM and SEM micrographs.
- ! A comparison between both microinjection technologies was performed for neat polymer and nanocomposites P3HB/C20 and P3HB/C116. In both cases, no

significant changes were reported for the calorimetric study and revealed a good mechanical properties for all nanocomposites studied.

- ! The USM technology could process the entire prepared nanocomposites. In contrast, the conventional micro-injection molding fail during the process to obtain micropieces with the P3HB loaded by 8 wt.% of the unmodified nanoclays.
- ! SEM micrographs revealed an improvement of the surface homogeneity for the samples processed by USM technology in comparison with the conventional process.
- ! The conventional technology revealed a slightly change in the chemical structure verified by GPC and FTIR. The band that corresponds to the ester group (C=O) in  $1719\text{ cm}^{-1}$  had a slightly change that indicates the initiation of the degradation phenomena. The result was confirmed comparing the FTIR spectra of the conventional micro-injected sample with material that suffered thermal degradation.
- ! USM technology was demonstrated to be an optimal option to obtain micropieces with improved properties for nanocomposites with treated and untreated nanoclays.

### **Processing and properties of polymer nanocomposites and nanocoatings and their applications in the packaging, automotive and solar energy fields**

- ! A reporting of several studies focused on the application of the nanotechnology developing new materials and their process transformation for sectors such as automotive, solar energy and packaging were performed.
- ! A comprehensive study in the fast-growing research in the mentioned field was reported in order to understand the potential application of polymer nanocomposites.
- ! There are different processes for the preparation of polymer nanocomposite materials each of each has its own advantages and drawbacks; therefore, it was



found that the suitable methods should be adjusted to the target application, composition, dispersion performance, etc.

- ! In terms of process improvements, ultrasonic-assisted dispersions have shown some encouraging results both in liquid media and melt plastic stream. These faces questioning related with the nano-safety of workers when handling nanoparticles, as well as with their use within consumer applications.
- ! Besides packaging, automotive and solar energy, nanocomposites' applicative potential is endless; it includes bio-/chemical sensing, electronic devices, drug delivery, microwave absorbing device, orthopedic application, etc.

### **Ultrasound assisted extrusion to prepare light and reinforced polypropylene nanocomposites for automotive applications**

- ! The main objective of this part of the Thesis work was to replace the commercial material used to obtain door panels by a new formulation that maintain the mechanical properties and decrease the density. For the automotive sector the lightweight materials are one of the main focused of applied research. The new formulation with the new procedure to obtain the nanocomposite were obtained a weight reduction of 11-13 wt.% for the selected piece.
- ! To reach the successful result, the method to obtain nanocomposites were the twin-screw compounding extrusion assisted with an ultrasound system optimized with the new approach of nodal point. Polypropylene were loaded with nanoclays Cloisite 20 and Garamite 1958, in combination with glass bubbles. The strategy was reducing the amount of added reinforcement within the neat polymer including the glass bubbles (hollow spheres) to reduce the final density of the material.
- ! The ultrasound system with a nodal point approach was the optimal option to improve the dispersion of nanofillers that increase the mechanical properties, reaching similar values to the commercial material but with lower density. In addition, the ultrasound system was demonstrated to be stable in continuous production for several hours.

! The results revealed that a lightweight material can be obtained with the ultrasound system coupled to the compounding extruder, to reduce the density of the materials, therefore, to reduce the weight of the plastic components in automobile, that can reduce de CO<sub>2</sub> emissions.